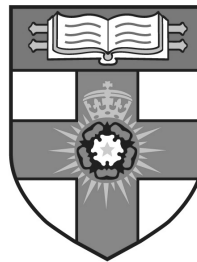


Optimization of Geometric Characteristics of Axial and Centrifugal Pumps For Mechanical Circulatory Support Devices

SAHAND MOZAFARI



School of Engineering and Materials Science
Queen Mary University of London

January 2017

This dissertation is submitted for the degree of Doctor of Philosophy

Declaration

I confirm that the research included within this thesis is the result of my own work and includes nothing which is the outcome of work done in collaboration except where specifically indicated in the text.

I confirm that this thesis has not been previously submitted for the award of a degree by this or any other university.

The copyright of this thesis rests with the author and no quotation from it or information derived from it may be published without the prior written consent of the author.

Signature:

Date:

Optimization of Geometric Characteristics of Axial and Centrifugal Pumps For Mechanical Circulatory Support Devices

Sahand Mozafari

Summary

The physiological and clinical considerations of centrifugal and axial pumps as ventricular assist devices (VADs) demands limitations on the power, size and geometry of the impellers. A typical pump design method is to rely on the characteristics of previously designed pumps with known performance using empirical equations and nondimensional parameters based on fluid dynamics similarity law. Such data are widely available for industrial pumps operating in Reynolds number region of 10^8 . VADs operate in $Re < 10^6$ and therefore the similarity concept does not apply between the industrial diagrams and the medical application of small pumps.

The present dissertation employs a parametric approached analytical model to investigate more than 150 axial and centrifugal pumps. The design parameters are optimised using the response surface methodology. The effect of different design parameters on the performance, force analysis and hemocompatibility of the pumps is thoroughly investigated by modelling the hæmolysis through a power-law equation. The results show an explicit and consistent relationship between the number of blades, outlet width, outlet angle and the hemocompatibility of the device. Centrifugal pumps showed significantly lower probability of blood complications compared to axial pumps. The evaluation of the design characteristics helps pump designers to select their parameters accordingly for a low probability of blood complications.

Furthermore, experimental techniques are employed to test more than 70 pumps in different conditions of flow, pressure and rotational speed. The experimental results validate the numerical simulations and create a database of empirical equations and data points for small axial and centrifugal pumps. The specific speed and specific diameters of the pumps are plotted on an $n_s - d_s$ diagram to enable preliminary design of small pumps for VADs suitable for different stages of congestive heart failure (CHF).

Acknowledgments

Getting very close to the finish line, I look back and see how far I have come and I see all the people that supported me through this long journey. First and foremost, I am indebted to my supervisor, Professor Theodosios Alexander for his continuous support, patience, motivation and immense knowledge. I could not have imagined having a better advisor and mentor along the way.

Besides my advisor, I would like to thank the rest of my research group: Dr. Gordon Paul, Dr. Amin Rezaenia and Mr. David Bosak for all the support they provided me with, all the brainstorming sessions, all the conferences and travels we went together and for all the beers we had in Wetherspoons. I am grateful to Mr. Dennis Ife for supporting me with his expertise and for knowing how everything works!

I would have not called the past four years the best years of my life if it were not for my friends. I am lucky to be surrounded by Michalis, Stefania, Charline, Olivier, Gordon, Amin, David, Halimat, Ghazal and Amir during my time in SEMS. I am grateful for all the coffee breaks, circuit trainings and lunch times we enjoyed together.

To my family and friends who were standing by my side from the day I started this journey until this very moment. Thank you for listening, offering advice and keeping me sane along the way. Your support and encouragement was worth more than I can express on paper. Thank you Desi for the beginning, for the end, and for every moment in-between. To Farshid - for being there when things went down. I am lucky to have Mehran and Parvaneh, Shahin, Leon, Miros, Ali, Mehrshad, Zoya, Sam and the rest of my beautiful BRC family in my life. You may be out of my sight, but never out of my mind.

I can imagine how proud my grandparents - Mohammad, Talat and Lotfali would be and how they always wanted to see me at the end of this road. I am grateful to have Firouzeh, who has drowned me in her unconditional love during this time. To my sister - Sahar and my mom- Dorina. Thinking about you has been the reason to smile when I needed the most.

Finally, I owe my deepest gratitude to my father - Ali. My supervisor in life, my role model and my hero. He is the reason I am standing where I am and the reason I always find the right path. I owe you my sanity during this journey and I consider it an honour to dedicate this thesis to you.

A special thanks to:

Dr. Gordon Paul, Dr. Olivier Picot, Dr. Desislava Hristova, Dr. Charline Sellam and Dr. Amin Rezaienia for their proofreading, which has profoundly improved the composition of this thesis.

“In my next life I want to live my life backwards. You start out dead and get that out of the way. Then you wake up in an old people’s home feeling better every day. You get kicked out for being too healthy, go collect your pension, and then when you start work, you get a gold watch and a party on your first day. You work for 40 years until you’re young enough to enjoy your retirement. You party, drink alcohol, and are generally promiscuous, then you are ready for high school. You then go to primary school, you become a kid, you play. You have no responsibilities, you become a baby until you are born. And then you spend your last 9 months floating in luxurious spa-like conditions with central heating and room service on tap, larger quarters every day and then Voila! You finish off as an orgasm!”

- *Woody Allen*

Contents

1	Introduction	21
1.1	Congestive Heart Failure	21
1.2	Treatment of Heart Failure	22
1.2.1	Pharmacological Treatment	22
1.2.2	Surgical Treatment	22
1.3	Mechanical Circulatory Support	24
1.3.1	Total Artificial Heart	25
1.3.2	Ventricular Assist Devices	26
1.4	Axial VADs	32
1.5	Centrifugal VADs	33
1.6	Axial vs. Centrifugal MCS Devices	34
1.7	Impeller Support and Rotation	36
1.8	VAD Complications and Considerations	36
1.8.1	Thrombosis and Embolism	36
1.8.2	Bleeding	37
1.8.3	Infection	38
1.8.4	Mechanical Failure	38
1.8.5	Hæmolysis	38
1.8.6	Heat Generation	40
1.8.7	Size	40
1.8.8	Physiological Conditions	40
1.9	Similarity Concept	41
1.9.1	Derivation of Specific Speed and Specific Diameter	43

1.10	$n_s - d_s$ diagrams	45
1.10.1	Why are conventional pump design methods not suitable for MCS devices?	45
1.11	Thesis and Substantiation	47
1.12	Statement of Novelty	48
1.13	Chapter Outline	48
1.14	List of Publications	50
2	Centrifugal and Axial Pumps As MCS Devices	52
2.1	Centrifugal Pumps Terminology	53
2.1.1	The Duty Frame	54
2.1.2	Volumetric Flow Rate	54
2.1.3	Head Rise (Pressure Rise)	54
2.1.4	Rotational Speed	54
2.1.5	Density	55
2.1.6	Inlet Flow Angle	55
2.1.7	Meridional Geometry	55
2.1.8	Meridional Velocity Ratio	56
2.1.9	Efficiencies	56
2.1.10	Shaft Diameter	58
2.1.11	D_{hub}/D_{shaft}	58
2.1.12	Leading Edge Blade Angle	58
2.1.13	Tip Diameter	59
2.1.14	Trailing Edge Blade Angle And Outlet Width	60
2.1.15	Rake Angle	63
2.1.16	Number of Blades	63
2.1.17	Slip	64
2.1.18	Hub Draft Angle	66
2.1.19	Impeller Blade Shape	66
2.1.20	Camberline/Thickness	67
2.1.21	Shroud Configurations	68

2.1.22	The Volute	69
2.2	Conventional Design Procedure	71
2.2.1	Velocity Triangles	71
2.2.2	Blade Outlet Conditions	75
2.2.3	Blade Inlet Conditions	82
2.2.4	Axial Clearance	87
2.2.5	Force Analysis	87
2.2.6	Radial Thrust	88
2.2.7	Axial Thrust	90
2.2.8	Experimental Force Measurement Techniques	93
2.3	Axial Pump Definitions and Terminology	95
2.3.1	Vane Cascades	95
2.3.2	Airfoils	96
2.3.3	Lift and Drag	97
2.3.4	Airfoil Profiles and Munk Method	97
2.3.5	Design Parameters	98
3	Numerical Methods	102
3.1	In-silico Investigations of Centrifugal Pumps as MCS Devices	103
3.1.1	Vista CPD	103
3.1.2	BladeModeler / BladeGen	103
3.1.3	TurboGrid	105
3.1.4	ANSYS CFX	107
3.1.5	Response Surface Methodology	113
3.1.6	Results and Discussion	115
3.2	In-silico Investigations of Axial Pumps as MCS Devices	132
3.2.1	Design MATLAB Program	132
3.2.2	Fluid Flow (CFX)	133
3.2.3	Results and Discussion	135

4	Experimental Techniques	145
4.1	In-vitro Investigations of Centrifugal Pumps as MCS Devices	146
4.1.1	SolidWorks	146
4.1.2	The O-loop	146
4.1.3	The Working Fluid	147
4.1.4	Measurement Systems	148
4.1.5	Experimental Errors and Uncertainties	148
4.1.6	Results and Discussion	151
4.2	In-vitro Investigations of Axial Pumps as MCS Devices	157
4.2.1	SolidWorks	157
4.2.2	The O-loop	157
4.2.3	The Working Fluid	158
4.2.4	Measurement System	158
4.2.5	Results and Discussion	159
5	Axial Flow versus Centrifugal Flow VADs	167
5.1	Technological Considerations	168
5.2	Clinical Considerations	169
5.3	A Comprehensive Analogy	170
6	Reflections and Outlook	174
6.1	Summary of Contributions	175
6.2	Future Directions & Outlook	176

List of Figures

1.1	The blood vessel graft in a CABG surgery, figure courtesy of El Camino Hospital.	23
1.2	The insertion of a ring to support the mitral valve [24].	23
1.3	Total Artificial Heart and its transplant steps, figure courtesy of Syn- cardia.	26
1.4	Classifications of VADs.	27
1.5	Schematic of LVAD (left) and RVAD (right) in the cardiovascular system [67]. Abbreviations: Ao, aorta; PA, pulmonary artery; RA, right atrium; LV, left ventricle.	28
1.6	HVAD® in LV-AAo configuration [116].	29
1.7	Jarvik pump in LV-DAo configuration [40].	30
1.8	10-F Reitan Catheter Pump, figure courtesy of Cardiobridge.	30
1.9	Thoratec IVAD supporting left and right ventricle, figure courtesy of Thoratec Corp.	31
1.10	DebKey VAD, figure courtesy of USC.	33
1.11	HeartMate II LVAD, figure courtesy of Thoratec Corp.	33
1.12	HeartMate III LVAD, figure courtesy of Thoratec Corp.	34
1.13	Thrombus formed on an axial impeller, figure courtesy of Thomas Jefferson University Hospital.	37
1.14	$n_s - d_s$ diagram for pumps [12].	46
2.1	Specific speed dictating the pump type, figure courtesy of the Hy- draulic Institute Standards book.	53
2.2	The meridional profile [149].	55
2.3	The meridional velocity profile, figure courtesy of ANSYS.	56
2.4	The hub and shaft diameter, figure courtesy of ANSYS.	58

2.5	The trailing edge blade angle, figure courtesy of ANSYS.	61
2.6	Ideal H-Q curve trend for different types of outlet angles.	62
2.7	The outlet width of the blade, figure courtesy of ANSYS.	62
2.8	A typical graph showing the influence of the number of blades on outlet width and angle.	64
2.9	Effect of slip on the flow between the blades [46].	65
2.10	The slip at the trailing edge [46].	65
2.11	The hub draft angle, figure courtesy of ANSYS.	66
2.12	A cubic Bezier curve with four control points.	67
2.13	Three types of volutes: Singular, double and circular [137].	70
2.14	The volute inlet width shown with tip width and clearances, figure courtesy of ANSYS.	70
2.15	Volute models with rectangular, circular and trapezoidal cross sec- tions [5].	71
2.16	The linear relationship between the taper angle of the diffuser and the fluid velocity at the throat [69].	72
2.17	A single volute with a circular cross section, figure courtesy of ANSYS.	72
2.18	Centrifugal impeller inlet and outlet velocity vectors [137].	73
2.19	Pump efficiency vs. specific speed for industrial single stage single suction pumps [12].	74
2.20	Blade outlet velocity triangle [137].	75
2.21	Percent pressure rise vs. specific speed for blade angle and number selection [76].	76
2.22	Head and flow coefficients for different outlet angles [128].	77
2.23	Speed constants for different number of blades [76].	77
2.24	Speed constants for impellers with 6 blades and a 22.5° outlet an- gle [128].	78
2.25	Actual impeller tip speed [137].	78
2.26	Meridional outlet velocity [137].	79
2.27	Euler absolute outlet velocity [137].	80
2.28	Actual absolute outlet velocity [137].	81
2.29	Blade inlet velocity triangle [137].	83

2.30	Impeller inlet diameter [137].	84
2.31	Impeller inlet tip speed [137].	84
2.32	Impeller inlet blade angle [137].	85
2.33	Impeller actual inlet blade angle [137].	86
2.34	The ideal absolute inlet velocity [137].	86
2.35	The actual absolute inlet velocity [137].	87
2.36	Axial blade Cascade.	95
2.37	Airfoil parameters.	96
2.38	Airfoil characteristics in terms of curvature $\beta_2 - \beta_1 = \theta_2 + \theta_1$ [128]. . . .	98
2.39	The velocity triangles at inlet and outlet.	100
3.1	Blade meridional profile.	104
3.2	$\theta - m'$ curves from the leading to the trailing edge.	105
3.3	Spanwise and streamwise lofting of the blade.	106
3.4	The impeller in ANSYS BladeGen.	106
3.5	The impeller passage and volute in TurboGrid.	107
3.6	The impeller and volute domains in ANSYS CFX, The arrows indicate the inlet and outlet of the domains.	108
3.7	Stationary and moving coordinate systems in MRF method.	109
3.8	Interface treatment for the MRF model.	110
3.9	The scatters of design variables distributed in the three dimensional design space.	114
3.10	Response surface graphs for the design variable optimizations.	115
3.11	Efficiency vs. flow ratio for different blade numbers.	116
3.12	Head ratio vs. flow ratio for different blade numbers.	117
3.13	Head ratio vs. flow ratio for different blade angles.	118
3.14	Efficiency vs. flow ratio for different outlet angles.	118
3.15	Head ratio vs. flow ratio for different outlet widths.	119
3.16	Efficiency vs. flow ratio for different outlet widths.	119
3.17	Head ratio vs. flow ratio for different rotational speeds.	120
3.18	Efficiency vs. flow ratio for different rotational speeds.	120
3.19	Axial and radial thrust predictions based on theoretical models	122

3.20	The simulated axial thrust in the representative impeller at different rotational speeds.	123
3.21	Static radial thrust magnitudes and directions for a representative impeller.	123
3.22	The simulated NIH for different blade numbers and outlet angles. . .	126
3.23	The simulated NIH for different outlet widths and outlet angles. . . .	127
3.24	Pressure distribution in three pumps at different rotational speeds. . .	128
3.25	Velocity streamlines in three pumps at different rotational speeds. . .	129
3.26	Impeller wall shear stress in three pumps at different rotational speeds.	130
3.27	Volute wall shear stress in three pumps at different rotational speeds.	131
3.28	The blade profile of a representative impeller generated by the MATLAB design code.	132
3.29	The representative impeller imported in DesignModeler.	133
3.30	The impeller and volute domain in ANSYS CFX. The arrows indicate the inlet and outlet of the domain.	134
3.31	Axial and radial thrust magnitude for the representative impeller A. .	136
3.32	Axial and radial thrust magnitude for different outlet angles, rotating at 7000 rpm.	137
3.33	The simulated NIH for different outlet angles at four rotational speeds.	138
3.34	The simulated wall shear stress on airfoil surface at 75% span for $\beta_2=2^\circ$.	138
3.35	The simulated wall shear stress on airfoil surface at 75% span for $\beta_2=10^\circ$	139
3.36	The simulated wall shear stress on airfoil surface at 75% span for $\beta_2=20^\circ$	139
3.37	The simulated wall shear stress on airfoil surface at 75% span for $\beta_2=30^\circ$	140
3.38	The simulated wall shear stress on airfoil surface at 75% span for $\beta_2=40^\circ$	140
3.39	Wall shear stress for different angles at different rotational speeds. . .	142
3.40	Pressure distribution on the impeller for different angles at different rotational speeds.	143
3.41	Pressure rise for different angles at different rotational speeds.	144
4.1	Drawing a blade in SolidWorks.	146

4.2	A shrouded 5 bladed impeller in SolidWorks	146
4.3	The schematic diagram of the O-loop [66].	147
4.4	The O-loop.	148
4.5	Accuracy and precision.	149
4.6	The Labview interface for data measurement and control.	150
4.7	Highest efficiency points on $n_s - d_s$ Cordier diagram for all impellers ($2 \times 10^4 < Re < 7 \times 10^4$) [66].	152
4.8	Profiles of the impellers A and B [66].	152
4.9	Numerical and experimental efficiency vs. Q/Q_{des} for impeller A [66].	153
4.10	Numerical and experimental efficiency vs. Q/Q_{des} for impeller B [66].	153
4.11	Numerical and experimental H/H_{des} vs. Q/Q_{des} for impeller A.	154
4.12	Numerical and experimental H/H_{des} vs. Q/Q_{des} for impeller B.	155
4.13	Numerical and experimental efficiency vs. n_s for impellers A (left) and B (right) [66].	155
4.14	Numerical and experimental head coefficient (ψ) vs. flow coefficient (ϕ) for impellers A (left) and B (right) [66].	156
4.15	Impeller A performing in steady condition and transient flow [66]. . .	156
4.16	Drawing the impeller blade in SolidWorks.	157
4.17	Impeller A, created in SolidWorks.	157
4.18	The schematic diagram of the axial O-loop.	158
4.19	The O-loop.	159
4.20	The profile of impeller A, selected for results presentation.	160
4.21	Performance curves of the impeller A at different rotational speeds. .	160
4.22	Performance curves for different outlet angles, rotating at 6000 rpm. .	161
4.23	Performance curves of three impellers with 20° outlet angle, rotating at 6000 rpm.	163
4.24	Efficiency and head-flow coefficients for 14 impellers.	164
4.25	Highest efficiency points on $n_s - d_s$ Cordier diagram for all impellers ($4 \times 10^4 < Re < 2 \times 10^5$).	165
5.1	Axial and centrifugal VADs HQ curves and flow waveforms recorded in LVAD clinical patients [45].	168

5.2	Centrifugal and axial LVAD head-flow, LV and aorta pressure wave- forms in a mock flow loop model [45].	169
5.3	Centrifugal and axial LVAD head-flow, LV and aorta pressure wave- forms, clinical observations [45].	170
5.4	Performance curves of selected axial and centrifugal pumps.	171
5.5	Highest efficiency points of centrifugal and axial pumps on $n_s - d_s$ Cordier diagram.	172
5.6	Highest efficiency points of small centrifugal and axial pumps on Balje's industrial $n_s - d_s$ Cordier diagram.	173

List of Tables

1.1	Classification of intracorporeal devices, mechanisms, effects and common indications.	26
1.2	Commercially available MCS devices with specifications [105].	35
1.3	Basic Dimensions [12].	42
1.4	Nondimensional parameters for pumps.	42
1.5	Conversion data for n_s and d_s [12].	44
2.1	Numerical investigation on three types of impellers.	69
3.1	Design parameters of a representative impeller.	104
3.2	Results of mesh independence.	107
3.3	Maximum and design point axial thrust at different rotational speeds.	121
3.4	Maximum and design point radial thrust at different rotational speeds.	121
3.5	Power-law equation constants for different proposed models [135] . . .	124
3.6	Results of mesh independence.	134
4.1	Numerical and experimental results of impeller A ($\beta_2=20^\circ$, 22mm diameter)	161
4.2	Numerical and experimental results of impellers with 16.5° - 35° outlet angle, rotating at 6000 rpm.	162
4.3	Data for axial pumps.	166
5.1	Design parameters, specifications and output values of two selected pumps.	172

Nomenclature

β	Blade angle	g	Gravitational acceleration
$\Delta freeHb$	The increase in plasma free hemoglobin	H_b	The hemoglobin concentration
Δp	Pressure difference	H_r	Relative enthalpy
η	Efficiency	H_t	Theoretical head
η_M	Mechanical efficiency	H_{ad}	Adiabatic head
η_V	Volumetric efficiency	Hct	Hematocrit
μ	Dynamic viscosity	HI	Hæmolysis index
ν	Kinematic viscosity	J	The polar moment of inertia
ϕ	Flow coefficient	k	Hemoglobin content of blood
ψ	Head coefficient	K_m	Capacity constant
ρ	Density	K_u	Speed constant
σ	Slip factor	K_{th}	Thrust factor
τ	Shear stress	l	Vane cord
θ_{draft}	Hub draft angle	m	Meridional component
A	Area	m'	Normalized meridional component
b_2	Outlet width	N_s	Rotational speed
C	Fluid velocity	n_s	Specific speed
c	Shaft radius	NIH	Normalized index of hæmolysis
C_D	Drag coefficient	P_s	Recirculation factor
C_L	Lift coefficient	P_{disk}	Power loss due to loss friction
C_m	Meridional velocity	P_{in}	Input power
D	Rotor diameter	Q	Volumetric flow rate
d_s	Specific diameter	Q_{leak}	Leakage flow rate
des	Design point	r	Rotor radius
E_r	Relative internal energy	Re	Reynolds number
F_r	Radial thrust	S	Source term
F_z	Axial thrust	s_u	Blade thickness
		stn	Standard
		T	Torque
		t	Pitch
		t_{exp}	Exposure time
		U_2	Rotor tip speed
		Z	Number of blades

Chapter 1

Introduction

The various forms of cardiovascular disease (CVD) are the leading cause of death in the world with 31% of all global deaths [36]. According to a World Bank analysis, over three quarters of CVD deaths take place in low- and middle-income countries. The European Heart Network organization reports that each year CVD causes over 4 million deaths in Europe (47% of all deaths) and over 1.9 million deaths in the European Union (40% of all deaths) [87]. CVD is estimated to cost the EU economy €196 billion a year. Congestive Heart Failure (CHF) is a common form of CVD in which the heart is unable to pump blood as well as it should, causing shortness of breath and fatigue in sufferers [158].

1.1 Congestive Heart Failure

CHF causes difficulty for the native heart in pumping blood around the body, and is characterized by ventricular dysfunction leading to an insufficient cardiac output, leading to lower exercise capacity and reduced cardiovascular endurance.

CHF is categorized into four stages of increasing severity by the American College of Cardiology Foundation (ACCF) and American Heart Association (AHA) [158]. Stage I represents the condition in which the patient has no structural heart disease or symptoms, but is at high risk of heart failure by having one or more risk factors. This might progress to structural heart disease without (stage II) or with (stage III) symptoms and eventually get to the refractory heart failure requiring specialized interventions (stage IV). Medications are effective in treating stages I and II, but their use is palliative in stages III and IV. More than seven million people are suffering from CHF in North America and Europe, among whom $\approx 6\%$ are diagnosed with stage IV [75].

1.2 Treatment of Heart Failure

There are two main therapies available for this condition. In the early stages, dietary changes to reduce weight and salt consumption as well as pharmacological treatments can be effective in preventing the progress of the disease. In the end-stages of the disease the patient does not respond to drugs and dietary changes and surgical treatments are the preferred options.

1.2.1 Pharmacological Treatment

Studies of heart failure have reported that several classes of drugs are suitable for the treatment of heart failure. Patients with heart failure may need one or multiple types of drugs, each one used to treat a different symptom or contributing factor. Blood thinners (Anticoagulants), Cholesterol lowering drugs (statin), Diuretics (water pills) and Angiotensin receptor blockers and inhibitors are some of the commonly prescribed heart failure medications [158].

1.2.2 Surgical Treatment

In the end-stages of CHF, where the patient does not respond to pharmacological treatments, surgical treatment is preferred. The surgery is aimed at stopping further damage to the native heart (or replacing it) and improving its function. This treatment includes conventional surgeries, Aneurysm repair surgery, heart transplant and mechanical circulatory support (MCS) device implantation.

Conventional Surgeries

- Coronary Artery Bypass Graft (CABG) Surgery:

If the coronary arteries have lower blood flow due to blockage or being lined with plaque, CABG surgery is recommended. The surgery involves a blood vessel graft to bypass the coronary arteries by going around the clogged artery and forming a new path for blood to flow. The grafts are normally taken from the arteries and veins in the patients chest, leg or arm. Figure 1.1 shows the position of the blood vessel graft after a CABG surgery.

- Valve Surgery:

In a later stage of heart failure, the papillary muscles become larger and therefore fail to support the mitral valve leaflets leading to a leakage in the valves. The surgery involves reshaping the leaflets and supporting the valve with a ring. This surgery is

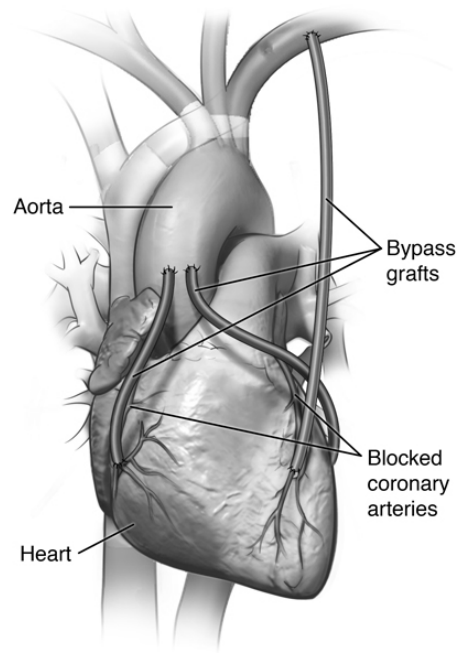
Coronary artery bypass graft (CABG)

Figure 1.1: The blood vessel graft in a CABG surgery, figure courtesy of El Camino Hospital.

also recommended for the aortic valve stenosis (stiffness) or regurgitation (leakage) by repairing or replacing the aortic valve. Figure 1.2 shows the different steps of this surgery.

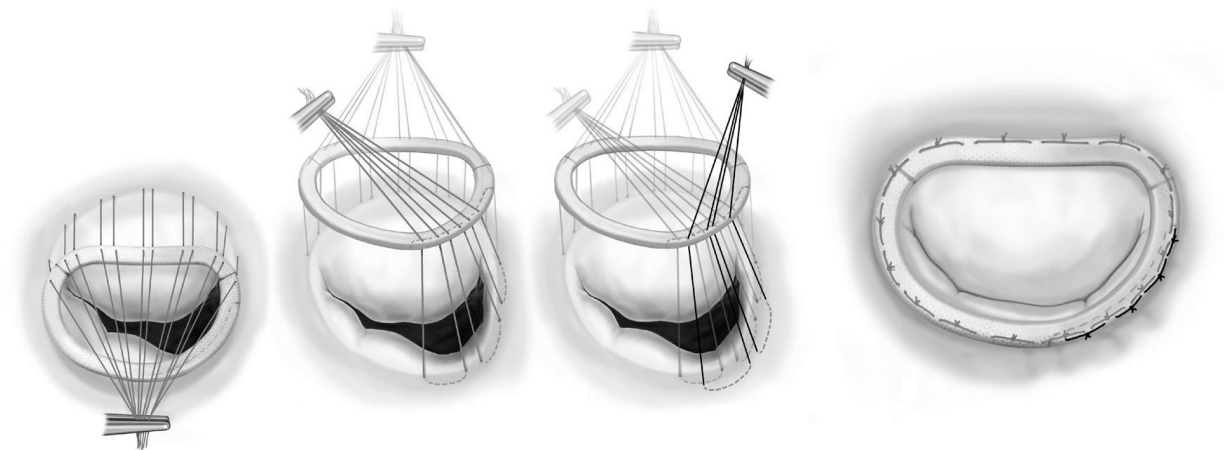


Figure 1.2: The insertion of a ring to support the aortic valve [24].

Aneurysm Repair Surgery

This surgery is used when a heart attack causes a scar in the left ventricle. The scarred zone can swell with every heartbeat. This zone is called an aneurysm and will cause the left ventricle to dilute and get weaker. In this surgery, the scarred

muscle and the aneurysm tissue are removed and replaced by a patch.

Heart Transplantation

Heart transplantation is the most well established surgical treatment and is the main option for patients in stage IV and some of the patients in stage III. Although in the early years of this method (1967), the survival rate was as short as a few weeks, four decades later in 2006, The New England Journal of Medicine (NEJM) reported [56] that $\approx 85\%$ of the patients survive more than a year after the transplant. However, there is currently a huge shortfall in the number of donor hearts available compared to those required. With the donor hearts supplying less than 2% of the demand, a large number of patients waiting for a heart transplant will not survive until they receive a donor heart [127]. Heart transplants are normally suggested only when absolutely necessary and as a last option. The surgery is a significantly prolonged and invasive surgery and therefore the patients on the heart transplant waiting list must not have any medical conditions that would prevent a successful surgery and recovery and there must be a good chance of long term transplant success. During the surgery, most of the heart is removed and the donor heart is inserted and attached to the major vessels.

Mechanical Circulatory Support Devices

The shortage of donor hearts has led to the development of mechanical circulatory support devices. The inlet and outlet of most of these pumps are designed to be anastomosed in the apex of the ventricles and the aorta respectively, and these devices are called Ventricular Assist Devices (VAD). Such devices are designed for implantation adjacent to the heart and act as pumps to help blood flow around the body, in a manner that some or all of the pumping function is provided by the VAD. The other major type of MCS devices are total artificial hearts (TAH). These devices replace the native heart and consist of two blood pumps as the left and right ventricles.

1.3 Mechanical Circulatory Support

MCS devices can be employed to provide circulatory support for patients and bridge them to a heart transplant, to recovery, or as a destination alternative as well as restoring the healthy level of physiological conditions for patients with cardiac dysfunction. Such devices offer an alternative to heart transplant and allow patients

on the waiting list to relocate from intensive care units to general wards, or leave the hospital altogether [137]. MCS device implantation can be classified into three categories based on their application.

Bridge to Transplantation

Due to the shortage of donor hearts, the application of MCS devices as a bridge to transplant has been increasingly important in recent years [109]. Studies have reported [1] a 90% survival rate after the heart transplant in patients who were supported with an MCS device during the waiting period. Before this stage, between 30% to 40% of the waiting list patients die during the cardiac support. Therefore, 54-63% of the patients on MCS support as a bridge to transplant, survive after the heart transplant. A previous study [90] suggests that this percentage could be much lower without the mechanical support before the transplant.

Bridge to Recovery

Studies have reported cases of CHF patients recovering normal cardiac function after one year post-implantation [90]. MCS devices provide circulatory support as a bridge to recovery and help the patient to regain cardiac function during this support by reducing the workload of the left ventricle. The device can be removed after this period without the need of heart transplant.

Bridge to Destination

The application of MCS devices as bridge to destination is the only alternative solution for patients with chronic irreversible heart failure [50]. Patients who are not able to find a donor heart can have improved life expectancy and quality of life after a permanent implantation of an MCS device. The MCS device for this purpose should meet three main requirements; long term safety, durability and efficiency. The new generation of MCS devices are reliable for this prolonged application due to their simplicity, efficiency and small size. This application has decreased morbidity and mortality in patients over the past decades [40, 33, 143, 85, 78].

The classification of intracorporeal MCS devices, mechanisms and haemodynamic effects are shown in Table 1.1. TAHs and VADs from this table will be discussed in more details.

1.3.1 Total Artificial Heart

In the 1960's, several attempts and considerable efforts were made by several research groups to design and develop total artificial hearts. In 1969 a TAH was implanted

Table 1.1: Classification of intracorporeal devices, mechanisms, effects and common indications.

Device	Mechanism	Effects	Applications
LVAD RVAD BiVAD	Pumps are implanted with two cannulas, withdrawing blood from ventricles and delivering to the aorta.	Increase in the relevant ventricle cardiac output and unloading ventricle.	Bridge to Recovery Bridge to Transplant and Bridge to Destination
Total Artificial Heart	Pneumatic pulsatile pump replacing both ventricles and 4 valves.	Replaces both ventricles function.	Bridge to Transplant

in a heart failure patient for the first time [14]. The device was used as a bridge to transplant and performed well for 64 days before the surgery.

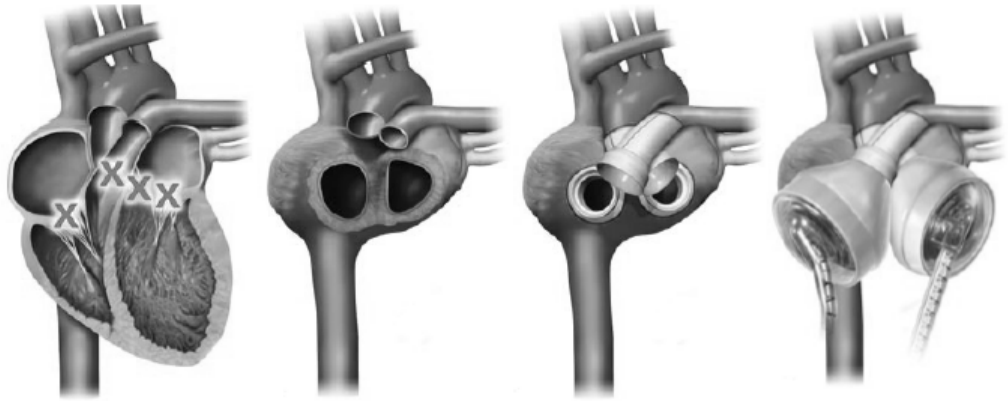


Figure 1.3: Total Artificial Heart and its transplant steps, figure courtesy of Syncardia.

A TAH consists of two blood pumps (Figure 1.3) that replace for left and right ventricular function. Older devices are mainly pneumatically actuated and are normally large in size, heavy and inefficient. Examples include the Jarvik 7 and SynCardia devices [14, 117, 32]. The newer devices are electrically actuated, smaller and more efficient than the older versions, such as AbioCor device [32].

However, a major problem with these devices is blood complications after the surgery, such as blood clotting, valve failure and bleeding, due to the complexity and severity of the surgery. Many researchers and cardiologists are still pursuing the design and development of smaller and more efficient TAHs.

1.3.2 Ventricular Assist Devices

The other type of intra-corporeal MCS devices are VADs. VADs are used to partially or completely replace a failing ventricle. The failing ventricle can be the right,

left or both ventricles. VADs do not replace the native heart and therefore are the only devices with capability of performing as bridge to recovery, transplant and destination altogether. VADs can be categorized based on their type of assistance, configuration or dynamic motion. Figure 1.4 shows a tree diagram showing the different categories of VADs.

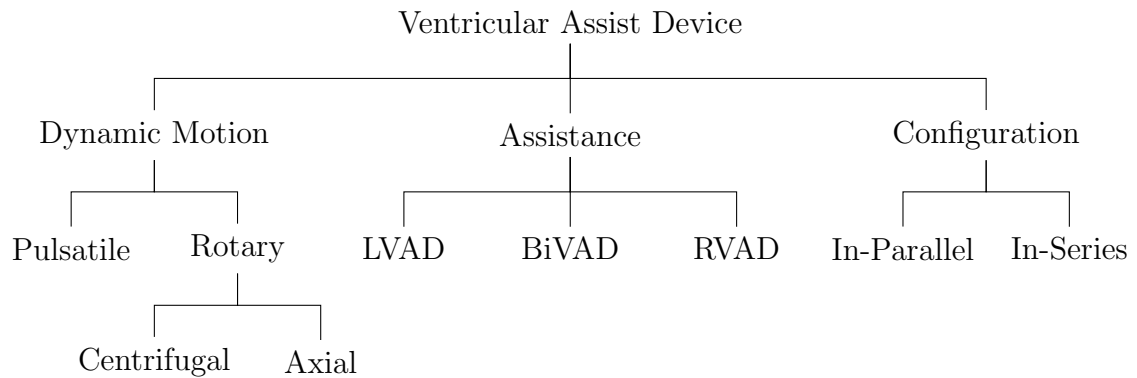


Figure 1.4: Classifications of VADs.

Assistance

Based on the severity and type of heart failure, VADs are implanted to support either left (LVAD), right (RVAD) or both (BiVAD) ventricles:

- Left Ventricular Assist Device (LVAD):

LVADs are designed and implanted to support the left ventricle. The device receives the blood from the left atrium (atrial cannulation) or the apex of the left ventricle (apical cannulation) and delivers it to the ascending aorta. The atrial cannulation has fewer complications for the native heart, but the VAD in apical cannulation performs better in unloading.

- Right Ventricular Assist Device (RVAD):

In this case, RVAD is designed and implanted to receive blood from the right atrium and deliver it to the pulmonary artery.

- BiVentricular Assist Device (BiVAD):

BiVADS combine the function of LVADs and RVADs in a single device. BiVADs assist the heart failure patients by withdrawing blood from the left ventricle and the right atrium and deliver it to the ascending aorta and the pulmonary artery respectively. Figure 1.5 shows the schematic of the LVAD and RVAD in the heart.

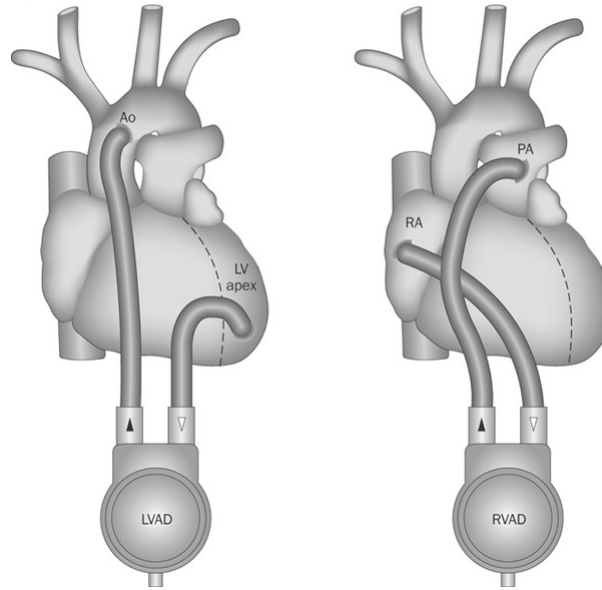


Figure 1.5: Schematic of LVAD (left) and RVAD (right) in the cardiovascular system [67].

Abbreviations: Ao, aorta; PA, pulmonary artery; RA, right atrium; LV, left ventricle.

Configuration and Implantation Technique

There are two methods for the surgical deployment of VADs into the cardiovascular system; median sternotomy and left thoracotomy. In median sternotomy method, the patients sternum is cracked and the VAD is installed next to the native heart. In the left thoracotomy method, VAD is installed through an incision in the left thoracotomy. Although in the left thoracotomy method the sternum is not cracked, however both methods have substantially invasive surgeries and require cardiopulmonary bypass (CPB) during the operation. Previous studies have reported [60] cases of infection, bleeding and other blood complications after these long and invasive surgeries. In recent years, there has been an increasing amount of research into developing less invasive techniques.

VADs are categorised based on their configuration into in-series and in-parallel configurations. Based on numerical and experimental results, MCS devices are required to produce different performance characteristics based on their configuration and implantation technique. For instance, the device should produce less pressure in-series than required in-parallel configuration, as a portion of this pressure rise is supplied by the native heart [104, 113, 103], therefore the design technique should be applicable to different performance requirements.

- In-Parallel Configuration

In this configuration, the device is placed between the left ventricle and the ascending or descending aorta. Based on the outlet of the pump, this configuration is categorised into two types.

From Left Ventricle to Ascending Aorta (LV-AAo):

In this method the device is placed between the apex of the left ventricle and the ascending aorta in a parallel configuration with the native heart via a sternotomy surgery. In-parallel LV-AAo generally improves cardiac output significantly [64, 74, 111]. However, a major problem with this configuration is the considerable post-operative complications due to the prolonged surgery and the use of CPB during the operation. Studies have reported the dysfunction of the ventricle, end-organ injury and internal bleeding in patients after this surgery [111]. The HVAD[®] pump made by HeartWare is placed in an in-parallel LV-AAo configuration as shown in Figure 1.6.

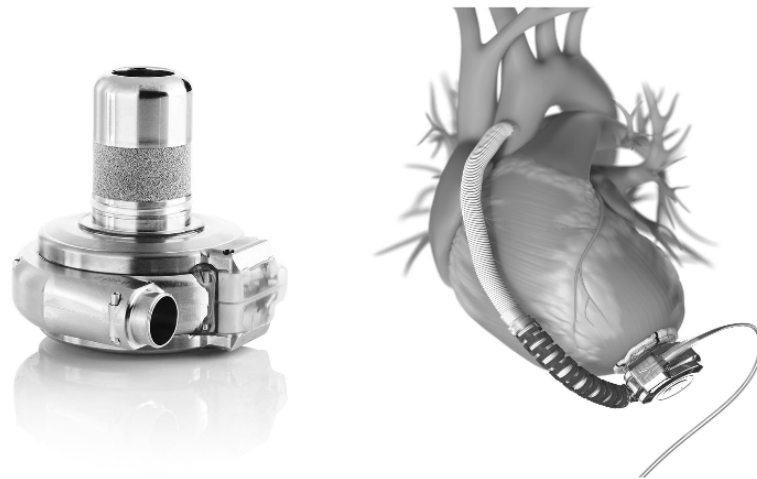


Figure 1.6: HVAD[®] in LV-AAo configuration [116].

From Left Ventricle to Descending Aorta (LV-DAo):

The left thoracotomy surgery technique is preferred to the median sternotomy technique and the VADs used in this method are smaller, lighter and have lower energy consumption compared to other generations. In general, this surgery requires the devices to be smaller, as the incision is smaller. In this technique, the VAD is installed through an incision into the left thorax. The inflow and outflow grafts are sewn into the apex of the LV and the descending aorta (DAo) respectively. The device is adjacent to the left atrium, in-parallel configuration with the native heart [53, 111, 49, 93]. This surgery is less likely to need CPB during the operation [111]. The Jarvik pump is shown in Figure 1.7 in the LV-DAo configuration.

The advantage of LV-DAo method compared to LV-AAo is the shorter operation and therefore, a lower probability of post-operative complications. The disadvantage of this method is the reduction in perfusion to the aortic arch due to the connection between the outlet graft and the descending aorta. This leads to haemodynamic inefficiency of the device in higher support levels and eventually causes aortic valve



Figure 1.7: Jarvik pump in LV-DAo configuration [40].

stenosis [106, 60, 93, 13].

- In-Series Configuration

VADs operating in in-series configuration with the native heart pump the blood directly from the ascending to the descending aorta. The reduced pressure upstream of the device reduces the after-load pressure on the LV to facilitate cardiac output [105]. A number of researchers have reported [116, 106, 99, 100, 118] a lower probability of post-operative complications and less invasive surgeries with VADs in the descending aorta.

The 10F-Reitan catheter pump, shown in Figure 1.8, consists of two folding vanes placed in a double umbrella casing. The pump operates with a DC motor via a flexible wire shaft covered by a catheter. The pump is implanted in-series with the native heart in the descending aorta via an incision through the femoral artery. Once the pump system is at the right place in the descending aorta, the cage and the vanes are unfolded. The Reitan pump produces ≈ 25 mmHg pressure rise while rotating at 14k rpm [99].

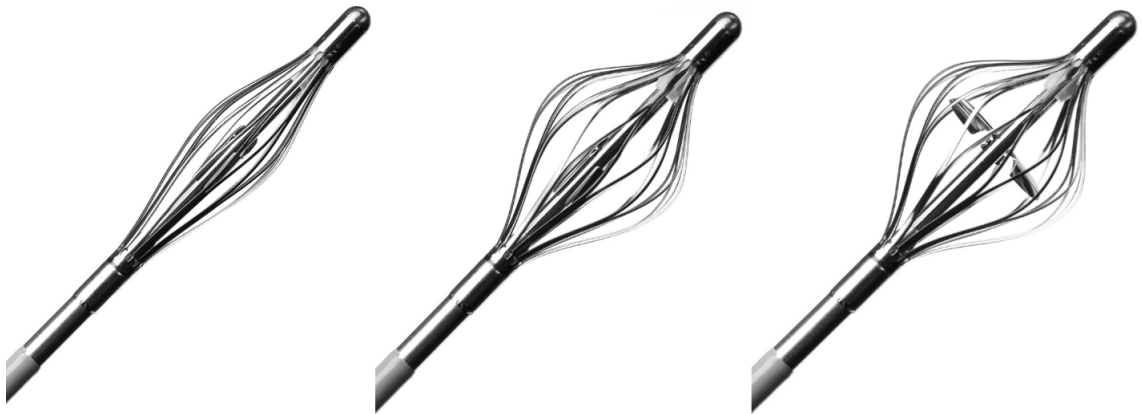


Figure 1.8: 10-F Reitan Catheter Pump, figure courtesy of Cardiobridge.

Dynamic Motion

VADs can be also categorised based on their dynamic motion or the flow type. Pulsatile flow is produced by pulsatile (displacement) VADs and continuous flow is produced by rotary VADs.

- Pulsatile VADs

In displacement pumps, pulsatile flow is created due to the periodic change of the pumps working volume. Pulsatile pumps are considered to be the first generation of VADs and can mimic the patient's left ventricle. The first pulsatile VAD was implanted in a patient in LV-DAo configuration [73]. The advantage of using these pumps is the direct relationship between outlet flow, stroke volume and the pumping frequency, resulting in a precise flow control under various conditions. The pump consists of a flexible pneumatically or electrically actuated diaphragm to produce the pulsatile flow and two valves to prevent the back-flow. Examples for pulsatile VADs are: BVS 5000 VAD - by Abiomed Inc. (extracorporeal) [108], Thoratec IVAD - by Thoratec Corporation. (extracorporeal) [35], Novacor LVA System - by World Heart Inc. (intracorporeal) [34] and LionHeart VAD - by Arrow International Inc. (totally implantable) [82]. Thoratec IVAD provides support to the left, right, or both ventricles and is shown as an example in Figure 1.9 used as a BiVAD.

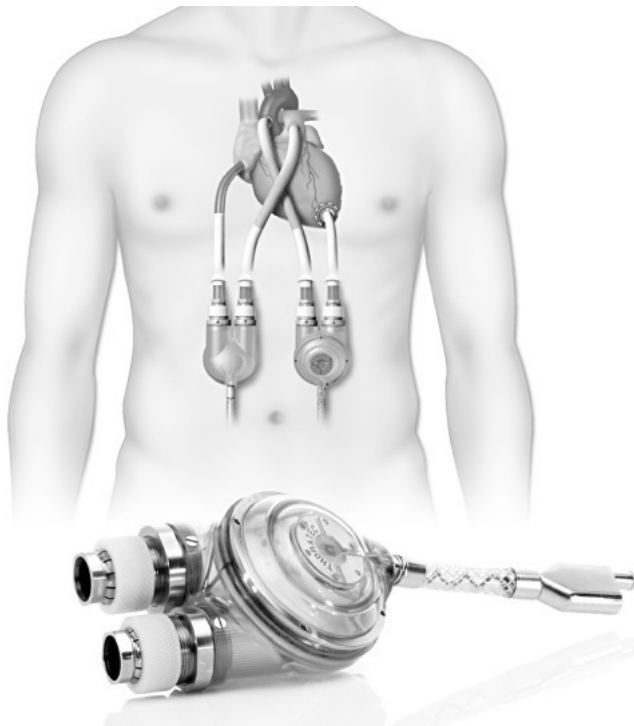


Figure 1.9: Thoratec IVAD supporting left and right ventricle, figure courtesy of Thoratec Corp.

Pulsatile flow has many advantages over a continuous flow. Pulsatile flow improves the micro-circulation in diseased cells and helps restore cardiac function. It also

oxygenates the kidneys and the livers [105, 62, 145, 112]. However, the large size, heavy weight and loud noise of the pulsatile devices led to the development of the next generation of VADs.

- Rotary VADs

Unlike the pulsatile pumps, which are suitable for low flow rate and high pressure rise, rotary flow VADs tend to provide larger volume flow rate and lower pressure rise. The disadvantages of pulsatile devices encouraged researchers to develop VADs with higher efficiency, smaller size, lighter and with fewer moving elements. Rotary blood pumps are the second and third generations of the VADs based on their bearing system. Each generation consists of axial or centrifugal pumps. Rotary axial or centrifugal pumps supported by pivot bearings are classified as the second generation VADs. The contact bearings in this generation devices resulted in higher risk of blood complications and led to the development of a third generation with contactless impeller suspension by hydrodynamic or magnetic means. The lack of mechanical contact results in a lower component wear and higher durability is reported for such devices compared to the second generation VADs [131].

1.4 Axial VADs

Axial flow pumps are employed to generate a low pressure gradient at high volume flow rate conditions. Axial pumps are smaller than pulsatile and centrifugal devices, which leads to less invasive surgery and lower risk of post-operative infections. The DeBakey axial VAD is shown in Figure 1.10 as an example of these devices. The pump consists of an impeller made of titanium rotating inside a cylindrical housing, a flow straightener at the upstream and a set of vanes at the downstream to act as a diffuser. Small magnets are embedded inside the impeller vanes to interact with the brushless magnet around the housing. The impeller is driven by the magnetic field between the vanes and the housing and blood flows inside the device. The diffuser converts the kinetic energy of the fluid to static pressure by converting the swirl velocity of the blood into axial velocity. The impeller's rotational speed is 8-12k rpm and the pump produces 3-6 L/min flow rate [53].

Devices such as Jarvik 2000 [78], HeartMate II [50] (shown in Figure 1.11) and Micromed [52], employ contact bearings to hold the impeller in place, resulting in a higher risk of blood complications. The third generation devices were developed using magnetic or hydrodynamic bearings to levitate the impeller in place. Devices such as Incore1 significantly avoids the friction force between the impeller and the housing by having a magnetically levitated impeller [53].

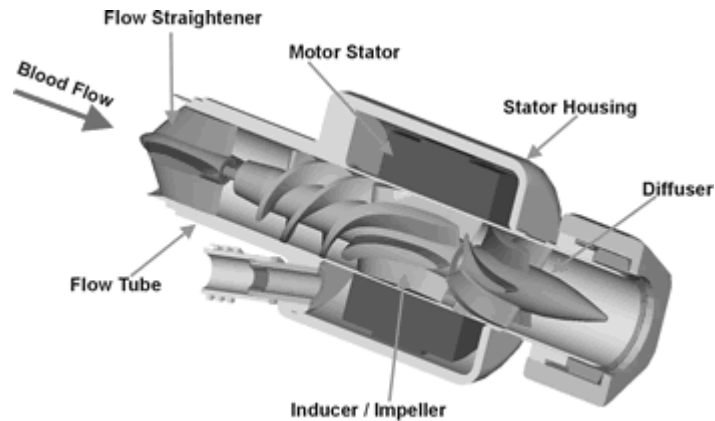


Figure 1.10: DebKey VAD, figure courtesy of USC.

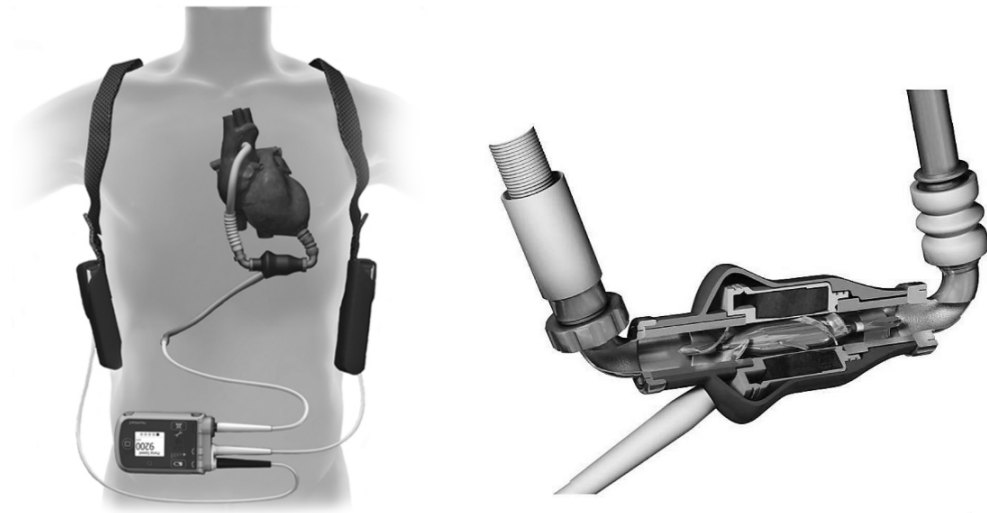


Figure 1.11: HeartMate II LVAD, figure courtesy of Thoratec Corp.

1.5 Centrifugal VADs

Centrifugal pumps have been used for CPB during surgeries since 1980 and the first implantable centrifugal blood pump was implanted in a patient as a bridge to transplant in 1985 [47].

Centrifugal pumps are used to produce pressure rather than flow rate and convert the axial velocity into radial due to the inlet and outlet flow being perpendicular. One of the most important advantages of centrifugal heart assist devices over axial flow pumps is that centrifugal pumps run at significantly lower rotational speeds (2-6k rpm compared to 3-25k for axial pumps [106]), and are therefore less likely to cause blood complications, making them a good option for long term support as a bridge to destination. The lower rpm in these pumps results in lower shear stress between the components and therefore minimal physiological consequences. However, centrifugal pumps are normally larger than axial pumps, leading to a

more invasive implantation surgery and increasing the chance of organ infections, neurological damages and cancer after the surgery [55]. HeartMate III is a long-term compact centrifugal LVAD by Thoratec and is shown in Figure 1.12.

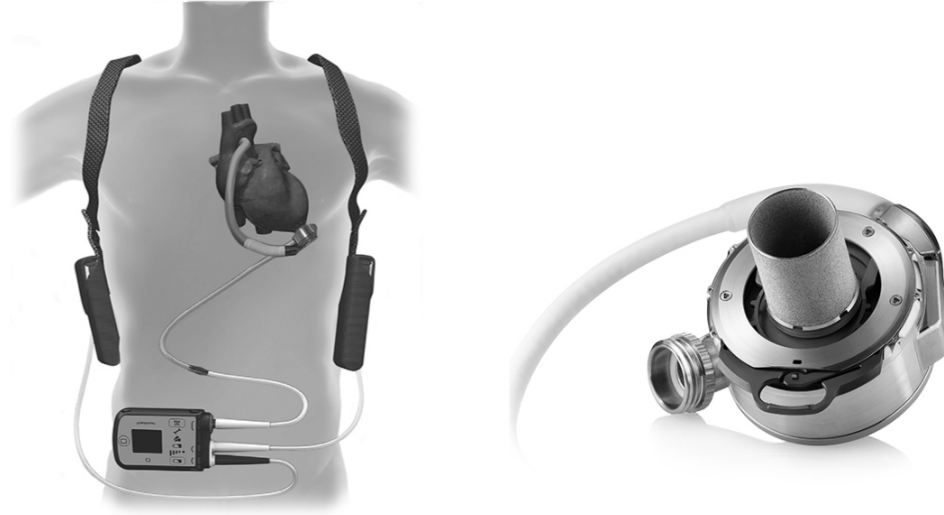


Figure 1.12: HeartMate III LVAD, figure courtesy of Thoratec Corp.

1.6 Axial vs. Centrifugal MCS Devices

Due to the different characteristics of centrifugal and axial pumps, these devices have different advantages and disadvantages compared to each other. Centrifugal pumps have higher efficiency and lower cost due to mechanical simplicity and lower probability of blood complications due to fewer moving elements and lack of valves [92, 88, 141, 129, 131]. Axial pumps need higher rotational speeds in order to produce the same pressure rise. The lower operating rotational speeds of centrifugal pumps compared to axial pumps results in longer bearing life, and lack of straightener and diffuser blades reduces the risk of thrombosis formation [156]. In older generations of centrifugal VADs, high friction in the bearing and seal generates heat and leads to the irreversible denaturation of protein in blood [4, 157]. Due to lack of valves, the retrograde of blood into the heart results in morbidity. In a previous study [146], the effect of a pump failure on the haemodynamic condition was investigated by a mathematical model of the cardiovascular system. The results showed an increase in aortic flow in order to compensate for the blood retrograde. This increase was managed by an expansion in stroke volume and self-contraction to maintain perfusion and arterial pressure.

Table 1.2 presents the specifications of the commercially available heart assist devices.

Table 1.2: Commercially available MCS devices with specifications [105].

Device	ΔP	Q	D	ω	P	Dimensions	Weight	Bearing	Configuration
Debakay	100-120	5-10	12	7.5-12	10	86x25	95	Mechanical	Pa(LV-AAo/DAo)
HeartAssist5(H)	100-120	1-10	12	8.5-10.6	10	71x30	92	Mechanical	Pa(LV-DAo)
Jarvik(A,H)	100	2-7	11	8-12	12	55x25	85	Mechanical	Pa(LV-DAo)
Thoratec(A,H)	100	6.5	-	8-12	3-7	55x25	85	Mechanical	Pa(LV-AAo)
IncorLVAD(A,H)	100	6	13	30	5	123x30	200	Magnetic	Pa(LV-AAo/DAo)
MicroVAD(H)	80	4	7	12.5	-	50x12	-	Mechanical	Pa(LV-DAo)
MagneVAD(A,H)	100	6	14	6-15	5	60x30	89	Magnetic	Pa(LV-DAo)
HeartMateII(A,H)	80-100	10	11	30	10-12	81x43	281	Mechanical	Pa(LV-AAo)
Impella2.5(A,P,T)	-	4.5	-	10-15	10	65x4.5	-	Mechanical	Pa(AAo)
Reitan(A,P,T)	14-34	5	15	2-2.5	1.11	21x25	-	Mechanical	Pa(DAo)
GyroCIE3(C)	110-150	5-8	68	2.6	-	53x65	305	Mechanical	Pa(LV-DAo)
EvaHeart(C)	100	5-9	40	1.8-3	9-10	55x64	370	Mechanical	Pa(LV-DAo)
VentrAssist(C)	100	5	16-40	1.2-2.6	7-8	60	298	Hydrodynamic	Pa(AAo)
DuraHeart(C)	150	2-10	50	2-5.5	8-13	72x45	540	Magnetic	Pa(DAo)
HeartMateIII(C)	135	7	44	2.5-3.5	10	30x69	535	Magnetic	Pa(AAo)
MiTi(C)	100	2-7	34.5	-	6.5	80x50	300	Magnetic	Pa(DAo)
HeartMateXVE(C)	20	1-10	-	-	5-15	-	1255	-	-
Excure Pediatric	-	0-6	60-120	-	-	-	-	-	-
MiTi Heart LVAD(C)	20-160	1-11	50	2-5	-	50x85	640	-	-
HVAD(Pu)	20	3-8	-	1.8-4	2.5-8.5	-	145	Magnetic/Hydrodynamic	-
MVAD(A)	-	1-10	-	16-28	-	-	75	-	-

ΔP : Pressure rise (mmHg); Q: Flow rate (L/min); D: Diameter (mm); ω : Rotational speed (x1000 rpm); P: Power (W); Weight: (g); A: Axial; C: Centrifugal; Pu: Pulsatile; H: Helical; P: Percutaneous; T: Temporary; LV: Left Ventricle; RV: Right Ventricle; AAo: Ascending Aorta; DAo: Descending Aorta

1.7 Impeller Support and Rotation

The simplest way to support and rotate an impeller is via a shaft, bearing and seal system [7, 6]. One major problem with this method is the seals being subjected to failure and creating a zone of heat generation and blood clotting. Therefore there was need for a new system to drive the impeller. In the past decades, a number of researchers have proposed new methods of impeller support such as a purged ball bearing system [114], a bearing/seal system [80] and a mono-pivot bearing [155]. However, to date, magnetically and hydrodynamically levitated impellers have shown the best outcome in impeller support and rotation [81]. In blood immersed bearing system, the bearing is surface lubricated with blood and the ball bearings have rubbing contact. In hydrodynamic systems, a thin layer of fluid film is placed between the impeller and housing and provides support with no rubbing contact. In this system, the bearing clearance is the most important aspect as it may cause high shear stress and therefore damage to the blood cells [147, 132, 133, 148, 79, 7, 6]. In magnetic bearing systems, a magnetic field in the casing supports the levitating impeller which has small magnets embedded [79].

1.8 VAD Complications and Considerations

The design of implantable devices, such as VADs, is associated with many considerations due to the effect of the device on the body and vice versa. There will be some physiological variations in the blood circulation leading to further blood complications such as haemolysis, thrombosis and infection [85]. The device should be efficient with low power consumption ($<10W$) in order to have smaller batteries and generate low heat for device to tissue interface ($<42^{\circ}C$) [90]. The device should to be designed to generate a straight flow path with minimal deviations in order to avoid haemolysis and thrombosis. Some of the most important complications and considerations of VADs are discussed in this section.

1.8.1 Thrombosis and Embolism

Thrombosis is the human body's mechanism to prevent blood loss when the skin is broken. The blood will form a clot or thrombus in areas of stagnation on rough surfaces. This phenomenon can be fatal if the formed clot becomes dislodged and transported to a smaller vessel, blocking the blood supply, called an embolus. Thrombosis depends on the properties of the contact surface [94]. The gap between the rotor and housing, underneath the impeller, is a potential area for irregular flow pattern

due to the retrograde of the blood [83, 89]. Thrombus can also occur due to genetic, haemodynamic and dietary factors and subsequent inflammatory conditions in the vessels [42].

The endothelial cells of the arteries conceal certain chemical substances that prevent the formation of clots on their inner walls. Artificial materials used in VADs or other MCS devices lack this ability and thrombosis may happen when these devices expose to blood. Biocompatible materials or use of anticoagulants (e.g. Heparin) may decrease the chance of thrombosis [65, 121, 122, 123]. The formation of a clot in the VAD may disrupt the VAD's function. The clot can also circulate as a free clot and block smaller veins and vessels in vital organs [18].

Thrombosis is more likely to occur in turbulent flow. Pulsatile VADs are more likely to form clots due to their inherent dynamic motion and subsequent turbulent flow. This thrombus may gradually develop and affect the inlet and outlet valves [8]. The formation of a turbulent flow in rotary VADs (centrifugal and axial) depends on the geometry of the impeller and casing and the operating conditions. Figure 1.13 shows a thrombus formation on an axial VAD impeller.



Figure 1.13: Thrombus formed on an axial impeller, figure courtesy of Thomas Jefferson University Hospital.

1.8.2 Bleeding

Bleeding complications are normally due to long and invasive implantation surgeries in older patients. In some cases the use of anticoagulants during the surgery may cause post-operative bleeding. Anticoagulants are used to avoid thrombosis and therefore prevent blood clotting, but this leads to more bleeding. The short term solution to bleeding is choosing the right type of coagulation protocol that results in

minimal bleeding. The long term solution is to develop new implantation techniques that are less invasive and reduce the surgery time [26].

1.8.3 Infection

There are two major reasons for infection after VAD implantation surgery; VAD pocket infection and VAD drive-line infection. In general, implanting a large device into the body involves an extremely invasive tissue dissection surgery and subsequent infections. Smaller VADs and new implantation techniques with less invasive surgeries have been areas of interest for researchers in the past decades to overcome this problem. The VAD drive-line infection is due to the skin perforation which can be avoided by Transcutaneous Energy Transmission, which eliminates the need for a drive-line [26].

1.8.4 Mechanical Failure

The probability of mechanical failure is another risk factor that needs to be considered in the design and development process. The operational lifetime of the device depends on the components and their durability. The moving elements are subjected to stress, strain and fatigue. Motor and bearing failures are the most common technical complications of a VAD. Pulsatile devices with diaphragms are larger in size and have high mechanical wear and tear in their valves which leads to a short operational lifetime (<3 years) in adult patients (>40 kg) [110, 23]. Another source of mechanical failure is inlet graft blockage that can occur in dehydrated patients after the surgery. This is due to the absence of blood inside the left ventricle during the surgery and therefore, myocardial tissue is accumulated [48].

1.8.5 Hæmolysis

Hæmolysis is the breakdown or destruction of red blood cells (RBC) and consequent release of contained oxygen-carrying pigment hemoglobin into the bloodstream. Hæmolysis results from shear rates higher than 42,000/s [70]. Such shear rates are unphysiological but commonly occur in MCS devices. The release of hemoglobin into the bloodstream may activate platelets and lead to blood clots and continuous damage to the red blood cells will affect the blood's ability to transport oxygen. The intensity of the damage depends on the magnitude of the shear stress and cell residence time [95, 44]. A large and growing body of literature has investigated the evaluation of hæmolysis and its correlation with shear force and exposure time, as well as a threshold value for maximum allowable shear stress.

The available centrifugal blood pumps normally have a shear stress of 20-100 Pa with 1 s exposure time. This value is higher for axial pumps (≈ 400 Pa) with lower exposure time (≈ 100 ms) due to higher rotational speeds [101]. In 1969, a value of 150 Pa for shear stress was established as the start of hæmolysis [86]. The majority of RBCs were ruptured at the shear stress values >300 Pa and no significant damage was noticed at values lower than 100 Pa. In another study [95] the threshold value of 425 Pa and 0.62 s exposure time was concluded for a Couette shearing device within the range 30-450 Pa and 0.025-1.25 s exposure time.

There are two major models for hæmolysis evaluation. Strain based models and power law models [135, 160, 54]. In the strain based model, the deformation of red blood cells and the corresponding strain of the cell membrane are modeled and the released hemoglobin is calculated [135, 39]. The power law model is based on empirical observations. A power law equation is a functional relationship between some quantities, where a relative change in one results in a proportional relative change in others, independent of the initial size of the quantities. Under a constant uniform shear stress, the increase in plasma free hemoglobin is a power law function of two other quantities, shear stress and exposure time.

The power law model is the most popular of the two approaches due to its easy implementation [135, 39]. The first power law model for hæmolysis evaluation was introduced by Giersiepen in 1990. He conducted in-vitro investigations on a Couette device with shear stress <255 Pa and exposure time <0.7 s and proposed a power law equation in the form:

$$HI(\%) = \frac{\Delta freeHb}{Hb} \times 100 = Ct_{exp}^{\alpha} \tau^{\beta} \quad (1.1)$$

Where:

HI	Hæmolysis index
Hb	The total hemoglobin concentration
$\Delta freeHb$	The increase in plasma free hemoglobin
τ	The shear stress
t_{exp}	The exposure time.

The terms α , β and C are constants based on experimental data. Many researchers [44, 160, 54] have conducted experiments using the power law equation and determined the constants based on their results. Most of the published studies related to numerical estimation of hæmolysis are based on the power law and the constants proposed by Giersiepen [44].

A previous study [152] investigated the different conditions and phenomenons, which lead to hæmolysis, thrombus formation and platelet activation and found the following risk factors: cavitation, high and very low shear stress zones, flow separation, surfaces with irregularities like sharp edges or high roughness, narrow passages or gaps, recirculation zones and blood pooling due to flow stagnation.

1.8.6 Heat Generation

Temperatures higher than 44°C lead to the denaturation of proteins in the blood [139]. This excessive heat may be generated due to the electrical power supply or due to friction between the moving elements of the device. An in-vitro heat generation study [134] on a polycarbonate and an aluminum motor housing showed an effective path for heat distribution from the motor unit to the blood circulation in the aluminum unit. Using aluminum showed a maximum heat flux of 620 W/m^2 . In another study [157], a purged fluid system was used to keep the temperature below 40 °C. The device operated at 2500 rpm, delivering 7 L/min and producing a pressure rise of 100 mmHg. The power consumption was reported at 9W.

1.8.7 Size

The size of the VAD is another important consideration in the design process. The first generation of devices were relatively larger and mainly for male adults. The subsequent generations are smaller rotary pumps and therefore, more suitable for patients of all size and age. A designer should consider the size of the device so that the VAD fits in the available space in the patients' abdomen or minimizes the required portal that must be created by the surgeon. The device should also suit smaller patients such as children.

1.8.8 Physiological Conditions

The physiological control of a VAD is extremely important due to the patients change of physical activity. Different levels of physical exertion require different flow rates, and so different work by the heart or VAD. Previous studies have proposed different control systems to adjust pump activity to return the perfusion, mean arterial and end diastolic pressures back to the normal range during physical activity. A control algorithm proposed by one research group [153] uses motor signals as feedback to control the pressure rise across the VAD. The algorithm set a safe zone of end diastolic pressure to prevent pulmonary congestion and suction in the ventricles ($-3 < P < 15 \text{ mmHg}$).

A sudden change in the outlet flow of a pump causes negative inlet flow pressure and subsequent suction in the atrial or ventricular walls, especially in the left ventricle. Another study [91] attempted to control the outlet flow of two centrifugal pumps performing as a TAH. One simple way to control the change in the outlet flow is to reduce the rotational speed of the pump for lower flow rate, however, this method only applies to LVADs and not TAHs. In LVADs, the native ventricles can assist a limited flow, whereas in TAHs, the body is exclusively relying on the device for flow

and pressure rise and reducing the rotational speed leads to a very low perfusion. The study proposed an alternative solution to this problem by controlling the outlet flow of the right pump in order to maintain a satisfactory volume flow. In this mechanism, any reduction in the outlet flow is compensated by a rise in the right pump outlet flow. The problem with this method is the delay between the right pump and the left atrium which results in undesirable right pump outlet flow leading to the right atrial suction. Pulmonary circuit dynamics may be used to overcome this problem.

1.9 Similarity Concept

Fluid dynamic similarity considerations [12] are a convenient tool to aid in the design of turbomachines. They help designers to reach a "preliminary design" for given performance specifications. The principle of this concept is that machines which satisfy four conditions will have equal fluid dynamic characteristics, that is, will have equal efficiencies. The four conditions are:

- (1) The machines are geometrically similar;
- (2) The machines have similar velocity triangles at similar points in the flow path;
- (3) The machines have the same ratio of gravitational to inertia forces acting in the flow path; and
- (4) The machines operate with fluids that have the same thermodynamic quality in their properties,

The formal derivation of this concept is based on considering that any physical quantity Q_1 is interrelated to other physical quantities related to significant variables of the turbomachine, Q_2 to Q_n by

$$Q_1 = f_1(Q_2, Q_3, Q_4, \dots, Q_n) \quad (1.2)$$

For example, Q_1 can be the efficiency of a turbomachine. Since this equation must be dimensionally homogeneous each Q_i term must be of the same dimension, or the Q_i terms must be transformed into dimensionless form using the primary dimensions: length [L] in meters; time [T] in seconds; and either mass [M] in kilograms or force [F] in Newtons. Since there are three primary dimensions the n quantities Q_i must be transformed into $n - 3$ dimensionless π_i quantities (non-dimensional parameter groupings, or similarity parameters).

$$\pi_1 = f_2(\pi_2, \pi_3, \pi_4, \dots, \pi_{n-3}) \quad (1.3)$$

This is known as the Buckingham π theorem [21, 22], where each π and the resulting product must become dimensionless when each Q term is expressed in the primary

dimensions. This argument can be used to determine the number of π terms, or parameter groupings needed to determine a physical process. Nine independent variables can be defined for turbomachines so six independent dimensionless similarity parameters can be formulated. These are: efficiency; Reynolds number; Mach number; ratio of specific heats; specific speed and specific diameter. Tables 1.3 and 1.4 show these variables and dimensionless parameters.

Table 1.3: Basic Dimensions [12].

Symbol	Dimension	Parameter
N	T^{-1}	Speed
D	L	Diameter
Q	L^3T^{-1}	Volume Flow
ρ	ML^{-3}	Density
H	L^2T^{-2}	Head
μ	$ML^{-1}T^{-1}$	Viscosity
P	ML^2T^{-3}	Power
e	$ML^{-1}T^{-2}$	Compressibility
k	-	Ratio of Specific Heats

Table 1.4: Nondimensional parameters for pumps.

Symbol	Parameter	Equation
n_s	Specific Speed	$N_s \cdot \sqrt{Q} / (\frac{\Delta p}{\rho})^{0.75}$
d_s	Specific Diameter	$D \cdot (\frac{\Delta p}{\rho})^{0.25} / \sqrt{Q}$
Re	Reynolds Number	$\rho C D / \mu$
M	Mach Number	$C / \sqrt{k R T_{st}}$
k	Ratio of Specific Heats	C_p / C_v
η	Efficiency	ideal power / actual power

The adiabatic head of the pump is given by Equation 1.4.

$$H_{ad} \equiv \frac{\Delta p}{\rho g} \quad (1.4)$$

where Δp is the pressure difference between inlet and outlet of the pump.

Different types of efficiency can be defined for pumps and compressors: isentropic, polytropic, isothermal (depending on the ideal process), stagnation-to-stagnation, stagnation-to-static and fluid or shaft, based on whether the bearing and disk friction losses are accounted for in the definition.

For the purposes of this work, the author will use isentropic stagnation to stagnation efficiency definitions, and will only consider the energy rate delivered to the fluid.

The Reynolds number, Re , is a characteristic dimensionless number which compares the inertia forces to the viscous forces in the fluid, defined by:

$$Re \equiv \frac{\rho CD}{\mu} = \frac{CD}{\nu} \quad (1.5)$$

where μ and ν are dynamic ($Pa.s$) and kinematic viscosity (m^2/s) of the fluid respectively, C is the velocity of the fluid (m/s), ρ is the density of the working fluid (kg/m^3) and D is the hydraulic diameter (m).

Specific diameter and specific speed are characteristic dimensionless numbers indicative of the rotor diameter and rotational speed respectively.

The specific diameter is given by Equation 1.6.

$$d_s = \frac{D \cdot (\frac{\Delta p}{\rho})^{0.25}}{\sqrt{Q}} = \frac{\psi^{0.25}}{\phi^{0.5}} \quad (1.6)$$

The specific speed is given by Equation 1.7

$$n_s = \frac{N_s \cdot \sqrt{Q}}{(\frac{\Delta p}{\rho})^{0.75}} = \frac{\phi^{0.5}}{\psi^{0.75}} \quad (1.7)$$

Where N_s is the rotor speed (rad/s), Q is the volumetric flow rate (m^3/s), Δp is the pressure difference (N/m^2) from inlet to outlet of the pump and ϕ and ψ are the flow and head (pressure) coefficients. The specific speed and specific diameter terms can be interrelated with other commonly used characteristic values, such as the head and flow coefficients. The head coefficient ψ is a characteristic coefficient indicative of the operating behaviour and it characterises the head of the pump and is given by Equation 1.8.

$$\psi = \frac{\Delta P}{\rho N_s^2 r^2} \quad (1.8)$$

And the flow coefficient characterises the flow rate of the pump and is given by Equation 1.9

$$\phi = \frac{Q}{\rho N_s r^3} \quad (1.9)$$

Since pumps of similar design geometry having the same specific speed and specific diameter values are similar in flow mechanism, it follows that they have equal efficiencies, as long as Re and Mach number effects are neglected.

Although all six groupings are truly dimensionless, they are frequently quoted, for convenience in different dimensional forms as described in Table 1.5.

1.9.1 Derivation of Specific Speed and Specific Diameter

The equations for specific speed and specific diameter can be derived by investigating the relationship between the pump outlet flow, the adiabatic head, and the rotor

Table 1.5: Conversion data for n_s and d_s [12].

	ft^3/s	m^3/s	gpm
Dimensions	ft	m	ft
	rpm	rpm	rpm
n_s	N_s	N_s	N_s
1	128.8	52.9	2730
d_s	D_s	D_s	D_s
1	0.42	0.565	0.0198

diameter.

The flow rate passing through the pump, Q , is proportional to the characteristic velocity, c , and the throughflow area, A . The area is proportional to the square of the rotor diameter, D^2 , and the characteristic velocity is proportional to the rotor tip speed, U_2 , which itself is proportional to the product of the diameter and rotational speed, ND .

$$Q \propto cA \propto CD^2 \propto U_2 D^2 \propto ND^3 \quad (1.10)$$

The adiabatic head, H_{ad} is proportional to the square of the tip speed or the characteristic velocity, c^2 or U_2^2 and therefore proportional to the product of the square of the rotational speed and the diameter, $N^2 D^2$.

$$H \propto c^2 \propto U_2^2 \propto N^2 D^2 \quad (1.11)$$

Comparing the flow rate and head of the pump to that of a standard pump (subscript stn), the following equations are derived:

$$\frac{Q}{Q_{stn}} = \frac{ND^3}{N_{stn}D_{stn}^3} \quad (1.12)$$

$$\frac{H}{H_{stn}} = \frac{N^2 D^2}{N_{stn}^2 D_{stn}^2} \quad (1.13)$$

Solving equations 1.12 and 1.13 for the rotor diameter, D , and assuming that the head and flow rate of the standard pump are unity ($Q_{stn} = H_{stn} = 1$) yields:

$$D = \frac{Q^{\frac{1}{3}} N_s^{\frac{1}{3}} D_s}{N^{\frac{1}{3}}} \quad (1.14)$$

$$N_s = \frac{NQ^{0.5}}{H^{0.75}}$$

Solving the two equations for the rotational speed, N , assuming that the head and flow rate of the standard pump are unity.

$$N = \frac{QN_s D_s^3}{D^3} = \frac{H^{0.5} D_s N_s}{D} \quad (1.15)$$

$$D_s = \frac{DH^{0.25}}{Q^{0.5}}$$

1.10 $n_s - d_s$ diagrams

It is a widely held view that the performance of a pump depends to a large extent on the compromises that the designer makes between producibility, cost, ruggedness, etc., and on the state of the art. Typical commercial pumps are likely to be designed in order to have long life, low manufacturing and maintenance costs and therefore perform with lower efficiencies and usually can be designed with relatively short development times.

Cordier [28] collected experimental data of different turbomachines and intended to correlate the data using nondimensional characteristics of the machines, specific speed and specific diameter. The Cordier diagram is an empirical diagram based on experimental measurements. The measured data are plotted as data points on a graph with specific speed as x -axis and specific diameter as y -axis. By relating the efficiency of the machines to their specific characteristics, Cordier was able to show that the data points could be fitted into curves based on their efficiency range. The graph was introduced as a practical guideline for the preliminary selection of turbomachines.

Although these diagrams were first demonstrated experimentally by Cordier and therefore were named after him, later in the 1980's, Balje [12] further developed the graph by collecting extensive experimental data from turbomachine designers and manufacturers. He published various $n_s - d_s$ graphs for different types of turbomachines including single stage turbines, pumps, expanders and compressors. For the convenience of the application, he made a distinction between the working fluids (gas or liquid) as well as the subcategory of each type of turbomachine. Figure 1.14 shows the Balje $n_s - d_s$ graph for pumps. Different regions of the graph show the nondimensional data of different pump types including axial, centrifugal, mixed-flow, partial emission and drag pumps.

In this diagram, Balje has assumed a higher peripheral Reynolds number ($Re = 10^8$) than for compressors. Comparing the $n_s - d_s$ graph for pumps and compressors also shows a higher efficiency potential for pumps.

1.10.1 Why are conventional pump design methods not suitable for MCS devices?

The application of centrifugal and axial pumps as VADs imposes limitations on the design process of the impellers. A considerable amount of literature has been published on pump characteristics for MCS devices. A common pump design method is to rely on the performance of other previously designed pumps (industrial pumps) of known performance using the concepts of fluid dynamic similarity (affinity law) [66]. However, one major theoretical issue that has dominated the field for many years

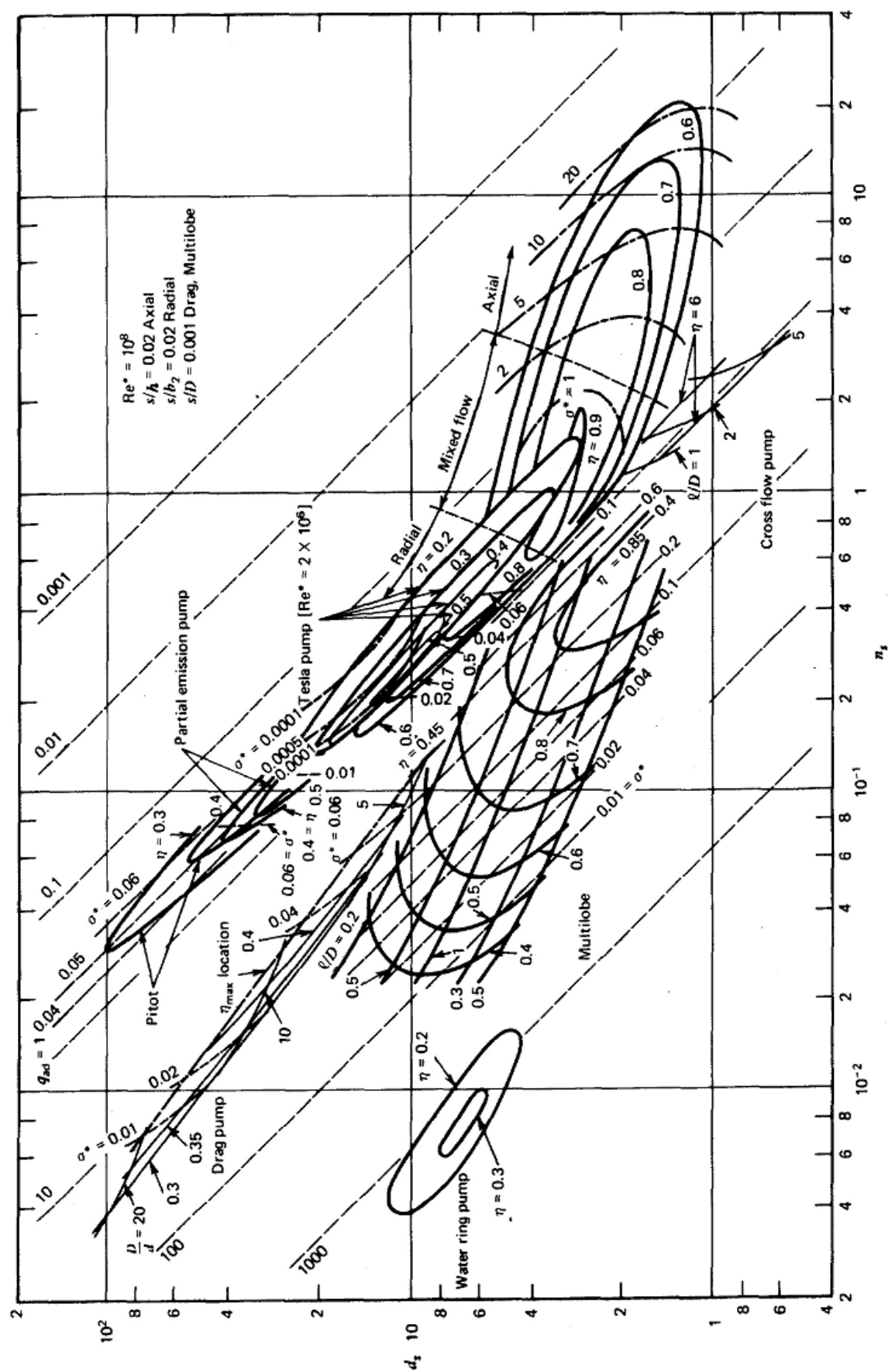


Figure 1.14: $n_s - d_s$ diagram for pumps [12].

concerns the third condition of the similitude:

Two machines have equal fluid dynamic characteristics if they have the same ratio of gravitational to inertia forces acting in the flow path (Reynolds number, Re).

Industrial pumps operate in Reynolds number region of $Re = 10^8$, whereas centrifugal and axial pumps in heart assist devices operate in $Re = 10^5 - 10^6$. The difference between the flow fields of industrial and medical pumps means that the similarity laws do not apply between Balje's diagrams and MCS devices. There has been insufficient quantitative analysis of centrifugal and axial pumps in this characteristic range to create a Cordier diagram for these devices.

Smith [119] collected nondimensional data of 37 rotary dynamic blood pumps containing axial, mixed flow, and radial pumps with different number of blades, splitters, and shroud configurations and different types of discharge. The nondimensional data points are plotted on a Cordier diagram. From these data, a pump designer can make a first estimate at the size, speed, and performance of a blood pump. The study is a pioneering work, based on reliable experimental data, but has insufficient data for a broad range of pump types.

1.11 Thesis and Substantiation

The goal of this body of work is to combine theories, numerical simulations and experimental results with a nondimensional approach for extensive number of pumps, to enable preliminary design of centrifugal and axial pumps for MCS devices. As laid out in the preceding sections, blood pump design theory has been explored mainly in a conventional manner and many sources of rich nondimensional data have been untapped to such ends. Therefore, the thesis of this dissertation is that *a nondimensional and parametric approach can advance our understanding of the parametric effect on the performance and hemocompatibility of small sized pumps for MCS devices.*

The substantiation of this thesis will be incremental - starting with the exploration of conventional pump design methods. This will be followed by an expansion to similarity considerations and its limitations with the goal of understanding the effect of Reynolds number in the design and performance of small sized and industrial pumps. As a demonstration of the numerical simulations, we will also discuss a numerical comparison model where novel insights will be shown in the interconnection between geometric parameters and the hemocompatibility of a device. Ultimately, this dissertation will present multiple threads of experimental analysis evaluating the benefit of nondimensional modelling and analysis in comparison with current research and traditional pump design models.

1.12 Statement of Novelty

This dissertation makes several novel contributions. The novelty of this work originates from research into the effects of different design parameters on the performance and hemocompatibility of small pumps for use in MCS (Mechanical Circulatory Support) devices and particularly VADs (Ventricular Assist Devices). Although a growing body of literature has investigated the performance of small sized pumps for this application, in-silico and in-vitro investigations on a large number of axial and centrifugal pumps are conducted herein with a nondimensional approach, and the effect of different design parameters on the performance and hemocompatibility of the device is studied for the first time in this thesis.

The specific novelty claims in this study are as follows:

- In-silico and in-vitro investigations were conducted on pumps with similar characteristics to thoroughly investigate the effect of each design parameter (blade outlet angle, number of vanes, diameter, outlet width and rotational speed) on the performance and hemocompatibility of an MCS device.
- In-vitro investigations were conducted for over 150 impellers (centrifugal and axial) and the head-flow characteristics, specific speed, specific diameter, efficiency, head and flow coefficients data were measured, calculated and collected in relevant diagrams.
- A nondimensional $n_s - d_s$ diagram for 88 small sized centrifugal impellers, performing in low Reynolds number region of 10^5 , was produced for the first time in this thesis.
- A nondimensional $n_s - d_s$ diagram for 62 small sized axial impellers, performing in low Reynolds number region of 10^6 , was produced for the first time in this thesis.
- The diagrams were combined in one $n_s - d_s$ graph, similar to that of Balje for industrial pumps, to enable preliminary nondimensional design of blood pump sized impellers suitable for VADs and MCS devices.

1.13 Chapter Outline

In this dissertation, a review of literature relating to heart failure and the available treatments is provided to outline the necessity of the current research and identify areas for further investigations. A history of different categories of MCS devices and their design complications and considerations is presented in chapter 1, while the contributions made in this dissertation are detailed in the following chapters:

- **Chapter 2: Centrifugal and Axial Pumps As MCS Devices:** This chapter starts with defining the terms and parameters used in the design of a centrifugal pump, followed by the parameter selection and justification for this purpose and tables are presented for the design details and specifications of the pumps. The conventional pump design methods are described under the light of literature. The theoretical and experimental methods of force analysis are presented. The terminology of axial pumps is then introduced in a similar fashion to the preceding sections.
- **Chapter 3: Numerical Methods:** In this chapter, the numerical approach is outlined, starting from the CAD design of the impellers, followed by CFD methods and results. The numerical simulations, the assumptions made and their justifications are presented through cases shown in the literature or by comparison. The numerical investigations are presented in a parameter based approach to study the effect of design parameters on the performance, hemocompatibility and the force analysis of the pumps.
- **Chapter 4: Experimental Techniques:** In this chapter, the Impeller selection based on the numerical results is presented and the design and development of a single loop test rig is described. The experimental process and measurement techniques are introduced, followed by the experimental results, discussions and comparisons to the numerical outcomes. The chapter is concluded with the presentation of two $n_s - d_s$ diagrams for small centrifugal and axial pumps suitable for MCS devices.
- **Chapter 5: Axial Flow Vs. Centrifugal Flow VADs:** This chapter is a conclusive comparison between the two types of pumps investigated in this dissertation. The chapter starts with the technological and clinical considerations of axial and centrifugal pumps, followed by a comprehensive comparison between a representative axial and a centrifugal pump, selected from this thesis. The chapter is concluded by the $n_s - d_s$ diagram including both axial and centrifugal pumps data points. The data points are then mapped into the Balje's diagram for industrial pumps to observe the effect of change in Reynolds number on the location of the efficient pumps.

The final chapter in this dissertation, reflects on the findings and applications of this work by outlining a summary of contributions and provides a vision for future research.

1.14 List of Publications

The work carried out during my Ph.D. has been published in several journal publications. These consist of my sole efforts and technical contributions but would not have been possible without the support and guidance provided by my co-authors. I would like to acknowledge the following collaborators who have generously provided me with technical support and help described in this dissertation: [66] would have not been possible without Gordon Paul's expertise in electrical and electronics of rotary blood pumps and Amin Rezaienia for sharing his numerical analysis skills with me and helping me to thoroughly investigate the effect of geometry on the haemolysis in centrifugal blood pumps in [84]. [66, 84] are a consequence of Prof. Theodosios Korakianitis introducing me to the novel concept of nondimensional analysis of rotary blood pumps and his expertise provided on the subject.

[66], [84] and the article under review are the direct outcome of this thesis. The design, optimization, numerical analysis, prototyping, experimental setup design and in-vitro investigations are carried out by the author. The author has also contributed to the design, development and parameter selection of a centrifugal impeller in a rotary blood pump installed in the descending aorta in [102]. These publications are listed next.

- [66] T. Korakianitis, M. A. Rezaienia, G. Paul, A. Rahideh, M. T. Rothman and **S. Mozafari**.
Optimization of Centrifugal Pump Characteristic Dimensions for Mechanical Circulatory Support Devices.
ASAIO Journal, Sep-Oct 2016; 62(5): 545-551
Contributions: Design and optimization, prototyping, experimental setup and
- [84] **S. Mozafari**, M. A. Rezaienia, G. Paul, M. T. Rothman, P. Wen and T. Korakianitis.
The Effect of Geometry on the Efficiency and Hemolysis of Centrifugal Implantable Blood Pumps.
ASAIO Journal, Jan-Feb 2017; 63(1): 53-59
- T. Korakianitis, M. A. Rezaienia, G. Paul, E. Avital, M. T. Rothman and **S. Mozafari**.
Optimization of Axial Pump Characteristic Dimensions and Induced Hemolysis for Mechanical Circulatory Support Devices.
Forthcoming/ Under Review for ASAIO Journal, December 2016.

Other Publications:

- [102] M. A. Rezaenia, G. Paul, Eldad Avital, **S. Mozafari**, M. T. Rothman, T. Korakianitis.

In-vitro investigation of the hemodynamic responses of the cerebral, coronary and renal circulations with a rotary blood pump installed in the descending aorta.

Journal of Medical Engineering & Physics, Feb 2017; 40: 2-10

Chapter 2

Centrifugal and Axial Pumps As MCS Devices

This chapter starts with the terminology of centrifugal pumps followed by the conventional design methods and their limitations for medical applications. The design parameters are defined with reference to the published literature and their selection or calculation process for this study is justified.

The terminology of axial pumps is then introduced. The design parameters are described and their selection or calculation process for this application is discussed. Due to several terms and methods being held in common in centrifugal and axial pumps, these are not discussed to avoid repetition from the preceding sections.

2.1 Centrifugal Pumps Terminology

Four important factors are identified for impeller design in VADs [97]: dimension (pump type and size) and vane profile including the exit angle and the number of blades. Another study [29] finds that the shroud configuration and the outlet width are the most important parameters influencing the performance of the device. The dimension is selected based on the the pump speed, pressure rise and flow rate (specific speed) and leads to the pump type selection, Figure 2.1. Comparing the normalised head and flow rate for similar sized axial and centrifugal pumps shows that an axial impeller has to rotate ≈ 1.5 times faster than centrifugal impeller to produce the same head and flow requirements [154].

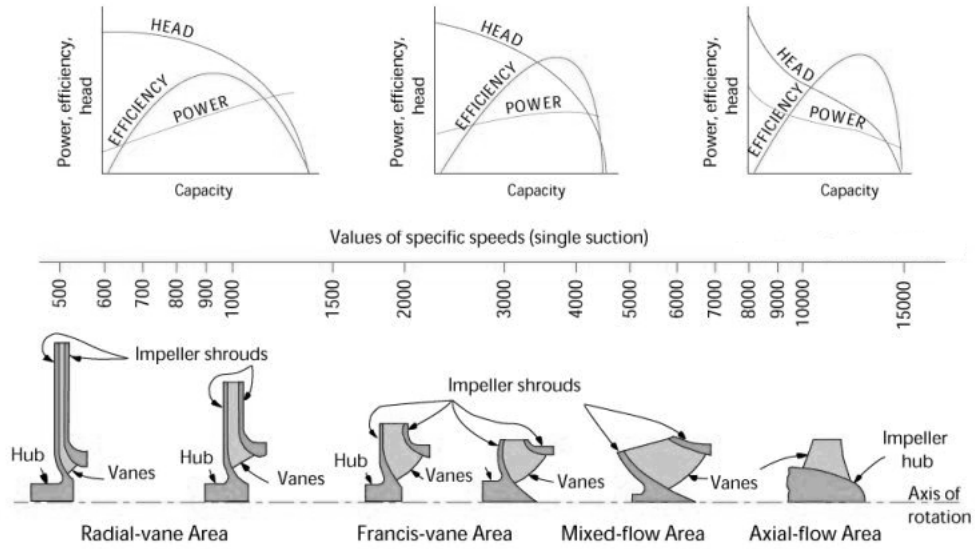


Figure 2.1: Specific speed dictating the pump type, figure courtesy of the Hydraulic Institute Standards book.

As mentioned in the previous chapter, hæmolysis is mostly influenced by the shear stress induced at the impeller tip. Higher tip speed leads to higher shear stress and the subsequent higher levels of hæmolysis. This implies that a centrifugal impeller is a more suitable choice for a rotary blood pump because of its lower required rotational speed. The design parameters, terms and their definitions are discussed in the following section.

This section provides information about the design parameters, constraints and characteristics of centrifugal pumps in this study and their selection.

2.1.1 The Duty Frame

In turbomachinery, the term *Duty Frame* is usually used to address a group of parameters including the volumetric flow rate, pressure rise and rotational speed of a pump. Specifying the three parameters along with the rotor diameter is the first step in a pump design.

2.1.2 Volumetric Flow Rate

The volume of flow that passes through the impeller is usually higher than the value used in the calculation due to some of the flow leaking past the impeller back into the inlet (secondary flow). There are several types of secondary flows in a pump including inlet pre-rotation (swirl), tip clearance flow (gap leakage), flow separation and, in MCS devices, flow in clearances between the impeller and casing which exists to prevent stagnation.

The volumetric flow rate is a design constraint in this study and is defined in the region of human cardiovascular system parameters corresponding to 3-7 L/min with 5 L/min at the design point.

2.1.3 Head Rise (Pressure Rise)

The head rise refers to the sum of the static head rise and velocity head rise. The velocity head is found by the area of the aperture, for a constant volume flow rate. In centrifugal pumps, smaller inlet area results in a larger inlet velocity head and vice versa. The head rise is a design constraint in this study and is defined in the region of human cardiovascular system parameters corresponding to 50-150 mmHg.

2.1.4 Rotational Speed

The rotational speed needs to be specified in the first step in order to draw the velocity diagrams and derive other parameters. Normally in industrial pumps, the rotational speeds at which the pump will operate are known and very few in number. A few modes of low, normal and high are typical. In this study, the rotational speed for each impeller was selected and changed manually until desirable combinations of outlet width (4-8 mm) were achieved, and it was further changed in numerical investigations to achieve a desirable pressure rise (within 50-150 mmHg).

2.1.5 Density

The density of 1050 kg/m^3 was defined, corresponding to that of human blood at 37°C .

2.1.6 Inlet Flow Angle

The inlet flow angle is denoted α and is the angle of the inlet flow at the impeller's leading edge, measured with respect to the tangential direction. When the flow enters the pump from a plane pipe (the assumption for this study), this value is assigned 90° .

2.1.7 Meridional Geometry

Centrifugal impellers rotate around an axis and therefore it is convenient to use a cylindrical coordinate system. If the rotation axis is the z -axis, the impeller's r - z projection is called the meridional geometry of the impeller and is the most convenient geometry to use while designing the blade profile. Figure 2.2 shows the 3D surface and the meridional profile projection.

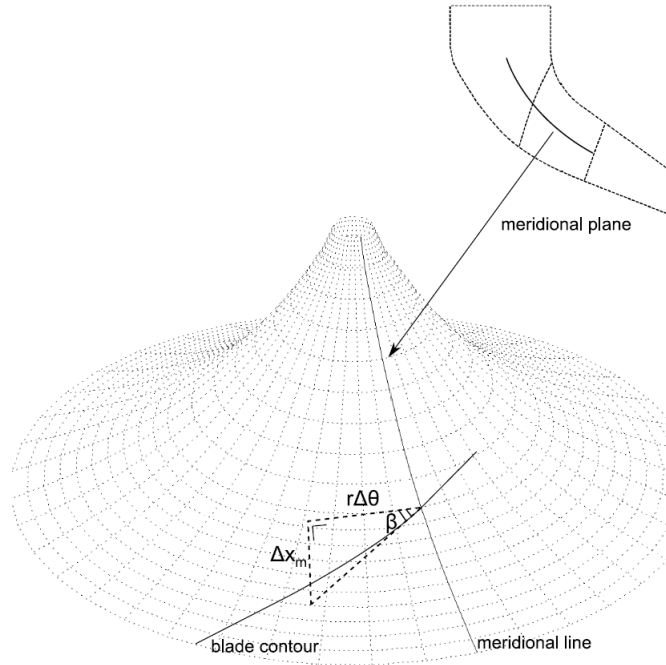


Figure 2.2: The meridional profile [149].

2.1.8 Meridional Velocity Ratio

This value is used to describe the linear velocity profile from the hub to the shroud at the leading edge. A value lower than 1 shows a smaller meridional velocity at the shroud than the hub, a value greater than 1 shows a larger meridional velocity at the shroud and the ratio of 1 shows a uniform velocity distribution at the two ends. Figure 2.3 shows the meridional velocity profile with a ratio greater than 1.

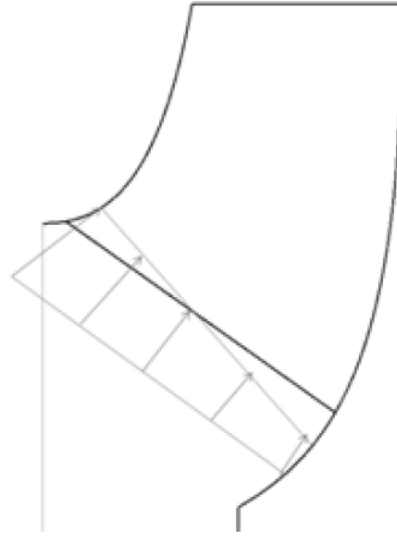


Figure 2.3: The meridional velocity profile, figure courtesy of ANSYS.

2.1.9 Efficiencies

The useful power delivered by a pump is always lower than the power applied to it due to losses. The theoretical study of a pump efficiency and loss has up to 30% uncertainty [46]. The total loss in a pump consists of three main components; hydraulic, mechanical and volumetric losses. Hydraulic losses have the largest influence on the total efficiency of a pump [128]. The volumetric losses indirectly affect the head rise and therefore the total efficiency by reducing the delivered volumetric flow rate. The mechanical losses do not affect the delivered head but contribute to the total loss by increasing the input power needed at the shaft. Different efficiencies based on three losses are explained here:

Mechanical Efficiency

The mechanical and viscous friction on the surface of the impeller (disk friction) results in drag on the impeller and the loss generated by this drag is called mechanical loss. The ratio between the shaft input power and the power lost due to disk friction

indicates this loss and therefore the mechanical efficiency of the pump is defined by

$$\eta_M = \frac{P_{in} - P_{disk}}{P_{in}} \quad (2.1)$$

where P_{in} is the shaft input power and P_{disk} is the power loss due to disk friction and other mechanical losses.

Volumetric Efficiency

The volumetric losses, also referred to as leakage losses, are due to the leakage of flow from the outlet region past the impeller back into the inlet. This normally occurs between the shroud and the inner wall of the volute. The designers can increase the target volumetric flow rate of the pump by the volume of leakage volume in order to deliver the desirable volume of flow at the outlet. The ratio between the delivered flow and the leakage flow indicates the volumetric loss and therefore the volumetric efficiency of the pump is defined by

$$\eta_V = \frac{Q}{Q + Q_{leak}} \quad (2.2)$$

where Q is the volume of the delivered flow and Q_{leak} is the leakage flow.

One of the methods to reduce the leakage flow and improve the volumetric efficiency is to decrease the gap between the impeller and the volute. However, pumps with smaller gap generally suffer more from disk friction and therefore have lower mechanical efficiency. There is often a trade-off between the two efficiencies and the designer needs to find an optimum value for this gap.

Hydraulic Efficiency

The hydraulic efficiency is associated with the reduction in head due to the pressure loss caused by the pump's hydrodynamic design. The hydraulic efficiency is the most significant parameter that can be influenced by the pump designer. The hydraulic losses are mostly caused by friction losses and vortex dissipation in the pump and are higher where there are curves or other geometric irregularities. Hydraulic losses are extremely hard to calculate theoretically and analytically, and therefore experimental and historical data are used to estimate the maximum achievable efficiency of the pumps.

As mentioned earlier, the main objective of this work is to study the different impeller characteristics and their effect on the efficiency of the impeller. The term efficiency, in this study, refers to the hydraulic efficiency and is given by

$$\eta = \frac{PumpHydraulicPowerOutput}{PumpInputShaftPower} = \frac{H.Q}{P_{in}} \quad (2.3)$$

2.1.10 Shaft Diameter

The minimum shaft diameter is calculated based on the maximum allowable shear stress of the shaft based on its material and application. The maximum allowable shear stress of a shaft is given by

$$\tau_{max} = \frac{T.c}{J} \quad (2.4)$$

where T is the maximum torque, c is the radius of the shaft and J is the polar moment of inertia of the material.

2.1.11 D_{hub}/D_{shaft}

This is a ratio of impeller hub diameter to the shaft diameter. It is recommended to select a maximum value of 1.5 for this ratio [137]. Figure 2.4 shows the hub and shaft diameters in a meridional profile view.

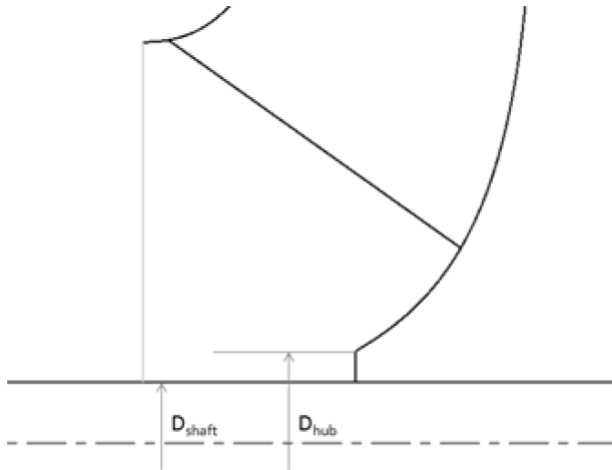


Figure 2.4: The hub and shaft diameter, figure courtesy of ANSYS.

2.1.12 Leading Edge Blade Angle

This parameter is the angle between the blade and the tangential direction at the leading edge and is calculated using different methods.

Hub and Meanline

There are two common methods to calculate the leading edge blade angles at the hub and meanline locations:

Method 1 - Cotangent:

$$\beta_1'^{hub} = \tan^{-1}\left(\frac{D_1^{shroud}}{D_1^{hub}} \tan(\beta_1'^{shroud})\right) \quad (2.5)$$

and similarly

$$\beta_1'^{mean} = \tan^{-1}\left(\frac{D_1^{shroud}}{D_1^{mean}} \tan(\beta_1'^{shroud})\right) \quad (2.6)$$

Method 2 - Cosine:

$$\beta_1'^{hub} = \cos^{-1}\left(\frac{D_1^{hub}}{D_1^{shroud}} \cos(\beta_1'^{shroud})\right) \quad (2.7)$$

and similarly

$$\beta_1'^{mean} = \cos^{-1}\left(\frac{D_1^{mean}}{D_1^{shroud}} \cos(\beta_1'^{shroud})\right) \quad (2.8)$$

Shroud

The leading edge blade angle at the shroud is calculated linearly based on the hub and meanline values. The Cotangent method has been used in this study to calculate the values of hub and meanline angles.

2.1.13 Tip Diameter

The tip diameter and the tip speed (a function of rotational speed) have the largest influence on the other dimensions of the pump and therefore are two of the most important parameters to be selected by the designer. There are two methods to specify the diameter of the impeller.

Method 1 - by the stability factor:

A stable head-flow curve means a continuous rise in pressure while the flow rate falls to zero. In this case, the impeller diffusion which in general is given by:

$$\frac{W_1 - W_2}{W_1} \quad (2.9)$$

equals zero, meaning $W_1 = W_2$, where W_1 and W_2 are the meanline relative velocities at the inlet and outlet of the pump. In this condition, the tip diameter can be assigned a value to fulfill:

$$U_{2m} - U_{1m} = C_{u2m} \quad (2.10)$$

Where U_{1m} and U_{2m} are the meanline blade speeds at the leading edge and trailing edge and C_{u2m} is the meanline tangential flow velocity at the trailing edge. The stability factor will then be defined as:

$$\frac{U_{2m} - U_{1m}}{C_{u2m}} \quad (2.11)$$

An ideal yet realistic value for the stability factor is at least 0.9 [137].

Method 2 - by the head coefficient:

This method relies on experimental data from existing pumps. The head coefficient is a nondimensional parameter defined earlier in this chapter and is given by

$$\psi = \frac{g.H}{U_2^2} \quad (2.12)$$

By using a known head coefficient of an existing design, U_2 can be calculated, and by the rotational speed already established, the tip diameter can be specified.

In this study, the tip diameter has been selected based on the proposed dimensions of the device. The tip diameter is chosen in the range 30-31.5 *mm* with 0.5 *mm* increments.

2.1.14 Trailing Edge Blade Angle And Outlet Width

The trailing edge blade angle, β'_2 , is another important parameter in pump design and represents the angle that the blade makes with respect to the tangential direction at the trailing edge of the blade. The angle is shown in figure 2.5.

Traditionally, it has been argued that an optimum blade angle exists for each centrifugal pump application. In simpler geometries, the inlet and outlet blade angles are designed to be equal, however, it is desirable to vary both angles as a function of radius. Computational fluid dynamics (CFD) is a convenient tool to study the effect of blade angle on pump performance.

It has been suggested [97] that the blade profile for medical applications should be a logarithmic spiral with 30° discharge angle. This was claimed based on the assumption that the fluid will follow streamlines based on mass and energy conservation and no turbulence and therefore a low blood damage will occur. The assumptions were confirmed by experimental results [97].

A previous study [130] compared the head and flow rate of two impellers and concluded that the impeller with the outlet angle of 83° delivered the desired characteristics at a lower rotational speed than the impeller with backward vanes and a 73° outlet angle. However, the efficiency was not studied in the work. A numerical

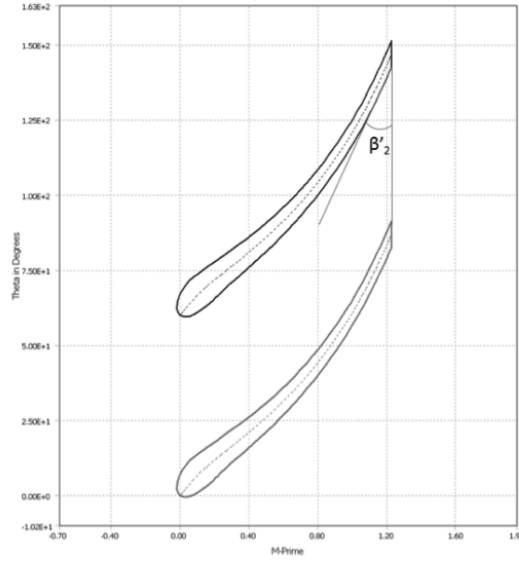


Figure 2.5: The trailing edge blade angle, figure courtesy of ANSYS.

study [29] confirmed a higher head rise in straight blades compared to backward vanes, but at the expense of hydraulic efficiency. The blade outlet angle has a considerable effect on the slope in the head-flow curve of a pump [154].

Based on the impeller blade shape, different blade angle values are categorised into three groups: $\beta_2 < 90$ Backward Blades, $\beta_2 = 90$ Radial Blades and $\beta_2 > 90$ Forward Blades.

The ideal head-flow curve of a centrifugal impeller depends on the outlet angle of the blade. Therefore, there is a linear pressure response with flow rate when friction loss, recirculation and slip between the blades are neglected, Figure 2.6. Backward blades ($\beta_2 < 90$) are suitable for higher efficiencies, with $\beta_2 = 22.5$ reported as the highest efficiency for industrial pumps. Radial blades ($\beta_2 = 90$) perform with lower efficiencies and a flat horizontal H-Q curve, up to 75% of the best efficiency point [61]. Forward blades have not been a subject of interest for researchers for several reasons. The casing for these impellers should catch and transform the high velocity into pressure while allowing an impulse action [128]. A previous study [61] simulated a forward blade impeller by rotating a backward blade impeller in a reverse direction and reported very low efficiency.

Another study [29] used CFD to investigate the effect of blade width, b_2 shown in Figure 2.7, on the performance. Two outlet widths were studied (1 and 3 mm) and the larger outlet width led to a lower meridional velocity and a subsequent increase in pressure rise for a constant rotational speed. The study suggested that the deviation in results from the traditional pump design methods is within an acceptable range due to the negligible effect of this parameter on small centrifugal pumps. The blade

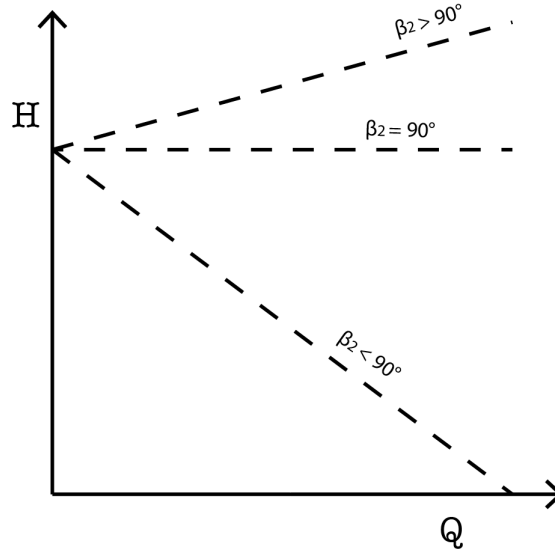


Figure 2.6: Ideal H-Q curve trend for different types of outlet angles.

angle has a direct relationship with the impeller outlet width.



Figure 2.7: The outlet width of the blade, figure courtesy of ANSYS.

The continuity equation determines the delivered flow rate by the meridional velocity, C_m , and the outlet area, A_{out} :

$$Q = C_m \cdot A_{out} \quad (2.13)$$

For a given rotational speed, a higher blade angle results in a higher meridional velocity. In order to keep the volumetric flow rate constant, the outlet area of the impeller has to decrease and the only way to decrease this area is either to increase the number of blades (not recommended) or to reduce the outlet width. Conversely, a lower blade angle at a given rotational speed and tip diameter results in a lower

meridional velocity, larger outlet area and therefore a larger outlet width. The well known 22.5° outlet angle is considered to be the standard value for industrial pumps for performance and manufacturing reasons. Both industrial and blood pump experimental results have shown that increasing this value will boost the produced head rise, but at the cost of a lower hydraulic efficiency. An optimum value for this parameter needs to be specified by the designer based on the design constraints, head requirements and manufacturing limitations. In this work, different values of outlet angle, between 10° - 45° , have been considered and examined in order to study the effect of this parameter on the pressure rise, efficiency, shear stress and haemolysis of the pump.

2.1.15 Rake Angle

The angle between the leading or trailing edge and a line parallel to the rotation axis is called the rake angle or blade lean. For the trailing edge, the value of 0° , also referred to as a straight lean, is recommended for manufacturing reasons, however, a small angle is likely to increase the volumetric efficiency by reducing the secondary flows through the distribution of flow in the spanwise direction (hub to shroud). In this work, the reduction in secondary flow volumes is achieved by studying the effect of the gap between the impeller and the volute and the trailing edge rake angle is chosen to be 0° . At the leading edge, 10° was chosen to create a slope towards the rotation.

2.1.16 Number of Blades

The number of blades in a pump directly influences the slip or blade recirculation. More blades results in lower slip because there is less space between the vanes to allow recirculation. However, due to the smaller size of blood pumps, viscous effects dominate the flow within the passage, while velocities are not large enough to cause flow separation from the vanes [29]. The effect of the number of blades on the pump performance and the magnitude of this effect depends on the viscosity of the working fluid. For lower viscosities, the number of blades has a larger impact on the performance than for higher viscosity fluids. An experiment [72] using laser doppler velocimetry confirmed this claim by showing an increase in disc friction loss and hydraulic loss in higher viscosity fluids. Therefore, higher number of blades may lead to a lower efficiency because of the viscous drag due to larger surface area. The kinematic viscosity of blood at normal body temperature (37°C) is $2.65 \text{ mm}^2/\text{s}$, which is relatively low compared to other fluids pumped by centrifugal impellers. In another study [97] three impellers with 5, 6 and 7 blades were tested and the results showed a lower level of haemolysis in the impeller with 6 blades. However,

the efficiencies of the impellers were not studied.

Increasing the number of blades results in a better control over the flow direction (better flow guidance) in the impeller, so the fluid leaves the impeller closer to the blade exit angle, meaning β_2 gets closer and eventually equal to β'_2 . This increase in β_2 will result in an increase in the meridional velocity at the trailing edge C_{m2} , which acts to reduce the impeller exit area leading to a smaller outlet width b_2 , as mentioned earlier. On the other hand, another effect of higher number of blades is higher solid surface to fluid surface and therefore increasing the blockage area to the flow. In order to maintain the flow rate, the outlet width, b_2 should be increased.

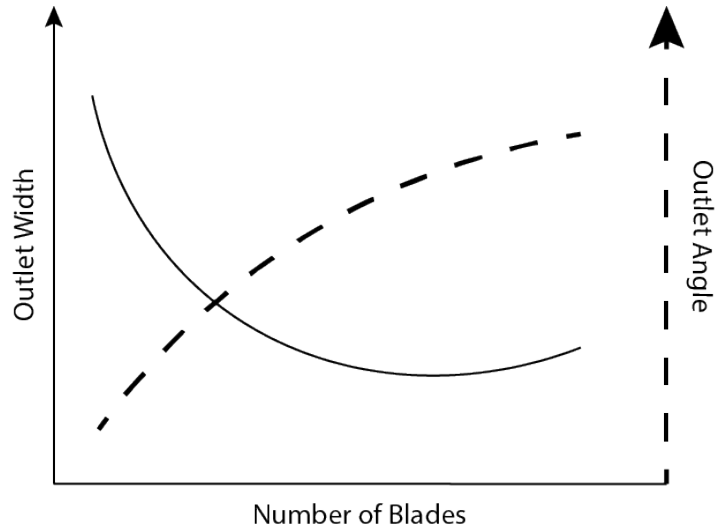


Figure 2.8: A typical graph showing the influence of the number of blades on outlet width and angle.

The previous paragraph clearly explains the two competing influences of the blade number on the outlet width. Figure 2.8 shows a typical graph indicating the effect of these two competing influences (β_2 and blockage) on the outlet width. For a low number of blades, the effect of β_2 dominates, with the outlet width decreasing while the number of blades increases and after a certain point, the blockage effect dominates, meaning the outlet width starts to increase as the number of blades increases. This trade-off point is different for every design and will be discussed for different impellers later on in the results.

2.1.17 Slip

The blade inlet and outlet angles influence the inlet and outlet flow angles respectively, although they do not always coincide. In fluid mechanics, it is established that a body must move faster than the flow in order to apply a force on the fluid that is moving in the same direction. This is known as impelling action [137]. The relative recirculation between the blades of the impeller leads to an increase in the

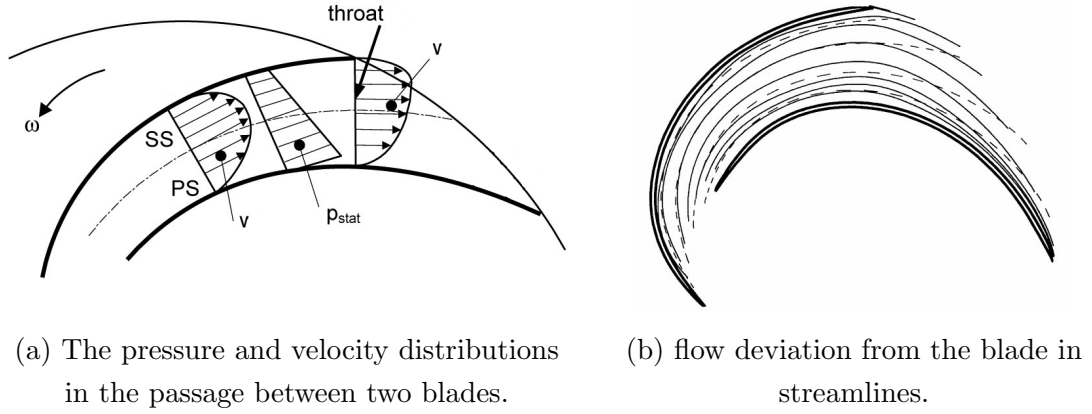


Figure 2.9: Effect of slip on the flow between the blades [46].

blade inlet angle and a slight drop in the outlet angle ($\beta'_2 < \beta_2$ and $\beta'_1 > \beta_1$). Therefore, the slip is influenced by the both number of blades and outlet angle.

To fully understand slip and its effect, it is necessary to analyse the flow within the blades. The path between the blades is a rotating curved channel with interactions between the solid (blade) and fluid to produce pressure and velocity rise. The pressure side of the blade has a higher pressure than the suction side. The different pressure distributions on the pressure and suction sides of a blade results in different velocity distributions (Figure 2.9a) and therefore, the fluid may not follow the exact blade shape and will instead deviate from its path (Figure 2.9b).

As shown in Figure 2.9b, larger deviations occur after the throat, where the flow has passed the trailing edge of one blade, the pressure gradient fades and the flow bends with a curving trajectory around the edge to follow the impeller outlet. The result is the deviation between the blade and the flow angles, defining the phenomenon slip, shown in Figure 2.10.

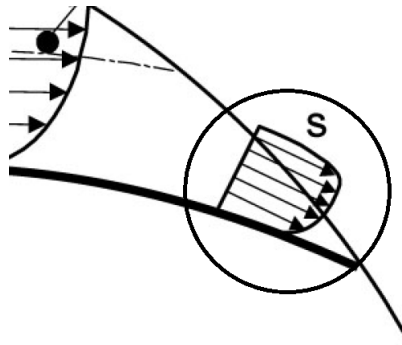


Figure 2.10: The slip at the trailing edge [46].

2.1.18 Hub Draft Angle

The hub draft angle, θ_{draft} , is the angle between the hub curve and the line parallel to the rotation axis. It affects the hub curve radius and is shown in Figure 2.11.

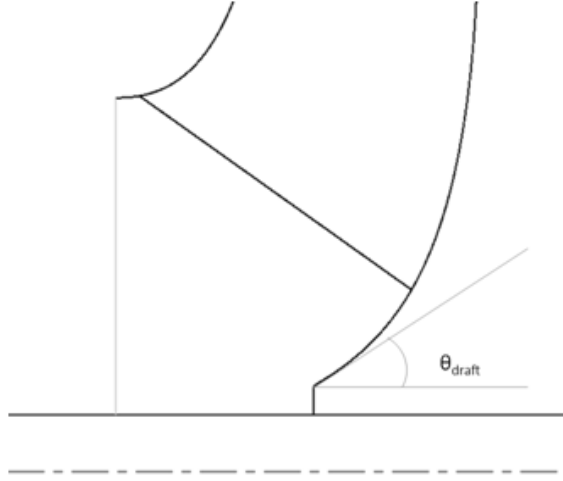


Figure 2.11: The hub draft angle, figure courtesy of ANSYS.

The lower draft angle results in a smaller hub radius and vice versa. The angle could be either chosen by the designer based on specific speed (similarity method), or could be determined by Bezier curves for meridional spans. The latter method has been used to define the hub radius in this study.

2.1.19 Impeller Blade Shape

In this thesis, the meridional coordinate system was used due to its convenience for the impeller and flow movement. The components of this coordinate system are $ZR\theta$ and stand for axial, radial and circumferential components. Having selected the inlet and outlet diameters and angles and outlet width, the meridional profile of the blade is the next step to design the impeller. From the hub to the shroud, the profile was divided into five equally spaced streamlines and the curve for each streamline was computed by applying a Bezier curve. For this purpose, a third degree (cubic) Bezier curve is used as a compromise between the simplicity of lower order curves and the smoothness of higher order curves.

Four points are used to define a cubic Bezier curve, as shown in Figure 2.12.

The curve starts at P_0 , going via P_1 and P_2 to reach P_3 . The curve will not normally pass P_1 and P_2 , but gets its direction from these points. The position and distance between the middle control points determine how smooth the curve is. The general form of the curve is equation 2.14 where t represents the parameter value of the curve.

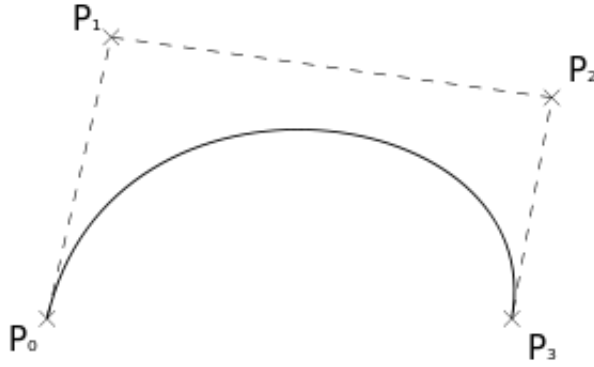


Figure 2.12: A cubic Bezier curve with four control points.

$$B(t) = (1-t)^3 P_0 + 3(1-t)^2 t P_1 + 3(1-t)t^2 P_2 + t^3 P_3 \quad 0 \leq t \leq 1 \quad (2.14)$$

The derivative of this Bezier curve with respect to t shows the slope of the blade's curve at the bend and is expressed by

$$B'(t) = 3(1-t)^2 (P_1 - P_0) + 6(1-t)t (P_2 - P_1) + 3t^2 (P_3 - P_2) \quad (2.15)$$

A smaller radius in the meridional profile results in higher flow velocity and subsequent flow separation. The radius of the curve at the bend, where the flow direction changes smoothly, should be as large as possible to avoid flow separation.

2.1.20 Camberline/Thickness

The coordinates of the camberline are m and θ . The m component (meridional component) is related to the axial (z) and radial (r) components in the Bezier curve and is calculated along the path by

$$m = \int \sqrt{\left(\frac{dr}{dx}\right)^2 + \left(\frac{dz}{dx}\right)^2} dx \quad (2.16)$$

The normalized meridional component is expressed by

$$m' = \int \frac{\sqrt{\left(\frac{dr}{dx}\right)^2 + \left(\frac{dz}{dx}\right)^2}}{r} dx \quad (2.17)$$

The thickness of the blade is selected to provide sufficient rigidity while minimizing flow blockage in the flow path, increasing from the leading edge to the trailing edge to deliver a uniform gradient in the passage area [137]. An ellipse is used at the leading edge for a shockless entry [31]. The general equation of an ellipse is given by

$$\left(\frac{x}{a}\right)^2 + \left(\frac{y}{b}\right)^2 = 1 \quad (2.18)$$

where x and y are the major and minor axes and a and b are the scale factors, meaning the thickness of the blade is $2b$ at the center of the ellipse. Therefore, the trigonometric parametric formulas are given by

$$x = r \cos \theta \quad (2.19)$$

$$y = r \sin(\theta \pm t) \quad (2.20)$$

where t is an offset from the camberline (x -axis of the ellipse) for the wrap angle θ , defined as

$$\theta = \int \frac{\tan \beta}{r} dm \quad (2.21)$$

2.1.21 Shroud Configurations

Centrifugal impellers can be categorised in three groups based on their shroud configuration: open, semi-open and closed impellers. Open impellers have neither hub nor shroud. They perform better in high specific speed pumps [128] due to reduction in disc friction losses. Semi-open impellers have a hub but no shroud on top. The lack of shroud results in leakage between the blades as well as stagnation under the impeller hub. Closed impellers are also referred to as shrouded impellers and have both the shroud and hub. The friction losses in these impellers are related to the flow relative to the inner wall of the shroud, $\frac{w^2}{2g}$.

A number of authors [9, 27, 81] have reported an improved hydraulic efficiency for shrouded impellers compared to open and semi-open. However, adding a shroud or a hub will increase the level of hæmolysis and thrombosis in the hub and shroud gaps. Based on the literature, shrouded impellers and semi-open impellers result in higher hydraulic efficiencies and are more desirable, as long as the shear stress levels are below the critical value.

A numerical investigation as part of this thesis, on three types of impellers, showed a high static head but also a high wall shear stress in the open impeller and lower efficiency due to high hydraulic losses. After considering this numerical investigation, along with the literature, semi-open and closed impellers are selected for this study. Table 2.1 shows the numerical results of the three impellers compared to each other.

Table 2.1: Numerical investigation on three types of impellers.

Configuration	Pressure rise (mmHg)	Hydraulic Efficiency	Max. wall shear stress (Pa)	NIH (g/100L)
Shrouded	73.2	78.26	44.5	0.003125
Semi-open	80.55	75.6	53.6	0.005558
Open	79.88	75.9	71.1	0.008787

2.1.22 The Volute

The volute is usually a spiral shaped passage with a circular, rectangular or trapezoidal cross section. In most cases, the cross section area gradually increases from the tongue (smallest radius) to the throat (largest radius) [142].

The main function of a volute is the conversion of the kinetic energy of the fluid to the pressure energy while collecting, guiding and delivering the fluid, by minimizing the losses in the conversion process [76]. Most of this energy conversion is done by the volute and the rest is carried out by the diffuser later on [69]. A major part of losses in a centrifugal pumps loss is a result of the diffusion inefficiency and therefore the diffusion process and the loss of energy during this process is a key factor on the overall performance of the pump [142, 69]

There are three main types of volute design: singular, circular, and double. A singular volute is the most common type of volute and is often used for low flow and low specific speed applications [76]. The circular volute has a constant radius from the tongue to the throat and has a ratio of diameters of 1.15-1.2 with the impeller [76]. It is often used for a very limited range of specific speeds and has less controlled flow guidance through the path compared to other types. The double volute is also referred to as split volute and consists of two single volutes opposite each other, or a single volute with a splitter plane, shown in Figure 2.13.

One significant effect of using different volute types is on the hydraulic radial forces on the impeller. This force is extremely important in cases when the impeller is suspended within the casing by contactless means. Higher radial force will result in a higher force to balance the impeller and therefore using more power and lower efficiency [66]. Based on an experimental study conducted by [20] on three types of volute, the single volute had the lowest radial force acting on the impeller at the design point (≈ 0 N), whereas the circular volute yielded the highest (≈ 2 N) and the double volute resulted in a force of approximately 0.5 N. The study showed that the double volute will be a better choice for contactless impellers in off design conditions, but the single volute will have a higher efficiency at the design point. In this thesis, the impellers are driven by an external electric motor through a shaft. The main objective of this thesis is to find the highest achievable efficiency for each

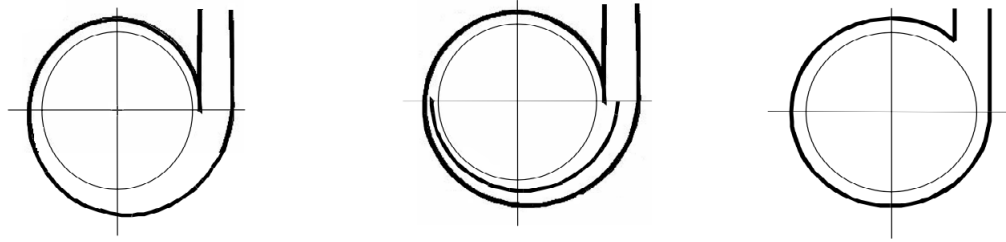


Figure 2.13: Three types of volutes: Singular, double and circular [137].

individual pump even if it is just a peak point. Therefore, a single volute is selected. The inlet width of the volute is calculated based on the sum of the impeller outlet width and the proposed axial clearance between the impeller and casing, shown in Figure 2.14.

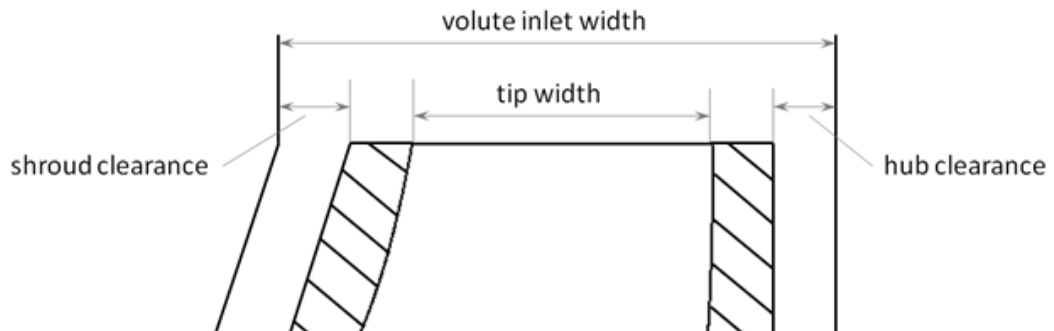


Figure 2.14: The volute inlet width shown with tip width and clearances, figure courtesy of ANSYS.

The tongue of the volute has the smallest distance to the impeller and the throat at the outlet of the volute has the largest. Lofting the tongue to the throat will make a spiral shape because of this difference in radii. The path is normally modified to keep a constant angular momentum, resolve the friction losses at the walls and avoid flow separation.

Volute Cross Section

There is no ideal form for the geometry of a volute's cross section, however, there are three shapes commonly used for this purpose: circular, rectangular and trapezoidal. The circular volute starts as a straight line at the tongue and covers a fraction of a circle based on the needed outlet area. The rectangular and trapezoidal cross sections are a rectangle and an isosceles trapezoid respectively.

A recent numerical investigation [5] on different volute cross sections (Figure 2.15) studied the effect of volute curvature and cross section on performance of centrifugal pumps at design and off-design conditions. The study suggests that the circular cross

section volute provides higher head and efficiency than the other cross sections at almost any flow rate. Trapezoidal and circular cross sections give lower radial force at high flow rates while rectangular cross section yields lower radial force at low capacity rates [5].

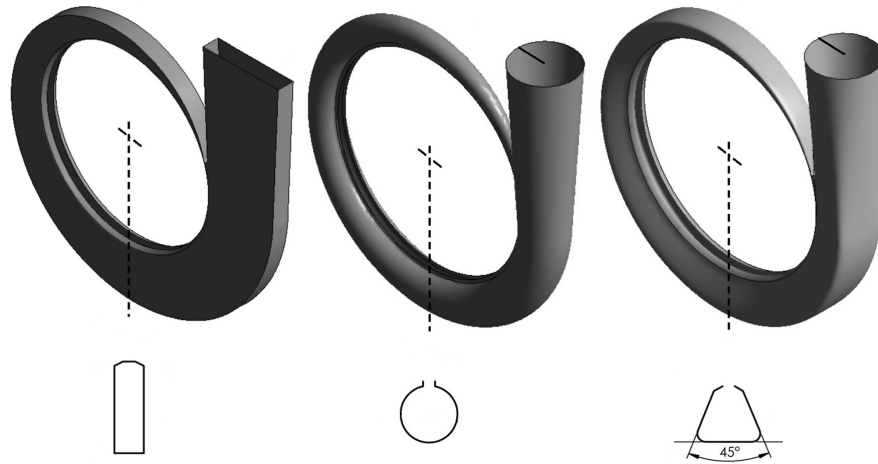


Figure 2.15: Volute models with rectangular, circular and trapezoidal cross sections [5].

The Diffuser

At the throat of the volute, there is a transitional section that is in fact an extension of the volute outlet. The length and the taper angle of this extension are designed in order to convert the remaining kinetic energy of the flow into pressure [128].

Lazarkiewicz [69] presented a graph showing a linear relationship between the taper angle of the diffuser and the velocity of the flow at the throat, shown in Figure 2.16. Values higher than 13 will result in flow separation on the diffuser walls [69, 76]. Figure 2.17 shows a typical single volute.

2.2 Conventional Design Procedure

In this section, the conventional pump design method has been discussed. The section starts with the definition of velocity triangles and their use in determining the inlet and outlet parameters. The force analysis of centrifugal pumps based on different proposed methods is then discussed in details.

2.2.1 Velocity Triangles

In turbomachinery, the motion of the fluid is specified according to the rotational motion of the impeller. Euler's velocity triangle or velocity diagram is the representation of this kinetic movement and shows the components of velocities of the

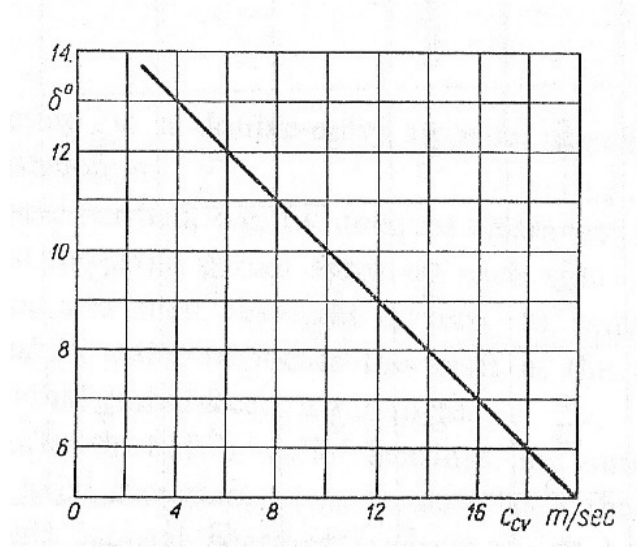


Figure 2.16: The linear relationship between the taper angle of the diffuser and the fluid velocity at the throat [69].

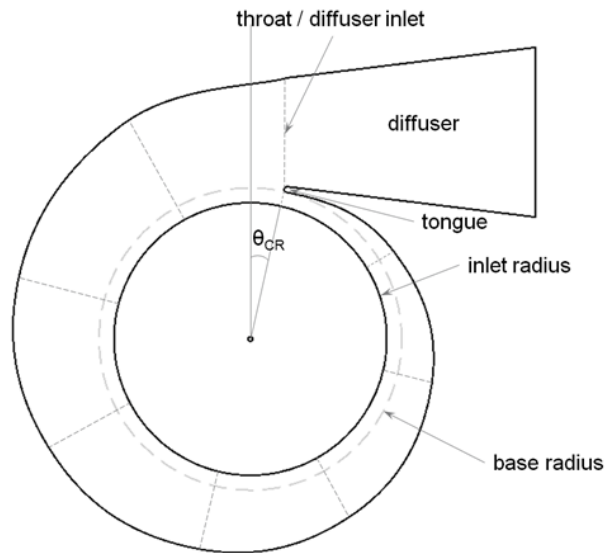


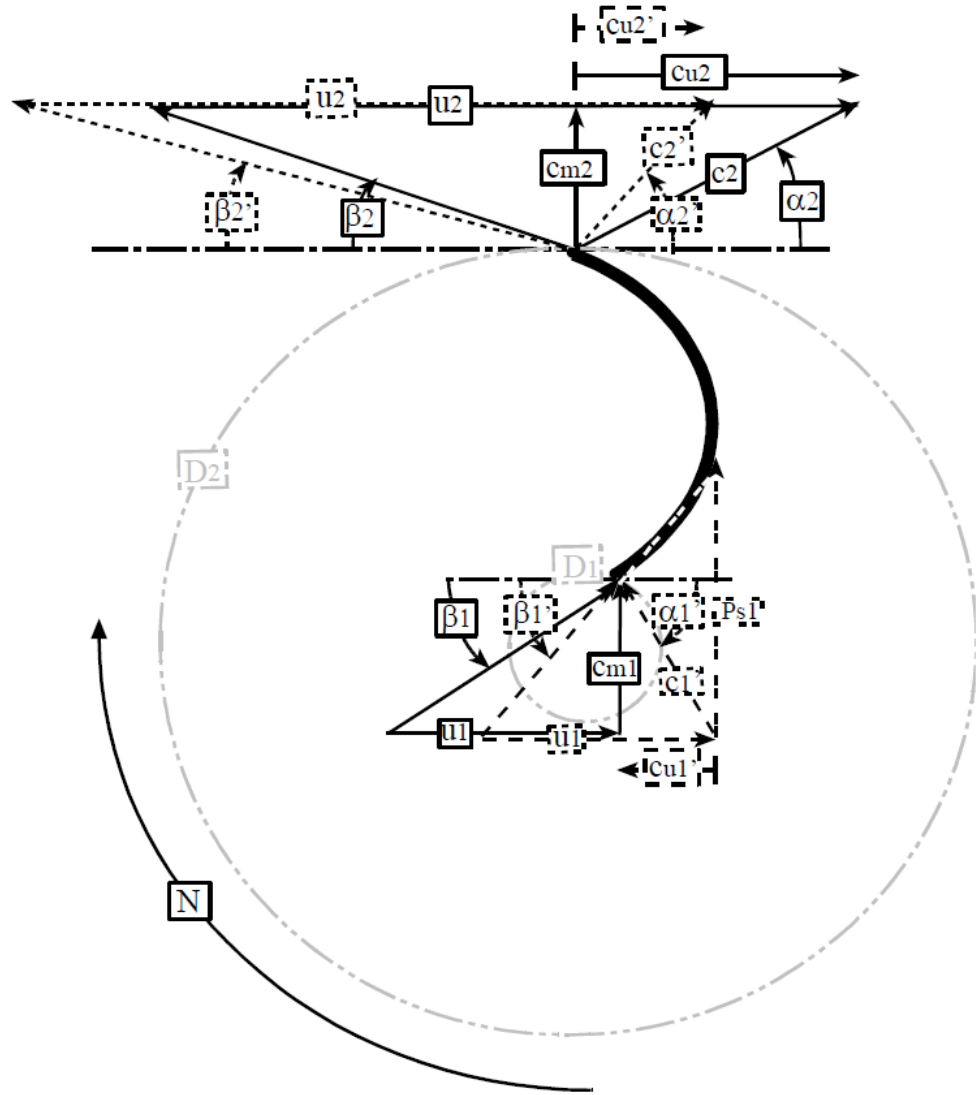
Figure 2.17: A single volute with a circular cross section, figure courtesy of ANSYS.

fluid with respect to the impeller blades. The velocity triangles are drawn for the inlet and outlet of a blade. The absolute velocity is the sum of two velocities; the peripheral velocity of the impeller and the fluid velocity relative to the impeller, as shown in Figure 2.18.

If the fluid enters with a tangential component, the theoretical head is given by Equation 2.22.

$$H_t = \frac{U_2 C_{u2} - U_1 C_{u1}}{g} \quad (2.22)$$

Equation 2.22 shows the pressure head is not influenced by the relative velocity and



u_2 : Outlet peripheral velocity
 c_{u2} : Outlet tangential velocity
 c_{m2} : Meridional outlet velocity
 β_2 : Impeller discharge angle
 c_2 : Fluid outlet velocity
 α_2 : Fluid discharge angle
 N : Rotational speed
 D_1 : Inlet diameter
 D_2 : Outlet diameter
 β_1 : Impeller inlet angle
 c_{u1} : Inlet tangential velocity
 c_{m1} : Inlet meridional velocity
 c_1 : Fluid inlet velocity
 α_1 : Fluid inflow angle
 P_s : Inlet recirculation ratio

Figure 2.18: Centrifugal impeller inlet and outlet velocity vectors [137].

is built up gradually as C_{u2} and U_2 increase. The impeller tip speed, U_2 , is the parameter that enables the centrifugal pump to meet the proposed head rise and flow rate. Since the value of the theoretical head, H_t , is the complete conversion of the kinetic energy from the impeller to the working fluid, the maximum tip speed may be calculated to achieve the desired pressure rise.

$$U_2 = \sqrt{2gH_t} \quad (2.23)$$

The impeller tip speed is also related to the impeller diameter and rotational speed. The tip speed is calculated by:

$$U_2 = \frac{\pi DN}{60} \quad (2.24)$$

With conventional design method, at this stage the rotational speed and the impeller diameter are calculated to meet the required head-flow conditions. Known rotational speed, pressure rise and flow rate establishes the specific speed of the pump and therefore the type of pump can be selected using a Cordier diagram. Higher specific speed results in a smaller pump and cheaper drivers [128].

The optimum hydraulic efficiency varies with the specific speed. Figure 2.19 shows a typical empirical diagram with efficiencies attained at various specific speeds for single stage single suction pumps [12].

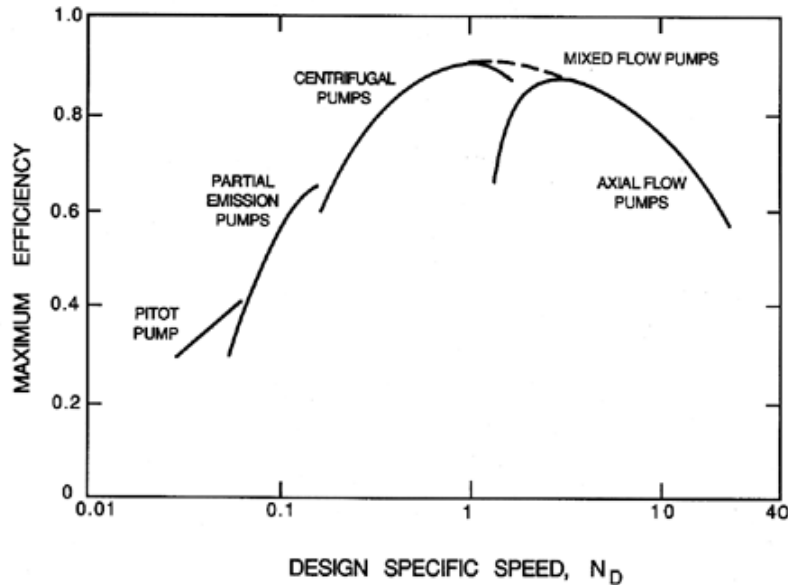


Figure 2.19: Pump efficiency vs. specific speed for industrial single stage single suction pumps [12].

If the required pressure rise is not produced with the proposed design, the design will be divided into more stages. The pressure rise per each stage influences the

final specific speed and therefore the final efficiency [128]. The designers use the design factors established experimentally from previous successful designs that provide them with empirical relationships between the pump performance and the elements of the velocity diagrams. For instance, the nondimensional velocity ratios are correlated to the different outlet angles based on specific speeds for industrial pumps, regardless of their size and rotational speed. The blade profile and layout is designed based on four elements: meridional velocity at the inlet and outlet, impeller diameter, blade leading edge angle and blade trailing edge angle. These four elements will also determine the inlet and outlet velocity diagrams. For a simple blade with a straight vane, the working fluid enters and exits the impeller at the same velocity, meaning that the inlet and outlet velocity triangles are similar for all sections from the hub to the tip of the blade. In other types of centrifugal impellers and in axial impellers, the blade is divided into several sections with different triangles due to the different radii of each section. The difference in these triangles and therefore angles is the reason for a curvature in the blade.

2.2.2 Blade Outlet Conditions

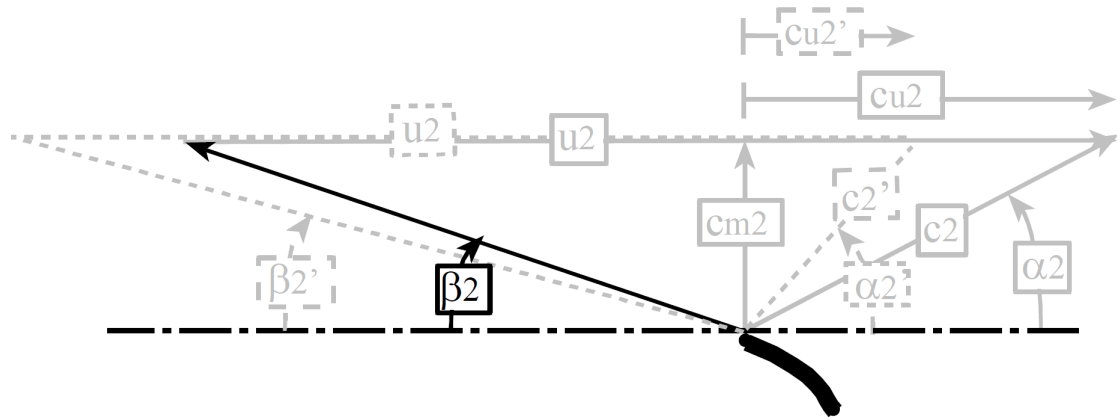


Figure 2.20: Blade outlet velocity triangle [137].

The blade discharge angle is the most important parameter in the design process, as all design constants relate to it directly or indirectly [128]. Selection is based on the desired slope of the head-flow curve since both flow rate and head rise increase with a higher blade angle. Figure 2.21 illustrates the percentage pressure rise from the best efficiency point (BEP) to shut off and the slope of the performance curve. The desired percentage pressure rise is selected and leads to the selection of blade number and outlet angle based on a known specific speed [76]. For low blade angles, it is recommended to pick >5 blades [128].

If there are no limitations on the geometric parameters based on the application, the priority is the hydraulic efficiency of the pump. For an efficient and manufac-

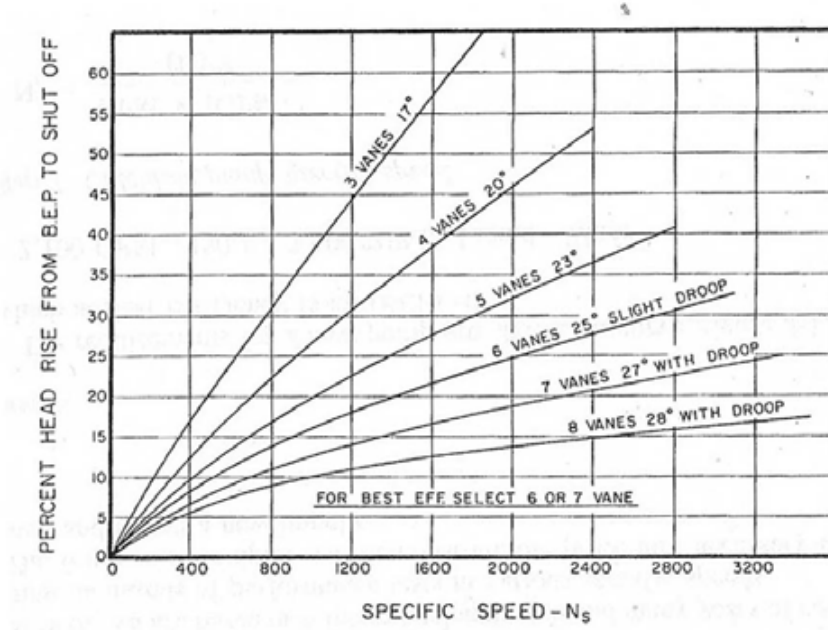


Figure 2.21: Percent pressure rise vs. specific speed for blade angle and number selection [76].

turable pump, an outlet angle in the range of 17.5° - 27.5° and specifically 22.5° is recommended for industrial pumps [12, 128, 76]. However, studies have shown better physiological control in case of larger outlet angles [133].

Head and Flow Coefficients

In industrial pumps, the head and flow coefficients are typically within the range of $\psi = 0.05 - 0.2$ and $\phi = 0.4 - 0.7$ [142]. Values of head and flow coefficients may be taken from diagrams based on empirical equations. Figure 2.22 shows the values of head and flow coefficients and specific speeds for various outlet angles [128].

Speed Constant

As discussed earlier, the impeller tip speed is calculated with the assumption that kinetic energy is completely converted to pressure energy. In reality this is not possible due to losses in the conversion process. The speed constant is a nondimensional parameter defined as the ratio of actual tip speed to the velocity under pressure head, presented as

$$K_u = \frac{u_2}{\sqrt{2gH}} \quad \text{or} \quad u_2 = K_u \sqrt{2gH} \quad \text{or} \quad H = \frac{1}{K_u^2} \frac{u_2^2}{2g} \quad (2.25)$$

Based on these relationships, the speed constant can also be presented as

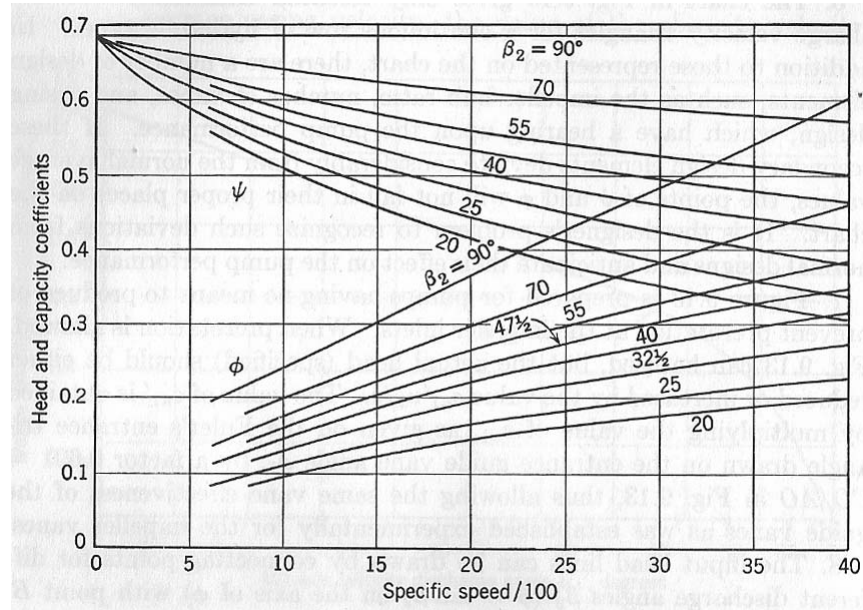


Figure 2.22: Head and flow coefficients for different outlet angles [128].

$$K_u = \sqrt{\frac{1}{2\phi}} \quad (2.26)$$

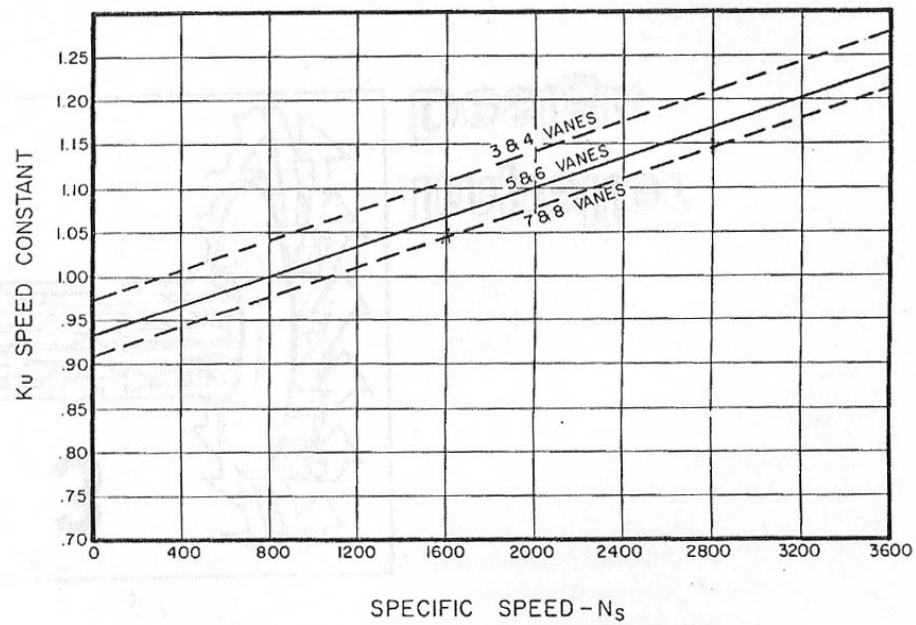


Figure 2.23: Speed constants for different number of blades [76].

The speed constant is influenced by the number of blades and the outlet angle. Figure 2.23 shows the effect of blade number on the speed constant and Figure 2.24 illustrates this constant for a specific case of 6 blades and 22.5° outlet angle.

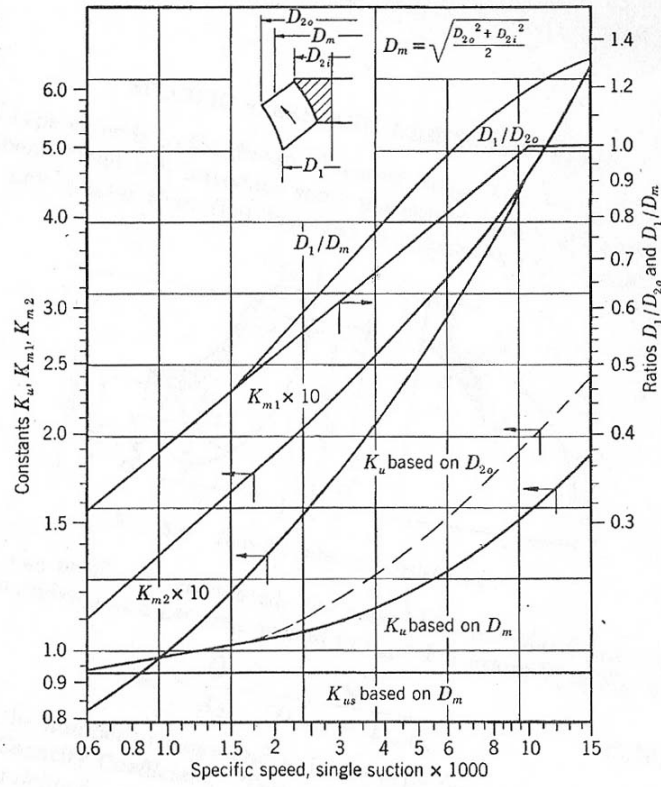


Figure 2.24: Speed constants for impellers with 6 blades and a 22.5° outlet angle [128].

Actual Tip Speed, Diameter And Rotational Speed

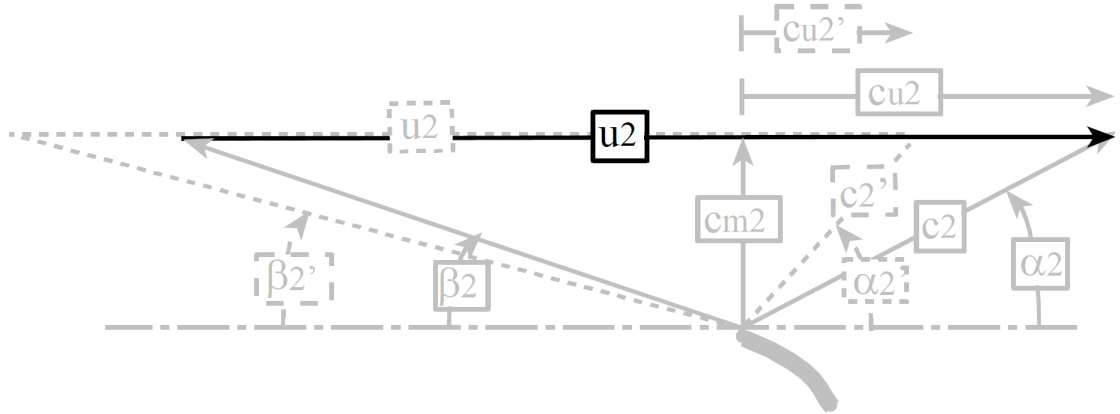


Figure 2.25: Actual impeller tip speed [137].

The actual tip speed of the impeller, u_2 shown in Figure 2.25 is derived using the speed constant and desired pressure rise by one form of equation 2.25. This equation takes the relative recirculation between the blades into account, which is the difference between the tangential and actual velocity vectors, U_2 and u_2 . As a result, determining the actual tip speed will lead to the actual diameter and rotational

speed of the proposed design by using equation 2.24.

Capacity Constant

The capacity constant, K_{m2} , is the ratio of meridional velocity at the outlet to the tip speed and is shown in Figure 2.25.

For a given specific speed, the capacity constant may be obtained using Figure 2.24. Alternatively, a known speed constant and flow coefficient produce the capacity constant for other outlet angles and blade numbers, based on Equation 2.27.

$$K_{m2} = \frac{c_{m2}}{\sqrt{2gH}} \quad (2.27)$$

$$K_{m2} = K_u \phi$$

Meridional Outlet Velocity

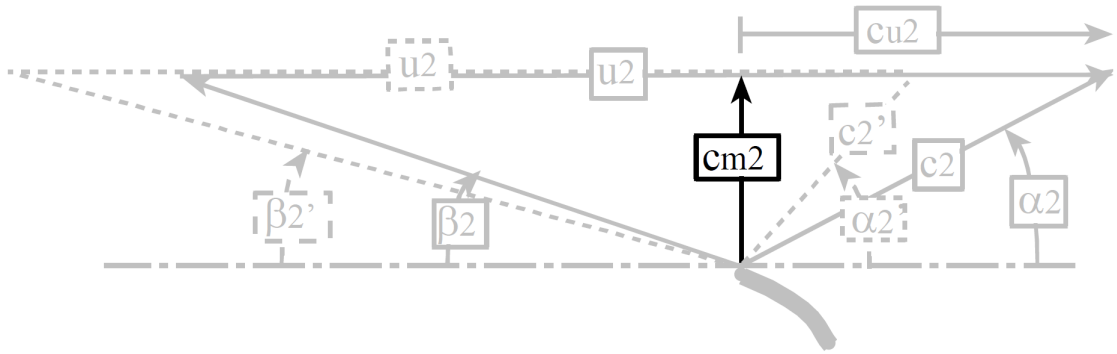


Figure 2.26: Meridional outlet velocity [137].

Meridional outlet velocity, shown in Figure 2.26, represents the capacity of the pump and can be derived by:

$$c_{m2} = K_{m2} \sqrt{2gH} \quad (2.28)$$

Consequently, once the capacity constant is defined, the meridional outlet velocity can be calculated.

Slip

The slip factor may be calculated from the values of head and flow coefficients using Equation 2.29.

$$\psi = \sigma - \phi \tan(90 - \beta_2) \quad (2.29)$$

Outlet Width

The meridional velocity is proportional to the flow rate and the exit area as discussed earlier. By relating the outlet area to the number of blades, diameter, outlet width and the thickness of blades, the outlet width can be derived as [128]:

$$c_{m2} = \frac{Q}{A} = \frac{Q}{(D\pi - z s_u) b_2} \quad (2.30)$$

Absolute Outlet Velocity

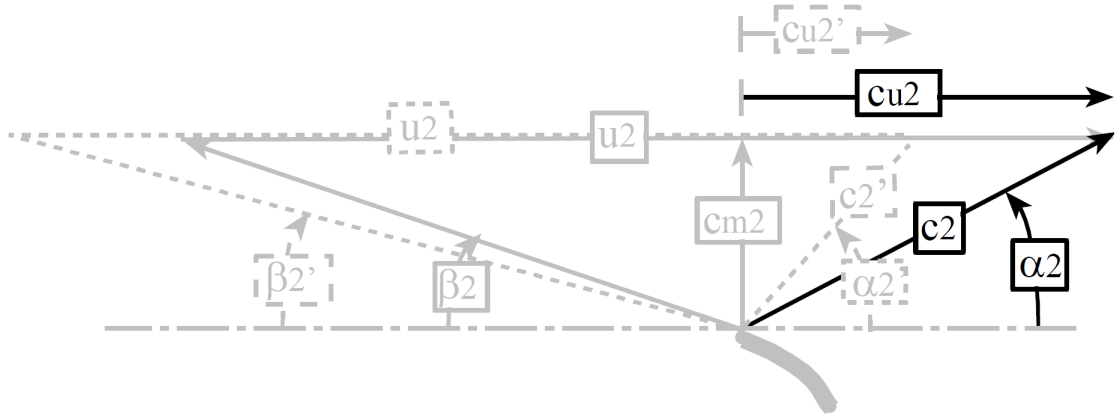


Figure 2.27: Euler absolute outlet velocity [137].

The Euler's absolute outlet velocity, shown in Figure 2.27, represents the working fluid at the outlet relative to a stationary frame. The magnitude has both radial and tangential components. The radial component represents the flow rate and the tangential component represents the pressure rise. The Euler velocity vector is in the case of ideal and 1-D flow, whereas in the case of realistic flow, the vectors are slightly different due to recirculation or slip, as has been discussed earlier.

- Euler

In order to derive the magnitude and direction of the ideal (Euler) working fluid's absolute velocity vector, c_2 and α_2 , the tangential velocity, c_{u2} , needs to be deter-

mined. Tip speed, meridional fluid velocity and the outlet angle can be used as in Equation 2.31 to find this velocity.

$$c_{u2} = u_2 - \frac{c_{m2}}{\tan \beta_2} \quad (2.31)$$

Therefore, the magnitude and direction may be calculated using the following equations:

$$c_2 = \sqrt{c_{m2}^2 + c_{u2}^2} \quad (2.32)$$

and

$$\alpha_2 = \tan^{-1} \frac{c_{m2}}{c_{u2}} \quad (2.33)$$

- Actual

The slip or recirculation of the working fluid in the flow path results in a different outlet angle and a deviation in tangential velocity and pressure rise from the ideal Eulerian model, as shown in Figure 2.28.

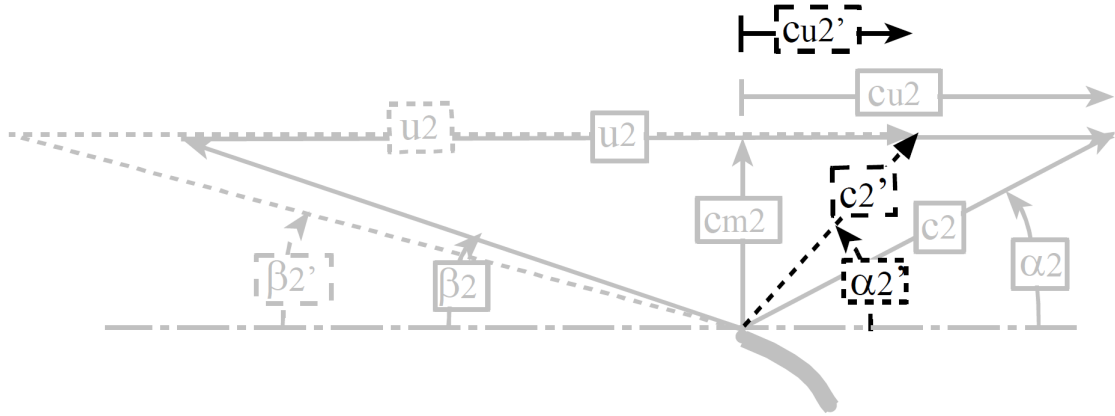


Figure 2.28: Actual absolute outlet velocity [137].

The value of actual tangential velocity, c'_{u2} , may be calculated using the head coefficient and the actual tip speed by:

$$c'_{u2} = \psi u_2 \quad (2.34)$$

The calculated value may be used to obtain the actual outlet angle, β'_2 , which is lower than the ideal designed value, β_2 .

$$\beta'_2 = \tan^{-1} \frac{c_{m2}}{u_2 - c'_{u2}} \quad (2.35)$$

The magnitude and direction of the actual outlet velocity vector are obtained using Equations 2.36 and 2.37. The direction is also related to the ratio of flow and head coefficients.

$$c'_2 = \sqrt{c_{m2}^2 + c'_{u2}{}^2} \quad (2.36)$$

$$\alpha'_2 = \tan^{-1} \frac{c_{m2}}{c'_{u2}} = \tan^{-1} \frac{\phi}{\psi} \quad (2.37)$$

The obtained values are expected to be slightly lower than the real (Euler) values due to slip.

Ratio of Absolute Tangential To Meridional Velocity

The ratio of absolute tangential flow velocity to meridional flow velocity, λ , is another parameter that is different for industrial and blood pumps due to the differences in their flow fields and Reynolds number. This ratio is derived by:

$$\lambda = \frac{c'_{u2}}{c_{m2}} = \cot \alpha' \quad (2.38)$$

and is normally within the range of 2-7 for industrial and may be up to ≈ 30 for centrifugal blood pumps [133, 128].

2.2.3 Blade Inlet Conditions

As discussed at the beginning of this chapter, the assumption of no pre-whirl is made in the design of the impeller inlet conditions. This implies an inlet angle, which is independent of the outlet angle and also different for each application.

Inlet Capacity Constant

The inlet capacity constant, K_{m1} , can be derived from Equation 2.27 and relates the tip speed to the meridional inlet velocity, c_{m1} .

Meridional Inlet Velocity

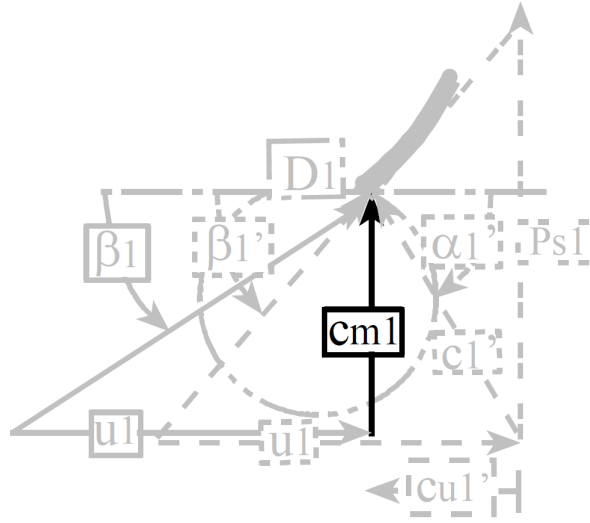


Figure 2.29: Blade inlet velocity triangle [137].

The meridional inlet velocity, shown in Figure 2.29, is calculated by:

$$c_{m1} = K_{m1} \sqrt{2gH} \quad (2.39)$$

c_{m1} is also related to the flow rate, inlet diameter and inlet width by:

$$c_{m1} = \frac{Q}{\pi D_1 b_1} \quad (2.40)$$

Inlet Diameter

The inlet diameter affects the probability of flow separation. This value needs to be selected by the designer in order to minimise the relative inlet velocity and therefore the ratio of inlet and outlet velocities

$$c_{r1}^2 = u_1^2 + c_{m1}^2 \quad (2.41)$$

Higher inlet diameter at a constant flow rate results in a higher rotational speed, higher inlet tip speed and lower meridional velocity. The inlet diameter is derived by:

$$D_1 = 1.533 \left(\frac{Q}{\omega} \right)^{1/3} \quad (2.42)$$

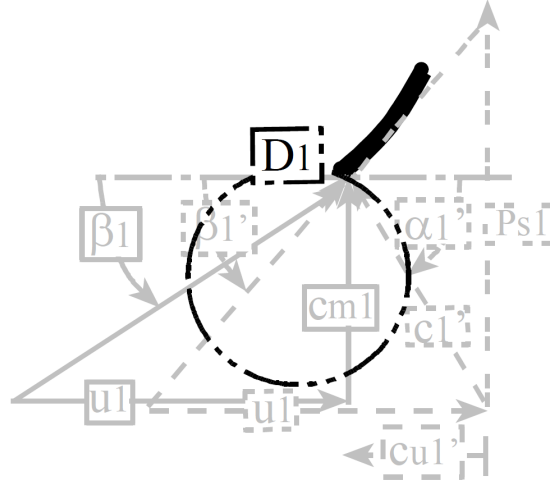


Figure 2.30: Impeller inlet diameter [137].

Inlet Width

A known inlet diameter will lead the designer to the inlet width by using Equation 2.40.

Impeller Inlet Tip Speed

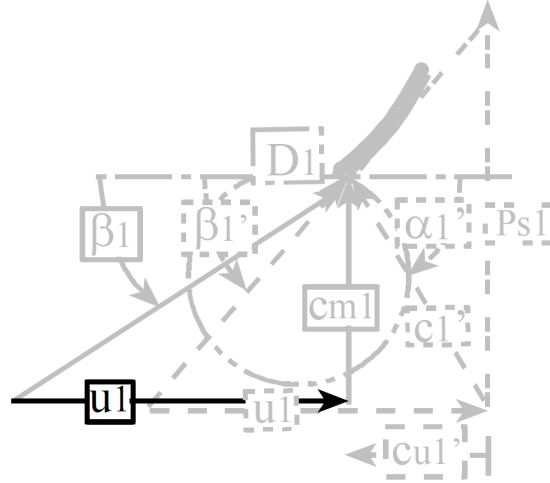


Figure 2.31: Impeller inlet tip speed [137].

The inlet tip speed may be calculated using the same principles as the outlet tip speed.

$$U_1 = \frac{\pi D_1 N}{60} \quad (2.43)$$

Blade Inlet Angle

The impeller inlet angle, β_1 , is derived by Equation 2.44, from known inlet tip and meridional velocities.

$$\beta_1 = \tan^{-1} \frac{c_{m1}}{u_1} \quad (2.44)$$

- Actual

The actual value of the inlet angle differs from the Euler value, due to the relative recirculation between the vanes ($\beta'_1 > \beta_1$). The recirculation ratio, P_s , is defined by:

$$P_s = c_{m1} R \quad (2.45)$$

where R is a constant and defines the ratio of ideal flow rate in the case where there is no recirculation to the rated flow rate. R has a value of 1.15-1.25 for single-inlet end-suction and 1.25-1.35 for double-inlet volute-suction pumps [128]. Calculating P_s will lead to the value of actual inlet blade angle

$$\beta'_1 = \tan^{-1} \frac{P_s}{u_1} \quad (2.46)$$

In practice, the ideal value of outlet angle and actual value of inlet angle are used for the final blade construction [128].

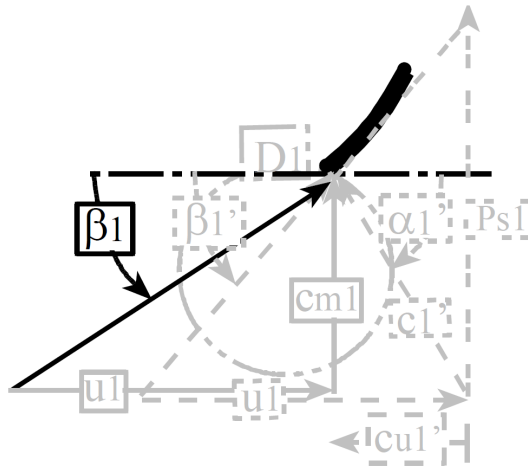


Figure 2.32: Impeller inlet blade angle [137].

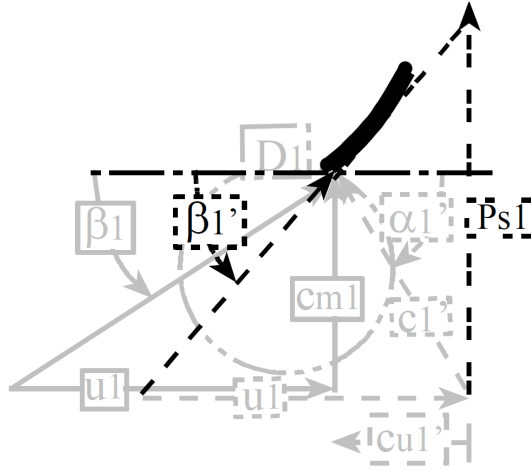


Figure 2.33: Impeller actual inlet blade angle [137].

Absolute Inlet Velocity

The ideal and actual values of the absolute inlet velocity are derived as follows.

- Euler

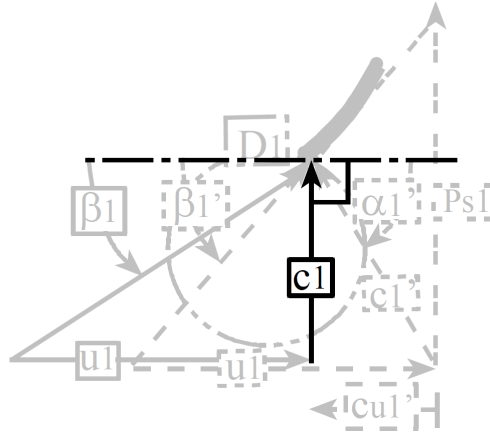


Figure 2.34: The ideal absolute inlet velocity [137].

The inlet flow angle, α_1 is chosen as 90° . The blade inlet angle, β_1 , is designed with this assumption to eliminate the tangential velocity, c_{u1} and therefore, the absolute inlet velocity, c_1 resolves to the value of meridional velocity, c_{m1} .

- Actual

The components of the actual absolute velocity, c_{m1} and c'_{u1} , are used to find its magnitude. In order to find the tangential component (c'_{u1}), the tip speed, meridional flow velocity and the actual calculated inlet angle are used.

$$c'_{u1} = U_1 - \frac{c_{m1}}{\tan \beta'_1} \quad (2.47)$$

and therefore:

$$c'_1 = \sqrt{c_{m1}^2 + c'_{u1}^2} \quad (2.48)$$

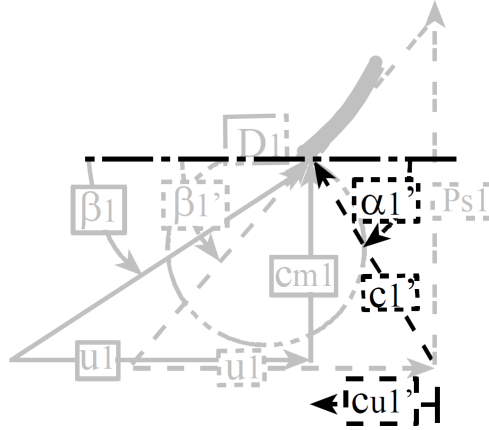


Figure 2.35: The actual absolute inlet velocity [137].

The direction of this vector is given by:

$$\alpha'_1 = \tan^{-1} \frac{c_{m1}}{c'_{u1}} \quad (2.49)$$

2.2.4 Axial Clearance

The axial clearance between the impeller's top surface and the volute influences the flow, pressure and efficiency. This effect is more pronounced in un-shrouded impellers due to higher gap to outlet width ratio. This ratio is defined by Stepanoff [128] and its optimum value is found at about 0.05 and the efficiency drops to 62.5% with a ratio of 0.6.

2.2.5 Force Analysis

Force analysis in a centrifugal blood pump is a key factor for the design of the bearing system for impeller suspension. It is especially critical in active magnetic suspension due to the power consumed by active magnetic bearings [58]. The impeller will be acted upon by forces; hydraulic forces due to the flow, impact forces due to the patient's activities and the g-force due to its weight. The daily activities of a patient do not normally create acceleration in excess of 30 m/s^2 [132] while a continuous 60

acceleration will cause fainting and a deceleration of ≈ 50 is fatal. A drop test was conducted [43] on a VAD and reported decelerations of 150 and 440 for the VAD falling from 1.2 and 4 meters respectively. Studies on the VentrAssistTMVAD have reported a 100 m/s^2 toleration. This acceleration causes axial and radial forces of 0.3 N and 1.4 N respectively on the device [132, 98].

Stepanoff [128] measured the axial and radial forces on a centrifugal impeller based on the size and duty frame for a known specific speed. A few years later, another study investigated the effect of specific speed on the impeller radial force [3]. During the 1980s, different studies investigated several methods of force measurement and analysis by studying the interaction between impellers and volutes [77] on and off-design, sources of static and dynamic forces [51] and the effect of impeller whirl on the produced force [2, 59]. A more recent experimental study [16] examined the effect of different impellers and volutes on the radial force induced in the pump. The hydraulic forces of a centrifugal impeller can be defined as static or dynamic. They can also be categorised by their direction into axial and radial forces [37].

2.2.6 Radial Thrust

The radial forces acting on a centrifugal impeller are those acting perpendicular to the rotational axis and is composed of a static and a dynamic component. The static component is due to the uneven pressure distribution around the impeller which is the result of the volute's asymmetry. The dynamic component is a periodic type of force and the total radial force is normally the superposition of the two components perpendicular to the rotation axis.

Static Radial Thrust

The static radial force is partially due to the unbalanced flow around the impeller which is a result of an uneven pressure distribution [59, 51]. Another major contributing factor is the flow separation at the tongue due to the difference in the outlet flow angle and the volute spiral angle. The magnitude and direction of the static radial thrust depends on the duty frame and the volute type [51, 5, 20].

Knowledge about the static radial force in a centrifugal impeller is largely based upon empirical studies. Several attempts [128, 69, 76, 77, 61] have been made to predict the theoretical magnitude and direction of this force, however no method has been established as the best or most appropriate technique [58].

Magnitude

The most common techniques to predict the magnitude of static radial thrust are:

- Stepanoff

In the late 1957, an equation was proposed [128] based on experimental results in three types of volutes: singular, circular and split.

$$F = \frac{K.H.D.B_2}{2.31} \quad (2.50)$$

F Static radial thrust (lbf)

H Pressure rise (ft)

D Diameter (in)

B_2 Width (in)

K Thrust factor

The thrust factor is a function of flow rate and type of volute and is calculated for single and double volutes by

$$K = K_{th} \left(1 - \left(\frac{Q}{Q_n} \right)^2 \right) \quad (2.51)$$

and for circular volutes by

$$K = 0.36 \frac{Q}{Q_n} \quad (2.52)$$

Q Flow rate

Q_n Flow rate at BEP

K_{th} 0.36 for single and 0.16 for double volute

- Lobanoff

Another empirical equation was introduced [76] for single and double volutes and was incorporated in the ANSI HI (Hydraulic Institutes American National Standard)

$$F = \frac{K.H.D.B_2(SG)}{2.31} \quad (2.53)$$

SG Specific Gravity

- Karassik

This latter method was introduced [61] for single volutes and includes a factor for different unit conversions

$$F = k K_r H D B_2 (SG) \quad (2.54)$$

F Static radial thrust (lbf/N)

H Pressure rise (ft/m)

D	Diameter (in/m)
B_2	Width (in/m)
SG	Specific Gravity
k	0.433/9790
K_r	Radial thrust factor

Direction

The direction of the radial thrust is determined by experimental data presented in diagrams [61, 3, 69]. Two contributing factors influence the direction of this force: flow separation at the tongue and the degree of acceleration at the throat, with the first one being the dominant factor.

Dynamic Radial Thrust

The dynamic radial force in a centrifugal impeller is due to eccentricity fluctuations in three frequency ranges. The first range is in the same frequency as the impeller rotational speed, due to the manufacturing errors which cause pressure fluctuations and subsequent imbalances [37]. Fluctuations at a higher frequency than the rotational speed are generated due to each blade passing the tongue, known as the vane passing frequency. Fluctuations also occur at a lower frequency than the rotational speed due to flow separation [37, 51, 61]. Dynamic forces are normally complicated to predict or calculate and are most significant at $\approx 30\%$ of the design point flow rate with a frequency ≈ 0.1 rotational speed [37].

2.2.7 Axial Thrust

The axial force in a centrifugal impeller acts parallel to the rotation axis. One major factor determining the axial thrust is the impeller shroud configuration. In the past decades several methods have been used to reduce this force in industrial pumps, such as secondary vanes and balance holes, and these have recently also been used in blood pumps to reduce the axial thrust and the subsequent secondary flow and thrombus between the impeller and volute [137].

Static Axial Thrust

The static axial thrust in a centrifugal impeller is due to the pressure difference between the top and bottom of the impeller [128]. This pressure is higher at the

circumference and diminished towards the center of the impeller [69]. In shrouded impellers, the forces resulting from pressure on the hub and shroud act in opposite directions resulting in a relatively low axial thrust. In semi-open impellers, the pressure at the hub is only partly countered by the pressure on the shroud leading to a relatively higher axial thrust in these impellers [128, 69, 61].

Magnitude

Several methods have been proposed for the prediction of axial force magnitude.

- Lazarkiewicz method for shrouded impellers

In this method [69], the axial thrust is divided into pressure distribution and momentum components and is given by:

$$T_1 = \gamma(A_{wr} - A_{sh}) \left[H_2 - \frac{1}{8} \left(\frac{u_2^2}{g} - \frac{u_{wr}^2 + u_{sh}^2}{2g} \right) \right] \quad (2.55)$$

$$T_2 = \frac{\gamma}{g} Q C_O \quad (2.56)$$

$$T_a = T_1 - T_2 \quad (2.57)$$

T_a	Axial thrust
A_{wr}	Impeller inner diameter/Wear ring area
A_{sh}	Shaft area
u_2	Outlet peripheral velocity
u_{wr}	Inlet peripheral velocity
u_{sh}	Shaft peripheral velocity
γ	Specific gravity
H_p	Outlet pressure
C_O	Inlet velocity

- Stepanoff method for shrouded impeller

In this method [128], the pressure difference between the two sides is used in the form

$$T = (A_1 - A_s)(P_1 - P_s) \quad (2.58)$$

T	Axial thrust (lbs)
A_1	Inlet area (in^2)
A_s	Shaft area (in^2)
P_1	Inlet pressure (Psi)
P_s	Suction pressure (Psi)

- Stepanoff method for semi-open impellers

In this method [128], the relative difference in pressure distribution acting on the bottom (T_b) and top (T_{bi}) of the impeller is used.

$$T_b = (A_2 - A_s) \left[H_v - \frac{1}{8} \left(\frac{u_2^2 - u_s^2}{2g} \right) \right] \gamma \quad (2.59)$$

$$T_{bi} = (A_2 - A_1) \frac{H_v}{2} \gamma \quad (2.60)$$

H_v	Outlet pressure
A_s	Shaft area
A_2	Outlet area
A_1	Inlet area
u_2	Outlet peripheral velocity
u_s	Shaft peripheral velocity

- Lobanoff method for shrouded impellers

Lobanoff [76] proposed an equation for the axial thrust based on the forces generated from the suction inlet pressure acting on the shaft area (T_A) and due to the pressure at the impeller bottom on the equivalent inlet diameter minus the shaft area.

$$T_A = P_s \cdot A_s \quad (2.61)$$

$$T_B = \frac{3}{4} P_D (A_1 - A_s) \quad (2.62)$$

$$T = T_A - T_B \quad (2.63)$$

T	Axial thrust
A_1	Inlet area
A_s	Shaft area
P_D	Outlet pressure
P_s	Suction pressure

- Lobanoff method for semi-open impellers

The thrust is calculated similar to shrouded impellers and the top thrust has another added term:

$$T_A = P_s \cdot A_s + \left[(A_3 - A_E) \frac{P_D}{2} \right] \quad (2.64)$$

$$T_B = \frac{3}{4} P_D (A_3 - A_s) \quad (2.65)$$

$$T = T_A - T_B \quad (2.66)$$

T	Axial thrust
A_1	Inlet area

A_s	Shaft area
A_3	Outlet area
A_s	Inlet area without the shroud
P_D	Outlet pressure
P_s	Suction pressure

- ANSI-HI method for shrouded impellers

This method [30] is the most recent method and gives the axial thrust as:

$$F_T = \Delta p \times [(K_{Avb}A_B) - (K_{Avf}A_F)] - p_s A_h \quad (2.67)$$

F_T	Net axial thrust (Pounds)
Δp	Pressure rise (psi)
K_{Avb}	Avg % developed pressure on the hub (0.675)
A_B	Area exposed to bottom pressure (in^2)
K_{Avf}	Avg % developed pressure on the shroud (0.68)
A_F	Shroud area (in^2)
A_h	Shaft area (in^2)
p_s	Suction pressure (psi)

Direction

There are three components contributing to the direction of static axial thrust; pressure distributions on the top and bottom of the impeller, and the fluid momentum due to the change of direction of the fluid induced by the pump.

Dynamic Axial Thrust

The dynamic thrust in the axial direction is due to periodic changes in flow rate and causes periodic stress to the shaft and bearing. In centrifugal impellers, small changes in flow rate may not produce a significant dynamic axial thrust due to the relatively small momentum compared to industrial pumps [61].

2.2.8 Experimental Force Measurement Techniques

This section describes the experimental techniques employed by different research groups to measure and analyse the forces on a centrifugal impeller.

Pressure Tapping

This method uses pressure tapings on the circumference of the impeller to measure

the pressure around it, integrate the measured pressure profile and calculate the magnitude and direction of the radial force between the impeller and volute sides. The major issue with this method is the low accuracy caused by the fact that the pressure is only measured at two dimensions [58, 51]. In a previous study [37], this issue was resolved by using Pitot tubes inside the volute to measure the static pressure.

Strain Gauge

The most common method is to use strain gauges on the bearings to measure and calculate the force from the impeller [128, 144, 37, 51, 2, 58]. However, despite established practical success, the method is unable to show static and dynamic forces individually and only presents the total force [51].

Strain gauges are also used to measure the radial forces by being placed on the impeller shaft in a similar fashion to the pressure tapping method [37, 51]. One type of strain gauges are called load cells and are used for force analysis of magnetic bearings by measuring the power requirements of the bearing [58, 17].

Proximity Sensors

Proximity sensors may be installed on the shaft to measure the shaft deflection due to the force acting on it. Despite its simplicity, this method has a lower accuracy compared to the other methods. [51].

2.3 Axial Pump Definitions and Terminology

2.3.1 Vane Cascades

In order to study the flow behaviour in an axial impeller, it is convenient to investigate the blades in three sections: Hub, tip and the mean effective diameter. For axial flow pumps, the mean effective diameter is derived by Equation 2.68.

$$D_m^2 = D_2^2(1 + \nu^2)/2 \quad (2.68)$$

Where D_1 and D_2 are the hub and tip diameters and ν is the hub ratio and is given by Equation 2.69.

$$\nu = D_1/D_2 \quad (2.69)$$

The blades are equally spaced around the hub with the distance t .

$$t = \pi D/Z \quad (2.70)$$

Where t is the pitch, Z number of blades and D is the diameter.

The ratio of the vane cord, l , to the pitch, t , is another important parameter, which defines the solidity of the blades. This ratio (l/t) relates the blade area to the surface perpendicular to the flow. It normally decreases from hub to tip. The blade angle gradually increases from β_1 to β_2 and the difference between the two ($\beta_2 - \beta_1$) represents the blade curvature at each sections, as shown in Figure 2.36.

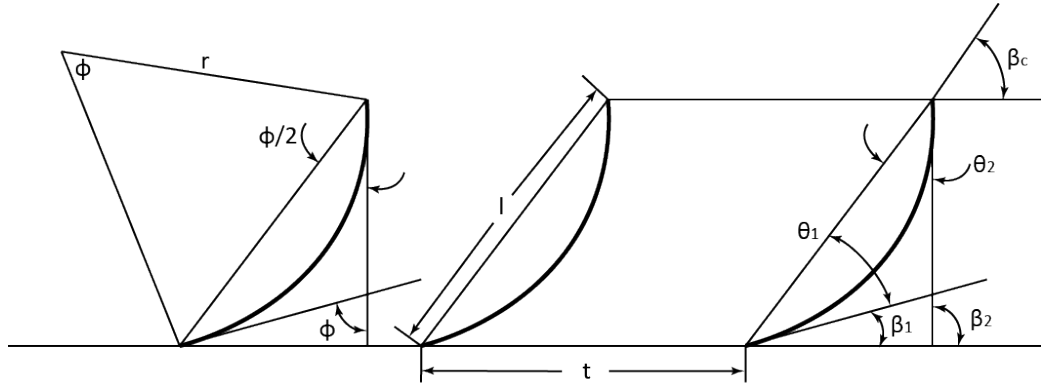


Figure 2.36: Axial blade Cascade.

Based on Figure 2.36, the following equations are derived:

- Blade Curvature

$$\phi = \beta_2 - \beta_1 = \theta_1 + \theta_2 \quad (2.71)$$

- Chord Angle

$$\begin{aligned} \beta_c &= \beta_1 + \theta_1 \\ \beta_c &= \beta_2 - \theta_2 \end{aligned} \quad (2.72)$$

- Circular Arc Blade

$$\begin{aligned}\theta_1 = \theta_2 = \theta &= \phi/2 \\ \beta_2 - \beta_1 = \phi &= \text{central angle} \\ l &= 2r \sin \theta\end{aligned}\tag{2.73}$$

2.3.2 Airfoils

Due to the lower pressure rise produced by axial pumps compared to that of centrifugal pumps, the skin friction loss is significantly important in the design of axial impellers. Therefore, a high precision in streamlining and polishing on the blade is needed to achieve high efficiencies. This has led to the development of airfoil shaped blades for axial flow pumps. The mean line of an airfoil determines the important hydraulic properties of the blade and the thickness is derived based on the strength requirements. Fine airfoil models normally have the same thickness variation along the mean line and the maximum value is different based on their profile [128]. The maximum distance between the chord and the mean line is expressed in percent of the chord length, c/l and is called camber, shown in Figure 2.37.

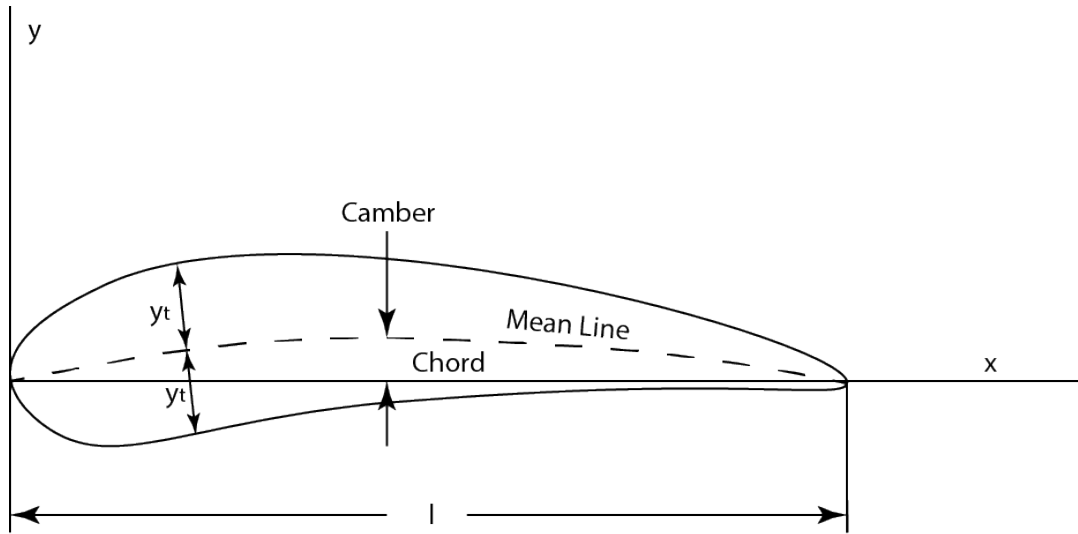


Figure 2.37: Airfoil parameters.

In 1933, the N.A.C.A report 460 presented airfoils with their geometry and classified them based on their curvature and thickness. Each profile is presented with four digits. The first digit represents the camber and the second one shows the distance of the camber point from the blade leading edge. The last two digits represent the percent of the blade thickness. The angle of attack, α , is the angle between the chord and the relative velocity of the flow.

2.3.3 Lift and Drag

The forces acting on an airfoil exposed to airflow can be resolved into two components: lift (L) is the component perpendicular to the air flow and drag (D) is the component in the flow direction. The magnitudes of the components are derived by:

$$L = C_L lb \left(\frac{1}{2} \rho v^2 \right) \quad (2.74)$$

and

$$D = C_D lb \left(\frac{1}{2} \rho v^2 \right) \quad (2.75)$$

C_L Lift coefficient

C_D Drag coefficient

l Chord length

b Airfoil width

v Relative air velocity

ρ Density

C_L and C_D are experimental coefficients at the desired angle of attack, Mach number and Reynolds number and depend on the profile of the airfoil. The experimental values of C_L and C_D have been established for a wide range of airfoils. The ratio of the two (C_D/C_L), defines γ which is the gliding angle and represents the condition that a plane can operate in gliding flight mode.

Two main contributing factors affect the magnitude of the drag force: the skin friction and eddy losses. The skin friction depends on the smoothness of the airfoil surface and the eddy losses are due to the eddies formed in the wake behind the blade and may be reduced by a more rounded leading edge and a sharper trailing edge [128].

2.3.4 Airfoil Profiles and Munk Method

The mean camber lines of the N.A.C.A 4-digit airfoil profiles may be defined by two tangents at the leading and the trailing edges, shown in Figure 2.38. This is due to the parabolic curves comprising the mean camber lines of this group of airfoils [128]. The tangent lines can be derived from the angles θ_1 and θ_2 shown in Figure 2.38. The vane can be divided into several sections and the tangents at each section can help to find the corresponding points. The intersection of the two tangents shows the maximum camber station.

Based on Figure 2.38, the vane curvature ($\beta_2 - \beta_1$) can be expressed by the the camber:

$$\tan \theta_1 = \frac{2ED}{AE} = \frac{2c}{l_c} \quad (2.76)$$

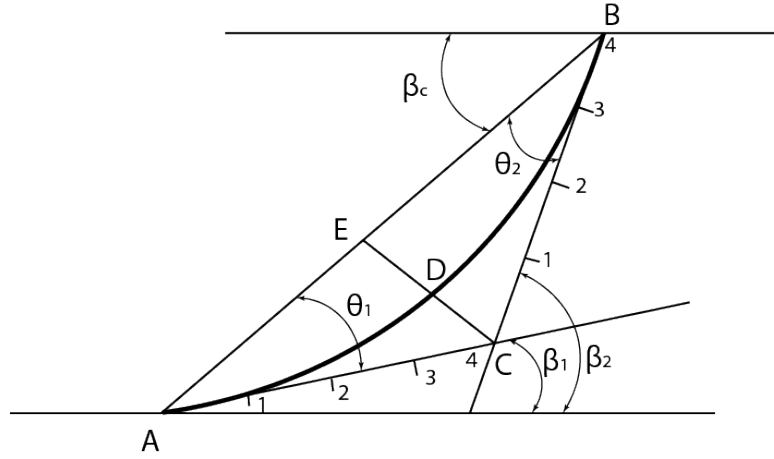


Figure 2.38: Airfoil characteristics in terms of curvature $\beta_2 - \beta_1 = \theta_2 + \theta_1$ [128].

$$\tan \theta_2 = \frac{2ED}{EB} = \frac{2c}{(l - l_c)} \quad (2.77)$$

where c is the camber and l_c is its location relative to the leading edge, expressed as fractions of the airfoil chord length [128]. The values of θ_1 and θ_2 are relatively small and therefore are assumed equal to their tangents.

$$\beta_2 - \beta_1 = \frac{2c}{l_c} + \frac{2c}{l - l_c} = \frac{2cl}{l_c(l - l_c)} \quad (2.78)$$

Therefore, the vane curvature establishes the hydrodynamic properties of the airfoil in N.A.C.A family. The N.A.C.A 65 airfoil profile was selected as the base profile for this study and the parameter selection process is discussed in the following sections.

2.3.5 Design Parameters

This section provides information about the design parameters and their selection.

Hub Ratio

The hub to tip diameter ratio is linked to the specific speed of the pumps and is usually based on experimental results. The nature of axial pumps and the relatively high specific speed of them dictates a smaller hub diameter, which leads to a greater flow area and greater flow rate and therefore a lower pressure rise. In this thesis, the outer diameter of 22 mm is the design constraint due to the aorta average diameter, which is 24 mm. Three values of 3.3, 5 and 10 mm were selected as the hub diameter with ratios of 0.15, 0.23 and 0.45 respectively, and the initial numerical simulations showed a relatively low pressure rise for the impeller with 0.15 hub ratio. The impeller required higher rotational speeds in order to produce the design point pressure rise. The impeller with 0.45 hub ratio had difficulty producing the required

flow rate at low stagger angles. The value of 5 mm was selected for the hub diameter in this thesis.

Chord Spacing Ratio

This is the ratio of chord length to the pitch and is normally selected based on experience. The ratio (l/t) is different at each section of the vane and at the hub is normally 1.25 to 1.3 times that of the tip [128]. The ratio is usually <1 for manufacturing reasons.

Number of Blades

The maximum number of blades is normally fixed since adding more blades restricts the flow area. By adding more blades, the flow rate decreases and leads to a slight drop in efficiency. On the other hand, the ideal flow guidance may be achieved by increasing the number of blades, so the flow leaves the impeller outlet at the exact blade angle. However, beyond a particular value, the slip factor decreases due to increased blockage area. 2, 4 and 6 blades are used as input parameters in order to study the effect of blade number and investigate this trade-off and its relationship to the pump performance.

Blade Curvature

Three impellers with different inlet and outlet angles but the same curvature ($\beta_2 - \beta_1$) were analysed. The results showed almost the same pressure rise produced for all models, meaning the performance is a function of the curvature rather than the inlet and outlet angles. Although the tangential component of the velocity, c_{u2} is higher at higher angles, however, c_{u1} is also higher by the same difference.

Blade Thickness

The thickness of the blade at each section depends on the chord in order to satisfy the parameter solidity. Excessive thickness results in separation and high noise levels. The advantage of the airfoil sections is in the fact that they permit the desired mechanical strength with a minimum sacrifice of efficiency [128]. The N.A.C.A report 460 states that the thickness form is of particular importance from a structural standpoint. On the other hand, the form of the mean line determines almost independently some of the most important aerodynamic properties of the airfoil section.

The thickness to chord ratio of the impellers are selected to be 0.15 at each section.

The Velocity Triangles

The velocity triangles are similar to that of centrifugal impellers and are used to establish the inlet and outlet velocity parameters. Figure 2.39 shows the inlet and outlet triangles followed by the equations to calculate the velocity and blade angles.

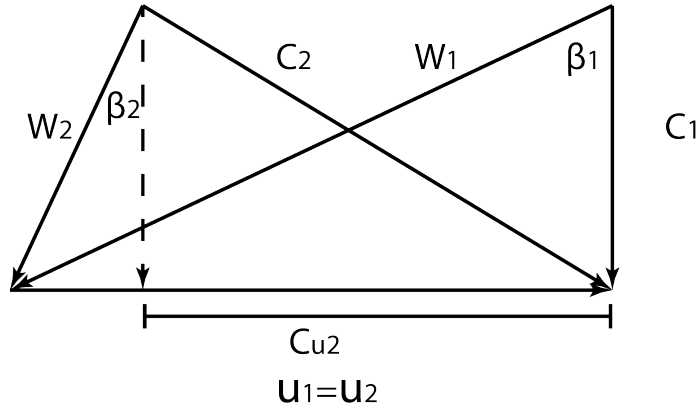


Figure 2.39: The velocity triangles at inlet and outlet.

$$C_1 = \frac{Q}{A} \quad (2.79)$$

where Q is the flow rate and A is the area.

$$u = u_1 = u_2 = r \cdot \omega \quad (2.80)$$

where ω is the rotational speed and r is the radius at each section.

$$\beta_1 = \arctan \frac{u}{C_1} \quad (2.81)$$

$$C_2 = \sqrt{C_1^2 + C_{u2}^2} \quad (2.82)$$

$$W_2 = \sqrt{C_1^2 + (u - C_{u2})^2} \quad (2.83)$$

$$\beta_2 = \arctan \frac{u - C_{u2}}{C_1} \quad (2.84)$$

Blade Profile

The blade profile was created using the base profile of N.A.C.A 65-series implemented into MATLAB. The airfoil section is created from the camber line and the

thickness distribution on the upper and lower curves. The camber line equation is defined by:

$$\begin{aligned} y_c &= \frac{M}{P^2}(2Px - x^2) & 0 \leq x < p \\ y_c &= \frac{M}{(1-P)^2}(1-2P+2Px-x^2) & p \leq x < 1 \end{aligned} \quad (2.85)$$

where M and P are the first two digits of the airfoil code and are the maximum camber in percent and its position respectively. The gradient of the camber is therefore given by:

$$\begin{aligned} \frac{dy_c}{dx} &= \frac{2M}{P^2}(P-x) & 0 \leq x < p \\ \frac{dy_c}{dx} &= \frac{2M}{(1-P)^2}(P-x) & p \leq x < 1 \end{aligned} \quad (2.86)$$

The thickness equation is given by

$$y_t = \frac{T}{0.2}(a_0x^{0.5} + a_1x + a_2x^2 + a_3x^3 + a_4x^4) \quad (2.87)$$

where

a_0 :0.2969

a_1 :-0.126

a_2 :-0.3516

a_3 :0.2843

a_4 :-0.1015 or -0.1036 for a closed trailing edge.

The constants are presented for a 20% thick airfoil. At the trailing edge, there is a finite thickness of 0.21% of chord width. By using Equation 2.87, the camber line position can be derived. It should be noted that the value of y_t is the half thickness and needs to be applied to both sides of the camber line. The position of the upper and lower curves of the airfoil are then calculated as:

$$\begin{aligned} x_u &= x_c - y_t \sin \theta \\ y_u &= y_c + y_t \cos \theta \end{aligned} \quad (2.88)$$

$$\begin{aligned} x_l &= x_c + y_t \sin \theta \\ y_l &= y_c - y_t \cos \theta \end{aligned} \quad (2.89)$$

where

$$\theta = \arctan\left(\frac{dy_c}{dx}\right) \quad (2.90)$$

The equations are implemented into MATLAB to generate the coordinates of three airfoil sections for the numerical investigations.

Chapter 3

Numerical Methods

Theoretical and numerical techniques are used to design more than 150 axial and centrifugal pumps with various design characteristics. This chapter demonstrates the numerical investigations by presenting the preliminary design of the impellers, optimization process and the simulation assumptions followed by justifications. The chapter particularly investigates the effect of various design parameters such as blade outlet angle, number of blades and rotational speed on the performance, hemocompatibility and force analysis of the designed pumps. Based on the results of numerical simulations, pumps are selected to be manufactured and tested in different operating conditions of flow, pressure and rotational speed.

The nondimensional values of specific speeds (n_s), specific diameters (d_s), head coefficients (ψ) and flow coefficients (ϕ) are calculated for all pumps and the data points of specific speeds and diameters are plotted on Cordier diagrams.

The nondimensional and hemocompatibility results presented in this chapter, enable preliminary design of centrifugal and axial pumps suitable for MCS devices.

3.1 In-silico Investigations of Centrifugal Pumps as MCS Devices

In-silico investigations of this study includes the preliminary 1D design of the impellers in Vista CPD, followed by the 3D modification in BladeGen. The numerical simulation process is then explained with the optimisation of design parameters. The 3D geometry of the impellers are then exported in CAD softwares for the next stage.

3.1.1 Vista CPD

Vista CPD is a program that employs a 1D approach for the preliminary design of centrifugal pumps. The program is a component of ANSYS Workbench and is able to generate an optimised initial impeller design and export it into other components of the Workbench. The initial input parameters of the pumps are selected in Vista CPD and optimised in the next stage, BladeGen. The velocity-based parameters are calculated using the velocity diagrams. The design point pressure rise, flow rate, density and viscosity of the working fluid are selected as the design constraints, however, the flow rate and pressure rise are investigated in wider ranges in the following stages.

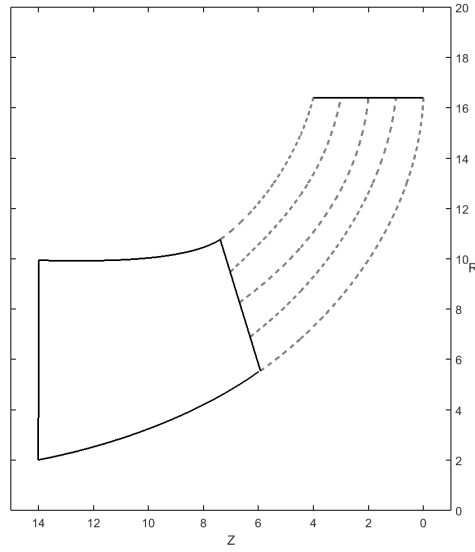
The rotational speed is changed manually to obtain the outlet width in the range of 4-8 mm with 0.2 increments. The outlet angle and the number of blades are selected in the range of 10° - 45° and 3-9 respectively in the optimisation process. With all the parameters known, the profile is generated based on the cubic Bezier curves. Five equally spaced spans including the hub and shroud are generated, shown in Figure 3.1.

A representative impeller is selected for presentation. Figure 3.2 shows the $\theta - m'$ curves for the blade from the leading to the trailing edge and Table 3.1 shows the design parameters of the representative impeller.

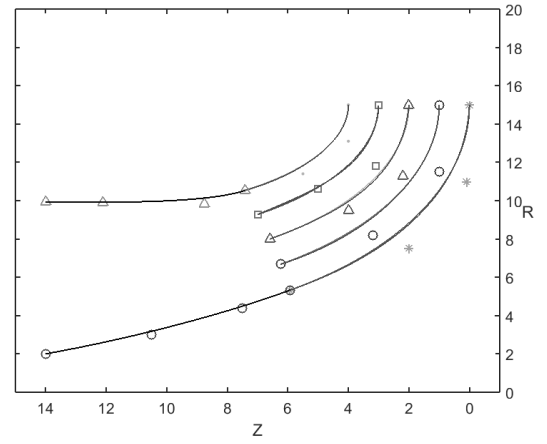
3.1.2 BladeModeler / BladeGen

BladeGen is a component of ANSYS BladeModeler, a geometry creation tool designed for turbomachinery. The package is a link between blade geometry design and the advanced simulation of the pump and can import the model data from an existing CAD file and enable further modifications on the design. The impeller data are imported into BladeGen from Vista CPD.

The blade design cell of BladeGen has properties that must be configured based on



(a) The meridional profile of an impeller obtained by cubic Bezier curves.



(b) The meridional profile with Bezier curves control points.

Figure 3.1: Blade meridional profile.

Table 3.1: Design parameters of a representative impeller.

Parameter	Symbol	Unit	Value	Parameter	Symbol	Value
Flow rate	Q	L/min	4.98	Inlet blade angle, S_1 (hub)	β_{1S_1}	76.71°
Pressure rise	ΔP	$mmHg$	69.97	Inlet blade angle, S_2	β_{1S_2}	73.52°
Inlet diameter	D_1	mm	18.80	Inlet blade angle, S_3	β_{1S_3}	70.50°
Outlet diameter	D_2	mm	30.0	Inlet blade angle, S_4	β_{1S_4}	67.66°
Inlet Area	A_1	mm^2	269	Inlet blade angle, S_5 (shroud)	β_{1S_5}	65.00°
Outlet Area	A_2	mm^2	377	Outlet blade angle	β_2	34.99°
Inlet Width	b_1	mm	5.41	Number of Blades	Z	5
Outlet Width	b_2	mm	4.0	Specific Speed	n_s	0.5478
Rotational Speed	ω	rpm	3060	Specific Diameter	d_s	5.7440

the design and application constraints. The important cell properties of this study are discussed here.

Hub

A Hub profile needs to be sketched for the non-flow path hub geometry and be revolved to create a body feature.

Blade Topology

The blades are either created with four faces including the leading and trailing edges and pressure and suction sides or by merging where they are tangent to one another.

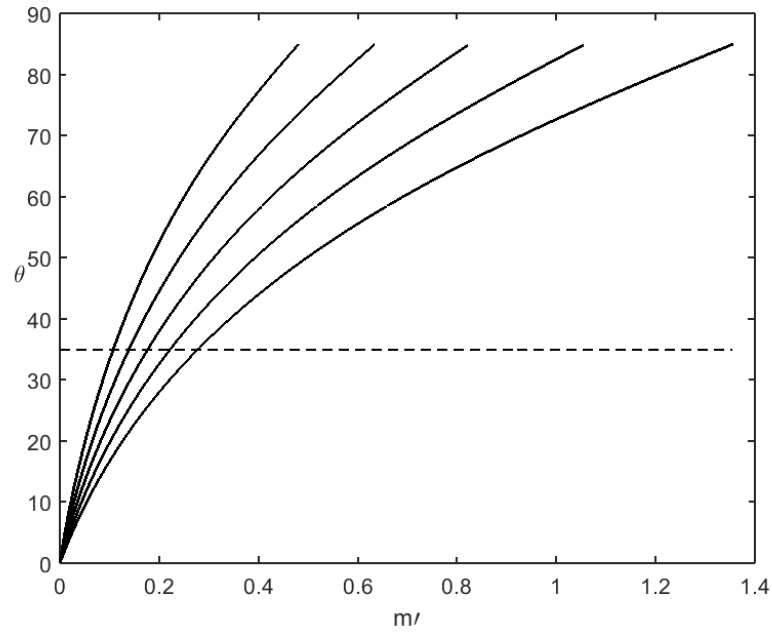


Figure 3.2: $\theta - m'$ curves from the leading to the trailing edge.

Blade Loft

The blade surfaces could be lofted streamwise (through curves that run from hub to shroud) or spanwise (through the blade profile curves).

Fluid Zone

A StageFluidZone body will be defined for the flow passage and the blade body is subtracted using an enclosure feature.

Blade and Periodic Surface Extension

Blades and periodic surfaces will be extended to ensure that the blade solid correctly matches the hub and shroud contours and the StageFluidZone is properly cut.

BladeGen provides an easy tool to the designer to change the control points of the Bezier curves manually and see the immediate change in the blade shape in a user friendly interface, as shown in Figure 3.4.

3.1.3 TurboGrid

ANSYS TurboGrid is a meshing tool for CFD analysis of turbomachines. The model is imported from BladeGen into TurboGrid for the mesh generation. The solution should be mesh independent, meaning it should not change by changing the mesh resolution. The method is to refine the mesh and run the initial simulation until the

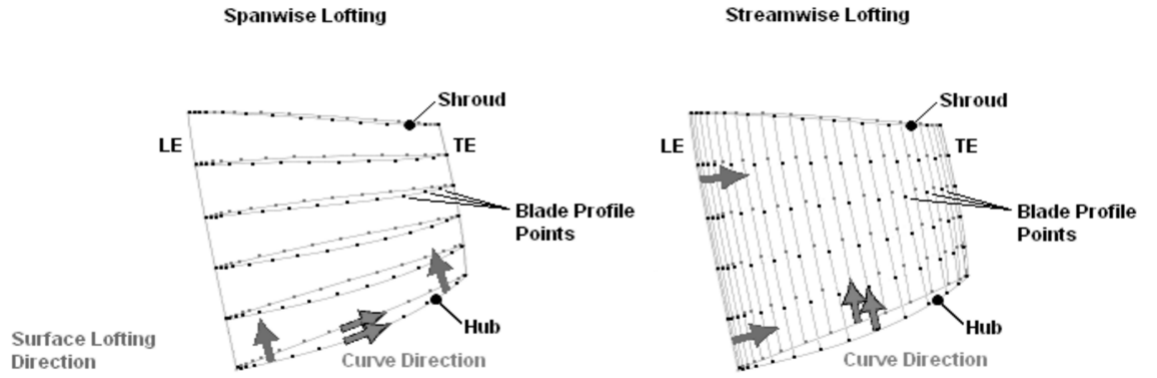
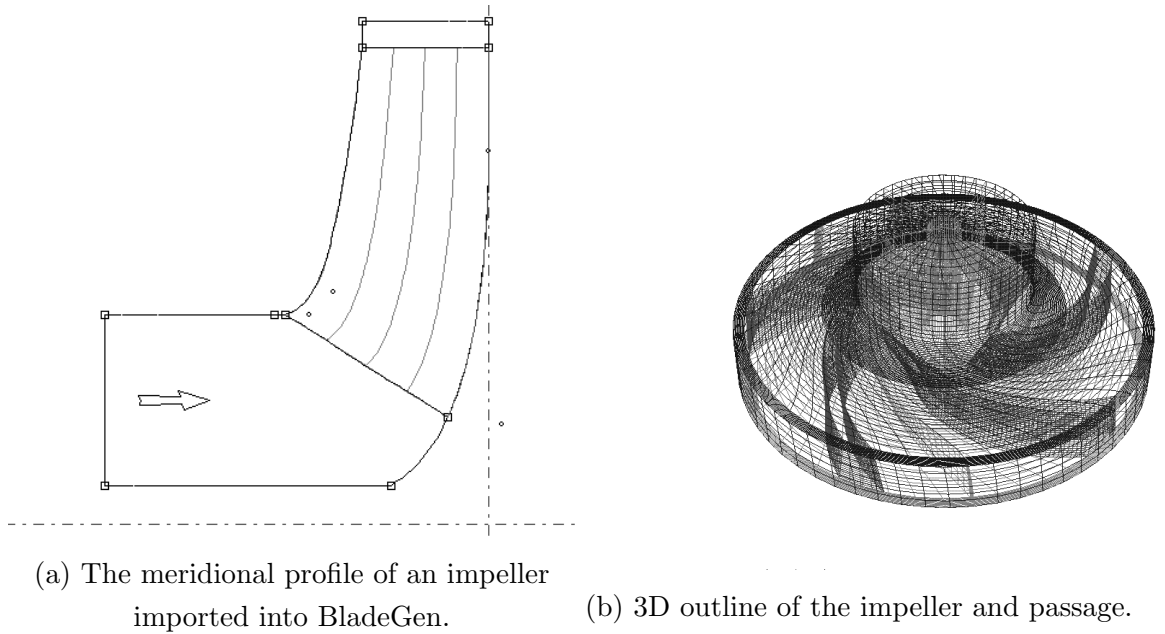


Figure 3.3: Spanwise and streamwise lofting of the blade.



(a) The meridional profile of an impeller imported into BladeGen.

(b) 3D outline of the impeller and passage.

Figure 3.4: The impeller in ANSYS BladeGen.

residual falls below 10^{-4} , imbalances are below 1% and monitor points are steady. The mesh is then refined globally and the monitor points values are compared to the previous step. If the values are not within an acceptable tolerance to the previous values, the mesh needs to be refined.

There are four methods to change the mesh density; changing the total passage mesh size, changing the global size factor, using proportional refinement in the boundary layer and changing the edge refinement on a specific edge including within the boundary layer.

The Mesh Independence Study

In this study, the default mesh quality (original mesh) was first used to solve the problem. The mesh parameters were then multiplied by 0.8 and 1.25 to generate fine and coarse mesh respectively in a similar fashion to a study conducted by Fraser et. al. [39]. Pressure rise was selected as the output value for comparison at this point. The pressure rise in original mesh was considered as the reference and the pressure rise for the original mesh and the coarse mesh were compared to this value. The differences were found to be negligible. The small percentage difference in the results between the original and fine mesh validated the use of original mesh for all models and confirmed the mesh independence. Table 3.2 shows the output values of three mesh sizes for the impeller and Figure 3.5 shows the meshed impeller passage and volute in TurboGrid.

Table 3.2: Results of mesh independence.

Mesh Quality	Number of Elements	Number of Nodes	Pressure rise (mmHg)	Percent Difference
$\times 0.8$	66240	75582	70.21	1.7%
Original	160625	176930	71.44	-
$\times 1.25$	387362	416395	69.89	2.1%

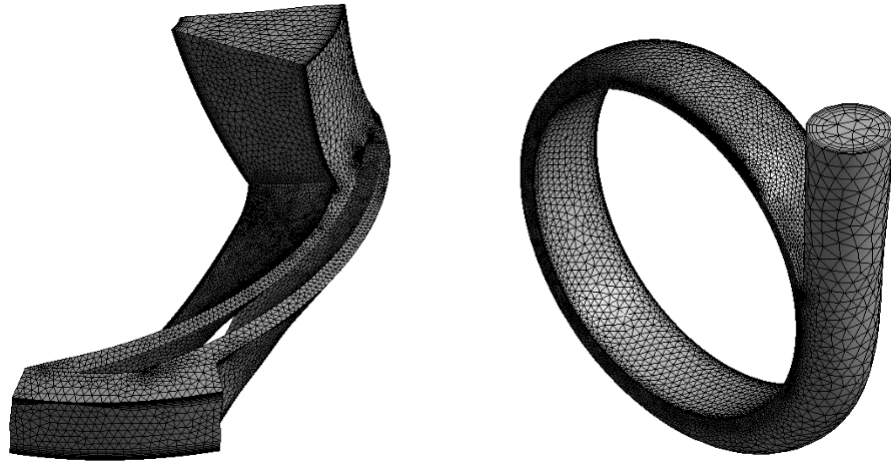


Figure 3.5: The impeller passage and volute in TurboGrid.

3.1.4 ANSYS CFX

ANSYS CFX was used as the advanced solver to achieve the reliable and accurate solution. The impeller and volute were imported separately into CFX and defined as the main domains, Figure 3.6.

The Impeller domain was subcategorized into four boundaries; Impeller blade, hub, inlet and shroud and the Volute domain was subcategorized into two; volute passage and outlet. An interface was defined where the fluid is delivered from the impeller outlet into the volute.

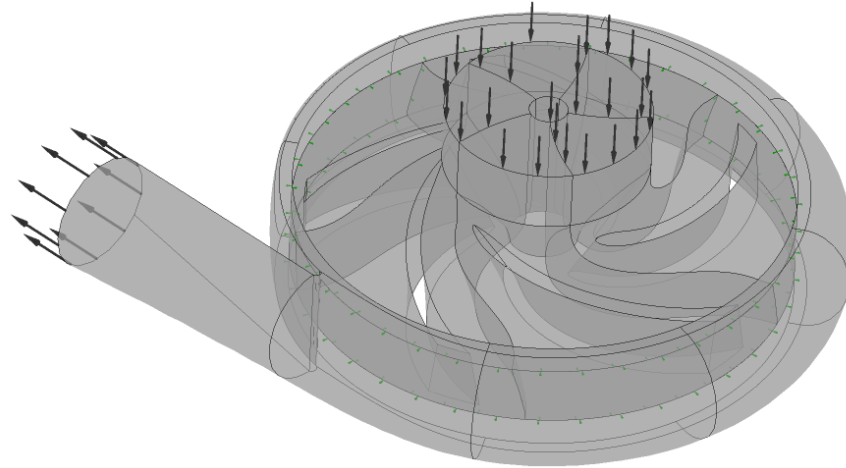


Figure 3.6: The impeller and volute domains in ANSYS CFX, The arrows indicate the inlet and outlet of the domains.

The incompressible Navier Stokes equations were used to predict and calculate the flow fields in the pumps. The model has one rotating domain and it is defined by creating the fluid volume around the rotor surface. The rotational motion of the impeller is calculated using Multiple Reference Frame (MRF). In this approach, the flow is assumed steady state, the grid remains fixed and the relative velocity is calculated throughout the domain.

MRF Model

The MRF model is the simpler of the two approaches (Sliding mesh approach and MRF approach) for multiple zones. Studies [138, 11] have reported better accuracy of computing time tradeoff and measured radial and axial velocities using frozen rotor interface model in impeller-volute assembly. It is a steady-state approximation where each cell zone can have different rotational speeds independently. The flow in each zone is solved using the equations of a moving reference frame. A local reference frame transformation is performed at the impeller-volute interface to enable flow variables in one zone to be used to calculate fluxes at the boundary of the adjacent zone.

The MRF model is useful for turbomachinery where rotor-stator interactions are weak and the flow between the two zones is not complicated.

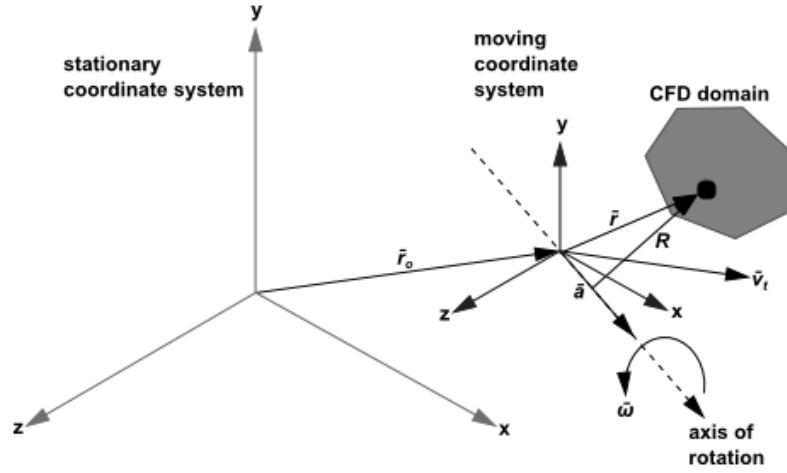


Figure 3.7: Stationary and moving coordinate systems in MRF method.

Equations

A moving coordinate system with a linear velocity of \vec{v}_t and angular velocity of $\vec{\omega}$ relative to a stationary frame is shown in Figure 3.7.

As Figure 3.7 shows, the origin of the moving coordinate system is shown by a vector, \vec{r}_0 .

The axis of rotation is shown in the figure and the unit direction is \vec{a} , therefore

$$\vec{\omega} = \omega \vec{a} \quad (3.1)$$

The fluid velocities from the volute zone to the impeller zone using the following relation

$$\vec{v}_r = \vec{v} - \vec{u}_r \quad (3.2)$$

where

$$\vec{u}_r = \vec{v}_t + \vec{\omega} \times \vec{r} \quad (3.3)$$

\vec{v}_r Relative velocity

\vec{v} Absolute velocity

\vec{u}_r Velocity of the moving frame relative to the stationary reference frame

\vec{v}_t Translation frame velocity

The equations can be formulated in two different modes; absolute or relative velocity formulations. The absolute velocity formulation is recommended for applications in which the flow in most of the domain is not moving (very large domains) and the relative velocity formulation is recommended where most of the fluid in the domain is moving. In this study the second method was used.

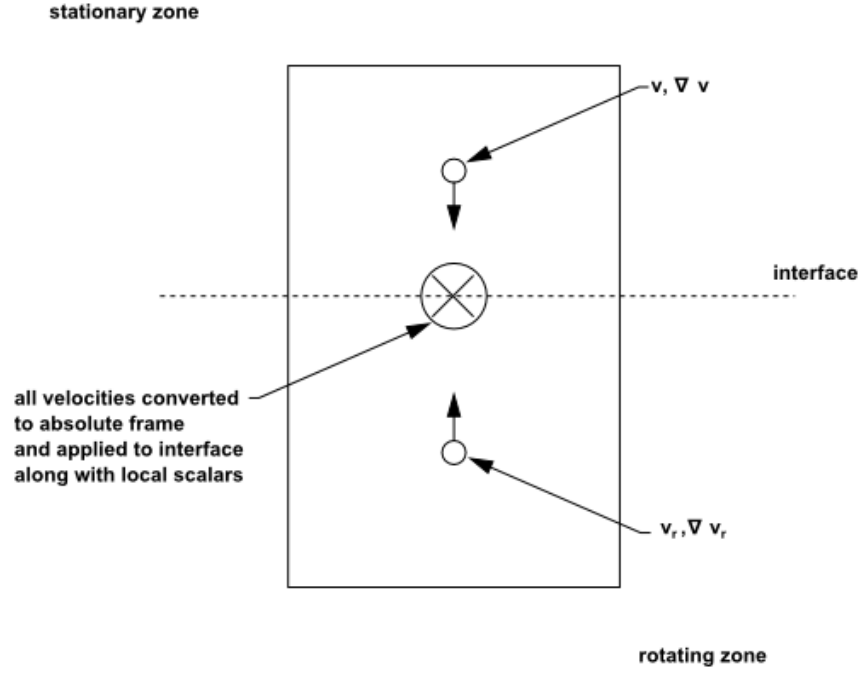


Figure 3.8: Interface treatment for the MRF model.

In this method, the velocities in each subdomain are calculated relative to the motion of that subdomain. The velocity and its gradients are converted from a moving reference frame to the absolute stationary frame using the equation

$$\vec{v} = \vec{v}_r + (\vec{\omega} \times \vec{r}) + \vec{v}_t \quad (3.4)$$

and the gradient is

$$\nabla \vec{v} = \nabla \vec{v}_r + \nabla (\vec{\omega} \times \vec{r}) \quad (3.5)$$

The conservation of mass is

$$\frac{\partial \rho}{\partial t} + \nabla \cdot \rho \vec{v}_r = 0 \quad (3.6)$$

and the conservation of momentum is

$$\frac{\partial}{\partial t} (\rho \vec{v}_r) + \nabla \cdot (\rho \vec{v}_r \vec{v}_r) + \rho (2\vec{\omega} \times \vec{v}_r + \vec{\omega} \times \vec{\omega} \times \vec{r} + \vec{\alpha} \times \vec{r} + \vec{a}) = -\nabla p + \nabla \cdot \vec{\tau}_r + \vec{F} \quad (3.7)$$

where $\vec{\alpha} = \frac{d\vec{\omega}}{dt}$ and $\vec{a} = \frac{d\vec{v}_t}{dt}$

and the conservation of energy is written as

$$\frac{\partial}{\partial t} (\rho E_r) + \nabla \cdot (\rho \vec{v}_r H_r) = \nabla \cdot (k \nabla T + \vec{\tau}_r) + S_h \quad (3.8)$$

The four additional terms in equation 3.7 are $2\vec{\omega} \times \vec{v}_r$, $\vec{\omega} \times \vec{\omega} \times \vec{r}$, $\vec{\alpha} \times \vec{r}$ and \vec{a} . The first two terms, $2\vec{\omega} \times \vec{v}_r$ and $\vec{\omega} \times \vec{\omega} \times \vec{r}$, are the Coriolis and the centripetal accelerations and $\vec{\alpha} \times \vec{r}$ and \vec{a} are due to the unsteady change of the rotational speed and the linear velocity. In this study, the third and fourth terms are zero due to the constant rotational speed and the moving coordinate system not having a linear velocity in the impeller zone.

The terms E_r and H_r used in equation 3.8 are the relative internal energy and the relative total enthalpy respectively and are defined as

$$E_r = h - \frac{p}{\rho} + \frac{1}{2}(v_r^2 - u_r^2) \quad (3.9)$$

$$H_r = E_r + \frac{p}{\rho} \quad (3.10)$$

The Limitations to MRF Model and the Solutions

Limitation- For a linearly moving frame, the zone's boundaries must be parallel to the linear velocity vector and for rotating frames, the interface must be the surface of revolution about the rotation axis defined for the fluid zone.

Solution- In this study the moving frame has only the rotational move (and not linear) and the interface is defined as the surface of revolution about the rotation axis.

Limitation- The MRF model is only for steady flow. However it could be used for unsteady flow by adding unsteady terms to the governing transport equations.

Solution- In this study, the pumps are simulated and tested in a steady flow.

Limitation- For particle trajectories, this model is only suitable for massless particles due to the streamlines based on relative velocity.

Solution- The streamlines were redefined and the particles were tracked based on absolute velocities.

Limitation- Translational and rotational velocities are constant.

Solution- The translational velocity is zero, the impeller zone has only rotational movement and the rotational speed is constant.

Limitation- Axisymmetric swirl cannot be modeled with MRF method.

Solution- The inlet flow angle has been assumed 90°, meaning the velocity triangles are used for a non-swirling inlet flow.

Limitation- There cannot be a single interface between the frames, where part of the interface is made of a coupled two-sided wall and the other is not coupled.

Solution- The interface between the impeller and volute zones is broken into two interfaces; one coupled interface and the other one is a standard fluid-fluid interface.

Boundary Conditions

Boundary conditions were specified to define the rotational speed, inlet pressure and outlet flow rate. It is common practice to set the opening static pressure at 120 mmHg to correspond to aortic pressure. However, in this study, a relative pressure of 0 Pa was defined at the inlet. Although it is not physically realistic, but in this case, the resulted outlet pressure will present the pressure rise of the pump. At the outlet, a healthy human body blood flow rate (5 L/min) was imposed.

Working Fluid

The rheology of the working has to be determined. Newtonian fluids have constant viscosity and the viscosity of non-Newtonian fluids vary with shear rate. Blood has complicated rheology and there are different methods to model it for numerical simulations. Although blood is a non-Newtonian fluid, for this study it was considered as an incompressible Newtonian fluid due to shear rates higher than 100/s in a centrifugal blood pump. In VADs shear rates are considered high enough to be in the shear independent viscosity region and the non-Newtonian properties of blood such as shear thinning and viscoelasticity are negligible [63, 38].

A density of 1050 kg/m^3 and viscosity of 0.0036 Pa.s were defined for the working fluid.

The Turbulence Model

The blood flow in human body is mostly laminar. However, under conditions of high flow, particularly in the ascending aorta, the Reynolds number exceeds the transition value and the flow becomes turbulent. A considerable body of literature exists on numerical investigation of VADs with different laminar and turbulent models. In a comprehensive study by Zhang et. al. [159], the laminar and five turbulence models (Spalart-Allmaras, $k - \epsilon$ [k-epsilon], $k - \omega$ [k-omega], SST [Menter's Shear Stress Transport], and Reynolds Stress) were implemented to predict blood flow in a clinically used circulatory assist device, the CentriMag centrifugal blood pump. A replica of the pump was also designed and prototyped and tested and the flow fields were measured with digital particle image velocimetry (DPIV). The experimental results were compared to the CFD results and showed the most deviation in the laminar model. The study concluded more accurate results with turbulent models compared to laminar, with $k - \epsilon$ and Reynolds Stress models as the most suitable models to predict the flow fields.

In this study the k-epsilon ($k - \epsilon$) turbulence model has been utilized. The model

uses the scalable wall-function approach to improve robustness and accuracy when the near-wall mesh is fine. In the $k - \epsilon$ turbulence model the mesh $y+$ value has to be greater than 30 and below 50. The average $y+$ value on the impeller wall was calculated for all models in ANSYS post processing in order to justify the use of $k - \epsilon$ model.

3.1.5 Response Surface Methodology

The response surface methodology is a collection of mathematical and statistical techniques to explore the relationship between several design, state and response variables. Generating a response surface is a powerful tool in ANSYS that can be used as a design optimization method. The main idea is to get as good response surface as possible with minimum input combinations. Each combination is solved by ANSYS and based on the results a response surface is created for each output parameter by fitting a curve through the design points. From this curve fit, the output results are predicted and investigated for input variable combinations that haven't been solved for.

The design variables are defined as

$$\begin{aligned} \vec{X} &= [x_1, x_2, x_3, \dots, x_n] \in D^n \\ x_{i,min} &\leq x_i \leq x_{i,max}, \quad i = 1, 2, 3, \dots, n \end{aligned} \quad (3.11)$$

Where n is the number of input parameters, D shows the design space and $x_{i,min}$ and $x_{i,max}$ are the lower and upper limits of the design variables. The state variables are defined to constrain the design and are shown as

$$g_{j,min} \leq g_j(\vec{X} \in D^n) \leq g_{j,max}, \quad j = 1, 2, 3, \dots, m \quad (3.12)$$

Where m is the number of state variables and $g_{j,min}$ and $g_{j,max}$ are the minimum and maximum values of each state variable. The objective function is expressed as

$$f_k(\vec{X} \in D^n), \quad k = 1, 2, 3, \dots, l \quad (3.13)$$

The best feasible solution for one single objective function is found by

$$\min[f_k(\vec{X} \in D^n)], \quad (3.14)$$

A region of optimum solutions R is defined for the function by

$$\min[f_k(\vec{X} \in D^n)] \leq f_k(\vec{X} \in D^n) \leq \min[f_k(\vec{X} \in D^n)] + \Delta f_k \quad (3.15)$$

Where Δf_k is a positive parameter defined to adjust the size of the optimum solution.

The Application

The design space was defined by selecting the input variables.

Design Space:

$$\vec{X} = [x_1, x_2, x_3] \quad (3.16)$$

$$\left. \begin{array}{l} x_{1,min} \leq x_1 \leq x_{1,max} \\ x_{2,min} \leq x_2 \leq x_{2,max} \\ x_{3,min} \leq x_3 \leq x_{3,max} \end{array} \right\} D^3 \implies \left. \begin{array}{l} 10 \leq \beta_2 \leq 45 \\ 3 \leq Z \leq 9 \\ 4 \leq b_2 \leq 8 \end{array} \right\} D^3$$

Figure 3.9 shows the design space represented numerically by points distributed based on the three ranges of the design variables. The state variables are flow rate (Q) and pressure rise (H) and the different combinations of the input parameters are solved in order to derive the efficiency as the output parameter. To determine the objective functions and state variables, separate finite element models are built for the analysis.

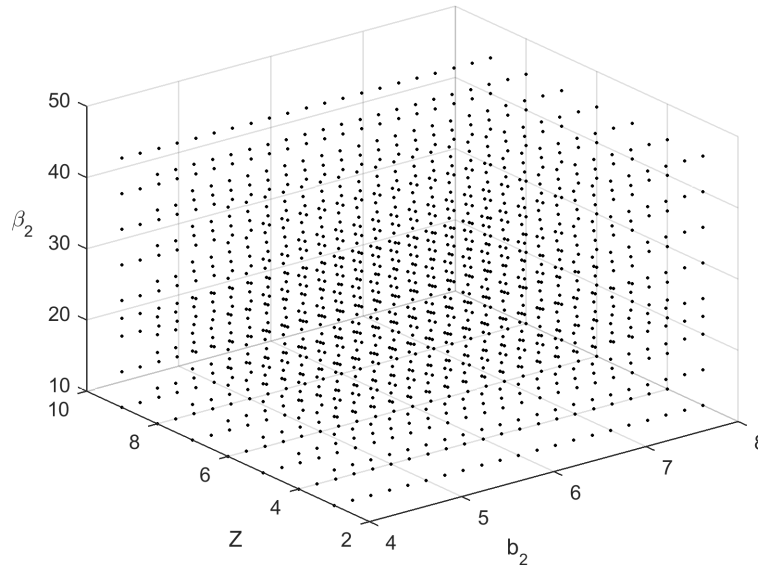


Figure 3.9: The scatters of design variables distributed in the three dimensional design space.

The values of objective functions and state variables are mapped to the scatters presented in Figure 3.9 and are investigated for optimum solutions. The response surfaces are presented in forms of two functions in this study:

$$\begin{aligned} \eta &= f_1(Z, \beta_2) \\ \eta &= f_2(Z, b_2) \end{aligned} \quad (3.17)$$

The optimization plots are plotted in separate graphs for the determination of the common optimum solutions and the design space is reduced in order to increase the accuracy of the common optimum solutions. Figures 3.10a and 3.10b show a sample of response surfaces created for the two applications.

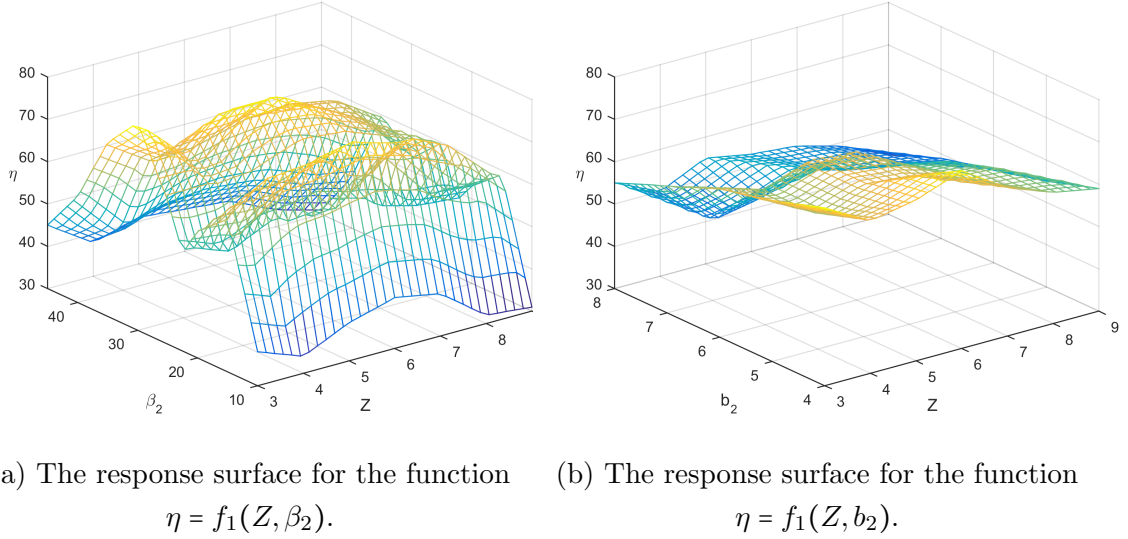


Figure 3.10: Response surface graphs for the design variable optimizations.

3.1.6 Results and Discussion

Numerical simulations have been carried out for extensive number of centrifugal impellers. The H-Q curves, efficiencies, force characteristics and the hemocompatibility of the pumps are studied and presented in the following sections. In each section, a group of impellers are presented for the results presentation based on their characteristics. In each group the impellers are selected to have similar geometric characteristics so that the effect of each parameter can be studied exclusively. The nondimensional approach of the study makes the results applicable to different performance characteristics and not just specific values. Q/Q_{des} and H/H_{des} show the ratio of volumetric flow rate and pressure rise to their values at the design point [66, 84].

Performance Curves

Figure 3.11 and 3.12 show the effect of blade number, Z , on the efficiency and head-flow characteristics (normalized) in a group of pumps. The effect of blade number on the performance depends on the viscosity of the working fluid. For lower viscosities, the number of blades has a larger impact on the performance than that of higher viscosity fluids. The kinematic viscosity of blood at normal body temperature (37°C)

is $2.65 \text{ mm}^2/\text{s}$ which is low compared with other fluids being pumped by centrifugal pumps.

Based on Figure 3.11, six, five, and three blades were the most efficient pumps, whereas nine and eight blades performed with the lowest efficiencies. The maximum difference between the highest and lowest (9 and 6 blades) efficiencies is $\approx 25\%$. The reason is the increased slip due to larger number of blades, and therefore accounts for one of the most important parameters for losses. Based on the theoretical and experimental equations for slip factor, the ideal flow guidance could be achieved by increasing the number of blades, so the flow leaves the impeller outlet at the exact blade angle. However, beyond a particular value, the slip factor decreases due to increased blockage area. According to the results, this particular optimum value is six. This value is considered a balance between the excessively high surface friction in pumps with too many blades and unguided diffusion in pumps with too few blades.

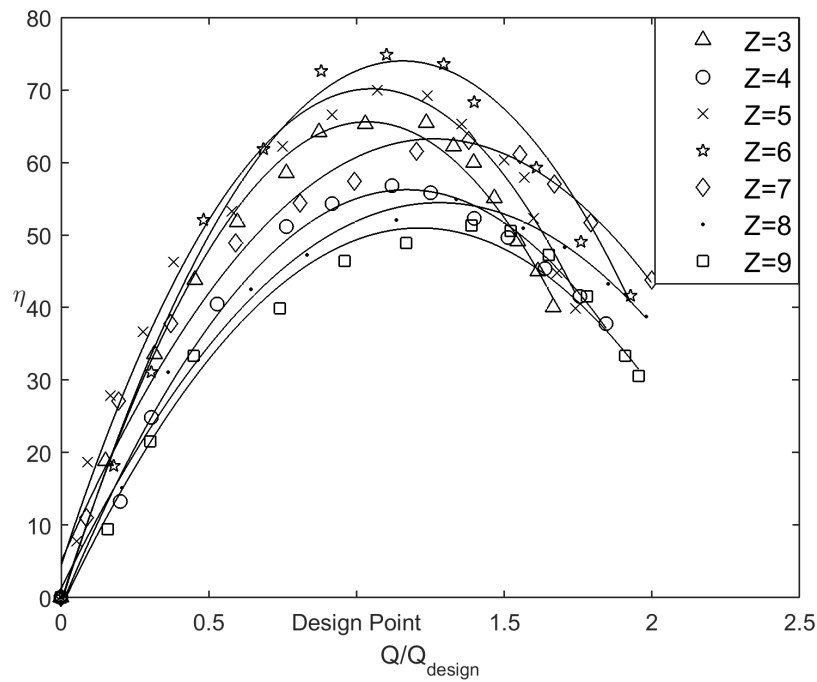


Figure 3.11: Efficiency vs. flow ratio for different blade numbers.

Figure 3.12 shows the effect of blade number on head ratio. Higher number of blades results in higher head ratio. The results show that impellers with five and six blades may meet the design point pressure rise at the flow rate of 5 L/min.

Figure 3.13 illustrates the effect of blade outlet angle on the head ratio. Higher outlet angle results in higher pressure ratio at the same rotational speed. This is due to the relationship between the total head and the peripheral velocity at the tip of the blade. The total head at any radius, which is equally divided between static and kinetic heads, is proportional to the square of peripheral velocity. By increasing

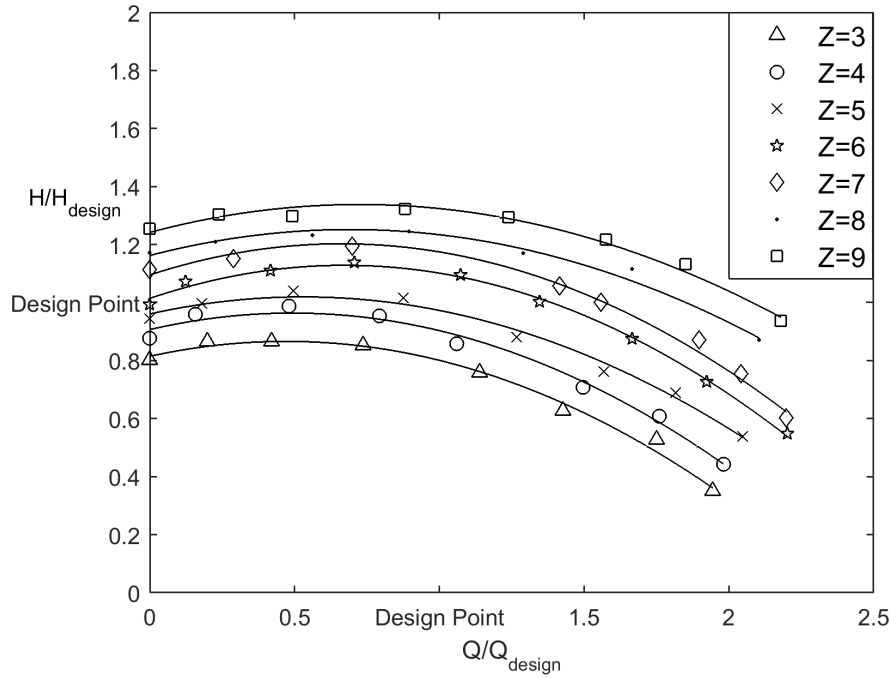


Figure 3.12: Head ratio vs. flow ratio for different blade numbers.

the outlet angle, the fluid leaves the impeller at a higher inclination and a higher velocity which results in higher pressure rise at the outlet. According to the test results, the difference is ≈ 30 mmHg between the minimum and maximum values which are obtained for 10° and 45° pumps, respectively. This effect is relatively smaller than that of change in number of blades.

Figure 3.14 illustrates the effect of blade outlet angle on the efficiency of the pumps. Based on Figures 3.13 and 3.14, angles 15° and 30° have the highest efficiencies but will result in different values of pressure rise. A 15° outlet angle results in the desired pressure rise at the design point. Based on the application and installation type of VADs and the desired pressure rise in the system, the relevant outlet angle could be selected by the designer.

Figures 3.15 and 3.16 show the effect of outlet width on the pump performance. An increase in outlet width results in a larger outlet area and higher flow rate. To keep this flow rate for comparison, there is need for higher resistance in the system which results in higher pressure rise. Therefore by increasing the outlet width and keeping the flow rate constant at the design point, the pressure increases and the efficiency decreases. This pattern is consistent for all impellers with no exceptions. The optimum value for the outlet width is the smallest value that meets the required pressure rise.

Figures 3.17 and 3.18 show the head-flow and efficiency curves of a representative impeller. In all cases, the highest efficiency was achieved at either 2400 or 2600 rpm with most cases at 2600 rpm (Figure 3.18). However, Figure 3.17 suggests a

rotational speed higher than 2800 rpm in order to meet the design point pressure rise.

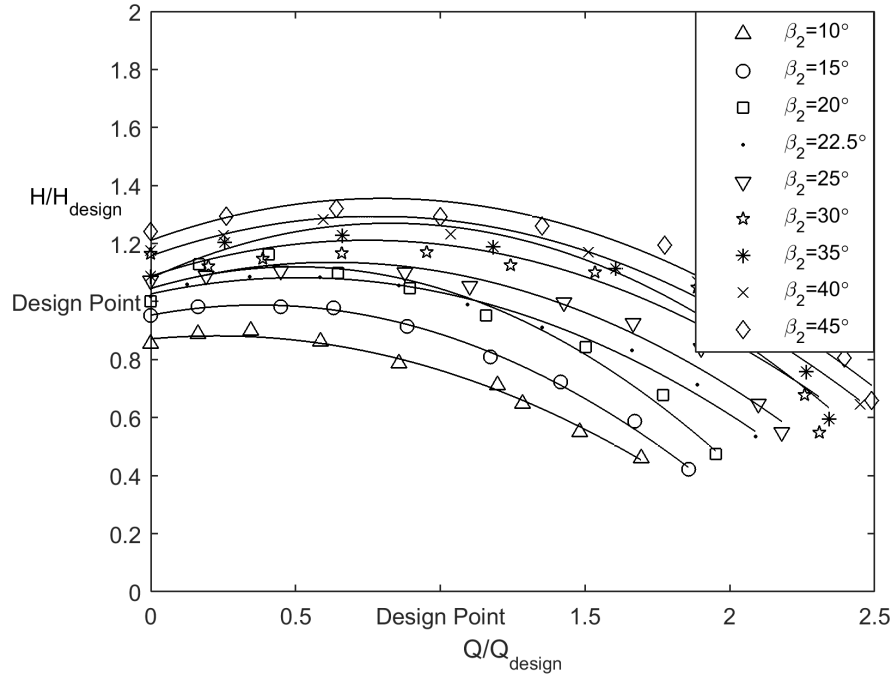


Figure 3.13: Head ratio vs. flow ratio for different blade angles.

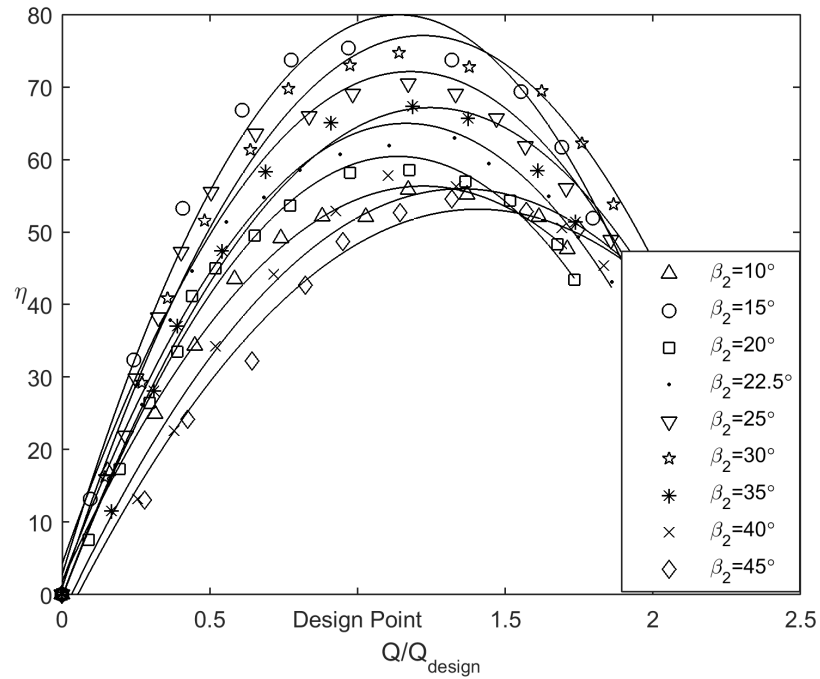


Figure 3.14: Efficiency vs. flow ratio for different outlet angles.

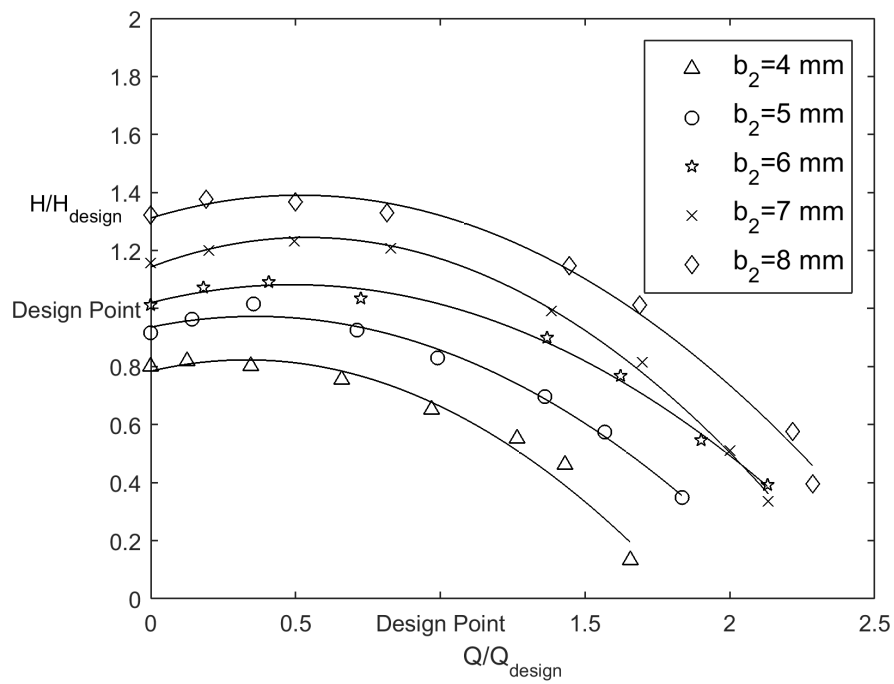


Figure 3.15: Head ratio vs. flow ratio for different outlet widths.

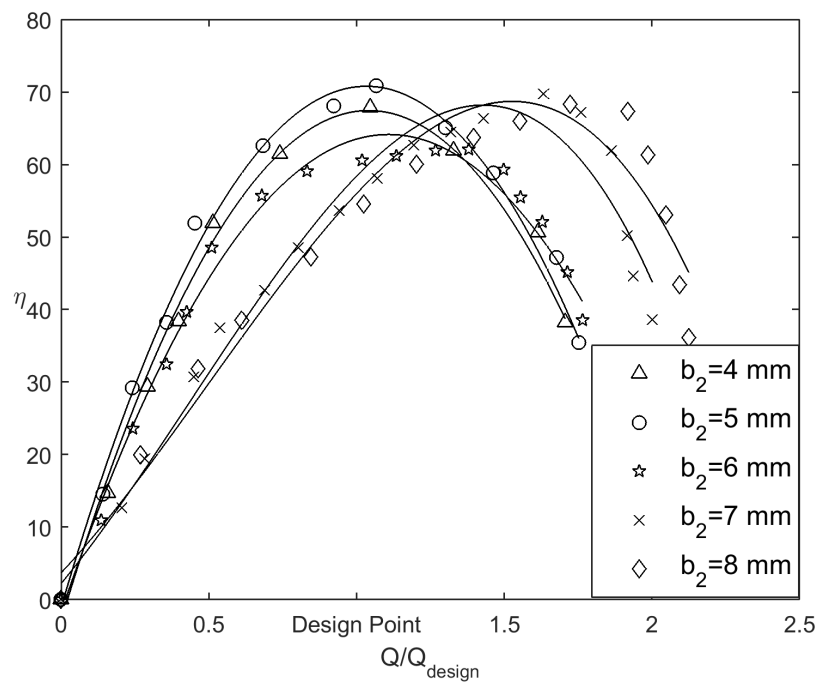


Figure 3.16: Efficiency vs. flow ratio for different outlet widths.

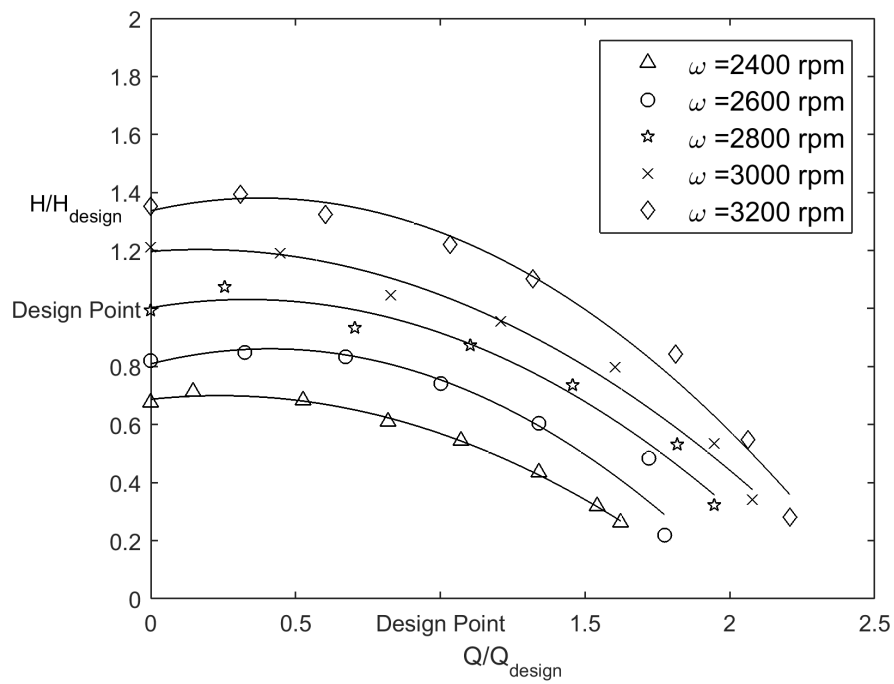


Figure 3.17: Head ratio vs. flow ratio for different rotational speeds.

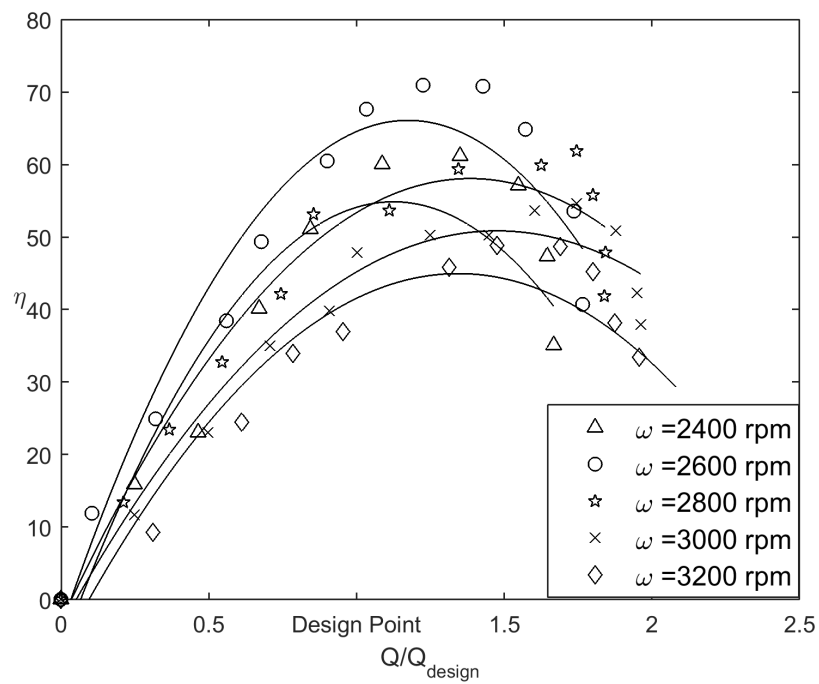


Figure 3.18: Efficiency vs. flow ratio for different rotational speeds.

Force Analysis

Figure 3.19 shows the axial and radial thrust predictions in a representative pump, based on theoretical models introduced in the "Force Analysis" section. The equation proposed by Lobanoff, Lazarkiewicz and Stepanoff were modeled and the design constraints were imposed in order to plot the theoretical axial and radial thrusts.

The simulated static axial forces on a representative impeller at different rotational speeds is presented in Figure 3.20. Table 3.3 compares the magnitudes of axial thrust, presented in Figure 3.20, at different rotational speeds at the design point as well as the maximum values. The radial thrust trends presented in this graph are similar to the theoretical trends and the values are closer to the values from the Lobanoff model.

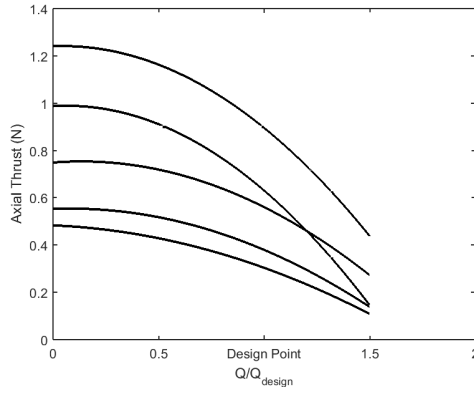
Table 3.3: Maximum and design point axial thrust at different rotational speeds.

Rotational Speed (ω) <i>rpm</i>	2400	2600	2800	3000	3200
Axial Thrust (F_Z) at DP <i>N</i>	0.690945	0.844488	1.104331	1.311024	1.529528
Max. Axial Thrust <i>N</i>	0.92126	1.098425	1.305118	1.535433	1.84252

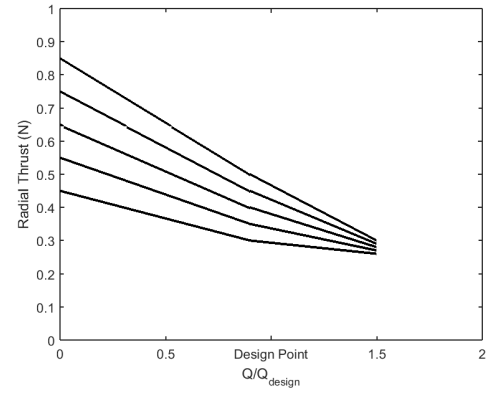
Static radial thrust magnitudes and directions are presented in Figure 3.21. Table 3.4 compares the magnitudes of these radial forces at different rotational speeds at the design point as well as the maximum values. Figure 3.21a shows a radial force trend similar to the theory proposed by Stepanoff.

Table 3.4: Maximum and design point radial thrust at different rotational speeds.

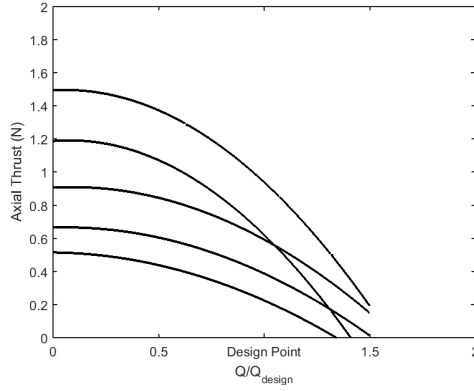
Rotational Speed (ω) <i>rpm</i>	2400	2600	2800	3000	3200
Radial Thrust (F_R) at DP <i>N</i>	0.041399	0.08432	0.091208	0.079588	0.134564
Max. Radial Thrust <i>N</i>	0.160111	0.241327	0.323705	0.253885	0.479062



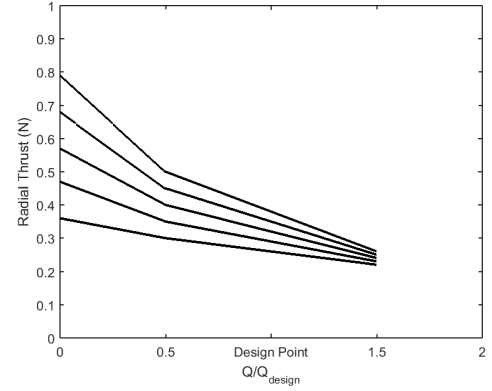
(a) Theoretical axial thrust by Lobanoff equations.



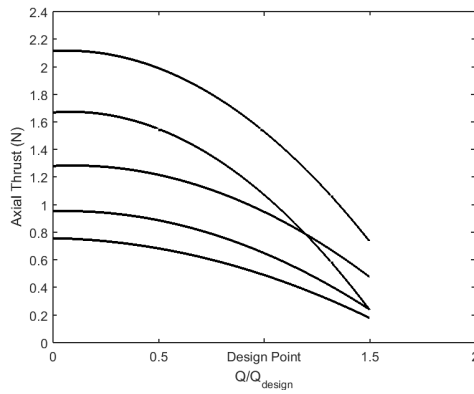
(b) Theoretical radial thrust by Lobanoff equations.



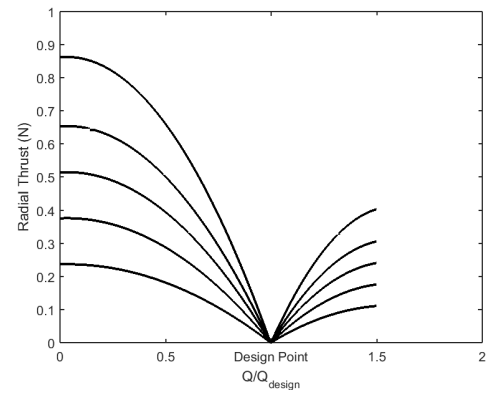
(c) Theoretical axial thrust by Lazarkiewicz equations.



(d) Theoretical radial thrust by Lazarkiewicz equations.



(e) Theoretical axial thrust by Stepanoff equations.



(f) Theoretical radial thrust by Stepanoff equations.

Figure 3.19: Axial and radial thrust predictions based on theoretical models

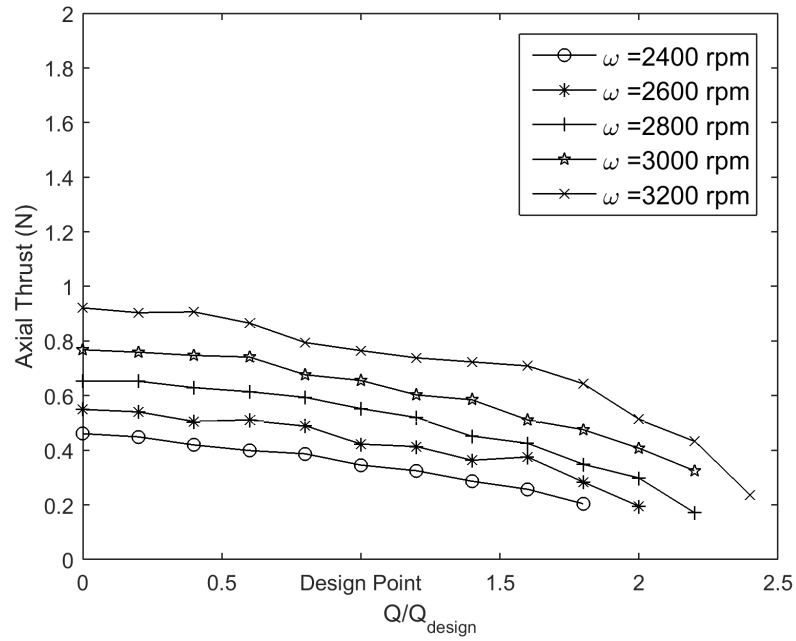
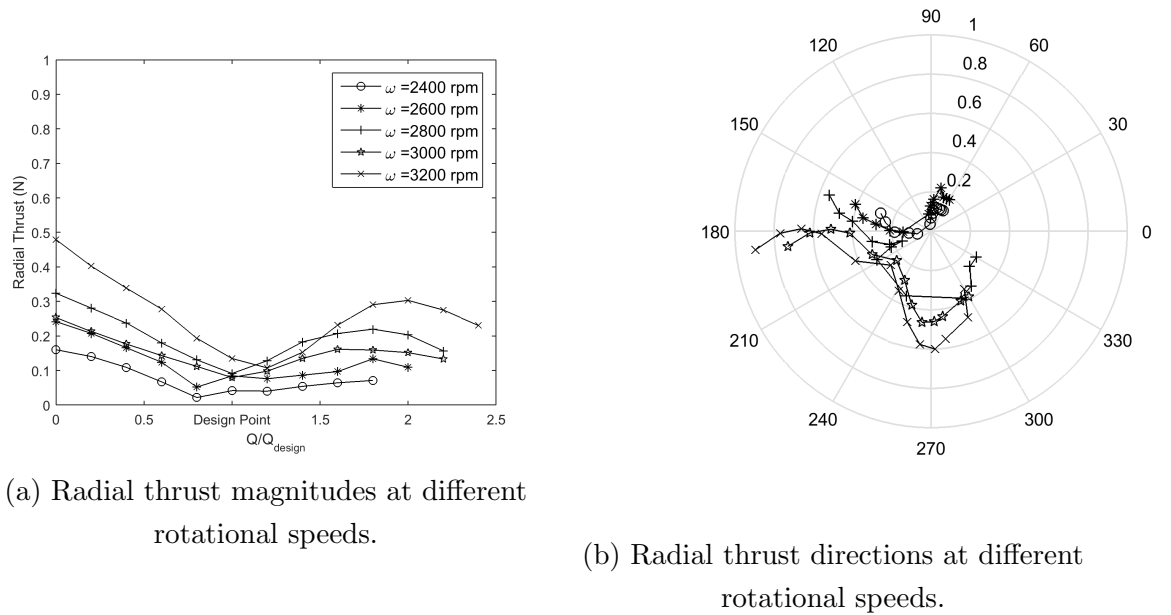


Figure 3.20: The simulated axial thrust in the representative impeller at different rotational speeds.



(a) Radial thrust magnitudes at different rotational speeds.

(b) Radial thrust directions at different rotational speeds.

Figure 3.21: Static radial thrust magnitudes and directions for a representative impeller.

Shear Stress and Hæmolysis

By assuming blood as a Newtonian fluid, the scalar shear stress induced on the fluid on each boundary is defined [135] by

$$\sigma = \left[\frac{1}{6} \sum (\sigma_{ii} - \sigma_{jj})(\sigma_{ii} - \sigma_{jj}) + \sum (\sigma_{ij}\sigma_{ij}) \right]^{1/2} \quad (3.18)$$

Hæmolysis is defined as the release of hemoglobin due to mechanical damage to red blood cells (RBCs) in VADs and MCS devices. The hæmolysis index is a dimensionless parameter used to quantify this concept. There are two major models for hæmolysis: strain-based and power-law model. The most common method is to relate hæmolysis to the shear rate and exposure time through a power-law form [135]. The general form of this equation is defined by

$$HI(\%) = \frac{\Delta freeHb}{Hb} \times 100 = C t_{exp}^{\alpha} \tau^{\beta} \quad (3.19)$$

Where

HI	Hæmolysis index
Hb	The total hemoglobin concentration
$\Delta freeHb$	The increase in plasma free hemoglobin
τ	The shear stress
t_{exp}	The exposure time.

The terms α , β and C are constants based on experimental data. Many researchers [44, 160, 54] have conducted experiments using the power law equation and found the constants based on their results. Most of the published studies related to numerical estimation of hæmolysis are based on the power law and the constants proposed by Giersiepen [44]. Table 3.5 represents the power law equations constants and their covering ranges.

Table 3.5: Power-law equation constants for different proposed models [135]

Model	Range		C	α	β
	Shear Stress (Pa)	Exposure Time (msec)			
Giersiepen [44]	<255	<700	3.620×10^{-5}	0.7850	2.4160
Heuser [54]	<700	<700	1.800×10^{-6}	0.7650	1.9910
Zhang [160]	50-320	<1500	1.228×10^{-5}	0.6606	1.9918

The most common method to model the hæmolysis is based on a general form of the power-law equation. The reason is the functional relationship between the two quantities, where a relative change in one results in a proportional relative change in the other one, independent of the initial size of the quantities. The first power-law equation was used for a Couette shearing device (shear stress <255 Pa, exposure time <700 msec) and the constants α , β and C were found to be 0.785, 2.416 and 3.62×10^{-5} respectively [44].

There are two approaches for computational models to estimate hæmolysis: Eulerian

and Lagrangian [135]. In the Eulerian approach, the damage index is integrated over the entire computational flow domain, so the high hæmolysis locations could be discerned inside the domain whereas in the Lagrangian formulation the integration is along the flow path lines. In a previous study [135] the two methods are compared and evaluated by experimental data in a shearing device and a clinical VAD. The study showed that both methods have high percentage errors, meaning they could not accurately predict the magnitude of the hæmolysis. However, the Eulerian approach had large correlation coefficients showing that it could be used to compare different devices and pump designs to each other by predicting relative hæmolysis. In this study, in the Eulerian scalar transport approach, $\Delta freeHb'$ was defined as a scalar and equal to $\Delta freeHb^{1/\alpha}$ [135, 39] and the transport equation was then proposed as

$$\frac{d(\Delta freeHb')}{dt} + v\rho.\nabla(\Delta freeHb') = S \quad (3.20)$$

Where v is the mean inlet velocity (m/s) and S is the source term and defined as

$$S = \rho(Hb.C.\tau^\beta)^{1/\alpha} \quad (3.21)$$

In order to express the degree of hæmolysis, Normalised Index of Hæmolysis (NIH) was proposed to account for the plasma volume based on the hemotocrit and it is given by

$$NIH(g/100l) = 100 \times \frac{\Delta freeHb}{Hb} \times (1 - Hct) \times k \quad (3.22)$$

Where Hct is the hematocrit and k is the hemoglobin content of blood and these quantities are 45% and $\approx 150g/L$ respectively for a healthy person [10].

Based on the values of linear velocity on the surface of the impeller (48 m/s) and inside the pipes (0.2 m/s), the shear stress in the pipe is negligible compared to that of the gap between the impeller and housing and on the impeller surface (20 to 40 times larger on the impeller). Figures 3.22 and 3.23 show how simulated NIH values change with the outlet width and number of blades with respect to the outlet angle. Based on Figure 3.22, by increasing the number of blades at a constant rotational speed, the pressure increases and results in higher shear stress and NIH. To compare the impellers at the same pressure rise, a lower rotational speed is needed for higher number of blades and it leads to a lower shear stress and NIH. Therefore higher number of blades at low rotational speeds and lower number of blades at high rotational speeds will have more or less the same effect on hæmolysis and shear stress. Therefore, the priority is lower number of blades at a higher rotational speed to keep the surface area minimum, which is another contributing factor to the hæmolysis.

The effect of change in outlet angle on hæmolysis is lower at low number of blades. However, higher outlet angle at the same rotational speed results in a slight increase

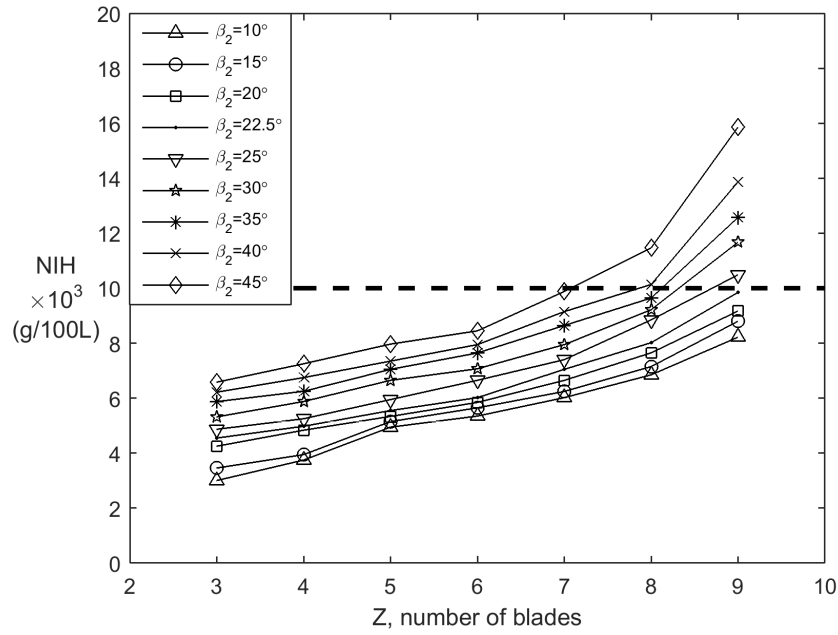


Figure 3.22: The simulated NIH for different blade numbers and outlet angles.

in pressure rise and therefore shear stress and NIH. One way to find the most hemo-compatible angle is to lower the needed rotational speed by increasing the angle to an optimum value. This value is an angle that leads to a pressure rise close to design point and NIH lower than the recommended critical value. This critical value for NIH is estimated at 0.01g/100L [25] and is marked with a dashed line in Figures 3.22 and 3.23.

Figure 3.23 shows a higher probability of hæmolysis by increasing the outlet width. The reason is the higher pressure rise and therefore higher shear stress and subsequent NIH. Lower values of outlet width are suitable for a larger variety of outlet angles. At higher outlet widths (>6 mm), the outlet angle needs to be selected carefully, as there is a high probability of hæmolysis in an impeller with high outlet width and angle.

Figures 3.24-3.27 illustrate the CFD results of pressure contours, velocity streamlines and the wall shear stress on the blades and inside the volutes for three pumps at five different rotational speeds. The first two rows show the results for two pumps with 3 blades and outlet angles 15° and 25° and the third row is a pump with 6 blades and 25°. These representative pumps were selected for presentation in order to separately illustrate the effect of blade number, outlet angle and rotational speed on the pressure, velocity and wall shear stress in the pumps. Figure 3.24 shows a significantly larger difference between the second and third impellers than the first two, meaning the effect on the pressure by adding three blades is more significant than increasing the outlet angle by 10° and this difference is more explicit at higher

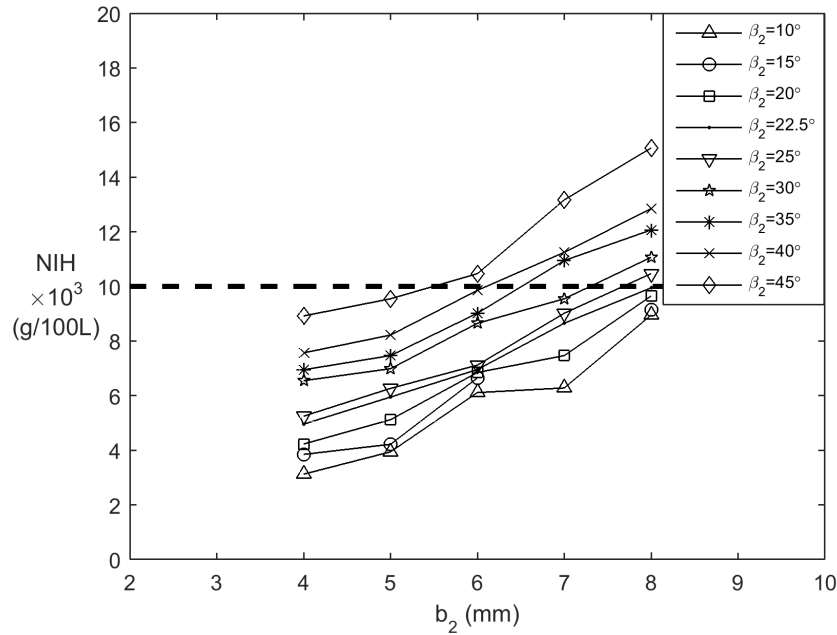


Figure 3.23: The simulated NIH for different outlet widths and outlet angles.

rotational speeds. Figures 3.13 and 3.12 also confirm the findings.

The velocity streamlines in Figure 3.25 show higher velocities at the volute tongue for the first and second pumps and around the snail for the second and third pumps. From the data, it is apparent that higher outlet angles result in higher velocity around the volute and fewer blades results in higher velocity at the tongue of the volute. The first two pumps show some vortices at the volute outlet whereas the second two pumps have more irregularities in between the vanes. The vortices are formed closer to the center at higher rotational speed. Another interesting finding is that the rotational speed mainly affects the velocity around the volute and has very small or no effect on the tongue velocity.

Figures 3.26 and 3.27 illustrate the wall shear stress on the blades and volutes respectively. As expected, the concentration is on the blade leading edge and is higher at higher rotational speeds. The results show higher shear stress in the pumps with fewer blades and lower outlet angles, whereas in Figure 3.22, higher NIH values are reported for higher angles and number of blades. This may be explained by taking the volute wall shear stress into account and consider the effect of pressure rise on the hæmolysis. Figure 3.27 also shows a high concentration of shear stress at the tongue of the volutes for the first two pumps. However, all the values on the blades and volutes are lower than 100 Pa and lower than the critical value (150 Pa) knowing the fact that the pumps have relatively low outlet widths (4.2 mm, see Figure 3.23).

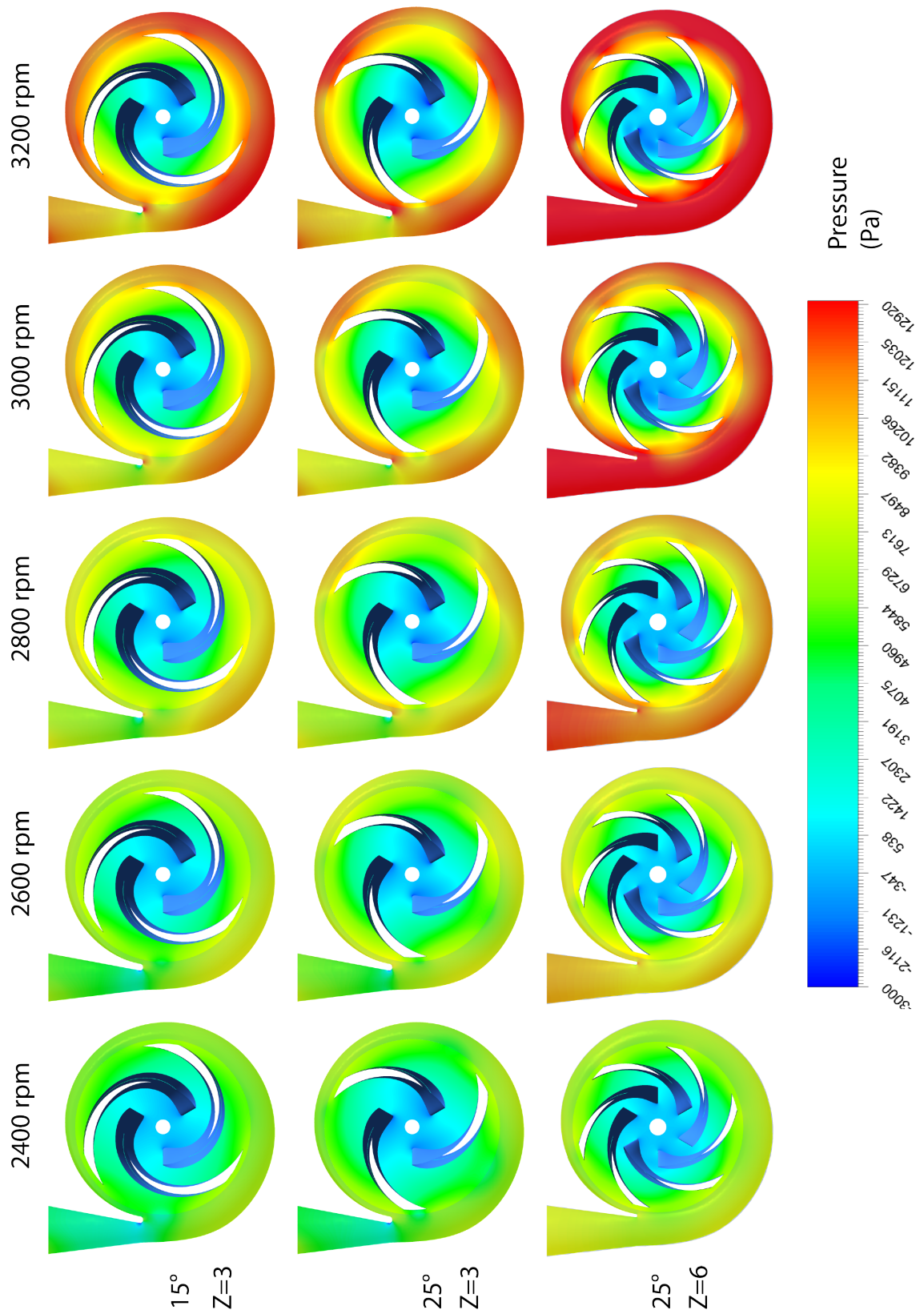


Figure 3.24: Pressure distribution in three pumps at different rotational speeds.

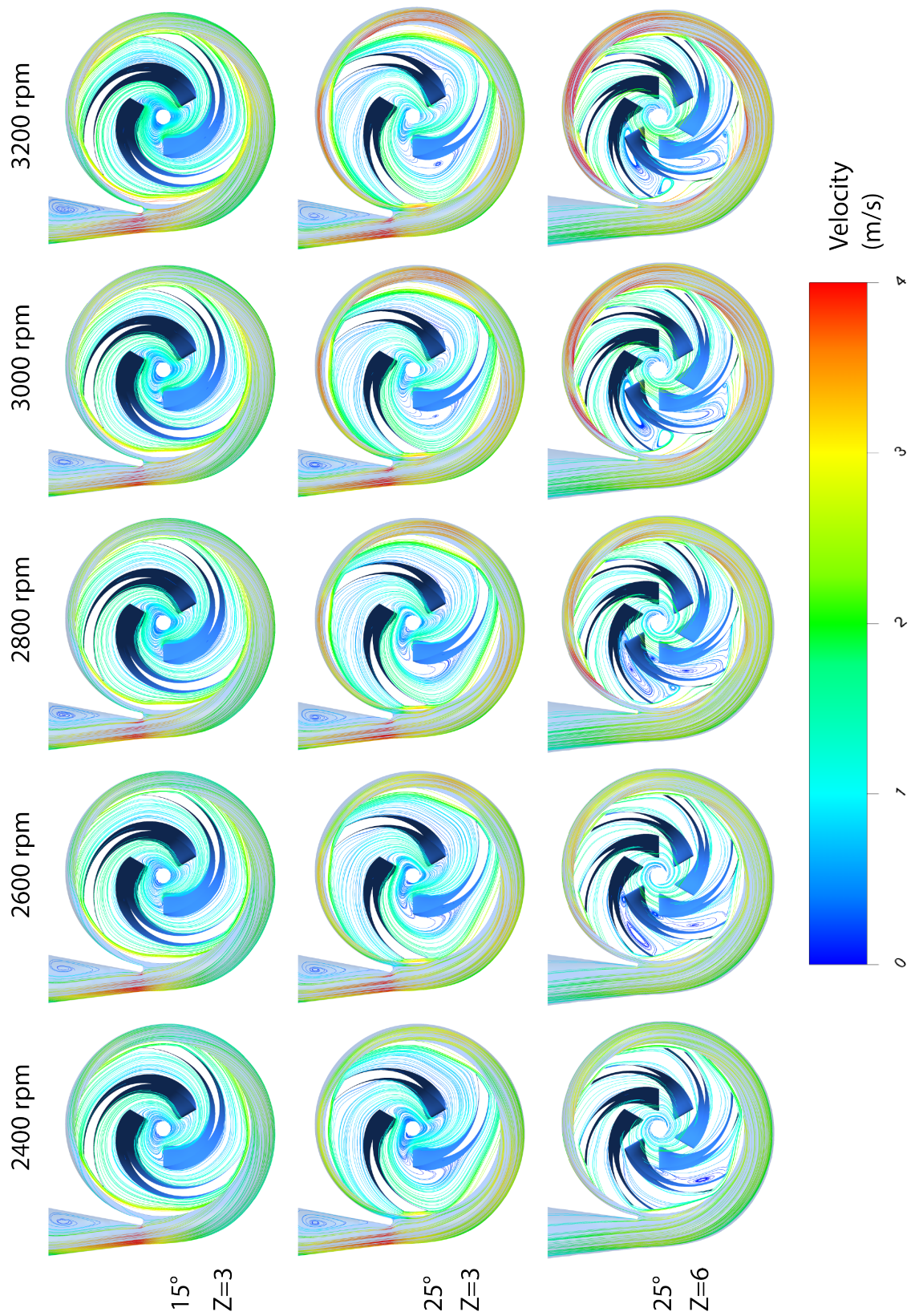


Figure 3.25: Velocity streamlines in three pumps at different rotational speeds.

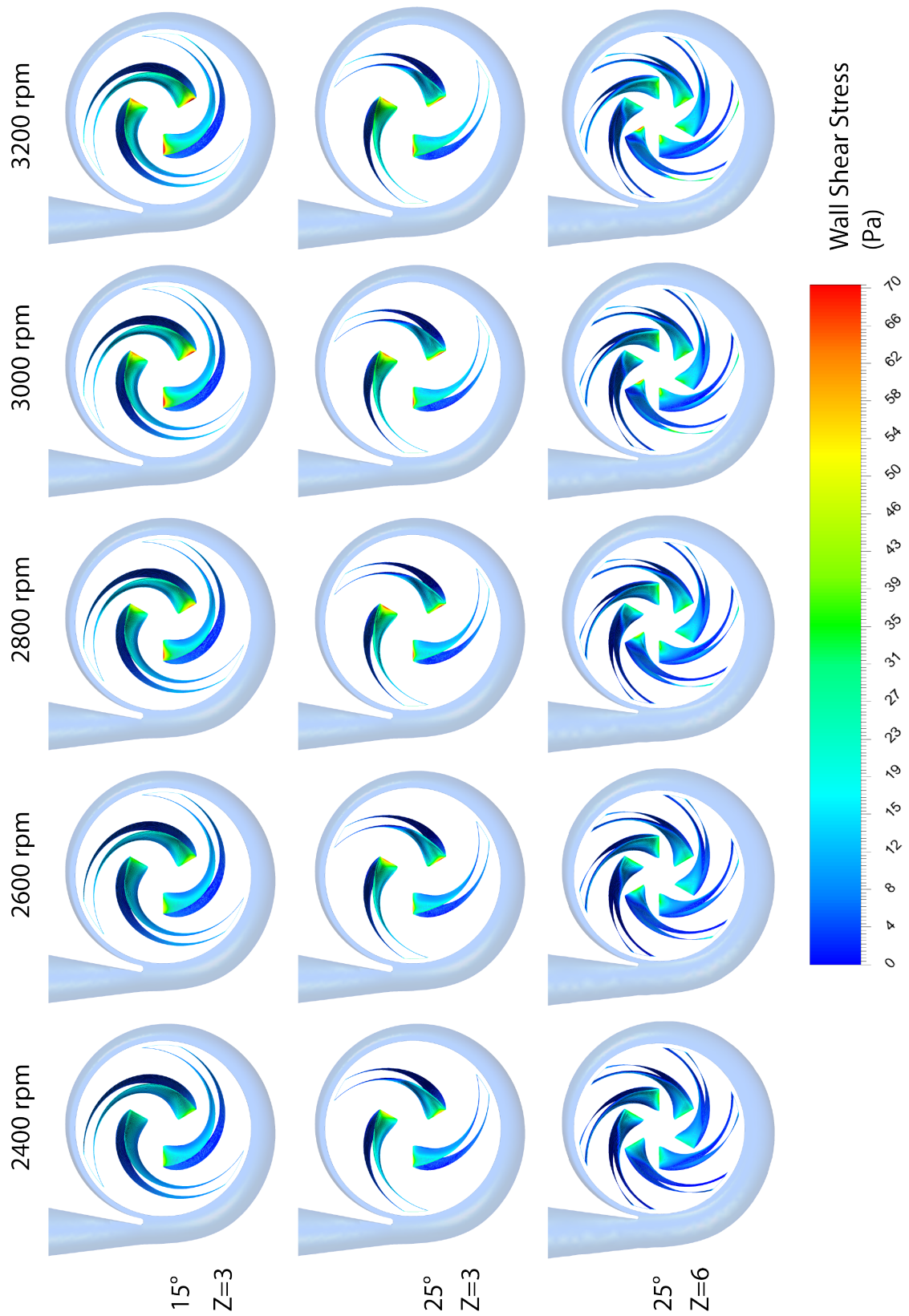


Figure 3.26: Impeller wall shear stress in three pumps at different rotational speeds.

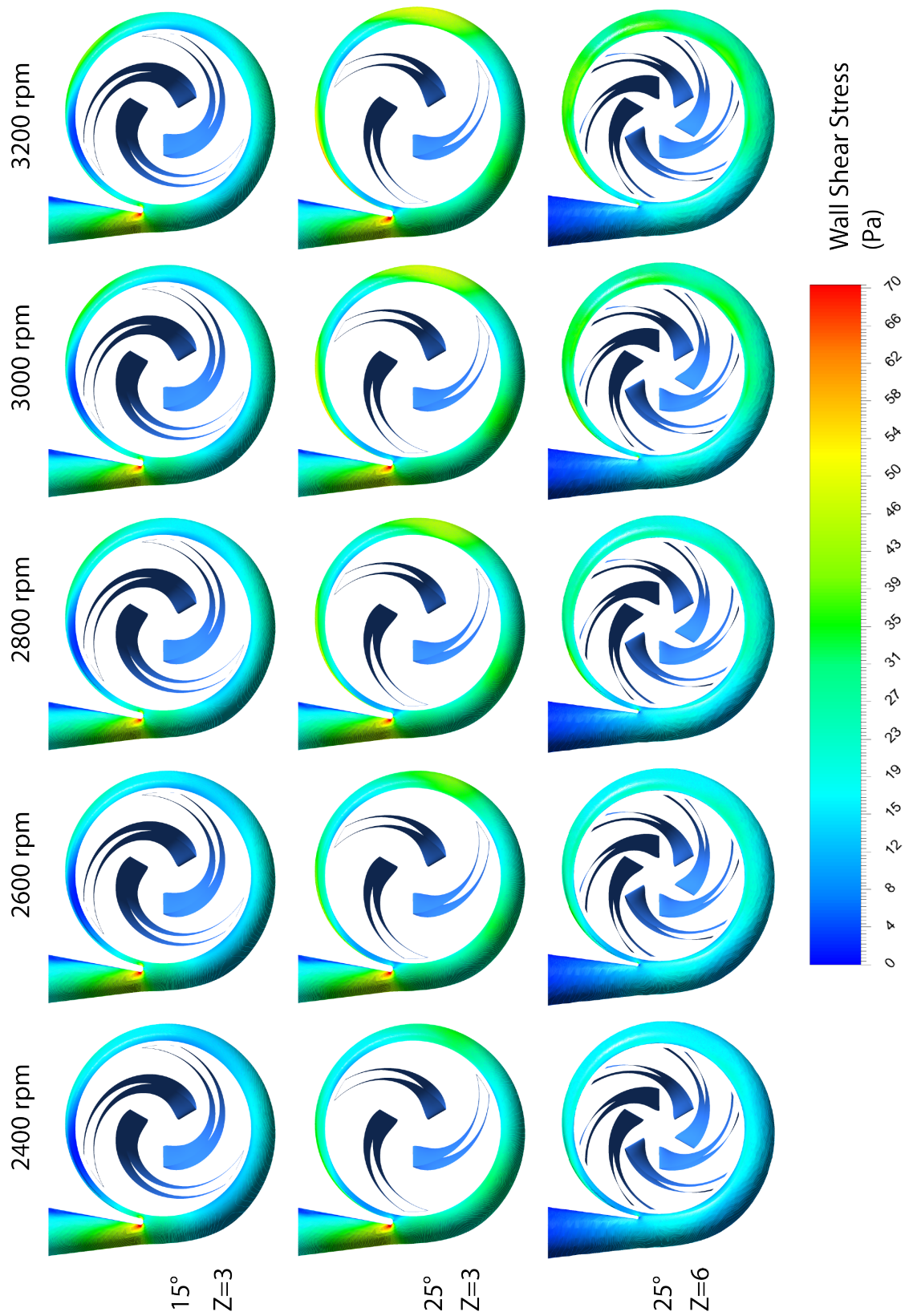


Figure 3.27: Volute wall shear stress in three pumps at different rotational speeds.

3.2 In-silico Investigations of Axial Pumps as MCS Devices

In-silico investigations of the axial pumps in this chapter include the design process in MATLAB, computational methods, numerical simulations and generating the 3D geometry in CAD softwares.

3.2.1 Design MATLAB Program

A MATLAB code was originally written by Dr. Akbar Rahideh and modified by Dr. Amin Rezaenia and myself during my Ph.D. studies for a general preliminary design for the geometry of the blades. The main purpose of the code is to generate 2D coordinates of three sections of a blade: hub, mean effective and tip. The design parameters are categorised into four groups in a similar fashion to the previous sections. The parameters based on empirical equations and graphs of industrial pumps are not used in the process in order to avoid the effect of Reynolds number. Preliminary parameters including the head and flow coefficients are selected based on previously successfully designed small axial pumps [119]. The velocity-based parameters are calculated using the velocity triangles equations implemented into MATLAB. The design point pressure rise, flow rate, density, viscosity and diameter are dictated as design constraints, as mentioned earlier, and were investigated in the numerical simulations in a wider range.

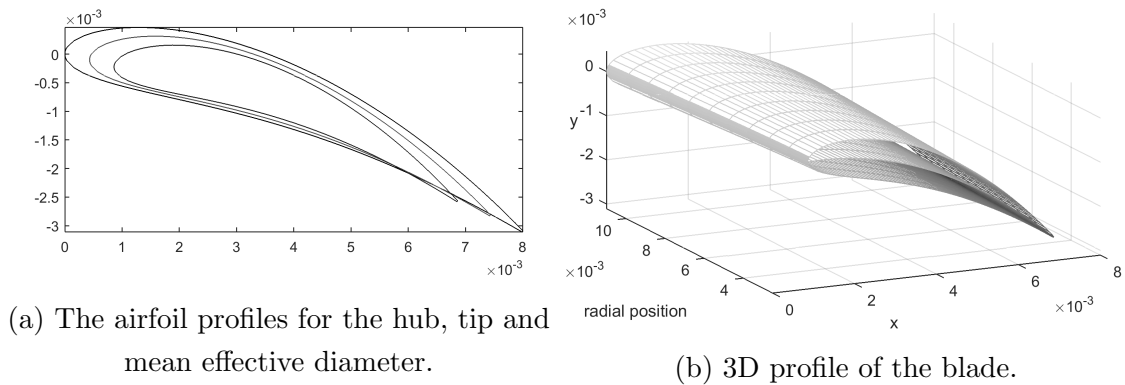


Figure 3.28: The blade profile of a representative impeller generated by the MATLAB design code.

The outlet angle is selected in the range 2° - 40° and the number of blades at 2, 4 and 6. The rotational speed is changed manually in order to obtain a suitable pressure rise at different selected angles and four different values are investigated in the numerical simulations and experiments. With these parameters known, three airfoil profiles are generated for the hub, tip and the mean effective diameter and

lofted gradually to generate the 3D blade profile. A representative impeller with a 20° outlet angle is selected for presentation. Figure 3.28 shows the airfoil profiles and the 3D blade of this impeller generated by MATLAB.

3.2.2 Fluid Flow (CFX)

The ANSYS Fluid Flow CFX is used to simulate the fluid domain. CFX is a complete package comprising of the DesignModeler, Mesh and the CFX setup, solution and results tools.

DesignModeler

The DesignModeler tool is a component of the Fluid Flow CFX and can import the 3D model data from an existing CAD file. The impellers are imported into this component and surfaces are defined as well as the volute fluid zone, which is a circular tube around the impeller. Figure 3.29 shows different views of the representative impeller in the DesignModeler.

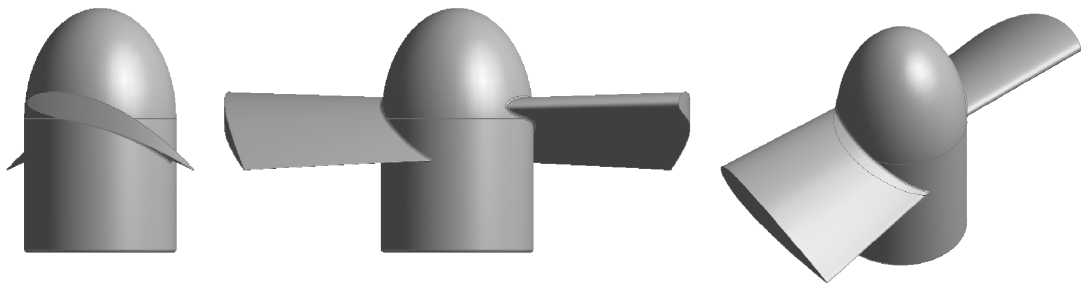


Figure 3.29: The representative impeller imported in DesignModeler.

Mesh

The mesh independence study was conducted in a similar fashion to the previous sections and the small percentage difference in the results between the original and fine mesh validated the use of the original mesh for all models and confirmed the mesh independence. Table 3.6 shows the values of three mesh sizes for the representative impeller. The pressure rise was selected as the output value and the original mesh is the reference point. The small differences of 2.3% and 1.6% for the coarse and fine mesh pressure rise validates the use of original mesh.

Table 3.6: Results of mesh independence.

Mesh Quality	Number of Elements	Number of Nodes	Pressure rise (mmHg)	Percent Difference
$\times 0.8$	77264	11349	48.312	2.3%
Original	174440	37287	47.228	-
$\times 1.25$	405668	310363	46.45	1.6%

CFX

ANSYS CFX is used as the advanced solver to achieve a reliable and accurate solution. Due to the simplicity of the flow in this type of pump, compared to centrifugal, there is only one domain defined in this part of the study. Figure 3.30 shows the defined domain in the CFX. The cylindrical flow passage is defined as the volume around the impeller and the impeller body is extracted from this volume.

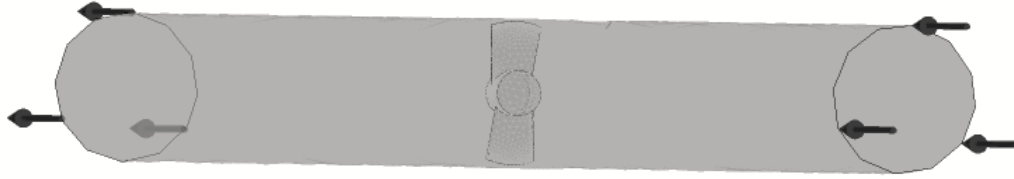


Figure 3.30: The impeller and volute domain in ANSYS CFX. The arrows indicate the inlet and outlet of the domain.

The incompressible Navier Stokes equations are used to predict and calculate the flow fields in the pumps. The model has one rotating domain and it is defined by creating the fluid volume around the rotor surface. The rotational motion of the impeller is calculated using Multiple Reference Frame (MRF). In this approach, the flow is assumed steady state, the grid remains fixed and the relative velocity is calculated throughout the domain. The MRF model has been fully discussed in the previous sections.

Boundary Conditions

Boundary conditions are specified to define the rotational speed, inlet pressure and outlet flow rate similar to the previous sections. At the outlet, a healthy human body blood flow rate (5 L/min) is imposed and at the inlet a relative pressure of 0 Pa is defined.

Working Fluid

The working fluid is defined with the human blood characteristics at 37°C and is assumed an incompressible Newtonian fluid due to the high shear rates in axial pumps. The density of 1050 kg/m^3 and viscosity of 0.0036 Pa.s are defined for the working fluid.

The Turbulence Model

In this chapter the k-epsilon ($k-\epsilon$) turbulence model is utilized. In order to validate the use of this model, the average mesh $y+$ value on the impeller wall is calculated for all models in ANSYS post processing and compared to the acceptable value (30-300).

The Tip Clearance

The gap between the impeller and housing has an impact on the efficiency as well as blood trauma. Smaller tip clearance results in higher efficiency but at the cost of a higher value of shear stress and therefore higher possibility of damaging the blood cells. The primary reason for close tip clearance is to minimize leakage around the tip and improve the volumetric efficiency [68]. An optimum value needs to be determined for every pump based on the operating conditions in order to maximize the efficiency while keeping the shear stress and NIH under the critical values. In this study, considering a 22 mm diameter for impellers and 24 mm diameter for an average human aorta, a tip clearance of 1 mm is modelled for the simulations and experiments.

3.2.3 Results and Discussion

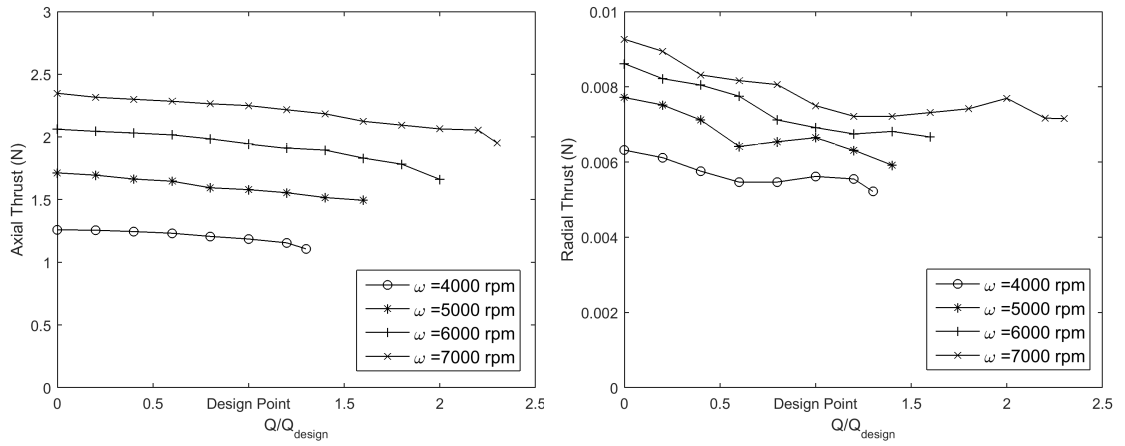
Numerical simulations are conducted for 62 axial impellers with different blade number and angles. Efficiencies, force characteristics and hemocompatibility of the pumps are analysed and presented in the following section. All the axial pumps analysed numerically in this part of the study, are then manufactured and tested. Therefore, the simulations are only used to compare the pumps in terms of hemocompatibility and force characteristics and the performance curves are presented for experimental results in the next section.

Similar to the previous sections, the results are presented in their nondimensional format of head and flow ratios, where Q/Q_{des} and H/H_{des} present the ratio of volumetric flow rate and pressure rise to their values at the design point [66, 84].

Force Analysis

The magnitudes of axial and radial forces acting on the impeller show much lower radial and higher axial forces compared to centrifugal impellers. The forces are compared in two forms: For the representative impeller for different rotational speeds and for 14 impellers with different outlet angles at a constant speed, in order to study the effect of β_2 on the force characteristics.

The simulated static axial forces on a representative impeller (A) with a 20° outlet angle is shown in Figure 3.31a for 4000-7000 rpm. As expected, higher rotational speed results in higher axial thrust. At lower rotational speeds the change is ≈ 0.5 N for every 1000 rpm and it decreases at higher speeds.



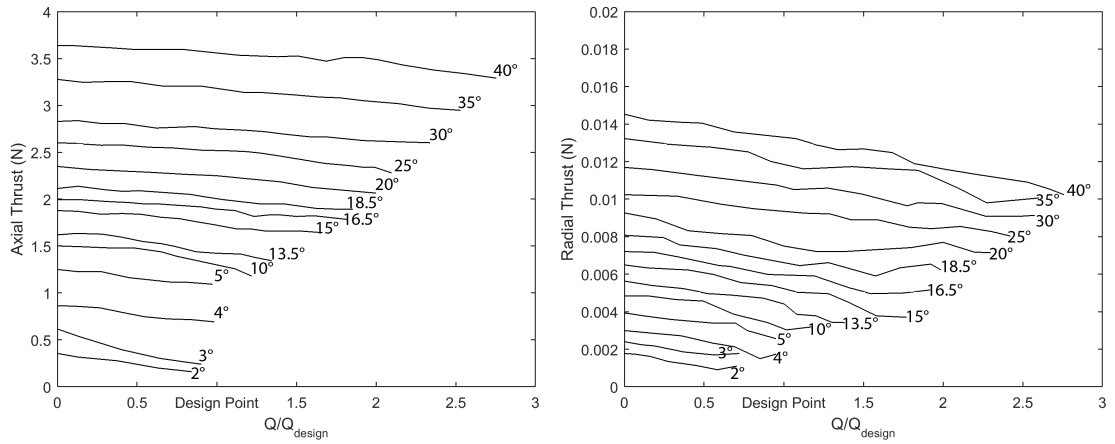
(a) The simulated axial thrust for impeller A ($\beta_2=20^\circ$) at different rotational speeds. (b) The simulated radial thrust for impeller A at different rotational speeds.

Figure 3.31: Axial and radial thrust magnitude for the representative impeller A.

Figure 3.32a shows the simulated axial thrust for 14 impellers with different outlet angles rotating at 7000 rpm. The graph may be used to study the effect of change in outlet angle on the force and to design the bearing system. Based on Figure 3.32a, higher outlet angles lead to higher axial forces on the impeller, however, it should be noted that the graph presents the impeller forces at 7000 rpm for all impellers. Based on the experimental results, presented in the next section, this speed is not a suitable speed for impellers with low outlet angles and may not produce the required head rise. Therefore, by increasing the rotational speed for impellers with lower outlet angles, the axial thrust increases.

Figures 3.31b and 3.32b illustrate the simulated radial thrust for the same impellers. As expected, the magnitude of radial thrust is much lower than that of centrifugal pumps.

The magnitudes of radial forces help in the design process of magnetic bearings. Higher rotational speed and outlet angle result in higher radial thrust. The effect



(a) The simulated axial thrust for different outlet angles at 7000 rpm.

(b) The simulated radial thrust in for different outlet angles at 7000 rpm.

Figure 3.32: Axial and radial thrust magnitude for different outlet angles, rotating at 7000 rpm.

of both parameters in the magnitude of radial forces is smaller than that in axial thrust. Based on the values of radial forces, the magnitudes are low even at high rotational speeds and therefore may not cause any limitations on the design of axial blood pumps. The direction of radial thrust is evenly distributed around the rotational axis due to the symmetric design of the impeller and housing.

Shear Stress and Hæmolysis

The Eulerian scalar transport approach is used to estimate the hæmolysis in the pumps. The power-law equation, based on the constants from Giersiepen [44], is used to model the hæmolysis in a similar fashion to the previous sections. Figure 3.33 shows the values of estimated hæmolysis in the pumps. The graph illustrates the values for different outlet angles at different rotational speeds.

The critical NIH value (0.01g/100L) [25] has been marked with a dashed line and in general shows a higher value of NIH for higher rotational speeds and higher outlet angles. At the given speeds, angles higher than 35° may reach the critical level of hæmolysis at 6000 rpm and this increases to 20° at higher rotational speeds (7000 rpm). Comparing at a constant rotational speed, the lower blade angles are suitable for this application, due to the lower NIH and therefore, lower probability of hæmolysis. However, lower blade angles produce much lower pressure rise compared to higher angles. This will be discussed in the experimental results section in the following chapter. These impellers need higher rotational speeds in order to reach the design point flow rate and pressure rise. The higher rotational speed will increase the value of NIH and therefore, there is a trade-off between the required pressure rise and NIH value in the pumps. An optimum value of angle needs to be determined to

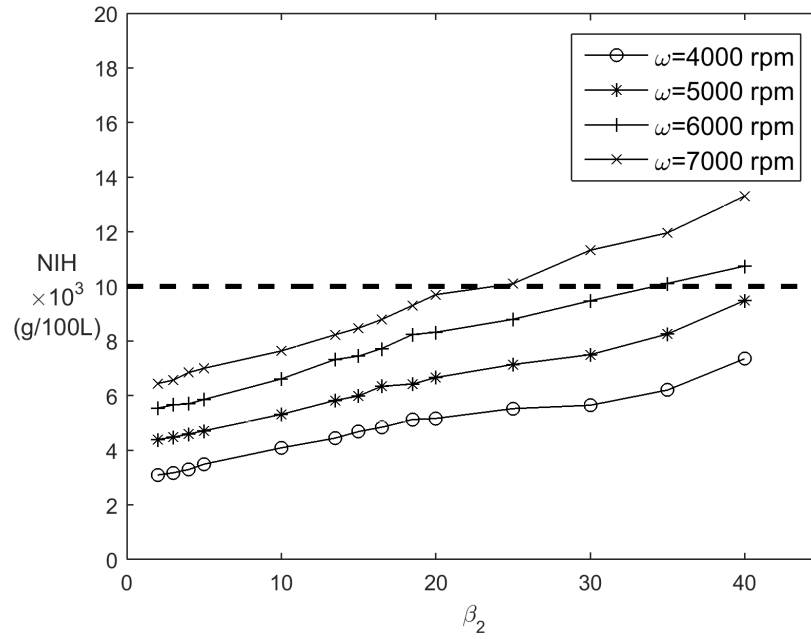


Figure 3.33: The simulated NIH for different outlet angles at four rotational speeds.

produce the required pressure head, as well as keeping the shear stress and NIH under the critical values. This trade-off will be discussed in more details in the following section where the experimental results of performance curves are presented.

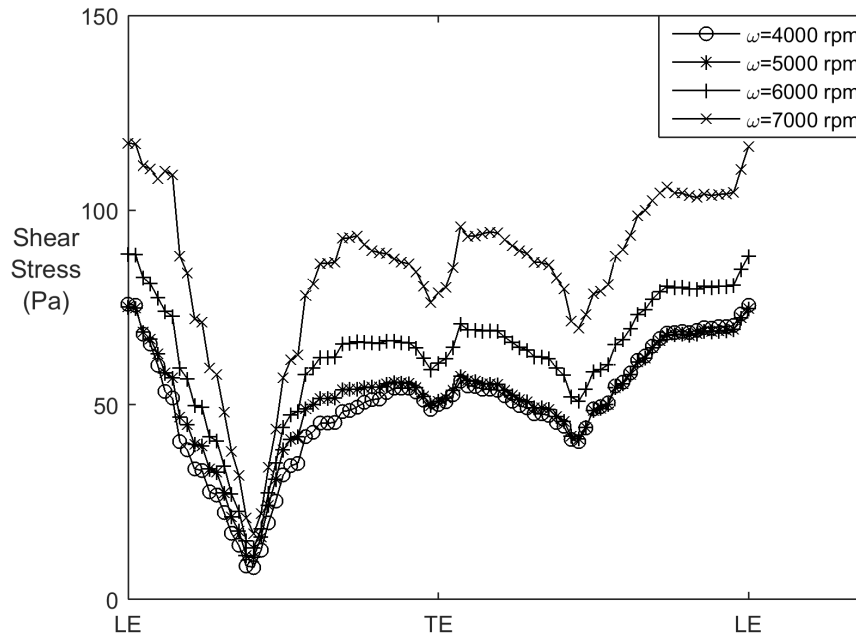


Figure 3.34: The simulated wall shear stress on airfoil surface at 75% span for $\beta_2=2^\circ$.

Figures 3.34-3.38 show the simulated wall shear stress on the airfoil of 5 impellers with different stagger angles. The values are calculated on a selected airfoil 2D

profile of the blades at 75% span for 4000-7000 rpm. The maximum values of shear stress show the leading edge of the blades.

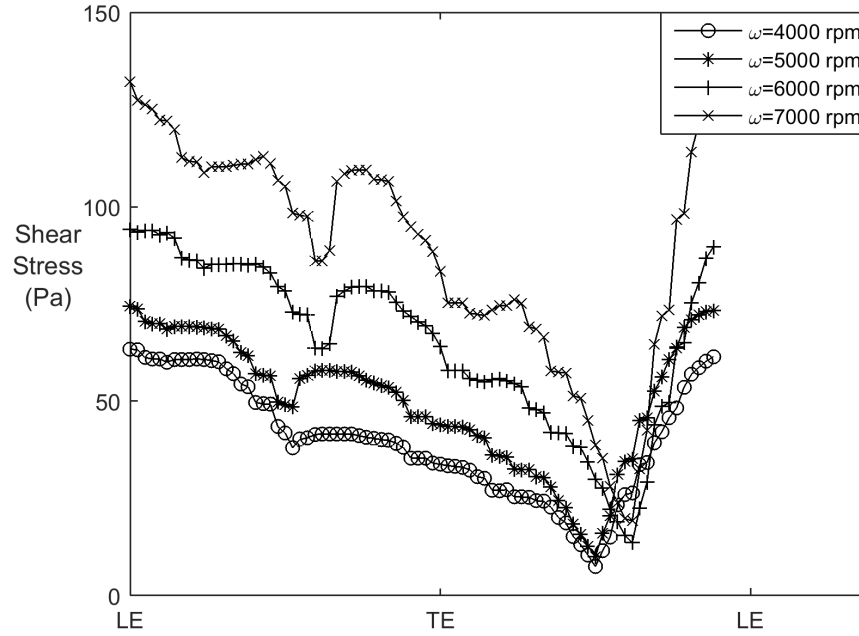


Figure 3.35: The simulated wall shear stress on airfoil surface at 75% span for $\beta_2=10^\circ$.

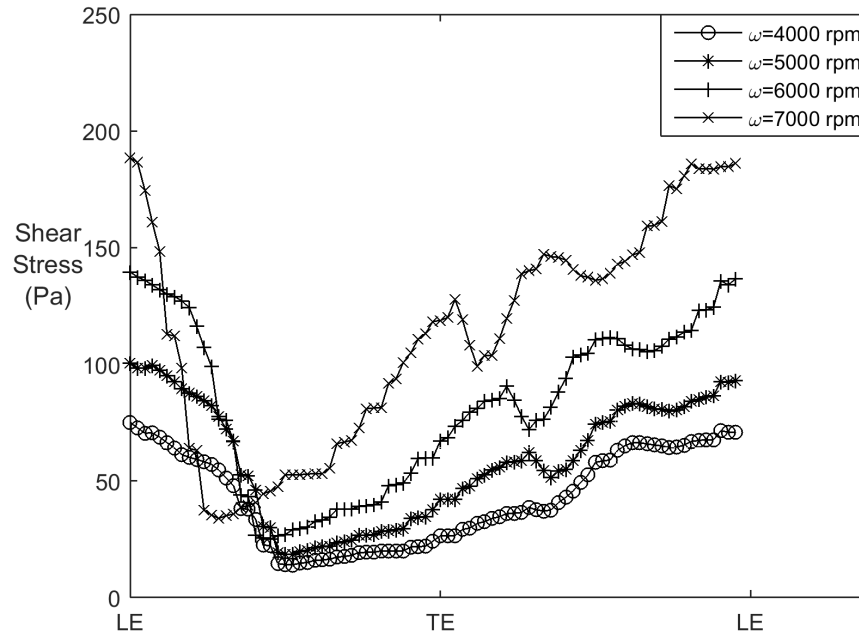


Figure 3.36: The simulated wall shear stress on airfoil surface at 75% span for $\beta_2=20^\circ$.

The graphs suggest angles $<20^\circ$ and/or rotational speeds <5000 rpm for shear stress values <150 Pa.

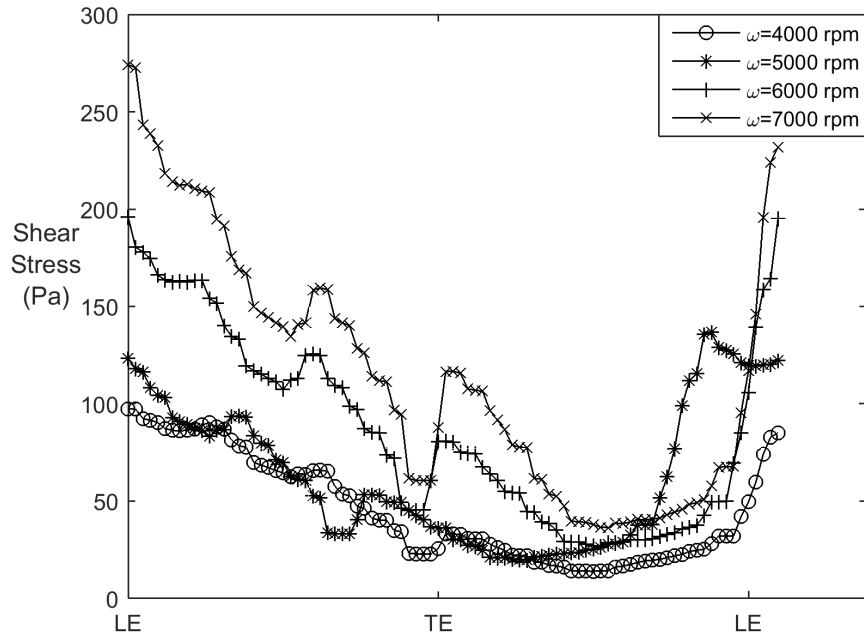


Figure 3.37: The simulated wall shear stress on airfoil surface at 75% span for $\beta_2=30^\circ$.

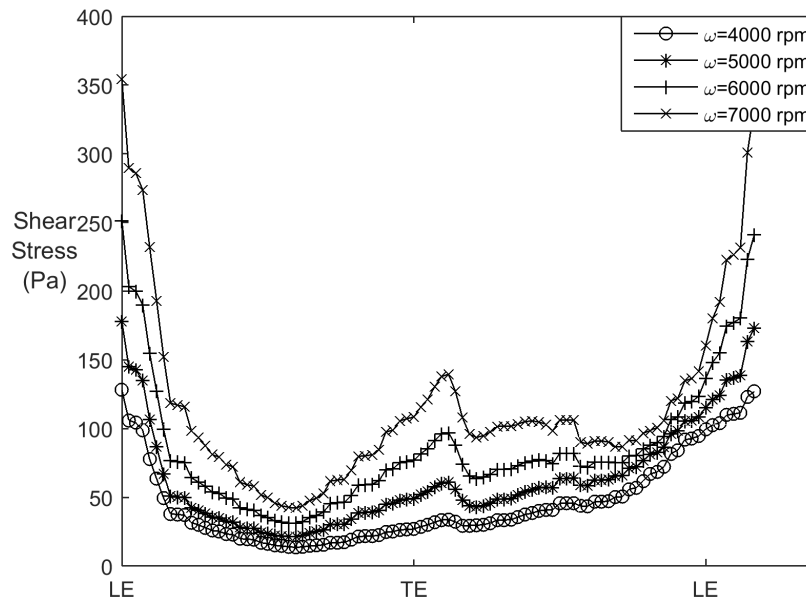


Figure 3.38: The simulated wall shear stress on airfoil surface at 75% span for $\beta_2=40^\circ$.

Figures 3.39, 3.40 and 3.41 illustrate the wall shear stress and the pressure distribution on, before and after the impellers for 5 different outlet angles at 4 different rotational speeds. The columns and rows will help to observe the effect of angle and rotational speed on the induced shear stress and pressure rise. Figure 3.39 shows a concentration of wall shear at the leading edge of the impellers and towards the suction side and the tip span of the blades. The reason is the high velocity gradient

(shear rate) at the tip and on the leading edge of the blades. This is consistent for all models at all speeds. Considering the critical shear stress of 150 Pa, stagger angles higher than 25° rotating at >6000 rpm result in shear stress >150 Pa and may cause hæmolysis.

Figures 3.40 and 3.41 help to see the effect of outlet angle and rotational speed on the pressure gradient on, before and after the impeller. Higher pressure is observed near the tip for all models as expected. The change of pressure from inlet to outlet is also shown. A drop in pressure is noticed near the hub and the drop is larger at higher rotational speeds and higher stagger angles. The pressure drop near the wall is a result of the change in flow from the upstream to the cavity of the hub area and the vane surface. The design point pressure rise may be delivered by increasing the rotational speed and the stagger angle but with the cost of higher shear stress and higher probability of hæmolysis. The designer can find a trade-off based on the desired pressure rise and the application of the device.

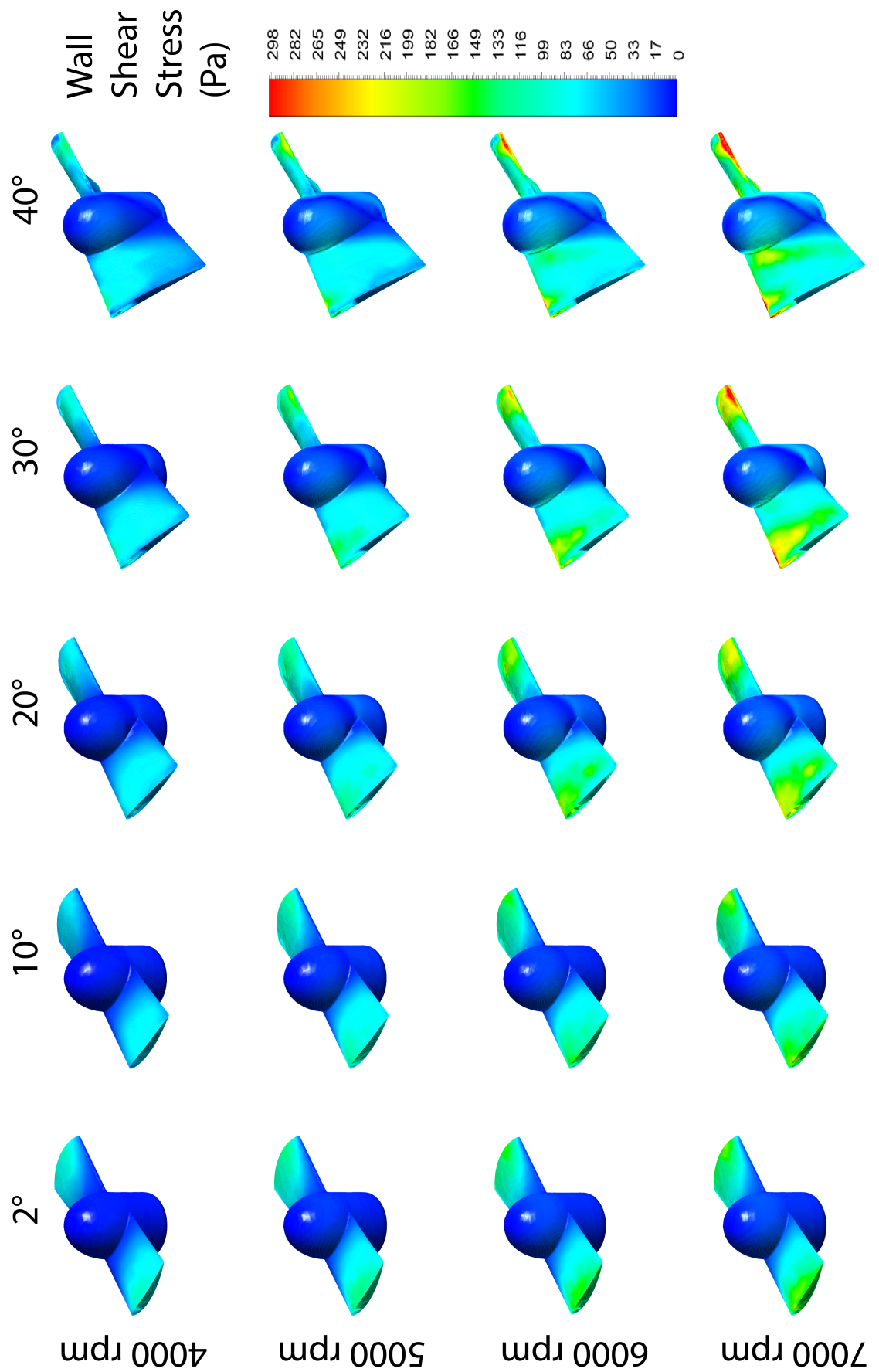


Figure 3.39: Wall shear stress for different angles at different rotational speeds.

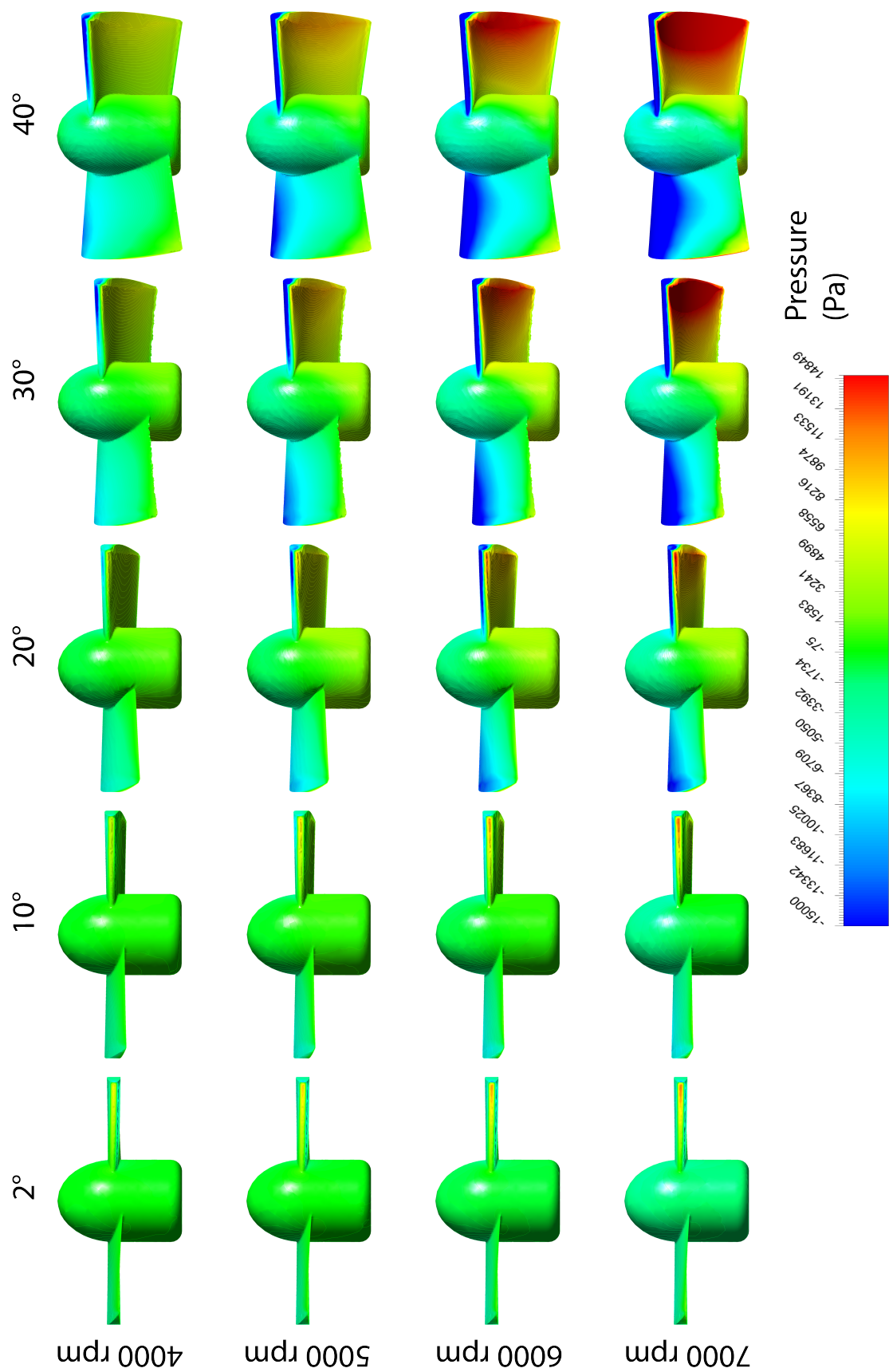


Figure 3.40: Pressure distribution on the impeller for different angles at different rotational speeds.

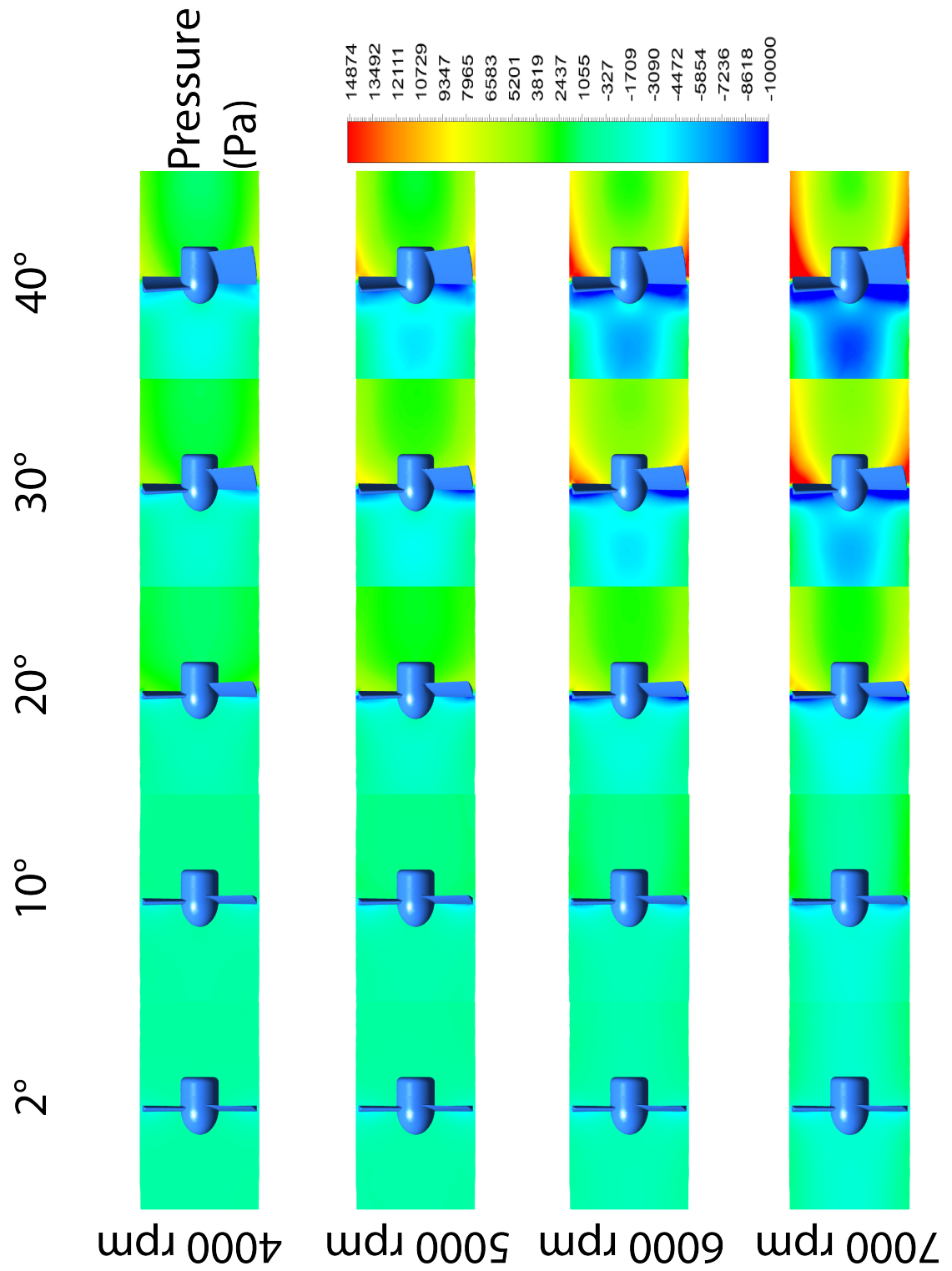


Figure 3.41: Pressure rise for different angles at different rotational speeds.

Chapter 4

Experimental Techniques

In this chapter, the Impeller selection based on the numerical results is presented. The CAD design of the impellers and the design and development of a single loop test rig is described. The experimental process and measurement techniques are introduced, followed by the experimental results, discussions and comparisons to the numerical outcomes. The nondimensional values of specific speeds (n_s), specific diameters (d_s), head coefficients (ψ) and flow coefficients (ϕ) are calculated for all pumps and the data points of specific speeds and diameters are plotted on Cordier diagrams.

The chapter is concluded with the presentation of two $n_s - d_s$ diagrams for small centrifugal and axial pumps suitable for MCS devices, which enable the preliminary design of pumps suitable for MCS devices.

4.1 In-vitro Investigations of Centrifugal Pumps as MCS Devices

4.1.1 SolidWorks

The Vista CPD output is seven EXCEL files with xyz coordinates; five equally spaced streamlines of a single blade, one hub and one shroud. The files were imported to SolidWorks software as 3D curves. The curves were then converted to 3D surfaces and then lofted to create a single blade, Figure 4.1.



Figure 4.1: Drawing a blade in SolidWorks.

Using the coordinates of the hub and shroud, the curves are revolved around the rotation axis to create the hub and shroud (Figure 4.2). The single blade is then patterned around the hub and fillets on the edges are implemented to avoid the manufacturing complications.

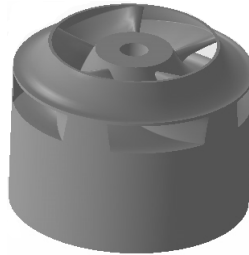


Figure 4.2: A shrouded 5 bladed impeller in SolidWorks

4.1.2 The O-loop

A single loop test rig, which will be denoted as O-loop hereafter, was designed and developed to test the 3D printed impellers. The O-loop is divided into three sections: the pump, the power system and the circulation system.

The pump

The pump consists of the impeller and housing, which includes the volute and two

support plates.

The Power System

The power system consists of a high-speed Brushless DC (BLDC) motor (Maxon EC 45, 45mm diameter, brushless, 250 Watt), a controller to vary the motor speed and a coupling mechanism to directly drive the rotor of the pump through sealed ball bearings.

The Circulation System

The circulation system consists of tubing, a hand operated Hoffman clip to manually change the resistance in the system, an electromagnetic Siemens flow meter to measure the flow rate, two pressure transducers to measure the pressure at the inlet and outlet of the pump.

Figures 4.3 and 4.4 show the schematic and the actual the O-loop.

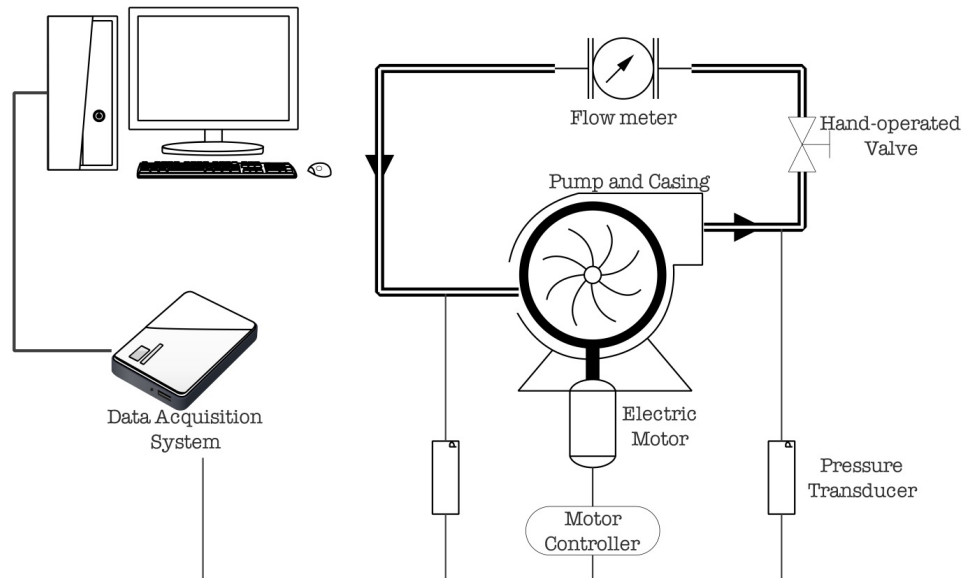


Figure 4.3: The schematic diagram of the O-loop [66].

4.1.3 The Working Fluid

A blood analog solution was used as the working fluid in the O-loop. The solution is 65% water and 35% glycerol (by volume) in order to obtain the closest values of density (1050 kg/m^3) and viscosity (0.0036 Pa.s) to those of human blood at 37°C .

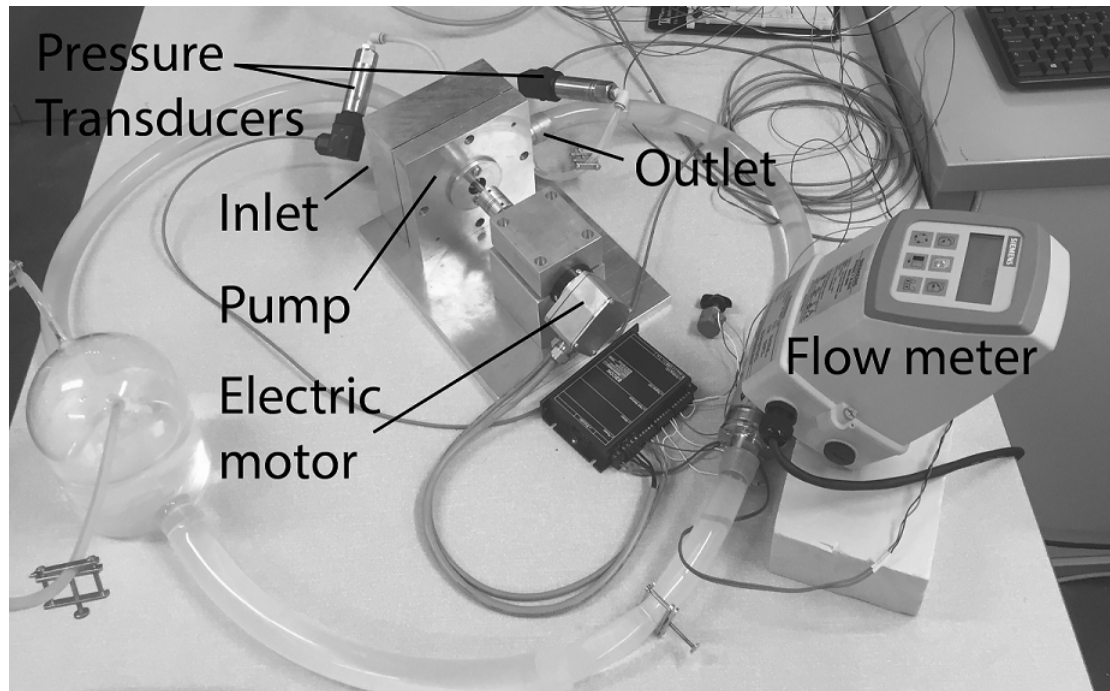


Figure 4.4: The O-loop.

4.1.4 Measurement Systems

The electric motor, pressure transducers and the flow meter were connected to a computer through a data acquisition system and the operating conditions were controlled or measured using LabView interface designed for this purpose, shown in Figure 4.6.

The experiments were conducted for five different rotational speeds, 2400 rpm to 3200 rpm with increments of 200. For each rotational speed, the resistance of the system was changed manually by closing the Hoffman clip, from low resistance (wide open, full flow) to high resistance (closed tube, no flow). The inlet and outlet pressure, flow rate, motor voltage and current were monitored, measured and recorded continuously. The data sampling rate was set to 1 kHz for flow rate and pressure measurements.

4.1.5 Experimental Errors and Uncertainties

The instruments were calibrated before every experiment and used with great care, however no physical quantity can be measured with perfect certainty and there are always errors in any measurement. This means that if we measure the pressure rise and flow rate and then repeat the measurement, we will most likely measure a different value. The experimental error is defined as the difference between measured values and the true value, or the difference between different measured values. This error is measured by its accuracy and precision. Accuracy measured how close the

measured value is to the true (or accepted) value and precision measures how closely the measured values agree to one another. Precision is also known as repeatability or reproducibility and if the precision of an experiment is within an acceptable range, the experiment is considered repeatable [19, 136]. Figure 4.5 shows the difference between accuracy and precision.

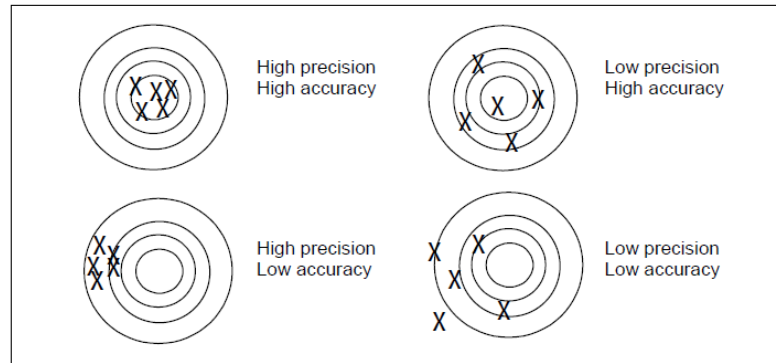


Figure 4.5: Accuracy and precision.

Significant Figures

The precision of a measurement can be measured by the number of significant digits with which the results are reported. The smallest unit every instrument can measure is used to determine the precision of that instrument. In general, in digital instruments, the measurement is usually reported with a precision of $\pm 1/2$ of the smallest unit of the instrument. In these experiments, the instruments precisions are $\pm 1/2$ 0.1 V or ± 0.05 V.

Percent Error

Percent error shows the accuracy of a measurement by the difference between the measured value M and the true or accepted value T .

$$\%Error = \frac{M - T}{T} \quad (4.1)$$

Percent Difference

The percent difference shows the precision of two measurements by the ratio of the difference between two measured values M_1 and M_2 to the mean value.

$$\%Difference = \frac{M_1 - M_2}{1/2(M_1 + M_2)} \quad (4.2)$$

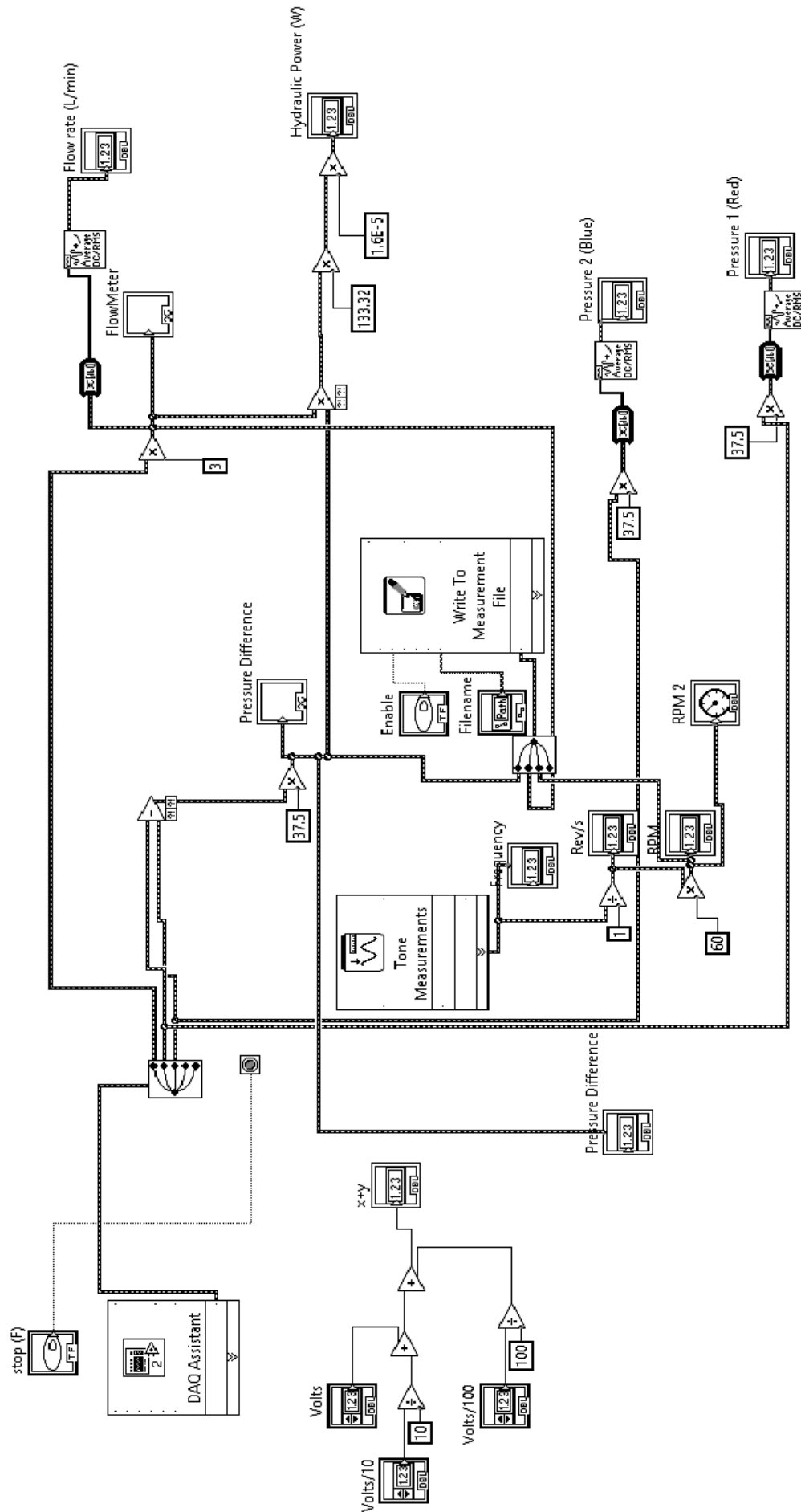


Figure 4.6: The Labview interface for data measurement and control.

Mean and Standard Deviation

In case of experiment repetition, the measured values could be grouped around a center value. This distribution can be defined by two quantities; the mean value, which shows average value of all the measurements, and the standard deviation, which shows the spread or deviation of the measured values around the average value. For N different measurements of the quantity x , the mean value is shown by

$$\bar{x} = \frac{1}{N} \sum_{i=1}^N x_i = \frac{1}{N} (x_1 + x_2 + x_3 + \dots + x_{N-1} + x_N) \quad (4.3)$$

The standard deviation of the measurement is calculated by

$$\sigma = \sqrt{\frac{1}{N-1} \sum_{i=1}^N (x_i - \bar{x})^2} \quad (4.4)$$

Finally, the result of the measurement is reported in the form

$$x = \bar{x} \pm \sigma \quad (4.5)$$

This means that the best estimate for the measured quantity is \bar{x} but may also vary from $\bar{x} - \sigma$ to $\bar{x} + \sigma$. In this study, the experiments are not meant to provide a pre-calculated theoretical value and/or to prove a theory, therefore there is no true value defined. This means the percent error is not suitable for results presentation. For sake of clarity, the mean and standard deviation were selected as the best way for presentation of the results. The experiments were repeated three times for each impeller in order to minimize the uncertainty and verify the repeatability of the experiments.

4.1.6 Results and Discussion

Efficiency, pressure rise, specific speed and diameter, head and flow coefficients were measured or calculated at different operating conditions and were plotted in relevant graphs. Figure 4.7 is a Cordier diagram showing specific speed and specific diameter of 88 efficient pumps based on the highest efficiency points of each pump. The numerical results, presented in the previous section, were used to make an initial estimation at the size, rotational speed, shape and the performance (pressure rise and flow rate) of a group of impellers.

The impellers with different characteristics were manufactured and tested in the O-loop.

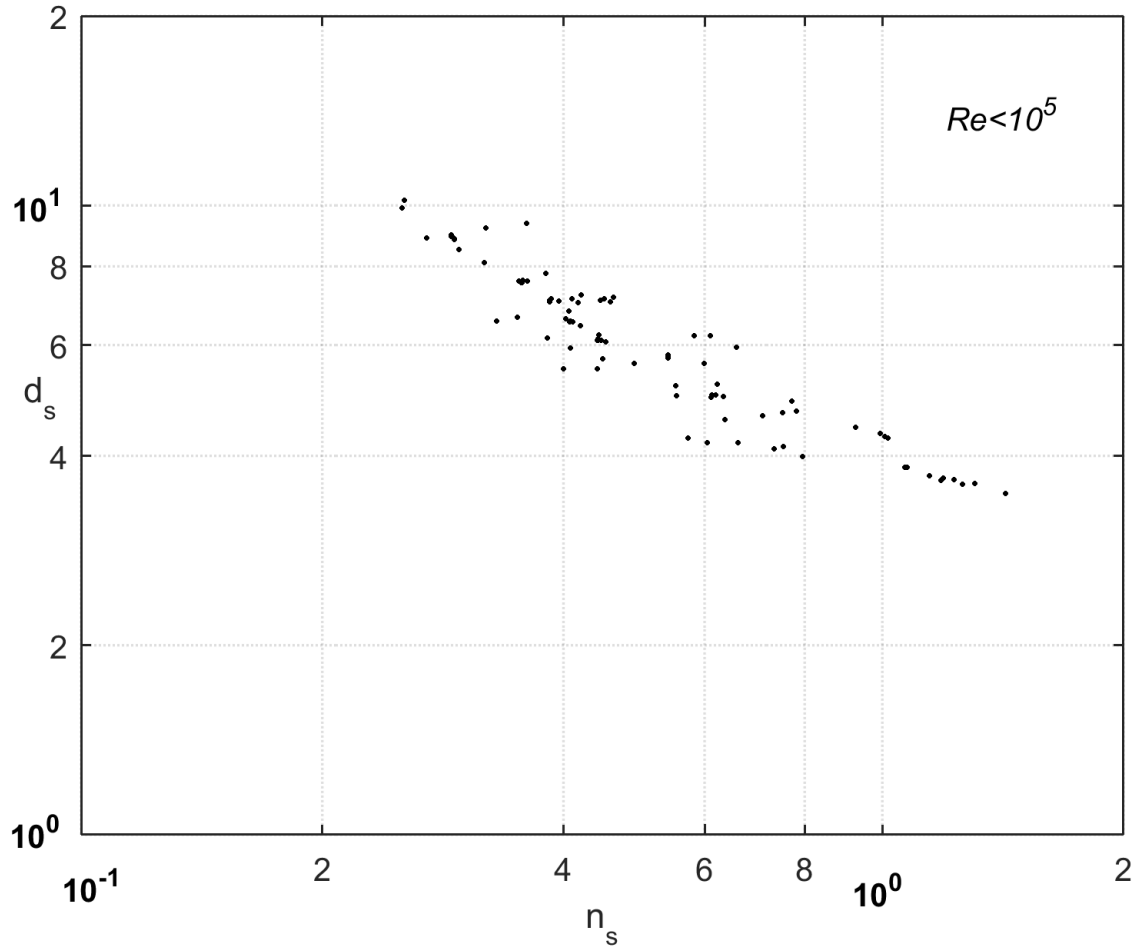


Figure 4.7: Highest efficiency points on $n_s - d_s$ Cordier diagram for all impellers ($2 \times 10^4 < Re < 7 \times 10^4$) [66].

Figure 4.8 shows the profile of two representative models selected for illustration; Impeller A (31 mm diameter, 4 blades, 22.5° outlet angle, 4.2 mm outlet width) and impeller B (31 mm, 7 blades, 27.5° , 4.0 mm).

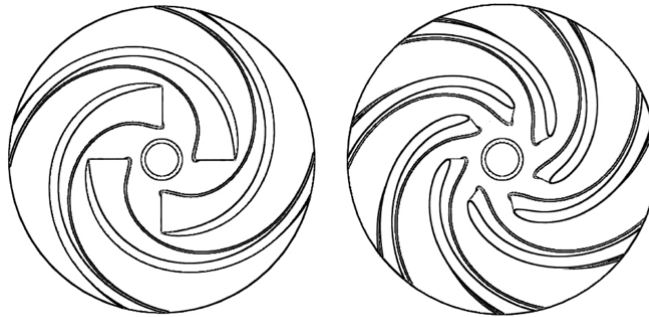


Figure 4.8: Profiles of the impellers A and B [66].

Figures 4.9-4.12 show the numerical and experimental efficiency and head ratio (H/H_{des}) versus flow ratio (Q/Q_{des}) for impellers A and B. Uncertainty is the standard error and the error bars are shown only in specific data points for clarity.

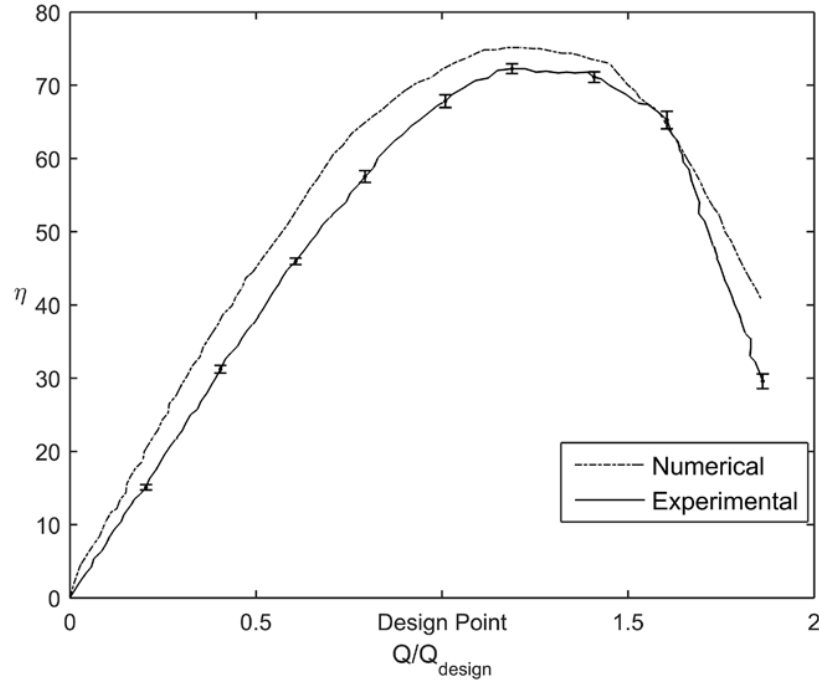


Figure 4.9: Numerical and experimental efficiency vs. Q/Q_{des} for impeller A [66].

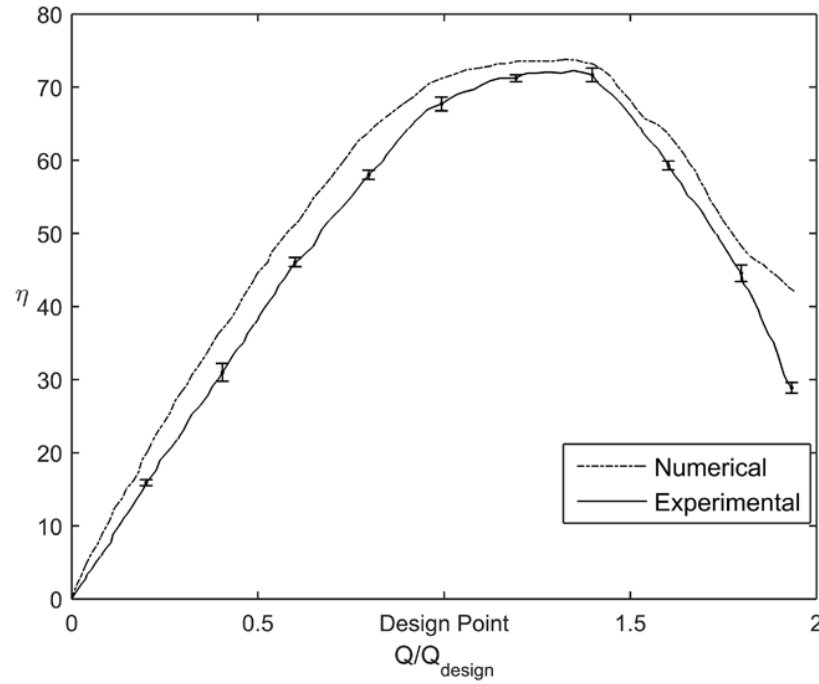


Figure 4.10: Numerical and experimental efficiency vs. Q/Q_{des} for impeller B [66].

The comparison between the experimental results and the expected numerical curves shows a consistent difference pattern for all models and is shown in Figures 4.9 and 4.10 for impellers A and B. The highest experimental efficiency of $72.28 \pm 0.41\%$ was obtained for impeller A at $Q/Q_{des} = 1.19$. This value was close to the numerical efficiency of 75.17% at the same flow rate (3.84% error). The difference between numerical and experimental efficiencies reaches a maximum ($\approx 7\%$) at $Q/Q_{des} = 0.8$

for impeller A. This difference is mainly due to the frictional head losses in the experiments. These losses are composed of the frictional losses in the suction and discharge piping system, which are the sum of frictional losses caused by the water flowing through the inlet and outlet pipes, fittings and measuring equipment, two bearings used on the shaft which are not modeled in the numerical simulations. Also, the impeller and the volute are manufactured with the finest possible surface precision, but are not as smooth as simulated models. This surface roughness effect is another factor contributing to this difference.

In all cases, it was observed that the numerical efficiency is closer to the real tested values at higher flow rates and higher rotational speeds. This could be the result of using the $k - \epsilon$ turbulence model in the computational analysis, which improves the accuracy and is closer to the real value at higher Reynolds numbers.

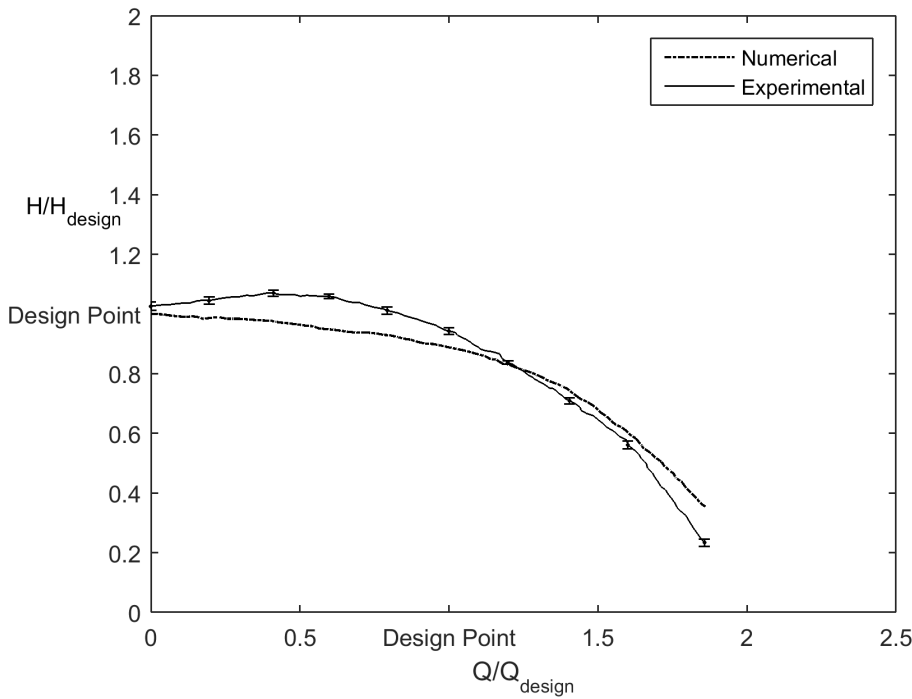
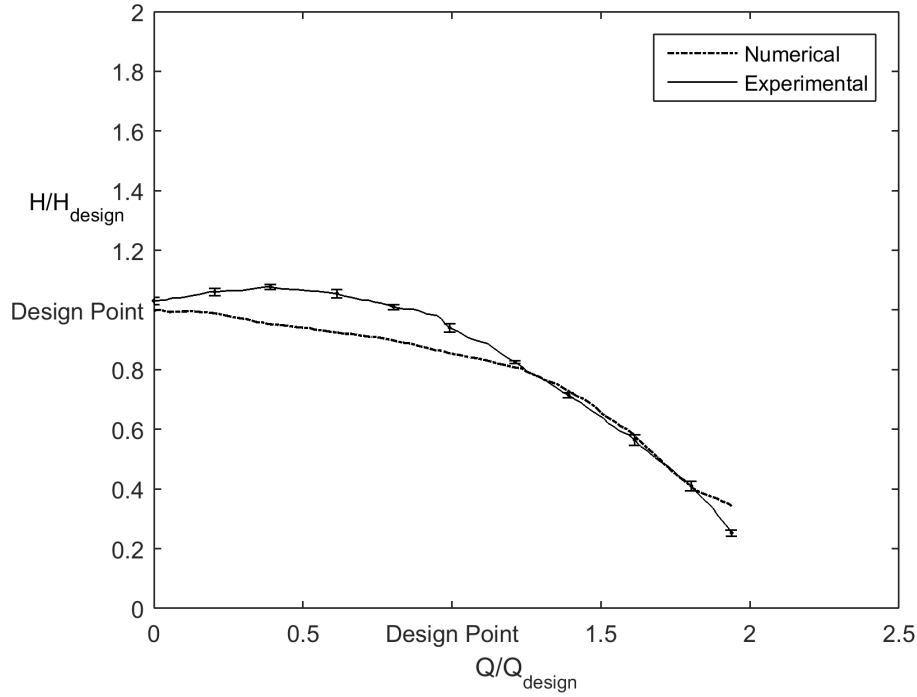
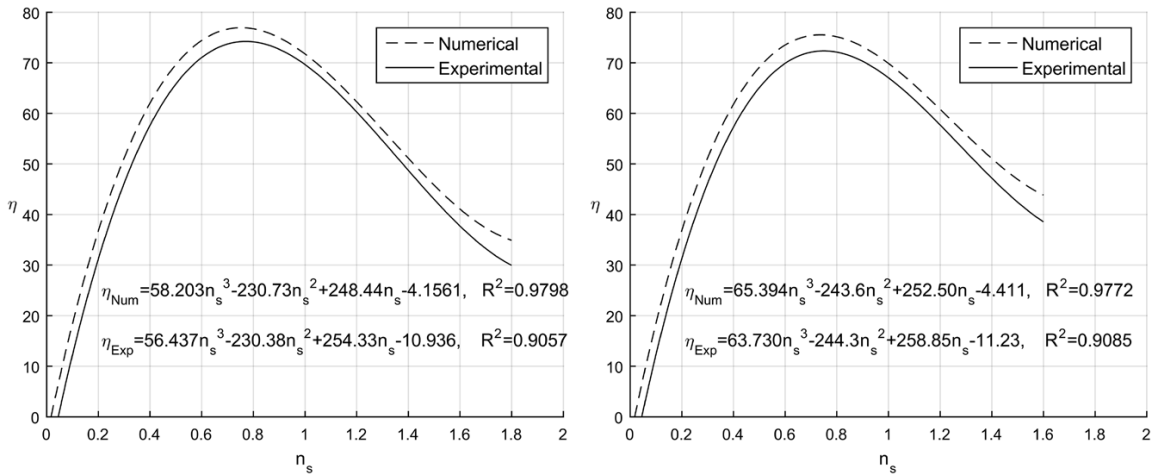


Figure 4.11: Numerical and experimental H/H_{des} vs. Q/Q_{des} for impeller A.

Figures 4.11 and 4.12 show the head ratio versus flow ratio for impellers A and B. In the numerical model, the highest pressure is at no flow condition, as expected from theory. However, in the experiments, pressure slightly increases by flow rate until it gets to a maximum value at flow rate of about half the design point and then decreases moderately. The reason is the slip between the fluid and the blades, which is higher at very low flow rates, because of higher resistance in the system. This difference is normally smaller in impellers with lower number of blades because of lower contact area and therefore lower slip factor.

Figure 4.13 plots the numerical and experimental hydraulic efficiency versus specific

Figure 4.12: Numerical and experimental H/H_{des} vs. Q/Q_{des} for impeller B.Figure 4.13: Numerical and experimental efficiency vs. n_s for impellers A (left) and B (right) [66].

speed for impellers A and B. Data points are deleted for clarity and third order polynomials are fitted to the data points, with their equations and R^2 values presented on the graph. The gap between the numerical and experimental efficiency gets large when $n_s \geq 1.5$ and this applies to all tested models. The reason is the higher rotational speed and flow rate and therefore lower pressure rise due to no or low resistance in the system. This leads to frictional head losses being the only factor in the difference between numerical and experimental pressure rise. Neglecting high specific speeds, the maximum difference between numerical and experimental efficiency is 7.1% for impeller A.

Figure 4.14 shows the numerical and experimental head and flow coefficients for

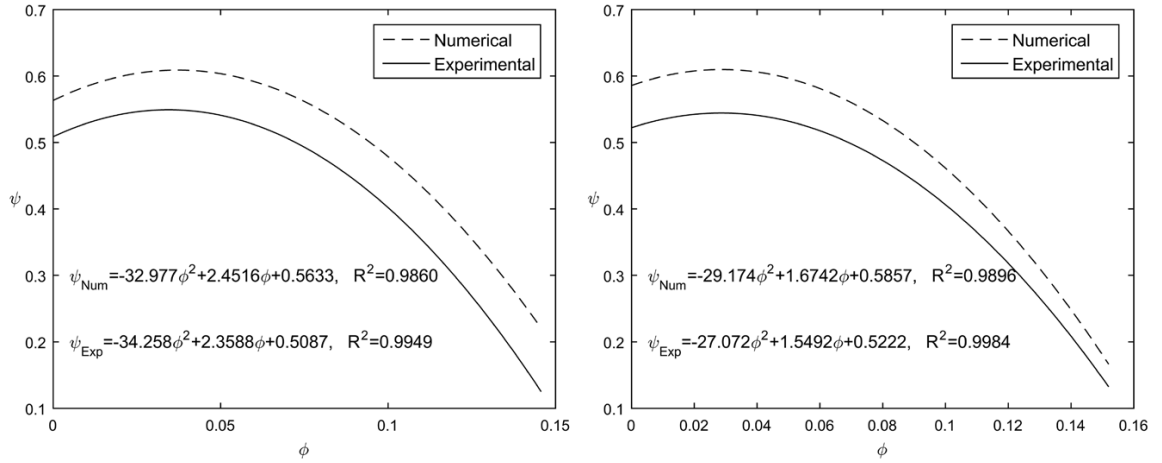


Figure 4.14: Numerical and experimental head coefficient (ψ) vs. flow coefficient (ϕ) for impellers A (left) and B (right) [66].

impellers A and B. The second order polynomials are fitted to the data points, with equations and R^2 values presented on the graphs. This graph in addition to Figures 4.13 and 4.7 is useful for preliminary design and finding the optimum diameter and rotational speed for a desired range of flow rate and pressure rise. The maximum difference between numerical and experimental head coefficients at the design point is 0.05, which is 9.1%.

Figure 4.15 is presenting a typical H-Q curve for impeller A in steady conditions of the O-loop in comparison with transient flow in a cardiovascular simulator [104, 103]. The top axis relates to the steady flow curve with a pressure of 90.84 mmHg at 5 L/min and the bottom axis is related to the transient flow at 5 L/min with maximum and minimum pressures of 115 and 78 mmHg and an average of 90.72 mmHg.

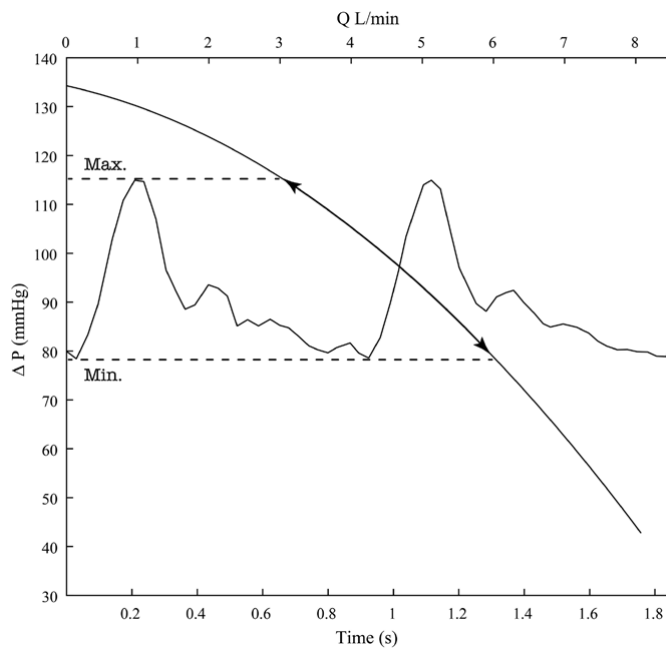


Figure 4.15: Impeller A performing in steady condition and transient flow [66].

4.2 In-vitro Investigations of Axial Pumps as MCS Devices

The in-vitro investigations of the axial pumps include designing the geometry of the blades in SolidWorks, manufacturing the impellers and testing them using a single loop test rig, designed and developed for this purpose.

4.2.1 SolidWorks

The MATLAB code output is three EXCEL files with (x, y) coordinates of the airfoils representing the hub, tip and the mean effective diameter. The files are imported into SolidWorks as 2D curves. The curves are then converted to surfaces and then lofted to create a single blade of impeller A, Figure 4.16.



Figure 4.16: Drawing the impeller blade in SolidWorks.

Using a suitable hub at the center, the blade is then patterned around the hub and fillets are implemented on the edges to avoid manufacturing complications. Figure 4.17 shows the representative impeller A in SolidWorks with a 20° outlet angle.

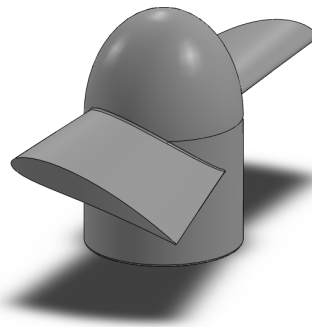


Figure 4.17: Impeller A, created in SolidWorks.

4.2.2 The O-loop

A single loop test rig similar to that for centrifugal pumps is designed to test the impellers. The O-loop is divided into three sections similar to the centrifugal test setup.

The Pump

The pump consists of the impeller and housing.

The Power System

The power system consists of a high-speed Brushless DC (BLDC) motor (Maxon, EC max 22, 25 Watts), a controller to vary the motor speed and a coupling mechanism to directly drive the rotor of the pump through sealed ball bearings.

The Circulation System

The circulation system consists of tubing, a hand operated Hoffman clip to manually change the resistance in the system, an electromagnetic Siemens flow meter to measure the flow rate and two pressure transducers to measure the pressure at the inlet and outlet of the pump.

Figures 4.18 and 4.19 show the schematic and the actual O-loop.

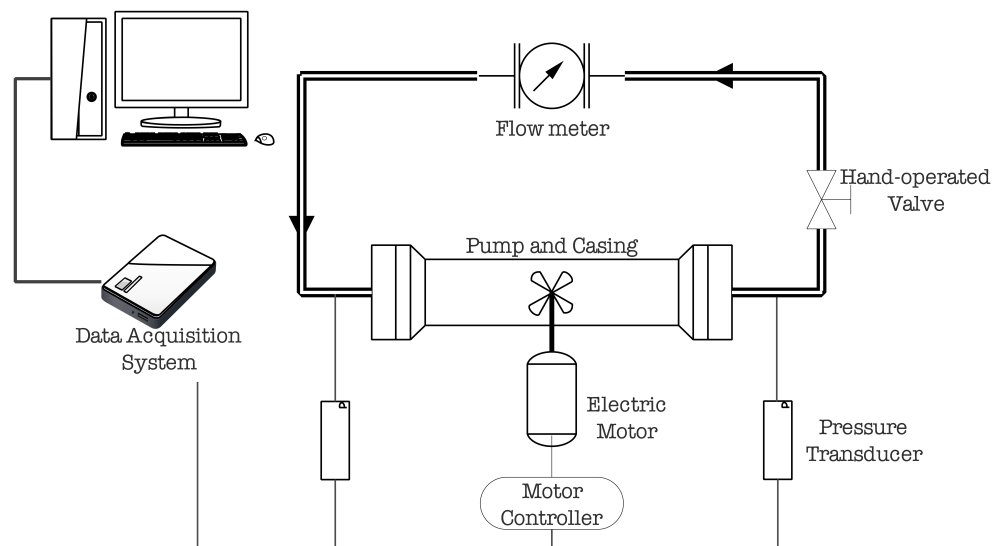


Figure 4.18: The schematic diagram of the axial O-loop.

4.2.3 The Working Fluid

A blood analog solution was used as the working fluid in the O-loop. The solution is 65% water and 35% glycerol (by volume) in order to obtain the closest values of density (1050 kg/m^3) and viscosity ($0.0036 \text{ Pa}\cdot\text{s}$) to those of human blood at 37°C .

4.2.4 Measurement System

The same measurement system used in the centrifugal pump test setup is employed to measure and record the data. The electric motor, pressure transducers and the

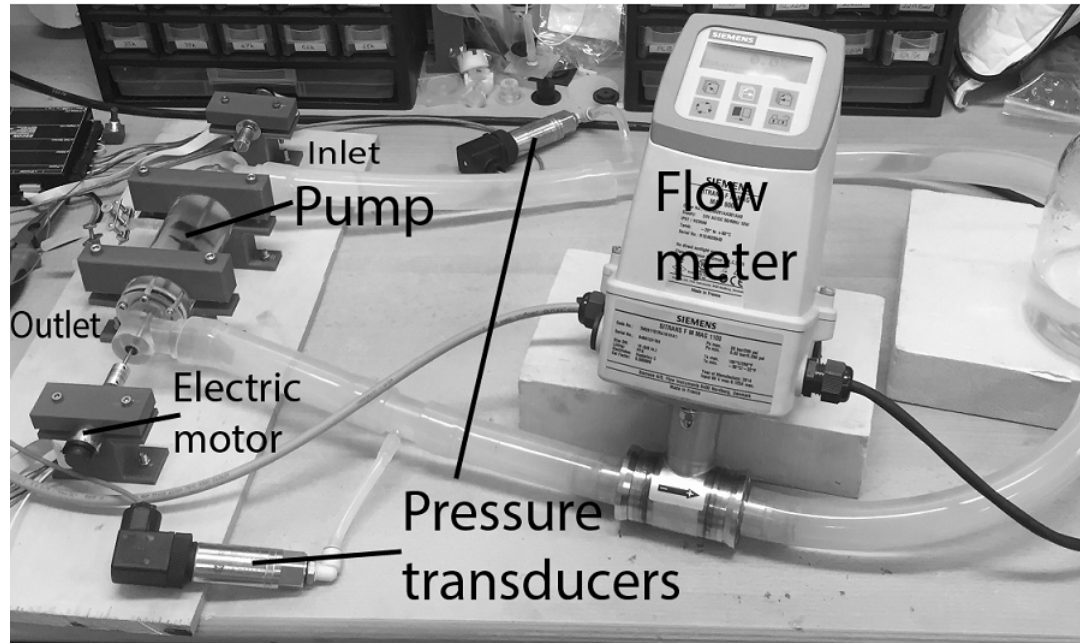


Figure 4.19: The O-loop.

flow meter are connected to a computer through a data acquisition system and the operating conditions are controlled (rotational speed) and recorded (pressure rise, flow rate, current, voltage) using LabView program created for this purpose.

4.2.5 Results and Discussion

Efficiency, pressure rise, specific speed and diameter, head and flow coefficients are measured or calculated at different operating conditions and are plotted in relevant graphs. The experimental results are presented in several forms. The performance curves are presented for the representative impelle A, with a 20° outlet angle, operating at different rotational speeds in order to study the effect of rotational speed on the performance for a typical impeller. The curves are also presented for a group of impellers with different outlet angles, in order to study the effect of outlet angle on the pump performance. The nondimensional characteristics of efficiency, specific speed and specific diameter of the manufactured pumps are presented in $\eta - n_s$ and $n_s - d_s$ Cordier diagram.

Figure 4.20 shows the profile of impeller A with 22mm diameter and a 20° outlet angle.

Rotational Speed

The first set of analyses examined the impact of rotational speed on the pump performance. Figure 4.21b shows the experimental efficiency (η) versus flow ratio

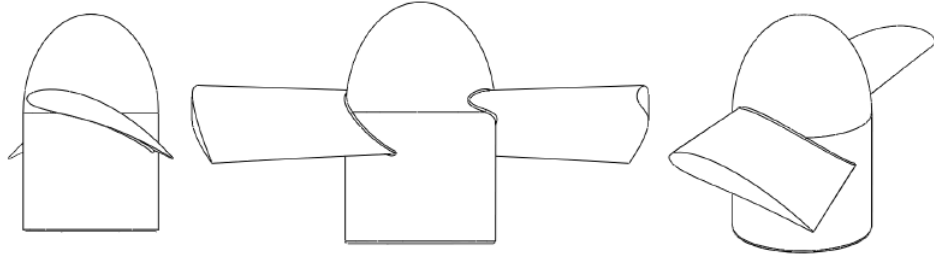


Figure 4.20: The profile of impeller A, selected for results presentation.

(Q/Q_{des}) for impeller A at different rotational speeds 4000-7000 rpm. In general, for axial pumps, the efficiency increases with the flow rate for the entire range, whereas in centrifugal pumps, there is an optimum point of efficiency where it decreases after a certain point and is normally higher than the design point flow rate.

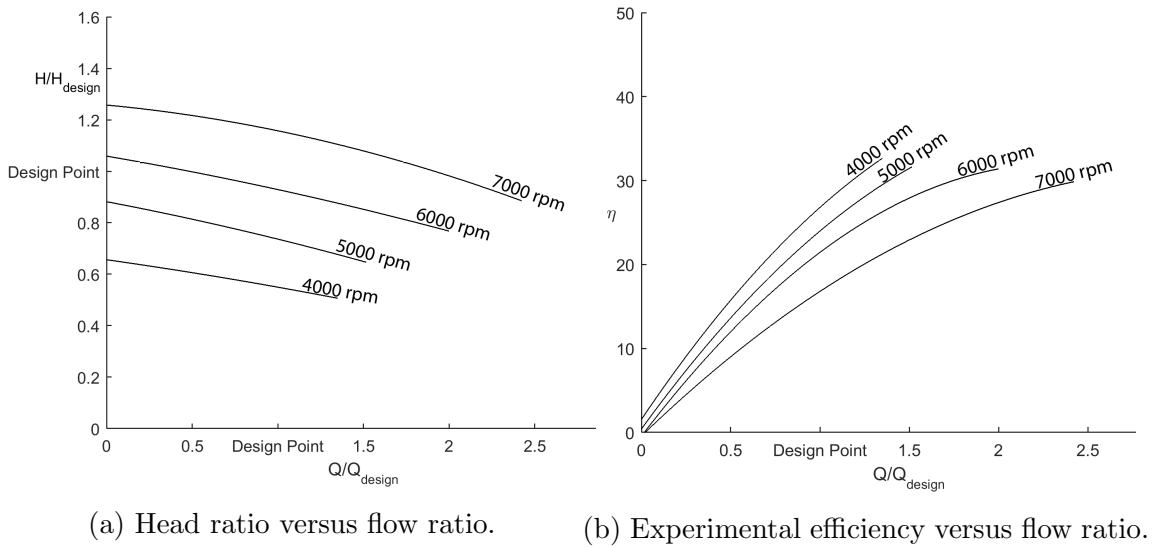


Figure 4.21: Performance curves of the impeller A at different rotational speeds.

Figure 4.21b shows the same values of maximum efficiency at different rotational speeds ($\approx 30\%$) for the pump, but at different flow rates. The slope of the curve is higher for lower rotational speeds, resulting in a higher efficiency at the design point. Therefore, the lowest rotational speed is the most favourable in terms of efficiency. However, the rotational speed needs to be sufficient for the pump to produce the required pressure rise. It is necessary to consider both efficiency and head rise graphs in order to select the most suitable rotational speed.

Figure 4.21a illustrates the head ratio (H/H_{des}) versus flow ratio (Q/Q_{des}) for the same impeller at the same rotational speeds. For this particular impeller ($\beta_2=20^\circ$), 5000-6000 rpm results in the required pressure rise being delivered by the pump. 4000 rpm produces $\approx 60\%$ and 7000 rpm results in ≈ 1.2 times the design point pres-

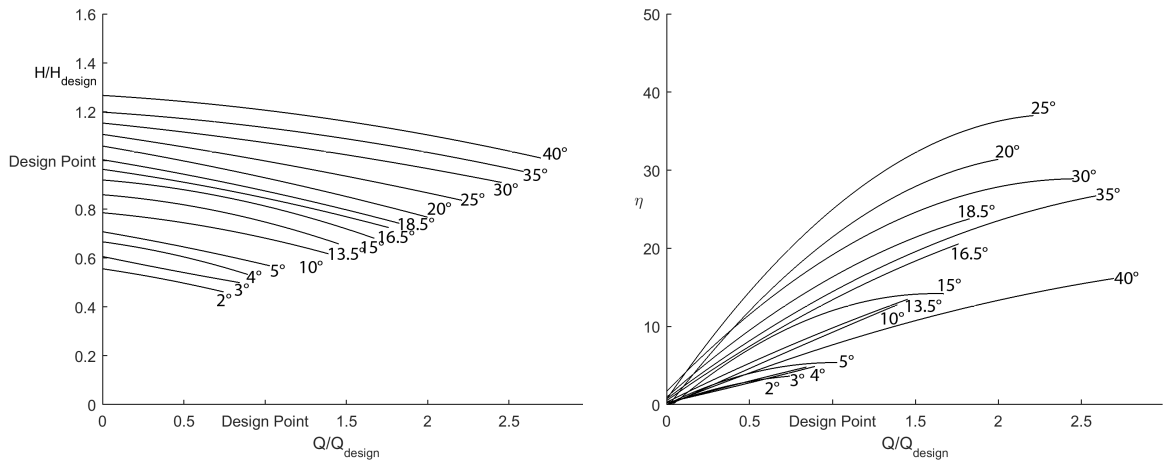
Table 4.1: Numerical and experimental results of impeller A ($\beta_2=20^\circ$, 22mm diameter)

Rotational Speed (ω)	Axial Thrust (N)	Radial Thrust (N)	NIH (g/100L)	Max. Efficiency (%)	Efficiency at DP (%)	Head ratio at DP
4000 rpm	1.186	0.006	0.0052	32.74	27.81	0.54
5000 rpm	1.580	0.007	0.0067	31.66	25.25	0.74
6000 rpm	1.945	0.007	0.0083	30.98	19.95	0.92
7000 rpm	2.250	0.008	0.0097	30.37	17.64	1.14

sure rise. Figures 3.31a, 3.31b and 4.21 present a complete set of numerical and experimental results for impeller A. The data extracted from these graphs are presented in Table 4.1. The data suggest that for this particular impeller, 5000-6000 rpm is a suitable range for rotational speed. 6000 rpm may have advantage over 5000 rpm in terms of the required pressure rise. The impeller will almost meet the design point pressure rise at 6000 rpm compared to $\approx 75\%$ of pressure rise at 5000 rpm. However, the probability of hæmolysis is higher (0.0083) and closer to the critical value at 6000 rpm.

Outlet Angle

The effect of blade outlet angle on the pump performance is studied by testing a group of 14 impellers. Figures 4.22b and 4.22a compare the experimental efficiency and head ratio (H/H_{des}) versus flow ratio (Q/Q_{des}) for the impellers rotating at 6000 rpm.



(a) Head ratio versus flow ratio for different outlet angles at 6000 rpm. (b) Experimental efficiency versus flow ratio for different outlet angles at 6000 rpm.

Figure 4.22: Performance curves for different outlet angles, rotating at 6000 rpm.

The results show that low outlet angles ($<10^\circ$) may not reach the required flow rate and angles lower than 15° may deliver the design point pressure rise, but fail to

meet the required pressure rise at this rotational speed. Increasing the rotational speeds for these pumps to reach the design point characteristics may lead to high shear stress and subsequent NIH and therefore increase the probability of haemolysis. Impellers with higher outlet angles ($>30^\circ$) may reach both design point flow rate and pressure rise at relatively low speeds, however, the efficiency of the pump decreases at these outlet angles.

Table 4.2: Numerical and experimental results of impellers with 16.5° - 35° outlet angle, rotating at 6000 rpm.

Outlet Angle (β_2)	Axial Thrust (N)	Radial Thrust (N)	NIH (g/100L)	Max. Efficiency (%)	Efficiency at DP (%)	Head ratio at DP
16.5°	1.593	0.005	0.0077	20.69	12.98	0.85
18.5°	1.696	0.006	0.0082	24.14	16.58	0.88
20°	1.945	0.007	0.0083	30.98	19.95	0.92
25°	2.218	0.009	0.0088	37.77	25.50	0.98
30°	2.458	0.010	0.0094	30.57	20.36	1.07
35°	2.870	0.012	0.0101	16.01	7.64	1.13

Based on the graphs, the optimum outlet angle for achieving the highest efficiency is within the range 20° - 30° and the required pressure rise is met for the impellers with 18.5° - 30° outlet angle. The values slightly differ for other rotational speeds. Considering the data for 4000-7000 rpm, the favourable range of outlet angle is 20° - 30° for efficiency and 16.5° - 35° for pressure rise. Figures 4.22b and 4.22a alongside 3.32a, 3.32b and 3.33 provide sufficient information for the selection of outlet angle and rotational speed for this application. The data points are extracted from the graphs for the desired range of outlet angle and presented in Table 4.2.

Number of Blades

Five impellers with high outlet angles (20° , 25° , 30° , 35° and 40°) are manufactured with 2, 4 and 6 blades (15 in total) in order to study the effect of blade number on the performance of the pumps. The results show a consistent pattern for all angles and the performance curves of impellers with 20° outlet angle are presented in Figure 4.23, rotating at 6000 rpm.

Based on the theoretical and experimental equations for slip, the ideal flow guidance may be achieved by increasing the number of blades, so the flow leaves the impeller outlet at the exact blade angle. However, beyond a particular value, the slip factor decreases due to increased blockage area. This value is considered a balance between the excessively high surface friction in pumps with too many blades and unguided diffusion in pumps with too few blades. The pressure rise results as shown in Figure 4.23a follow this argument. The 2 bladed impeller produced the lowest pressure rise

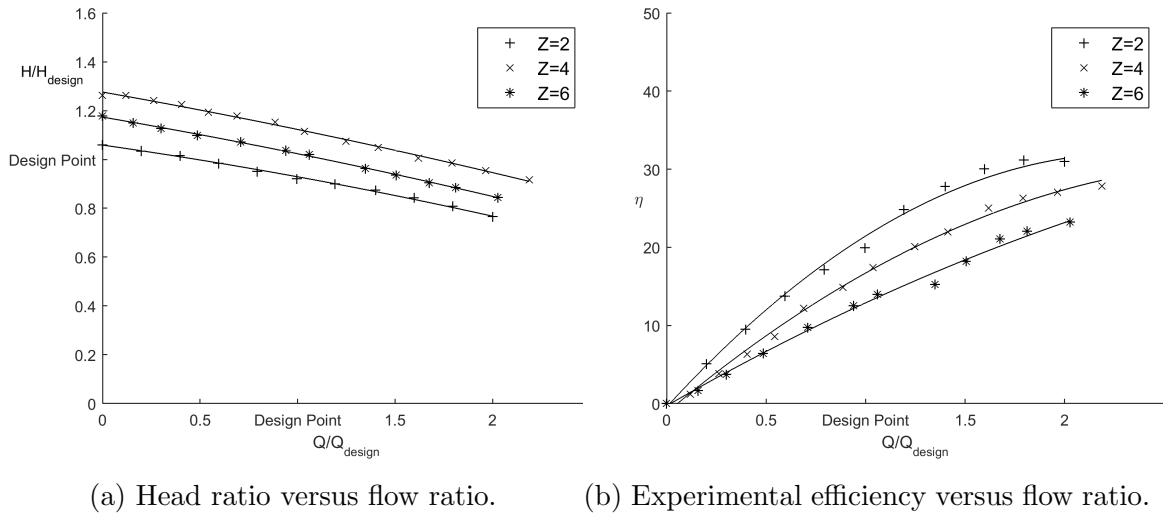


Figure 4.23: Performance curves of three impellers with 20° outlet angle, rotating at 6000 rpm.

among the three with $\approx 90\%$ design point. The 4 bladed impeller performed with the highest pressure ratio (≈ 1.2 times) and the head ratio decreased to < 1.1 for the impeller with 6 blades.

It is apparent from Figure 4.23b that the efficiency of the pumps are higher with lower number of blades. However, this is the result of a constant rotational speed which leads to different values of pressure rise for the pumps (Figure 4.23a). In order to compare the efficiencies, the pumps must rotate at different rotational speeds in which they produce the design point pressure rise. For this purpose, the rotational speeds are changed to 6400, 5300 and 5500 rpm for the 2, 4 and 6 bladed impellers respectively. The impellers produced the design point pressure rise at these speeds and achieved design point efficiencies of 18%, 19% and 16% respectively. This was implemented for the analysis of all 5 groups of impellers and showed very close efficiencies for 2 and 4 bladed and slightly lower for 6 bladed impellers.

Nondimensionals

Figure 4.24a plots the hydraulic efficiency versus specific speed of 14 impellers with different characteristics, presented in Table 4.3. The data points are not presented for clarity and third order polynomials are fitted.

Once an impeller is selected, design and off-design efficiencies may be predicted from the data of a relevant impeller. The results show that the highest efficiencies are achieved within the range of specific speeds 0.6-1. This range is slightly different for industrial axial pumps due to different region of Re number. The published nondimensional data of industrial pumps suggests a specific speed of 1-2 for highest efficiencies in axial pumps ($1 < n_s < 6$ for axial pumps) [12]. The industrial pumps

perform in $Re=10^8$, whereas the blood pumps in this study are in $Re<10^6$.

Comparing the $\eta - n_s$ graph of industrial and small blood pumps shows a much smaller slope for the descending part of the curves. high efficiencies are obtained at high specific speeds. The data of high specific speed small pumps are very limited compared to industrial pumps, but the efficiency of these pumps have not yet been demonstrated to reach the levels seen in equivalent specific speed industrial pumps [119].

Figure 4.24b plots the head and flow coefficients for the impellers. Second order polynomial curves are fitted to the data points as they were the lowest degree that fitted most of the data. The shape of the curves are useful for preliminary design of an impeller. It is possible to find an impeller with the required pattern of performance characteristics through scaling the dimensions using the head and flow coefficients (ψ and ϕ) in order to produce the required pressure rise and flow rate. The graph shows a slight depression in most of the pumps in the flow coefficient range of 0.05-0.15 and is indicative of the flow separation. By mapping this part of the curves ($0.05<\phi<0.15$) into the H-Q curves of the pumps, the critical head-flow region of each pump can be investigated individually.

Table 4.3 provides the $\eta - n_s$ and $\psi - \phi$ curve fits and the R^2 values that are presented in Figures 4.24a and 4.24b. The combination of Figures 4.24a and 4.24b together with Table 4.3, is useful for the preliminary design when combined with the pump geometry data.

Figure 4.25 is a Cordier diagram showing specific speed and specific diameter of all 62 pumps based on the highest efficiency points of each pump.

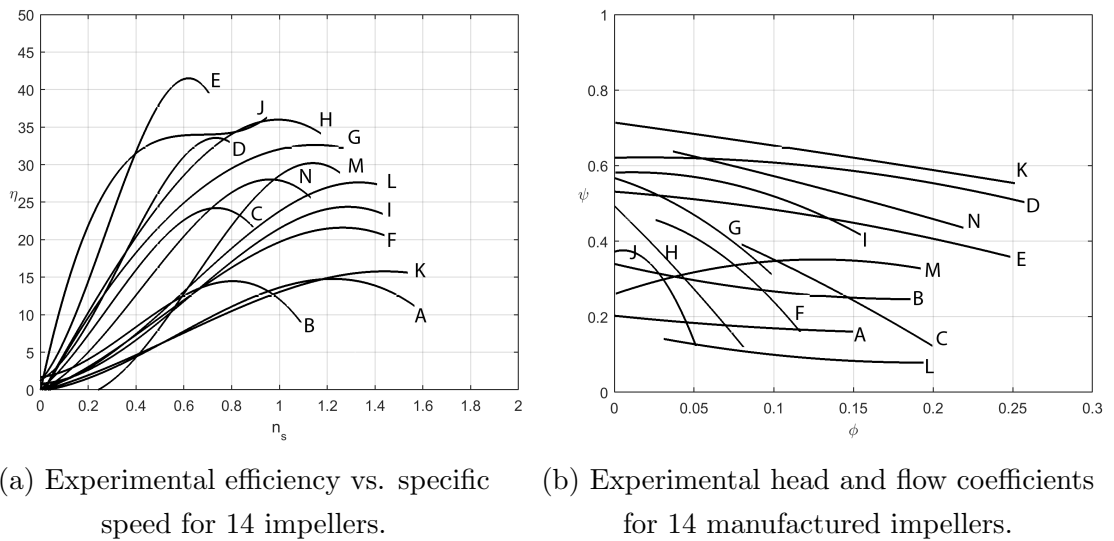


Figure 4.24: Efficiency and head-flow coefficients for 14 impellers.

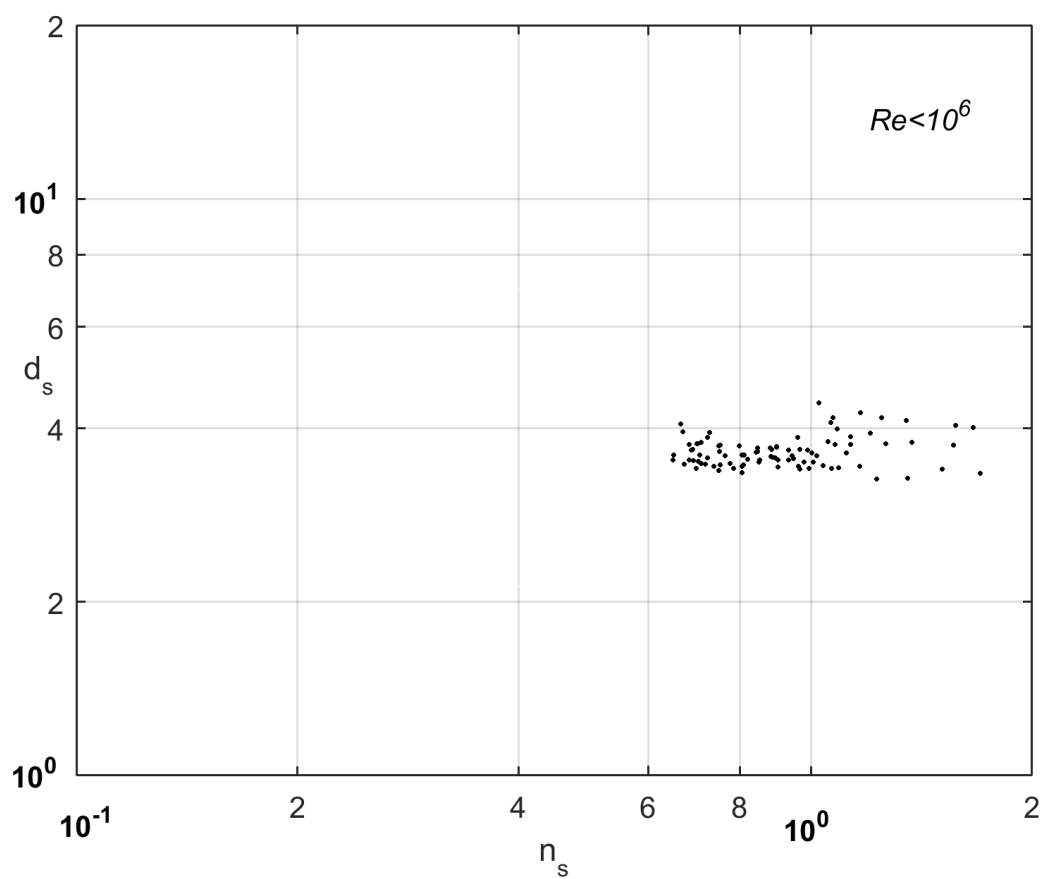


Figure 4.25: Highest efficiency points on $n_s - d_s$ Cordier diagram for all impellers ($4 \times 10^4 < Re < 2 \times 10^5$).

Table 4.3: Data for axial pumps.

Pump	Z	(β_2)	Shut off ψ	$\eta = f(n_s)$	R^2	$\psi = f(\phi)$	R^2
A	6	35°	0.19	$\eta = -13.342n_s^3 + 22.649n_s^2 + 4.474n_s - 0.1715$	0.9786	$\psi = 1.0387\phi^2 - 0.43369\phi + 0.2025$	0.852
B	6	30°	0.32	$\eta = -43.847n_s^3 + 50.855n_s^2 + 3.3511n_s + 1.6885$	0.9651	$\psi = 2.639\phi^2 - 0.9926\phi + 0.3397$	0.893
C	2	10°	0.38	$\eta = -70.748n_s^3 + 59.56n_s^2 + 27.387n_s + 0.0019$	0.9805	$\psi = 2.5586\phi^2 - 1.5286\phi + 0.5297$	0.9986
D	2	16.5°	0.59	$\eta = -133.03n_s^3 + 135.47n_s^2 + 16.192n_s + 1.2957$	0.9734	$\psi = -2.0905\phi^2 + 0.0808\phi + 0.6209$	0.8725
E	2	25°	0.52	$\eta = -242.2n_s^3 + 195.69n_s^2 + 36.834n_s + 1.1703$	0.992	$\psi = -1.4742\phi^2 - 0.32872\phi + 0.5311$	0.9889
F	2	3°	0.38	$\eta = -13.715n_s^3 + 21.066n_s^2 + 12.535n_s - 0.2068$	0.9959	$\psi = -20.705\phi^2 - 0.3167\phi + 0.4783$	0.9926
G	2	35°	0.51	$\eta = -0.2091n_s^3 - 25.031n_s^2 + 58.364n_s - 1.07$	0.9866	$\psi = -13.044\phi^2 - 1.2968\phi + 0.567$	0.9869
H	4	25°	0.37	$\eta = -17.505n_s^3 - 2.3826n_s^2 + 56.711n_s - 0.8329$	0.9932	$\psi = -6.6264\phi^2 - 4.0732\phi + 0.493$	0.998
I	4	15°	0.58	$\eta = -20.86n_s^3 + 39.419n_s^2 + 2.1413n_s + 0.7912$	0.9886	$\psi = -8.0285\phi^2 + 0.1765\phi + 0.5813$	0.9362
J	2	13.5°	0.37	$\eta = 108.37n_s^3 - 220.45n_s^2 + 15.08n_s - 0.1912$	0.9943	$\psi = -120.99\phi^2 + 1.3153\phi + 0.372$	0.9921
K	6	25°	0.61	$\eta = -6.5516n_s^3 + 11.173n_s^2 + 8.5762n_s - 0.1809$	0.9989	$\psi = -0.1943\phi^2 - 0.5902\phi + 0.714$	0.8999
L	4	30°	0.11	$\eta = -19.516n_s^3 + 36.563n_s^2 + 6.4985n_s + 0.2291$	0.9987	$\psi = 2.3797\phi^2 - 0.9201\phi + 0.1673$	0.9392
M	4	20°	0.36	$\eta = -62.124n_s^3 + 119.25n_s^2 - 29.638n_s + 1.0549$	0.9803	$\psi = -5.6509\phi^2 + 1.4402\phi + 0.2596$	0.793
N	4	18.5°	0.56	$\eta = -46.471n_s^3 + 58.744n_s^2 + 15.756n_s - 0.1294$	0.9954	$\psi = -0.6196\phi^2 - 0.9503\phi + 0.6734$	0.9887

Chapter 5

Axial Flow versus Centrifugal Flow VADs

In the previous chapters we observed how small centrifugal and axial pumps have grown in medical industry because of their small size, ease of implantation, reliability and efficient performance. We discussed how these pumps perform in different conditions of flow, pressure and rotational speed as heart assist devices. In this chapter, we will further explore these two types of pumps and whether one type has hemodynamic or clinical advantages. Significant clinical advantages have been reported [120] for axial flow VADs due to faster reduction in ventricular pressure but in cost of a higher ventricular suction. The study states that there may be a custom selection of VADs in the future based on the patient's specific conditions. For instance, during exercise or stressful conditions, an axial flow VAD may be advantageous over centrifugal VADs for patients with pulmonary hypertension.

In this chapter, we will evaluate the technological and clinical considerations of axial and centrifugal pumps and compare the two types and discuss their potential differences as heart assist devices. We further apply the transient flow conditions into the discussion in order to compare the pump performance in transient and continuous flow conditions.

5.1 Technological Considerations

The different flow paths of centrifugal and axial pumps leads to different pressure and flow characteristics. In a recent study [45], the pressure unloading of HeartMate II and VentrAssist were investigated in a mock flow loop model. The study reported technological advantages of the centrifugal device due to lower power consumption and higher sensitivity to pre and after-load. The authors further characterized the hemodynamic performance of the devices by their HQ curves to determine the differences between them.

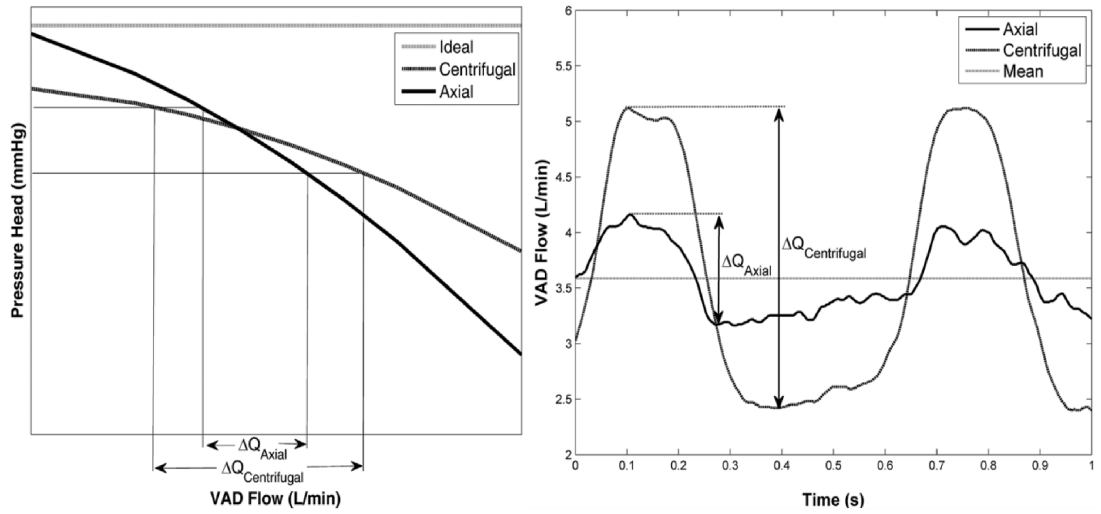


Figure 5.1: Axial and centrifugal VADs HQ curves and flow waveforms recorded in LVAD clinical patients [45].

It is undeniable that a constant pressure head versus flow rate (horizontal HQ line) is an ideal performance for a blood pump. Although there are various HQ curve trends for the two types of pumps, it is evident that in general, centrifugal pump HQ curve has a lower slope and is *flatter* compared to that of axial pumps. The higher sensitivity to pre and after-load is a result of this difference [41]. This higher sensitivity leads to a lower probability of ventricular suction but also a lower flow rate at an elevated after-load [45].

Centrifugal pumps produce a larger span of variation of flow rate compared to axial pumps at the same range of pressure rise due to the same reason (pressure sensitivity), seen in Figure 5.1. The native ventricular contraction and the subsequent higher span of variation in pressure rise and flow makes the centrifugal pump flow more similar to the pulsatile flow of human body. Therefore, these pumps result in a larger range of left ventricular end systolic and diastolic volume and higher aortic pulsatile pressure [126]. However, at a constant flow rate and pre and after-load, the mean aortic pressures and flow rates are quite similar in axial and centrifugal pumps, shown in Figure 5.2.

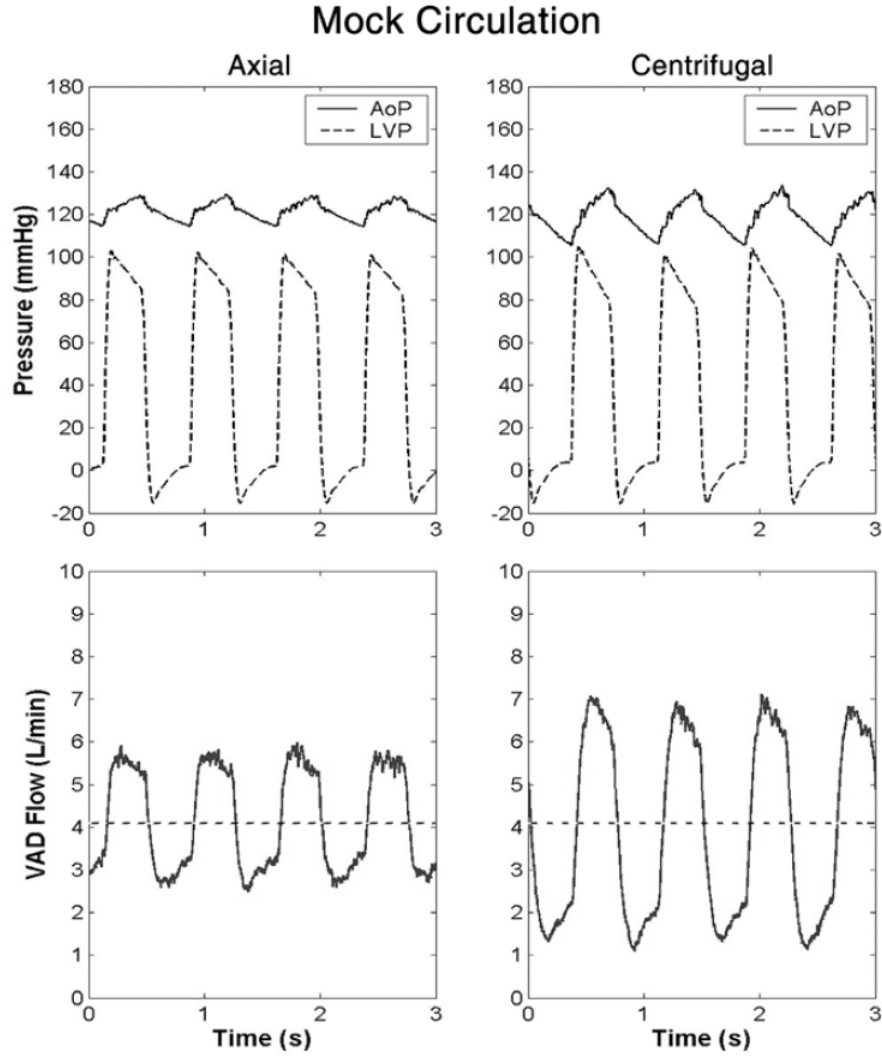


Figure 5.2: Centrifugal and axial LVAD head-flow, LV and aorta pressure waveforms in a mock flow loop model [45].

The higher slope of head-flow curves for axial flow pumps results in a higher degree polynomial relationship between current and flow and leads to an inaccurate estimation of flow. This argument has been confirmed by a clinical studies [115, 96] showing inconsistency in the flow measurements compared to the estimated values.

5.2 Clinical Considerations

Centrifugal pumps have higher efficiency compared to axial flow pumps and therefore smaller battery packs and longer power supply may be an advantage of using these devices. However, the battery and controller size decrement of heart assist devices is not likely to have a significant impact on the evaluation of the device. As mentioned earlier, centrifugal LVADs are more sensitive to pre and after-load, however, compared to the native heart, both types of pumps are relatively insensitive [107, 71].

Figure 5.3 shows clinically observed LV and aortic pressure waveforms for the same axial and centrifugal LVADs. Centrifugal pumps produce a higher range of pressure compared to axial pumps at the same flow rates. However, the variation in the flow and pressure is reduced for this generation compared to pulsatile devices. The potential adverse events due to this reduced pressure pulsatility may not be compensated [140, 15, 124, 125].

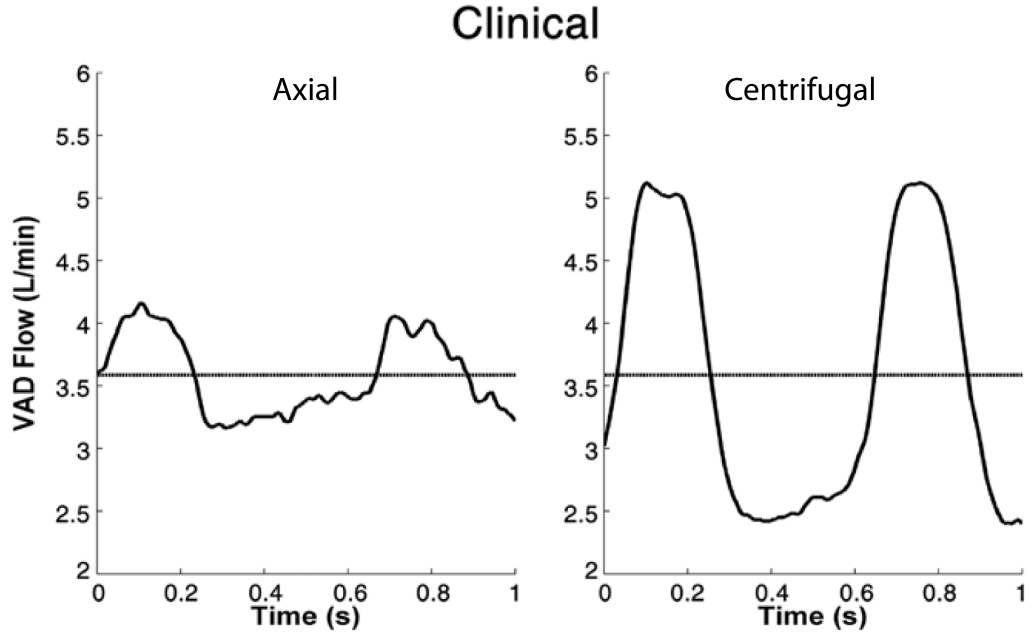


Figure 5.3: Centrifugal and axial LVAD head-flow, LV and aorta pressure waveforms, clinical observations [45].

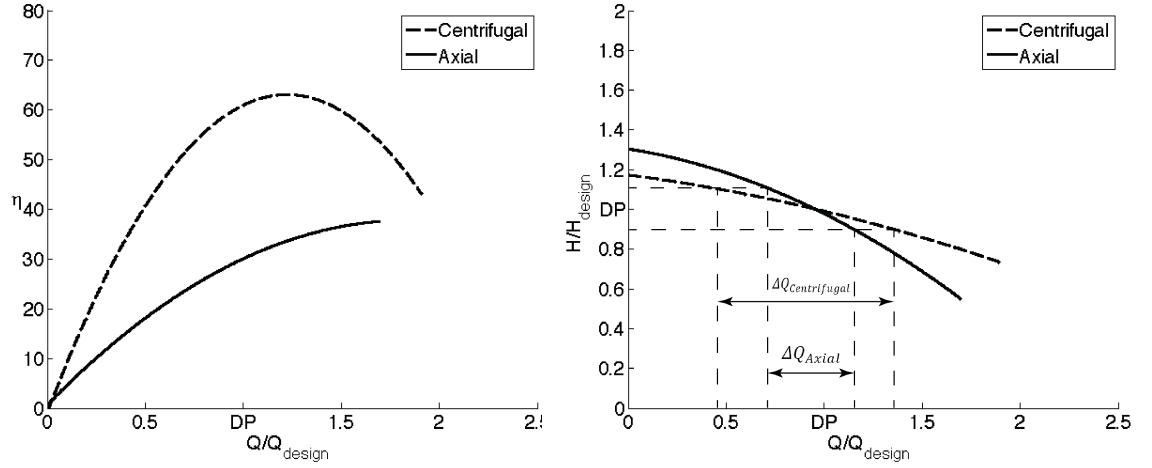
Although axial and centrifugal pumps have differences in their flow characteristics, these differences are not as significant as the contrast between continuous and pulsatile flow devices. The differences between axial and centrifugal VADs are mainly pressure and flow range and therefore may be controlled by changing the resistance or rotational speed. The result will be a slight change in the efficiency, battery size or supply period rather than the flow nature.

5.3 A Comprehensive Analogy

The chapter is concluded with a comprehensive comparison between two selected pumps. An axial and a centrifugal pump are selected based on numerical and experimental results. Both pumps are suitable in terms of hemocompatibility, performance and force characteristics.

Figure 5.4 shows the efficiency and HQ curves for axial and centrifugal pumps. The efficiency of the centrifugal pump has a peak value at about flow ratio of 1.2 and

then decreases. For the axial pump, the efficiency increases with flow rate and gets close to the efficiency of the centrifugal pump at high flow rates. At the design point, the efficiency of centrifugal pump is twice as the axial pump. The head ratio range of 0.9-1.1 is selected in Figure 5.4b and the range of flow rates corresponding to the head ratios are shown for both pumps. The trends are similar to the axial and centrifugal LVAD results reported by Giridharan [45], shown in Figure 5.1.



(a) Centrifugal and axial efficiency vs. flow ratio. (b) Centrifugal and axial head ratio vs. flow ratio.

Figure 5.4: Performance curves of selected axial and centrifugal pumps.

Figure 5.5 shows the data points of Figures 4.7 and 4.25 altogether. The graph is an $n_s - d_s$ Cordier diagram with the highest efficiency points of axial and centrifugal pumps investigated in this study. Figure 5.6 shows the same data points on Balje's diagram (Figure 1.14) in order to compare the regions of high efficiency small pumps with that of industrial pumps.

Table 5.1 show the axial and centrifugal pumps specifications and output values.

The results show higher magnitudes of axial thrust for axial pumps and higher radial thrust for centrifugal pumps, as expected. The force analysis and the effect of design parameters and rotational speed on axial and radial forces will help in the design process of mechanical, hydrodynamic or magnetic bearings of heart assist devices. The axial pump also shows a higher probability of hæmolysis, mainly due to their higher rotational speeds and shear stress induced in the pump.

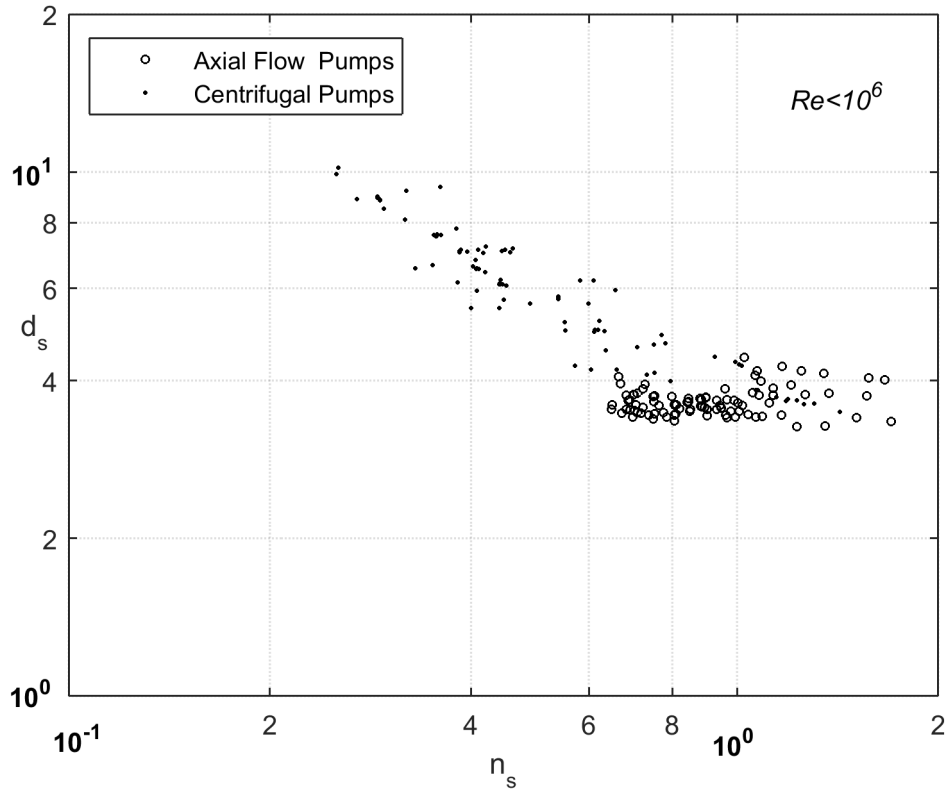
Figure 5.5: Highest efficiency points of centrifugal and axial pumps on $n_s - d_s$ Cordier diagram.

Table 5.1: Design parameters, specifications and output values of two selected pumps.

Pump	Axial	Centrifugal
Rotational Speed, ω (rpm)	6625	2615
diameter, D (mm)	22	31.5
number of blades Z	2	5
outlet angle β_2	25°	27.5°
Max. Efficiency %	37.26	65.77
Efficiency at DP %	30.28	61.56
ΔQ (L/m)	3.6-6	2.4-6.75
Pressure rise at DP (mmHg)	89.77	90.56
NIH (g/100L)	0.072	0.046
Radial Thrust (N)	0.0016	0.361
Axial Thrust (N)	2.066	0.768
Shear stress (Pa)	116	64

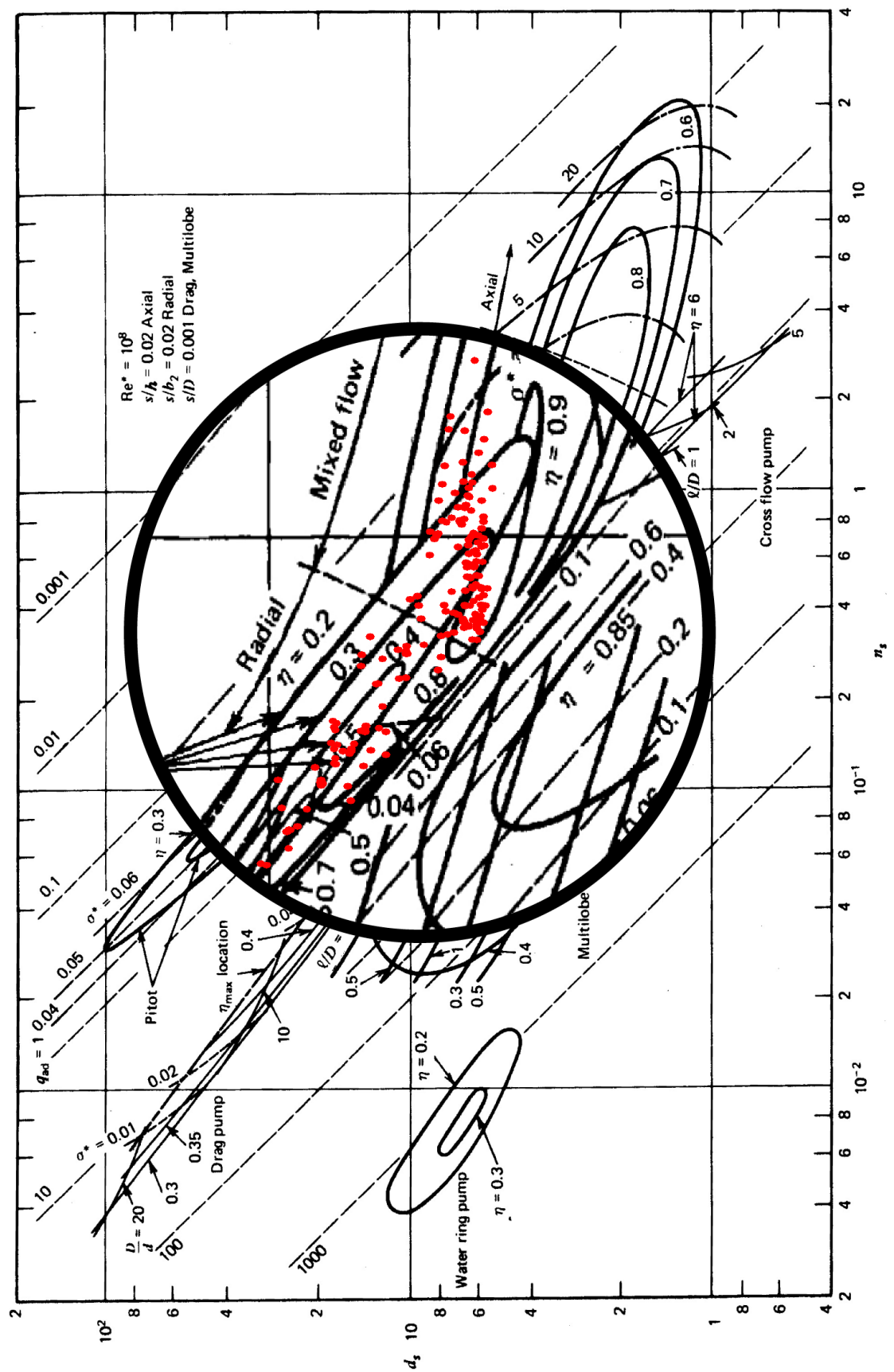


Figure 5.6: Highest efficiency points of small centrifugal and axial pumps on Balje's industrial $n_s - d_s$ Cordier diagram.

Chapter 6

Reflections and Outlook

Decades of disciplinary studies have advanced our understanding of engineering based design of heart assist devices where the preconception that the conventional pump design methods can tackle certain problems has prevailed in science. However, with the emergence of new sources of in-vivo and clinical data, empirically grounded and large-scale studies of old and new problems have become possible through a combination of computational analysis and experimental techniques. This thesis has demonstrated the use of such methods and more importantly has collected a database of nondimensional parameters of small centrifugal and axial pumps for ventricular assist devices.

The work presented in this dissertation is the product of three segments; the preliminary design of axial and centrifugal pumps based on conventional methods and experimental data of previously designed blood pumps, computational analysis of the designed pumps and data-driven parameter optimization, in-vitro investigation of the selected models and validation of the proposed numerical methods.

The approach taken has been different for axial and centrifugal pumps. For centrifugal pumps, +100 impellers were numerically modeled and studied for performance and hemocompatibility. The experimental investigations were conducted on 15 impellers in order to validate the computational models and the numerical results and therefore, the presented nondimensional data are mainly the results of in-silico analysis. For axial pumps, all the numerically analyzed impellers are tested and the nondimensional data are entirely experimental results. The numerical results were used for the hemocompatibility study of the pumps and the force analysis for future bearing calculations.

6.1 Summary of Contributions

The thesis that *a nondimensional and parametric approach can advance our understanding of the parametric effect on the performance and hemocompatibility of small sized pumps for MCS devices* has been substantiated through the following contributions presented in this dissertation:

Parametric approach numerical analysis of axial and centrifugal pumps:

In chapter 3, we introduced a simple parametric approach to the numerical analysis of the pumps. We modeled the hæmolysis with an Eulerian approach and related the hæmolysis index (HI) to the shear rate and exposure time through a power law equation based on empirical observations. We evaluated each pump by calculating the Normalized Index of Hæmolysis (NIH) and investigated the effect of different design parameters (number of blades, outlet width and angle and rotational speed) on the hemocompatibility of the device by several graphs. The analytical model presented in this work will help the blood pump designers to select their design parameters accordingly for a lower probability of blood complications.

Parametric approach in-vitro investigations of axial and centrifugal pumps:

In chapter 4, we introduced a parametric approach to the experimental evaluation of small axial and centrifugal pumps. We conducted in-vitro investigations on +150 pumps with different design characteristics in various conditions of flow, pressure and rotational speeds. The flow rate, pressure rise, efficiency, head coefficient and flow coefficient of each pump was measured or calculated at different conditions and presented in relevant diagrams for comparison. The results and equations presented in this work provides reliable empirical relationships between the design parameters and the performance of small pumps. Such data will help the designers to select their parameters accordingly and reach their desired output.

Nondimensional database:

In chapter 5, we evaluated and compared the small axial and centrifugal pumps and discussed their advantages and disadvantages with technological and clinical considerations. We collected the nondimensional specific speed and specific diameter data of the pumps ($n_s - d_s$) and plotted the data points on a Cordier diagram. We also mapped the data points on the Balje's Cordier diagram of industrial pumps for comparison and to investigate the effect of Reynolds number on the performance of the pumps. The empirical equations, Cordier diagrams and nondimensional data presented in this work will enable the preliminary design of small axial and centrifugal pumps for VADs and MCS devices suitable for different stages of congestive heart failure.

6.2 Future Directions & Outlook

This dissertation presented a computational and experimental approach to the evaluation of small axial and centrifugal pumps, which has been under-explored in the predominantly theoretical field of pump design for heart assist devices. The nondimensional analysis of the pumps holds the key to understanding the similarity concept of fluid mechanics. With new medical application of rotary pumps, studying how the pump design parameters affect the performance and reliability of the device will become increasingly popular. Furthermore, the differences between the flow fields of blood pumps and industrial pumps will necessitate the use of new empirical data, shifting the parametric and nondimensional data of rotary pumps from an approach to a necessary method of evaluating the performance and hemocompatibility of the devices.

The coefficients and nondimensional characteristics and the diagrams made by the data points are routine in the field of turbomachinery pump design and testing [12, 128, 151, 57, 150]. Blood pumps differ from those historically reported due to their different flow fields, Reynolds number region and the constraints imposed related to hemocompatibility conditions. As illustrated in this dissertation, the performance of small axial and centrifugal pumps follows expected trends but shifted to different regions on the graph due to the change in Reynolds number. To the best of our knowledge, the nondimensional database produced in this body of work is significantly larger compared to similar studies previously reported in this field. The parametric approach introduced in this dissertation for the purpose of comparison is thoroughly focused on particular variables, making it a suitable approach for the evaluation of the design parameters.

However, this dissertation, like all works of its type, includes insufficient detail to perfectly and precisely design new pumps from an existing model. More data would have to be published by authors and designers in nondimensional forms. It is fascinating how the test results from different research projects fall into a recognizable concerted pattern in a nondimensional format. By collecting more experimental results and creating a more comprehensive database, a blood pump designer can make a first estimation at the size, type, rotational speed and performance of a pump for patients with particular conditions. A newly designed pump may be compared with this data to check whether the potential performance is equivalent, below or above the similar pumps.

The author hopes that the blood pump designers and developers will publish and report more nondimensional experimental data of small pumps and not only limited to axial and centrifugal types. Considerably more work will need to be done to

determine a more extensive and comprehensive version of these diagrams and be able to predict and generate iso-efficiency lines on them.

This dissertation has also made a contribution to the National Health Service (NHS) project TURBOCARDIA, awarded £1.2m by the Invention for Innovation (i4i) program of the National Institute for Health Research (NIHR) of the United Kingdom. The project is on the design and development of a novel centrifugal blood pump. The analytical model and experimental results presented in this dissertation have been used in TURBOCARDIA project to design an efficient and hemocompatible impeller to be featured in the designed product. The team has submitted a new proposal for the design and development of a novel axial blood pump. Hopefully in case of proposal acceptance, the axial pump results presented in this dissertation will help to design an efficient and hemocompatible axial impeller for the device.

Bibliography

- [1] K. D. Aaronson, M. J. Eppinger, D. B. Dyke, S. Wright, and F. D. Pagani. Left ventricular assist device therapy improves utilization of donor hearts. *Journal of the American College Of Cardiology*, 39(8):1247–1254, 17th Apr. 2002.
- [2] D. Adkins and C. Brennen. Analysis of hydrodynamic radial forces on centrifugal pump impellers. *Journal of Fluids Engineering*, 110:20–28, March 1988.
- [3] A. Agostinelli, D. Nobles, and C. R. Mockridge. An experimental investigation of radial thrust in centrifugal pumps. *Journal of Engineering for Power*, pages 120–126, April 1960.
- [4] T. Akamatsu, T. Nakazeki, and H. Itoh. Centrifugal blood pump with a magnetically suspended impeller. *Artificial Organs*, 16(3):305–308, 1992.
- [5] H. Alemi, S. Nourbakhsh, M. Raisee, and A. Najafi. Effects of volute curvature on performance of a low specific-speed centrifugal pump at design and off-design conditions. *Journal of Turbomachinery*, 137(4), 2015.
- [6] P. E. Allaire, H. C. Kim, E. H. Maslen, D. B. Olsen, and G. B. Bearnson. Prototype continuous flow ventricular assist device supported on magnetic bearings. *Artificial Organs*, 20(6):582–590, 1996.
- [7] P. E. Allaire, E. Maslen, H. Kim, G. B. Bearnson, and D. B. Olsen. Design of a magnetic bearing supported prototype centrifugal artificial heart pump. *Tribology Transactions*, 39(3):663–669, 1996.
- [8] G. S. Allen, K. D. Murray, and D. B. Olsen. The importance of pulsatile and nonpulsatile flow in the design of blood pumps. *Artificial Organs*, 21(8):922–928, Aug. 1997.
- [9] J. B. Anderson, H. G. Wood, P. E. Allaire, G. B. Bearnson, and P. Khanwilkar. Computational flow study of the continuous flow ventricular assist device, prototype number 3 blood pump. *Artificial Organs*, 24(5):377–385, 2000.

- [10] D. Arora, M. Behr, and M. Pasquali. Hemolysis estimation in a centrifugal blood pump using a tensor-based measure. *Artificial Organs*, 30(7):539–547, 2006.
- [11] M. Asuaje, F. Bakir, S. Kouidri, F. Kenyery, and R. Rey. Numerical modelization of the flow in centrifugal pump: Volute influence in velocity and pressure fields. *International Journal of Rotating Machinery*, 3:244–255, 2005.
- [12] O.E. Balje. *Turbomachines*. Wiley, 1981.
- [13] L. A. Baloa, J. R. Boston, and J. F. Antaki. Elastance-based control of a mock circulatory system. *Annals of Biomedical Engineering*, 29(3):244–251, 2001.
- [14] L. E. Barker. The total artificial heart. *AACN Clin Issues Crit Care Nurs*, 2(3):587–597, 1991.
- [15] C. R. Bartoli, G. A. Giridharan, K. N. Litwak, M. Sobieski, S. D. Prabhu, M. S. Slaughter, and S. C. Koenig. Hemodynamic responses to continuous versus pulsatile mechanical unloading of the failing left ventricle. *ASAIO*, 56:410–416, 2010.
- [16] D. Baun and R. Flack. Effects of volute design and number of impeller blades of lateral impeller forces and hydraulic performance. *International Journal of Rotating Machinery*, 9(2):145–152, 2003.
- [17] D. O. Baun and R. D. Flack. A plexiglas research pump with calibrated magnetic bearings / load cells for radial and axial hydraulic force measurement. *Journal of Fluids Engineering*, 121:126–132, 1999.
- [18] M. Behbahani, M. Behr, M. Hormes, U. Steinseifer, D. Arora, O. Coronado, and M. Pasquali. A review of computational fluid dynamics analysis of blood pumps. *European Journal of Applied Mathematics*, 20(4):363–397, AUG 2009.
- [19] P.R. Bevington and D.K. Robinson. *Data Reduction and Error Analysis for the Physical Sciences*. McGraw-Hill, 3 edition, 2003.
- [20] F. Boehning, D. L. Timms, F. Amaral, L. Oliveira, R. Graefe, P. Hsu, T. Schmitz-Rode, and U. Steinseifer. Evaluation of hydraulic radial forces on the impeller by the volute in a centrifugal rotary blood pump. *Artificial Organs*, 35(8):818–825, 2011.
- [21] E. Buckingham. On physically similar systems; illustrations of the use of dimensional equations. *Physical Review*, 4:345–376, 1914.
- [22] E. Buckingham. The principle of similitude. *Nature*, 96:396–397, 1915.

- [23] D. J. Burke, E. Burke, F. Parsaie, V. Poirier, K. Butler, D. Thomas, L. Taylor, and T. Maher. The heartmate ii: Design and development of a fully sealed axial flow left ventricular assist system. *Artificial Organs*, 25(5):380–385, May 2001.
- [24] A. Carpentier, D. H. Adams, and F. Filsoofi. *Carpentier's Reconstructive Valve Surgery*. Saunders, 2010.
- [25] Chris H.H. Chan, Ina Laura Pieper, Rebecca Hambly, Gemma Radley, Alyssa Jones, Yasmin Friedmann, Karl M. Hawkins, Stephen Westaby, Graham Foster, and Catherine A. Thornton. The centrimag centrifugal blood pump as a benchmark for in vitro testing of hemocompatibility in implantable ventricular assist devices. *Artificial Organs*, 39(2):93–101, 2015.
- [26] C. Christiansen, A. Klocke, and R. Autschbach. Past, present, and future of long-term mechanical cardiac support in adults. *Journal of Cardiac Surgery*, 23(6):664–676, Nov-Dec 2008.
- [27] L. P. Chua, K. S. Ong, C. M. Yu, and T. Zhou. Leakage flow measurements in a biocentrifugal ventricular assist device model. *Artificial Organs*, 27(10):942–959, 2003.
- [28] O. Cordier. *Ahnlichkeitsbedingungen fur Stromungsmaschinen*, volume 5. BWK Zeitschrift, 1953.
- [29] Anthony R. Curtas, Houston G. Wood, Paul E. Allaire, James C. McDaniel, Steven W. Day, and Don B. Olsen. Computational fluid dynamic modelling of impeller designs for the heartquest left ventricular assist device. *ASAIO*, 48:552 – 561, 2002.
- [30] Hydraulic Institute definition. Centrifugal pumps - for nomenclature, definitions, application and operation. ansi-hi standards. hydraulic institute, new jersey 1994.
- [31] Milos Teodor Dimitris Papantonis. *Centrifugal Pumps*. InTech, 2012.
- [32] R. D. Dowling, L. A. Gray, S. W. Etoch, H. Laks, D. Marelli, L. Samuels, J. Ebtwhistle, G. Couper, G. J. Vlahakes, and O. H. Frazier. The abiocor implantable replacement heart. *Annals of Thoracic Surgery*, 75(6, S):S93–S99, Jun. 2003.
- [33] T. Drews, M. Jurmann, D. Michael, P. Miralem, Y. Weng, and R. Hetzer. Differences in pulsatile and non-pulsatile mechanical circulatory support in long-term use. *Journal of Heart and Lung Transplantation*, 27(10):1096–1101, Oct. 2008.

- [34] E. A. Farkas and J. A. Elefteriades. Assisted circulation: experience with the novacor (r) left ventricular assist system. *Expert Review of Medical Devices*, 4(6):769–774, Nov. 2007.
- [35] D. J. Farrar, W. R. Holman, L. R. McBride, R. L. Kormos, T. B. Icenogle, P. J. Hendry, C. H. Moore, D. Y. Loisanse, A. El-Banayosy, and H. Frazier. Long-term follow-up of thoratec ventricular assist device bridge-to-recovery patients successfully removed from support after recovery of ventricular function. *Journal of Heart and Lung Transplantation*, 21(5):516–521, May 2002.
- [36] J. A. Finegold, P. Asaria, and D. P. Francis. Mortality from ischaemic heart disease by country, region, and age: Statistics from WHO and UN. *International Journal of Cardiology*, 168(2):934 – 945, 2013.
- [37] R. Flack and P. Allaire. Lateral forces on pump impellers : A literature review. *Shock and Vibration Digest*, 16(1):5–14, 1984.
- [38] K. H. Fraser, M. E. Taskin, B. P. Griffith, and Z. J. Wu. The use of computational fluid dynamics in the development of ventricular assist devices. *Med Eng Phys*, 33(3):263–280, 2011.
- [39] K. H. Fraser, T. Zhang, M. E. Taskin, B. P. Griffith, and Z. J. Wu. A quantitative comparison of mechanical blood damage parameters in rotary ventricular assist devices: shear stress, exposure time and hemolysis index. *Journal of Biomechanical Engineering*, 134, 2012.
- [40] O. H. Frazier, T. J. Myers, R. K. Jarvik, S. Westaby, D. W. Pigott, I. D. Gregoric, T. Khan, D. W. Tamez, J. L. Conger, and M. P. Macris. Research and development of an implantable, axial-flow left ventricular assist device: the jarvik 2000 heart. *Annals of Thoracic Surgery*, 71:125–132, 2001.
- [41] K. Fukamachi, A. Shiose, A. Massiello, D. J. Horvath, L. R. Golding, S. Lee, and R. C. Starling. Preload sensitivity in cardiac assist devices. *Thoracic Surgery*, 95(1):373–380, 2013.
- [42] M. J. Gartner, C. R. wilhelm, K. L. Gage, M. C. Fabrizio, and W. R. Wagner. Modeling flow effects on thrombotic deposition in a membrane oxygenator. *Artificial Organs*, 24:29–36, 2000.
- [43] R. L. Gerhart, D. J. Horvath, Y. Ochiai, A. Y. Krogulecki, and L. A. Golding. The effects of impact on the coraide ventricular assist device. *ASAIO*, 48(4):449–452, 2002.
- [44] M. Giersiepen, L.J. Wurzinger, R. Opitz, and H. Reul. Estimation of shear stress-related blood damage in heart valve prosthesesin vitro comparison of 25 aortic valves. *Artificial Organs*, 13:300–306, 1990.

- [45] G. A. Giridharan, S. C. Koenig, and M. S. Slaughter. Do axial-flow lvads unload better than centrifugal-flow lvads? *ASAIO*, 60(2):137–9, 2014.
- [46] Johann Friedrich Glich. *Centrifugal Pumps*. Springer Science & Business Media, 2007.
- [47] L. R. Golding, G. Jacobs, T. Murakami, S. Takatani, F. Valdes, H. Harasaki, and Y. Nose. Chronic non-pulsatile blood-flow in an alive, awake animal 34-day survival. *Transactions American Society for Artificial Internal Organs*, 26:251–255, 1980.
- [48] M. Goldowsky. Magnevad - the world’s smallest magnetic-bearing turbo pump. *Artificial Organs*, 28(10):945–952, Oct. 2004.
- [49] I. D. Gregoric, S. La Francesca, T. Myers, W. Cohn, P. Loyalka, B. Kar, C. Gemmato, and O. H. Frazier. A less invasive approach to axial flow pump insertion. *Journal of Heart and Lung Transplantation*, 27(4):423–426, Apr. 2008.
- [50] B. P. Griffith, R. L. Kormos, H. S. Borovetz, K. Litwak, J. F. Antaki, V. L. Poirier, and K. C. Butler. Heartmate ii left ventricular assist system: From concept to first clinical use. *Annals of Thoracic Surgery*, 71(3, S):S116–S120, Mar. 2001.
- [51] W. Guelich, J. F. and Jud and S. F. Hughes. Review of parameters influencing hydraulic forces on centrifugal impellers. *Proc Instn Mech Engrs*, 201(A3):163–174, 1987.
- [52] R. Hetzer, E. V. Potapov, Y. G. Weng, H. Sinawski, F. Knollmann, T. Komoda, E. Hennig, and M. Pasic. Implantation of micromed debakey vad through left thoracotomy after previous median sternotomy operations. *Annals of Thoracic Surgery*, 77(1):347–350, Jan. 2004.
- [53] R. Hetzer, Y. G. Weng, E. V. Potapov, M. Pasic, T. Drews, M. Jurmann, E. Hennig, and J. Muller. First experiences with a novel magnetically suspended axial flow left ventricular assist device. *European Journal of Cardio-Thoracic Surgery*, 25(6):964–970, Jun. 2004.
- [54] G. Heuser and R. Opitz. A couette viscometer for short time shearing of blood. *Biorheology*, 17(1-2):17–24, 1980.
- [55] J.D. Hill and O. Reinhartz. Clinical outcomes in pediatric patients implanted with thoratec ventricular assist device. *Seminars in Thoracic and Cardiovascular Surgery: Pediatric Cardiac Surgery Annual*, 9(1):115–122, 2006.

- [56] Sharon A. Hunt. Taking heart - cardiac transplantation past, present, and future. *New England Journal of Medicine*, 355(3):231–235, Jul 20 2006.
- [57] D. Japikse and N. C. Baines. *Introduction to Turbomachinery*. Oxford University Press, Oxford, 1994.
- [58] D. Japikse, W. Marscher, and R. B. Furst. Centrifugal pump design and performance. Technical report, Concepts EI, Vermont, USA, 1997.
- [59] B. Jery, C. E. Brennan, T. K. Caughey, and A. J. Acosta. Forces on centrifugal pump impellers. *Proceedings of the Second International Pump Symposium, TEXAS*, 1985.
- [60] B. Kar, R. M. Delgado, O. H. Frazier, I. D. Gregoric, M. T. Harting, Y. Wadia, T. J. Myers, R. D. Moser, and J. Freund. The effect of lvad investigation aortic outflow-graft placement on hemodynamics and flow - implantation technique and computer flow modeling. *Texas Heart Institute Journal*, 32(3):294–298, 2005.
- [61] I. J. Karassik, J. P. Messina, P. Cooper, and C. Heald. *Pump Handbook*. McGra, 3 edition, 2000.
- [62] H. K. Kim, H. S. Son, Y. H. Fang, S. Y. Park, C. M. Hwang, and K. Sun. The effects of pulsatile flow upon renal tissue perfusion during cardiopulmonary bypass: A comparative study of pulsatile and nonpulsatile flow. *ASAIO Journal*, 51(1):30–36, Jan.-Feb. 2005.
- [63] S. Kim, Y. I. Cho, W. N. Hogenauer, and K. R. Kensey. A method of isolating surface tension and yield stress effects in a U-shaped scanning capillary-tube viscometer using a Casson model. *Journal of Non-Newtonian Fluid Mechanics*, 103(2-3):205 – 219, March 2002.
- [64] T. Komoda, Y. Weng, C. Nojiri, and R. Hetzer. Implantation technique for the duraheart left ventricular assist system. *Journal of Artificial Organs*, 10(2):124–127, 2007.
- [65] R. Kopp, K. Mottaghy, and M. Kirschfink. Mechanism of complement activation during extracorporeal blood-biomaterial interaction: Effects of heparin coated and uncoated surfaces. *ASAIO*, 48(6):598–605, 2002.
- [66] T. Korakianitis, M. A. Rezaenia, G. Paul, A. Rahideh, M. T. Rothman, and S. Mozafari. Optimization of centrifugal pump characteristic dimensions for mechanical circulatory support devices. *ASAIO*, 62(5):545–551, 2016.

- [67] R. Krishnamani, D. DeNofrio, and M. A. Konstam. Emerging ventricular assist devices for long-term cardiac support. *Nature Reviews Cardiology*, 7:71–76, 2010.
- [68] B. LAKSHMINARAYANA and J. H. HORLOCK. Tip-clearance flow and losses for a compressor blade. Technical report, Ministry of Aviation, Aeronautical Research Council Reports and Memoranda, 1962.
- [69] S. Lazarkiewicz and A. Troskolanski. *Impeller Pumps*. Pergamon Press, 1965.
- [70] L. B. Leverett, J. D. Hellums, C. P. Alfrey, and E. C. Lynch. Red blood cell damage by shear stress. *Biophysics Journal*, 12:257–273, 1972.
- [71] B. D. Levine, L. D. Lane, J. C. Buckey, D. B. Friedman, and C. G. Blomqvist. Left ventricular pressure-volume and frank-starling relations in endurance athletes. implications for orthostatic tolerance and exercise performance. *Circu*, 84:1016–1023, 1991.
- [72] W. G. Li. Effects of viscosity of fluids on centrifugal pump performance and flow pattern in the impeller. *International Journal of Heat and Fluid Flow*, 21(2):207–212, 2000.
- [73] D. Liotta, C. W. Hall, D. A. Cooley, and M. E. De Bakey. Prolonged ventricular bypass with intrathoracic pumps. *Transactions - American Society for Artificial Internal Organs*, 10:154–156, 1964.
- [74] K. N. Litwak, S. C. Koenig, R. C. Cheng, G. A. Giridharan, K. J. Gillars, and G. M. Pantalos. Ascending aorta outflow graft location and pulsatile ventricular assist provide optimal hemodynamic support in an adult mock circulation. *Artificial Organs*, 29(8):629–635, Aug. 2005.
- [75] J. Lloyd. Heart disease and stroke statistics-2009 update: A report from the american heart association statistics committee and stroke statistics subcommittee (vol 119, pg e21, 2009). *Circulation*, 124(16):E424, Oct 18 2011.
- [76] V. Lobanoff and R. Ross. *Centrifugal Pumps: Design and Application*. Gulf Publishing Company, 1985.
- [77] J. A. Lorett and S. Gopalakrishnan. Interaction between impeller and volute of pumps at off-design conditions. *Journal of Fluids Engineering*, 108:12–18, March 1986.
- [78] M. Macris, T. J. Myers, and R. Jarvik. In vivo revolution of an electric intraventricular axial flow pump assist device. *Asaio Journal*, 40:719–722, 1994.

- [79] E. H. Maslen, G. B. Bearnson, P. E. Allaire, R. D. Flack, M. Baloh, E. Hilton, M. D. Noh, D. B. Olsen, P. S. Khanwilkar, and J. D. Long. Feedback control applications in artificial hearts. *IEEE Control Systems Magazine*, 18(6):26–34, 1998.
- [80] E. H. Maslen and M. Noh. Self sensing active magnetic bearings based on parameter estimation. *IEEE Transactions on Instrumentation and Measurement*, 1996.
- [81] T. Masuzawa, S. Ezoe, T. Kato, and Y. Okada. Magnetically suspended centrifugal blood pump with an axially levitated motor. *Artificial Organs*, 27(7):631–638, 2003.
- [82] S. M. Mehta, W. E. Pae, C. Rosenberg, A. J. Snyder, W. J. Weiss, J. P. Lewis, M. Eng, D. J. Frank, M. Eng, J. J. Thompson, and W. S. Pierce. The lionheart lvd-2000: A completely implanted left ventricular assist device for chronic circulatory support. *Annals of Thoracic Surgery*, 71(3, S):S156–S161, Mar. 2001.
- [83] Y. Miyazoe, T. Sawairi, K. Ito, Y. Konishi, T. Yamane, M. Nishida, B. Asztalos, T. Masuzawa, T. Tsukiya, S. Endo, and Y. Taenaka. Computational fluid dynamics analysis to establish the design process of a centrifugal blood pump : Second report. *Artificial Organs*, 23(8):762–768, 1999.
- [84] S. Mozafari, M. A. Rezaenia, G. Paul, M. T. Rothman, P. Wen, and T. Korakianitis. The effect of geometry on the efficiency and hemolysis of centrifugal implantable blood pumps. *ASAIO*, 63(1):53–59, 2017.
- [85] T. J. Myers, T. Khan, and O. H. Frazier. Infectious complications associated with ventricular assist systems. *ASAIO Journal*, 46(6):S28–S36, Nov.-Dec. 2000.
- [86] C. G. Nevaril, J. D. Hellums, C. P. Alfrey, and E. C. Lynch. Physical effects in red blood cell trauma. *AIChE Journal*, 15(5):707–711, 1969.
- [87] M. Nichols, N. Townsend, R. Luengo-Fernandez, J. Leal, A. Gray, P. Scarborough, and M. Rayner. European cardiovascular disease statistics 2012. European Heart Network, Brussels, European Society of Cardiology, Sophia Antipolis, 2012.
- [88] H. Nishida, H. Uesugi, T. Nishinaka, K. Uwabe, S. Aomi, M. Endo, H. Koyanagi, H. Oshiyama, A. Nogawa, and T. Akutsu. Clinical evaluation of pulsatile flow mode of terumo capiox centrifugal pump. *Artificial Organs*, 21(7):816–821, 1997.

- [89] M. Nishida, B. Asztalos, T. Yamane, T. Masuzawa, T. Tsukiya, S. Endo, Y. Taenaka, Y. Miyazoe, K. Ito, and Y. Konishi. Flow visualisation study to improve hemocompatibility of a centrifugal blood pump. *Artificial Organs*, 23(8):697–703, 1999.
- [90] Y. Nose, M. Yoshikawa, S. Murabayashi, and T. Takano. Development of rotary blood pump technology: Past, present, and future. *Artificial Organs*, 24(6):412–420, 2000.
- [91] P. S. Olegario, M. Yoshizawa, A. Tanaka, K. Abe, H. Takeda, T. Yambe, and S. Nitta. Outflow control for avoiding atrial suction in a continuous flow total artificial heart. *Artificial Organs*, 27(1):92–98, 2003.
- [92] C. H. Park, K. Nishimura, T. Akamatsu, T. Tsukiya, K. Matsuda, and T. Ban. A new magnetically suspended centrifugal pump - in vitro and preliminary in vivo assessment. *Artificial Organs*, 20(2):128–131, 1996.
- [93] M. Pasic, P. Bergs, E. Hennig, M. Loebe, Y. G. Weng, and R. Hetzer. Simplified technique for implantation of a left ventricular assist system after previous cardiac operations. *Annals of Thoracic Surgery*, 67(2):562–564, Feb. 1999.
- [94] Karnal Patel. *Design and Development of a Pulsatile Axial Flow Blood Pump as a Left Ventricular Assist Device*. PhD thesis, Brunel Institute for Bioengineering, Brunel University, 2011.
- [95] R. Paul, J. Apel, S. Klaus, F. Schugner, P. Schwindke, and H. Reul. Shear stress related blood damage in laminar couette flow. *Artificial Organs*, 27(6):517–529, 2003.
- [96] K. A. Pennings, J. R. Martina, and B. F. et al. Rodermans. Pump flow estimation from pressure head and power uptake for the heartassist5, heartmate ii, and heartware vads. *ASAIO*, 59:420–426, 2013.
- [97] K. X. Qian, P. Zeng, W. M. Ru, and H. Y. Yuan. Streamlined design of impeller and its effect on pump haemolysis. *Journal Of Medical Engineering & Technology*, 24(6):79–81, 2002.
- [98] Y. Qian and C. D. Bertram. Computational fluid dynamics analysis of hydrodynamic bearings of the ventrassist rotary blood pump. *Artificial Organs*, 24(6):488–491, 2000.
- [99] O. Reitan, S. Steen, and H. Ohlin. Hemodynamic effects of a new percutaneous circulatory support device in a left ventricular failure model. *ASAIO Journal*, 49:731–736, 2003.

- [100] O. Reitan, J. Sternby, and H. Ohlin. Hydrodynamic properties of a new percutaneous intra-aortic axial flow pump. *ASAIO Journal*, 46:323–329, 2000.
- [101] H. M. Reul and M. Akdis. Blood pumps for circulatory support. *Perfusion*, 15:295–311, 2000.
- [102] M. A. Rezaenia, G. Paul, E. Avital, S. Mozafari, M. T. Rothman, and T. Korakianitis. In-vitro investigation of the hemodynamic responses of the cerebral, coronary and renal circulations with a rotary blood pump installed in the descending aorta. *Journal of Medical Engineering and Physics*, 40:2–10, 2017.
- [103] M. A. Rezaenia, A. Rahideh, B. A. Hamedani, D. E.M Bosak, Silvia. Zustiac, and T. Korakianitis. Numerical and in vitro investigation of a novel mechanical circulatory support device installed in the descending aorta. *Artificial Organs*, Article first published online, 2015.
- [104] M. A. Rezaenia, A. Rahideh, M. T. Rothman, S. A. Sell, K. Mitchell, and T. Korakianitis. In vitro comparison of two different mechanical circulatory support devices installed in series and in parallel. *Artificial Organs*, 38:800–809, 2014.
- [105] Mohammad Amin Rezaenia. *Design of a Cardiovascular Blood Flow Simulator and Utilization in Hemodynamic Evaluation of Mechanical Circulatory Support Devices*. PhD thesis, School of Engineering and Materials Science, Queen Mary University of London, 2013.
- [106] A. G. Rose, S. J. Park, A. J. Bank, and L. W. Miller. Partial aortic valve fusion induced by left ventricular assist device. *Annals of Thoracic Surgery*, 70(4):1270–1274, Oct. 2000.
- [107] R. F. Salamonsen, D. G. Mason, and P. J. Ayre. Response of rotary blood pumps to changes in preload and afterload at a fixed speed setting are unphysiological when compared with the natural heart. *Artificial Organs*, 35:E47–E53, 2011.
- [108] L. E. Samuels, J. C. Entwistle, E. C. Holmes, T. Parris, and A. S. Wechsler. Mechanical support of the unrepaired postinfarction ventricular septal defect with the abimed bvs 5000 ventricular assist device. *Journal of Thoracic and Cardiovascular Surgery*, 126(6):2100–2101, Dec. 2003.
- [109] D. D. Schocken, M. I. Arrieta, P. E. Leaverton, and E. A. Ross. Prevalence and mortality-rate of congestive-heart-failure in the united-states. *Journal of The American College of Cardiology*, 20(2):301–306, Aug. 1992.

- [110] R. Schoeb, N. Barletta, M. Weber, and R. von Rohr. A bearingless motor for a left ventricular assist device. In *International Symposium on Magnetic Bearings, ETH Zurich.*, 2000.
- [111] C. H. Selzman and B. C. Sheridan. Off-pump insertion of continuous flow left ventricular assist devices. *Journal of Cardiac Surgery*, 22(4):320–322, Jul.-Aug. 2007.
- [112] A. Sezai, M. Shiono, Y. Orime, K. Nakata, M. Hata, M. Iida, S. Kashiwazaki, J. Kinoshita, M. Nemoto, T. Koujima, M. Furuichi, K. Eda, H. Hirose, T. Yoshino, A. Saitoh, T. Taniguchi, and Y. Sezai. Major organ function under mechanical support: Comparative studies of pulsatile and nonpulsatile circulation. *Artificial Organs*, 23(3):280–285, Mar. 1999.
- [113] Y. Shi and T. Korakianitis. Numerical simulation of cardiovascular dynamics with left heart failure and in-series pulsatile ventricular assist device. *Artificial Organs*, 30(12):929–948, December 2006.
- [114] A. J. Sipin and et al. Bender, B. Purge system for rotary blood pumps. *Artificial Organs*, 21(7):611–619, 1997.
- [115] M. S. Slaughter, C. R. Bartoli, and M. A. et al. Sobieski. Intraoperative evaluation of the heartmate ii flow estimator. *Journal of Heart Lung Transplant*, 28:39–43, 2009.
- [116] M. S. Slaughter, M. A. Sobieski, D. Tamez, T. Horrell, J. Graham, P. S. Pappas, A. J. Tatroles, and J. LaRose. Heartware miniature axial-flow ventricular assist device design and initial feasibility test. *Texas Heart Institute Journal*, 36(1):12–16, Feb. 2009.
- [117] M. J. Slepian, Y. Alemu, J. S. Soares, R. G. Smith, S. Einav, and D. Bluestein. The syncardiatm total artificial heart: in vivo, in vitro, and computational modeling studies. *Journal of Biomechanics*, 46(2):266–275, 2013.
- [118] E. J. Smith, O. Reitan, T. Keeble, K. Dixon, and M. T. Rothman. A first-in-man study of the reitan catheter pump for circulatory support in patients undergoing high-risk percutaneous coronary intervention. *Catheterization and Cardiovascular Interventions*, 73:859–865, 2009.
- [119] W. A. Smith, P. Allaire, J. Antaki, K. C. Butler, W. Kerkhoffs, T. Kink, H. Loree, and H. Reul. Collected nondimensional performance of rotary dynamic blood pumps. *ASAIO Journal*, 50(1):25–32, 2004.

- [120] T. Snage, D. Fvriier, M. Michel, E. Pichot, D. Duveau, S. Tsui, and J. C. Roussel. A mock circulatory system to assess the performance of continuous-flow left ventricular assist devices (lvads): Does axial flow unload better than centrifugal lvad? *ASAIO*, 60(2):140–147, 2014.
- [121] X. Song, A. L. Throckmorton, A. Untaroiu, S. Patel, P. E. Allaire, H. G. Wood, and D. B. Olsen. Axial flow blood pumps. *ASAIO*, 49:355–364, 2003.
- [122] X. Song, A. L. Throckmorton, H. G. Wood, J. F. Antaki, and D. B. Olsen. Computational fluid dynamics prediction of blood damage in a centrifugal pump. *Artificial Organs*, 27:938–941, 2003.
- [123] X. Song, H. G. Wood, S. W. Day, and D. B. Olsen. Studies of turbulence models in a computational fluid dynamics model of a blood pump. *Artificial Organs*, 27:935–937, 2003.
- [124] K. G. Soucy, S. C. Koenig, G. A. Giridharan, M. A. Sobieski, and M. S. Slaughter. Defining pulsatility during continuous-flow ventricular assist device support. *Journal of Heart Lung Transplant*, 32:581–587, 2013.
- [125] K. G. Soucy, S. C. Koenig, G. A. Giridharan, M. A. Sobieski, and M. S. Slaughter. Rotary pumps and diminished pulsatility: Do we need a pulse? *ASAIO*, 59:410–419, 2013.
- [126] J. R. Stanfield and C. H. Selzman. In vitro pulsatility analysis of axial-flow and centrifugal-flow left ventricular assist devices. *Journal of Biomechanical Engineering*, 135(3):034505, 2013.
- [127] J. Stehlik, L. B. Edwards, A. Y. Kucheryavaya, P. Aurora, J. D. Christie, R. Kirk, F. Dobbels, A. O. Rahmel, and M. I. Hertz. The registry of the international society for heart and lung transplantation: twenty-seventh official adult heart transplant report-2010. *Journal of Heart and Lung Transplantation*, 29(10):1089–1103, Oct 2010.
- [128] A. J. Stepanoff. *Centrifugal and Axial Flow Pumps*. John Wiley & Sons, 1957.
- [129] Y. Takami, G. Otsuka, J. Mueller, Y. Sugita, K. Nakata, E. Tayama, Y. Ohashi, H. Schima, H. Schmallegger, E. Wolner, and Y. Nose. In vivo evaluation of the miniaturized gyro centrifugal pump as an implantable ventricular assist device. *Artificial Organs*, 22(8):713–720, 1998.
- [130] T. Takano, S. Schulte-Eistrup, M. Yoshikawa, K. Nakata, S. Kawahito, T. Maeda, K. Nonaka, J. Linneweber, J. Glueck, A. Fujisawa, K. Makinouchi, M. Yokokawa, and Y. Nose. Impeller design for a miniaturised centrifugal blood pump. *Artificial Organs*, 24(10):821–825, 2000.

- [131] S. Takatani. Can rotary blood pumps replace pulsatile devices ? *Artificial Organs*, 25(9):671–674, 2001.
- [132] G. Tansley and M. et al. Cook. Complete passive suspension of the ventrassist rotary blood pump. In *5th International Conference for Motion and Vibration Control (MOVIC 2000)*, 2000.
- [133] G. Tansley, S. Vidakovic, and J. Reizes. Fluid dynamic characteristics of the VentrAssist rotary blood pump. *Artificial Organs*, 24(6):483–487, 2000.
- [134] K. Tasai, S. Takatani, Y. Orime, G. Damm, Y. Ohara, K. Naito, K. Maki-nouchi, K. Mizuguchi, Y. Matsuda, and T. et al Shimono. Successful thermal management of a totally implantable ventricular assist system. *Artificial Or-gans*, 18(1):49–53, 1994.
- [135] M. E. Taskin, K. H. Fraser, T. Zhang, C. Wu, B. P. Griffith, and Z. J. Wu. Evaluation of eulerian and lagrangian models for hemolysis estimation. *ASAIO*, 58(4):363–372, 2012.
- [136] John R. Taylor. *An Introduction to Error Analysis: The Study of Uncertainties in Physical Measurements*. University Science Books, 1997.
- [137] Daniel L. Timms. *Design, Development and Evaluation of Centrifugal Type Ventricular Assist Devices*. PhD thesis, School of Mechanical, Manufacturing and Medical Engineering ,Faculty of Built Environment and Engineering, Queensland University of Technology, 2005.
- [138] N. Tonello, Y. Eude, B. de Laage de Meux, and M. Ferrand. Frozen rotor and sliding mesh models applied to the 3d simulation of the francis-99 tokke turbine with code saturne. In *Journal of Physics: Conference Series*, volume 782, page 012009, 2017.
- [139] G. J. Tortora. *Principles of Anatomy and Physiology*. Harper & Row, 1987.
- [140] A. R. Travis, G. A. Giridharan, and Pantalos G. M. et al. Vascular pulsatility in patients with a pulsatile or continuous flow ventricular assist device. *Journal of Thorac Cardiovascular Surgery*, 133:517–524, 2007.
- [141] T. Tsukiya, T. Akamatsu, K. Nishimura, T. Yamada, and T. Nakazeki. Use of motor current in flow rate measurement for the magnetically suspended centrifugal blood pump. *Artificial Organs*, 21(5):396–401, 1997.
- [142] J. Tuzson. *Centrifugal Pump Design*. John Wiley and Sons Inc., 2000.

- [143] E. Tuzun, K. Eya, H. K. Chee, J. L. Conger, N. K. Bruno, O. H. Frazier, and K. A. Kadipasaoglu. Myocardial hemodynamics, physiology, and perfusion with an axial flow left ventricular assist device in the calf. *ASAIO Journal*, 50(1):47–53, Jan.-Feb. 2004.
- [144] N. Uchida, K. Imaichi, and T. Shirai. Radial force on the impeller of a centrifugal pump. *Bulletin of the JSME*, 14(76):1106–1117, 1971.
- [145] A. Undar. Myths and truths of pulsatile and nonpulsatile perfusion during acute and chronic cardiac support. *Artificial Organs*, 28(5):439–443, May 2004.
- [146] S. Vandenberghe, P. Segers, B. Meyns, and P. R. Verdonck. Effect of rotary blood pump failure on left ventricular energetics assessed by mathematical modeling. *Artificial Organs*, 26(12):1032–1039, 2002.
- [147] R. Wampler, D. Lancisi, V. Indravudh, R. Gauthier, and R. Fine. A sealless centrifugal blood pump with passive magnetic and hydrodynamic bearings. *Artificial Organs*, 23(8):780–784, 1999.
- [148] P. A. Watterson, J. C. Woodard, V. S. Ramsden, and J. A. Reizes. Ventriassist hydrodynamically suspended, open, centrifugal blood pump. *Artificial Organs*, 24(6):475–477, 2000.
- [149] R. W. Westra. *Inverse-design and optimization methods for centrifugal pump impellers*. PhD thesis, University of Twente, 2008.
- [150] D. G. Wilson and T. Korakianitis. *The design of high-efficiency turbomachinery and gas turbines*. The MIT Press, 1984.
- [151] G. F. Wislicenus. *Fluid Mechanics of Turbomachinery*. McGraw-Hill Book Company, New York, 1947.
- [152] H. G. Wood, A. L. Throckmorton, A. Untaroiu, and X. Song. The medical physics of ventricular assist devices. *Reports on Progress in Physics*, 68(31), 2005.
- [153] Y. Wu, P. E. Allaire, G. Tao, M. Adams, Y. Liu, H. Wood, and D. B. Olsen. A bridge from short-term to long-term left ventricular assist device : Experimental verification of a physiological controller. *Artificial Organs*, 28(10):927–932, 2004.
- [154] T. Yamane, T. Ikeda, T. Orita, and T. Tateishi. Fluid dynamics of turbo pumps for artificial hearts. *Materials Science and Engineering*, C4:99–106, 1996.

- [155] T. Yamane, M. Nishida, T. Kijima, and J. Maekawa. New mechanism to reduce the size of the monopivot magnetic suspension blood pump - direct drive mechanism. *Artificial Organs*, 21(7):620–624, 1997.
- [156] K. Yamazaki, P. Litwak, R. L. Kormos, T. Mori, O. Tagusari, J. F. Antaki, M. Kamenava, M. Watach, L. Gordon, M. Umezu, J. Tomioka, H. Koyanagi, and B. P. Griffith. An implantable centrifugal blood pump for long term circulatory support. *ASAIO*, 43:686–691, 1997.
- [157] K. Yamazaki, P. Litwak, O. Tagusari, T. Mori, K. Kono, M. Kamenava, M. Watach, L. Gordon, M. Miyagishima, J. Tomioka, M. Umezu, E. Outa, J. F. Antaki, R. L. Kormos, H. Koyanagi, and B. P. Griffith. An implantable centrifugal blood pump with a recirculating purge system (cool-seal system). *Artificial Organs*, 22(6):466–474, 1998.
- [158] C. W. Yancy, M. Jessup, B. Bozkurt, J. Butler, D. E. Casey, M. H. Drazner, G. C. Fonarow, S. A. Geraci, T. Horwich, J. L. Januzzi, M. R. Johnson, E. K. Kasper, W. C. Levy, F. A. Masoudi, P. E. McBride, J. J. V. McMurray, J. E. Mitchell, P. N. Peterson, B. Riegel, F. Sam, L. W. Stevenson, W. H. W. Tang, E. J. Tsai, and B. L. Wilkoff. 2013 ACCF/AHA guideline for the management of heart failure, a report of the ACCF/AHA task force on practice guidelines. *Journal of the American College of Cardiology*, 62(16):e147–e239, 2013.
- [159] J. Zhang, P. Zhang, K. H. Fraser, B. P. Griffith, and Z. J. Wu. Comparison and experimental validation of fluid dynamic numerical models for a clinical ventricular assist device. *Artificial Organs*, 37(4):380–389, 2013.
- [160] Tao Zhang, M. Ertan Taskin, Hong-Bin Fang, Adam Pampori, Robert Jarvik, Bartley P. Griffith, and Zhongjun J. Wu. Study of flow-induced hemolysis using novel couette-type blood-shearing devices. *Artificial Organs*, 35(12):1180–1186, 2011.